2011

Polydispersed bubbly flow model for ship hydrodynamics with application to Athena R/V

Alejandro Miguel Castro
University of Iowa

POLYDISPERSED BUBBLY FLOW MODEL FOR SHIP HYDRODYNAMICS WITH APPLICATION TO ATHENA R/V

by

Alejandro Miguel Castro

An Abstract

Of a thesis submitted in partial fulfillment of the
requirements for the Doctor of Philosophy degree
in Mechanical Engineering
in the Graduate College of
The University of Iowa

December 2011

Thesis Supervisor: Associate Professor Pablo M. Carrica

ABSTRACT

Bubbly flows around ships have been studied for years, mostly in relation with ship acoustic signatures. Bubbles are generated at the bow and shoulder breaking waves, at the hull/free surface contact line, the propeller and the highly turbulent stern flow. These bubbles are further transported downstream by the flow forming a two-phase mixture in the wake that can be kilometers long. The presence of bubbles in the wake of a ship significantly affects the acoustic response of the medium and can be detected by measuring acoustic attenuation and backscattering making a ship vulnerable to detection. Additionally, the bubbly wake shows at the surface as a characteristic signature of *white water*, and given the length of the bubbly wake, it makes a ship visible from satellites. Therefore, the bubbly wake can be used to detect and identify surface ships.

Bubbly flows do not scale to model scale experiments, and experiments on full scale ships are scarce mostly due to difficult access areas and the high speeds involved. It is therefore of interest to simulate the bubbly flow around ships to provide information difficult, if not impossible, to obtain with experiments.

This work presents the development of a code for the simulation of polydispersed bubbly flows with a focus on ship hydrodynamics. The mathematical model implemented is based on a two-fluid formulation coupled with a Boltzmann-like transport equation describing the bubbly phase. The tool developed attempts to include most of the relevant physics of the problem to represent better the conditions of real scenarios. The resulting code allows the simulation of polydispersed bubbly flows in situations including free surface and air entrainment, high void fraction levels and moving control surfaces and propulsors. The code is two-way coupled, with a strong coupling between the two phases and between the bubble sizes.

The complexity of the problems tackled in this research required the develop-

ment of novel numerical methods solving issues never identified before or simply neglected. These methods play an essential role in the accuracy, robustness and efficiency of the code and include: a two-phase projection method that not only couples pressure and velocity but also implicitly couples void fraction, a time splitting marching scheme to solve separately coupling in space and in bubble sizes, and a stable numerical method to integrate the strong coupling introduced by collision forces.

The implemented code is applied to the simulation of the bubbly flow around a full scale ship using the latest available models and computational techniques. A study is performed on the influence of several mechanisms on the predicted bubbly wake and comparisons with available experimental data are presented. The influence of breakup in the boundary layer is analyzed in detail as well. In addition, this work identifies several modeling and implementations issues and attempts to provide a path for future studies.

To illustrate the flexibility and robustness of the code, a final demonstration case is presented that includes rotating propellers. The computation is performed at full scale, with the fully appended geometry of the vessel and includes incoming waves, oceanic background and rectified diffusion models. Many of these features are unique to this computation and make it the first of its kind.

Abstract Approved: _____

Thesis Supervisor

_____

Title and Department

_____

Date

POLYDISPERSED BUBBLY FLOW MODEL FOR SHIP HYDRODYNAMICS WITH APPLICATION TO ATHENA R/V

by

Alejandro Miguel Castro

A thesis submitted in partial fulfillment of the
requirements for the Doctor of Philosophy degree
in Mechanical Engineering
in the Graduate College of
The University of Iowa

December 2011

Thesis Supervisor: Associate Professor Pablo M. Carrica

Graduate College
The University of Iowa
Iowa City, Iowa

CERTIFICATE OF APPROVAL

PH.D. THESIS

This is to certify that the Ph.D. thesis of

Alejandro Miguel Castro

has been approved by the Examining Committee for the thesis requirement for the Doctor of Philosophy degree in Mechanical Engineering at the December 2011 graduation.

Thesis Committee: _____
Pablo M. Carrica, Thesis Supervisor

_____
Christoph Beckermann

_____
Mark Hyman

_____
Frederick Stern

_____
H.S. Udaykumar

To my parents and sister

ACKNOWLEDGEMENTS

First and foremost, I owe my deepest gratitude to my thesis supervisor Pablo M. Carrica, whose constant support helped me along my journey. Pablo, thank you for your guidance, encouragement, critique (lots of it) and, most of all, your friendship. Thank you for your constant and virtually endless willingness to teach and stimulate my imagination. I feel immensely fortunate for having had you as my thesis supervisor and I am deeply grateful for the lessons you have taught me not only on a professional level, but also on a personal level.

I am also very grateful to Marcela Politano, Pablo's wife, who would come downstairs to my cubicle to provide me with warm and calming words in times of deadlines when I was about to loose it. I also had the chance to professionally interact with Marcela and I can say that those interactions were very beneficial and influential for my education.

I would like to specially thank Dr. Mark Hyman, the first user of our code, for his suggestions, comments, useful discussions and for providing the geometry for Athena's propeller. Dr. Hyman traveled from Pasadena, CA to Iowa City not only for my final PhD defense but also for my comprehensive examination. I know how busy his schedule is and therefore I am very grateful for this.

I am grateful to my thesis committee members, who took time out of their busy schedule to review my thesis and provided helpful suggestions and advice.

This work was sponsored by the US Office of Naval Research grant N00014-08-1-1084, under the administration of Dr. Patrick Purtell whose support is greatly appreciated.

TABLE OF CONTENTS

LIST OF TABLES

Table

LIST OF FIGURES

Figure

CHAPTER 1
INTRODUCTION

1.1 Background

Two-phase flows are a particular branch of fluid mechanics involving fluid composites. Fluid composites are composites that can be made to flow and are often referred as multicomponent fluids (Drew and Passman, 1999). Multicomponent fluids occur very commonly in both nature and technology. Examples of multicomponent fluids in nature include clouds, which are a visible mass of droplets or frozen ice crystals, blood in vertebrates composed of blood cells suspended in a liquid called blood plasma and groundwater flow in which water and air flow through the soil. Examples in technology include steam generation in power plants, chemical processes involving mixing, emulsifying and catalysis and oil, gas and water mixtures found in oil wells, among many others.

The mathematical modeling and numerical solution of multiphase flows finds its utility in a wide variety of applications. Numerical simulations have proven the ability to provide detailed information that would be difficult if not impossible to obtain with experiments. Many times a numerical model can provide information in less time and with fewer costs. The numerical solution of multiphase flows finds applications in nuclear engineering (Lahey Jr. et al., 1993; Lahey Jr. and Drew, 2001; Politano et al., 2003; Krepper et al., 2005) where the prediction of bubbly flows in pipes is of interest, in bubble columns (Chen et al., 2005b; Darmana et al., 2005; Zhang et al., 2006) and vertical driven flows (Jakobsen et al., 1997) for the chemical industry, in porous media (Chao-Yang and Beckermann, 1993), in the prediction of Total Dissolved Gas (TDG) in hydropower dams (Politano et al., 2009), in spray atomization for combustors (Apte et al., 2003a; Laurent et al., 2004) and in fluidized beds (Huilin et al., 2003)

1.2 Bubbly Flow Around Ships

Bubbly flows around ships have been studied for years, mostly in relation with ship acoustic signatures. The presence of bubbles in the far-field wake can be determined by acoustic attenuation and backscattering thus making ships detectable by acoustic means (Borowski et al., 2008). In addition, the bubbly wake behind a ship can simply be seen at the sea surface as a characteristic signature of *white water*. This white signature can be used to detect and track ships from satellites.

Several experimental works exist on the acoustic characterization of bubbly wakes (see Trevorrow et al., 1994; Dumbrell, 1997). Acoustic attenuation and backscattering not only allows to acoustically characterize a bubbly wake but also to determine some hydrodynamic characteristics like void fraction and bubble size distribution (see Terrill et al., 2001). However, these kind of measurements are only possible in the far wake of a ship where reflections of acoustic signals on the ship hull are eliminated and where low void fractions make the application of acoustic techniques feasible. Specially difficult is the determination and characterization of the bubbly field in the near-field of a ship where void fractions are high and the presence of the hull makes difficult the use of these methods. In addition these experiments must be performed in full scale since two-phase phenomena do not scale to model scale experiments properly and air entrainment and turbulence are not nearly as high as in full scale. Performing experiments at full scale is a challenging task due to the high velocities involved and difficult access to the areas of interest.

It is for these reasons that while acoustic studies exist in the far wake, studies of the two-phase hydrodynamics in the near field are scarce. Recent developments in this area include the work by Terril and Fu (2008), where an array of conductivity probes was used to measure void fractions at the stern of the Athena II R/V, the work by Jeon et al. (2008) where defocussing DPIV (DDPIV) was used and the

work by Johansen et al. (2010) where optical probes were used to characterize the entrainment sources at the bow, stern and masker also of Athena II R/V.

It is due to this scenario, that the information that could be gained from CFD simulations of the bubbly flow around ships is of considerably importance. The use of CFD in the prediction of the bubbly wake behind a ship has already been used in the past in order to provide of void fraction and size distribution to acoustic dynamics codes (see Culver and Trujillo, 2007). Still, further research is necessary in order to improve the modeling of bubbly flows around ships.

A point of considerable importance is bubble generation and entrainment. Bubbles are generated at the ship's bow and shoulder waves, the hull/free surface contact line, the propeller and the highly turbulent stern flow. Several strategies were proposed in the past to model the entrainment of bubbles, from the manual specification by an experienced modeler (Carrica et al., 1998) to the most recent sub-grid scale models (Ma et al., 2010b). Entrainment modeling is an area that still requires additional research and it is currently one of the weakest points in the simulation of two-phase ship flows.

More recently, bubble-induced drag reduction has attracted increasing interest. Experiments in ships and flat plates reveal drag reductions ranging from 4% to 22% (see Latorre et al., 2003; Sanders et al., 2006; Murai et al., 2007; Elbing et al., 2008). CFD simulations include the works by Kunz et al. (2001) and Xu et al. (2002). Drag reduction in ships would have a major environmental impact considering that international maritime transport carries over 80 per cent of the volume of world trade (UNCTAD, 2009) and that the US Navy consumes roughly on average 4.0 million gallons of fuel per day (Lengyel, 2007).

1.3 Computational Ship Hydrodynamics

CFD has been increasingly used for the simulation of ship flows. One of the most challenging features of this kind of problems is the representation and tracking of the free surface. Surface-tracking methods were probably one of the first numerical discretization techniques used to tackle this problem. In surface-tracking methods the computational grid is fitted to the free surface and follows its motions. Examples of early applications using this technique include resistance computations (Wilson et al., 2001; Burg et al., 2002), forward speed diffraction (Wilson and Stern, 1998; Rhee and Stern, 2001) and pitch and heave in regular waves (Weymouth et al., 2005). Unfortunately, as the deformation of the free surface increases the grid quality deteriorates and eventually computations break down. The next generation of codes for free surface flows around surface-piercing bodies solved this problem with the use of surface-capturing methods. Surface capturing methods include volume of fluid (VOF) (Hirt and Nichols, 1981), front tracking (Unverdi and Tryggvason, 1992) and the level set method (Osher and Sethian, 1988). In CFDShip-Iowa V4.5, the code used for this thesis, the single phase level set method developed by Carrica et al. (2007b) is implemented. Nowadays, the capabilities of the CFD codes used for ship flows have increased considerably and successful applications include large amplitude motions (Carrica et al., 2008), self-propulsion with discretized propellers (Lübke, 2005; Carrica et al., 2010a; Castro et al., 2011), maneuvering with movable controlled appendages (Pankajakshan et al., 2002; Carrica and Stern, 2008) and very large scale computations (Yang et al., 2008; Carrica et al., 2010b).

1.4 Models and Numerical Methods for Two-Phase Flows

The mathematical models and numerical methods used for the simulation of two-phase flows varies according to the application at hand, the required level of

fidelity and the available computational resources (Lahey Jr., 2005). When dealing with a dispersed phase, like the case of bubbles in a main liquid phase or the case of droplets or solid particles in a gaseous phase, several approximations can be made and several models and numerical methods arise.

A first broad categorization is between Eulerian/Lagrangian and Eulerian/Eulerian descriptions. In an Eulerian/Lagrangian framework, the main continuous phase is treated in the usual Eulerian framework used in fluid mechanics while the dispersed phase bubbles or particles are tracked individually in a Lagrangian fashion. This method has been used in the simulation of spray atomization in combustors by Apte et al. (2003a), in sedimentation columns by Patankar and Joseph (2001) and in the prediction of microbubble drag reduction by Xu et al. (2002). In Apte et al. (2003a) breakup of droplets is incorporated in their Lagrangian framework using a stochastic model. Collision effects are more difficult to include and are computationally intensive since a collision detection problem between all particles must be addressed. Techniques from gas dynamics simulations have been adapted to this end by Schmidt and Rutland (2000). In the context of bubbly flows, the work by Zhang and Ahmadi (2005) presents a Lagrangian method for slurry reactors where coalescence is included. Since in the Lagrangian description particles are modeled from first principles, this modeling strategy allows to add complex physics such as shape and orientation in flows with rigid fibers as in Marchioli et al. (2010), agglomeration in gas-particle flows as in Sommerfeld (2010) or bubble size dynamics to include the effect of rectified diffusion as in Hsiao and Chahine (2005). The main drawback of Eulerian/Lagrangian descriptions is the need to interpolate and average particle concentrations and forces used to couple with the main Eulerian phase. A large number of particles per computational cell of the Eulerian phase are needed in order to attain good statistics and obtain smooth forces and concentrations suitable to be used in the Eulerian fluid phase equations. On the

other hand, the knowledge of each individual particle trajectory in the system may result to be an over-detailed description for many engineering applications where very often only mean quantities and maybe other statistics are enough to describe the problem.

In the Eulerian/Eulerian approach, the detailed description of each particle position and velocity is replaced with the solution of a set of conservation equations basically describing the mean probability of finding a dispersed phase particle at a certain point in space and time. In this regard, the Eulerian/Eulerian description offers a very convenient framework since mean quantities and, depending on the model, size distributions or other statistics, are a direct result of the computation and is not necessary to perform several simulations to perform statistics. The name of the method comes from the fact that, as well as for the main continuous phase, the sets of equations describing the statistics of the system are written in an Eulerian framework.

Either the Eulerian/Eulerian or Eulerian/Lagrangian descriptions can be mono or polydispersed. In the Lagrangian framework polydispersed systems are easily treated by just considering different particles classes that may have not only different sizes but also density, temperature, etc. In an the Eulerian/Eulerian framework there is a wide variety of models and levels of simplification that span from single sized particle systems to the more general polydispersed systems. In the Algebraic Slip Mixture Model (ASMM) (Manninen and Taivassalo, 1996; Sanyal et al., 1999) conservation of mass and momentum are postulated for a *mixture* phase with mean properties such as density and viscosity dependent on the concentration of the different phases. A mean slip velocity of the dispersed phase with respect to the main continuous phase is solved algebraically from a simplified dispersed phase momentum equation. In the original ASMM model, bubble size is not predicted but is imposed as a an external parameter based on the modeler experience and/or

available experimental data. In Sanyal et al. (1999) this model is applied to the simulation of cylindrical bubble column reactors. The ASMM model is applied to the prediction of *Total Dissolved Gas* (TDG) in hydropower dams by Politano et al. (2009). However, in the work by Politano et al. (2009), a transport equation for the number density of bubbles is added to the model in order to account for the change in bubble size as gas is dissolved into the water. Therefore, in Politano et al. (2009) only one bubble class is solved for but this is allowed to change its size as the computation evolves. The concept of a *mixture* phase in the ASMM model is also applied in other areas of engineering and appears in other similar models. As an example, the work by Chao-Yang and Beckermann (1993) presents a mixture model for gas flow and heat transfer in porous media.

While in the ASMM model one set of equations is solved for a mixture phase, another popular approach found in the literature is to solve a set of equations for the continuous and dispersed phase separately. Therefore, conservation of mass and momentum are stated for each phase. A model of this kind for monodispersed flows around ships is presented in Paterson et al. (1996) and in Carrica et al. (1998), who used a variable bubble size approach to account for dissolution. The monodispersed model for ship flows is useful when studying the interaction of small background oceanic bubbles with the hull of a ship as in Carrica et al. (1998) since in this case breakup and coalescence can be neglected and the use of one single dispersed phase velocity is a reasonable approximation.

The mixture and monodispersed models discussed so far neglect the effect of breakup and coalescence. In flows with strong turbulence fluctuations and high void fraction the effect of breakup and coalescence can no longer be neglected and a model that accounts for these effects must be used. The most general and popular way of describing polydispersed bubbly flows in the literature is using a *number density distribution* function that provides at every point in the domain and in time

the number density of bubbles and its size distribution. Other quantities such as void fraction, total number density, mean diameters and moments of the size distribution can be computed with the knowledge of this number density distribution. A conservation equation for the number density distribution that includes transport, breakup, coalescence and dissolution (and maybe other effects) can be written. This equation basically states a balance between production and destruction of bubbles of a given size at a given location and time. This conservation equation is referred as the *Boltzmann Equation* in the nuclear engineering field (Lahey Jr. et al., 1992; Guido-Lavalle et al., 1994) in analogy with the Boltzmann transport equation for neutrons and is known as the *Population Balance Equation* by the chemical engineering community (Singh and Ramkrishna, 1977; Jakobsen et al., 2005). From the general Boltzmann transport equation several models can be derived by typically taking moments of this equation and applying simplifying assumptions that allow to close the integral terms involving breakup and coalescence. As the simplest example, the monodispersed model presented in Carrica et al. (1998) can be derived by integrating the Boltzmann equation over all bubble sizes. A more complex model is presented by Wu et al. (1998) who derive an interfacial area transport equation including the effects of breakup and coalescence. An interesting feature of this model is that it only solves one transport equation for a mean interfacial area and still is able to include the effect of breakup and coalescence. In this regard, this model is as computationally intensive as an ASMM or monodispersed model but it includes breakup and coalescence to yield some information on bubble size.

Several numerical methods can be applied to solve the full Boltzmann equation. These methods basically differ from each other in the level of approximation used for the number density distribution function, ranging from methods that assume a given functional form of the size distribution to methods where the number density distribution can be completely arbitrary. As the numerical method is more

general, in terms of allowing more arbitrary size distributions, it becomes more computationally intensive as well. Therefore, the choice of a numerical method for a particular application is a trade-off between how precise the mathematical description needs to be and the computational cost involved to solve it. In the work by Kamp et al. (2001) a log-normal distribution is assumed for the bubble size distribution. This distribution is described in terms of two of its moments for which conservations equations are derived by taking moments of the general Boltzmann equation. Kamp et al. (2001) apply their model to the simulation of microgravity bubbly pipe flows. In the work by Lehr et al. (2002) on bubble breakup and coalescence in bubble columns, bubbles are modeled in two groups; *small* and *large* bubbles. The bubble size distribution is assumed to be a log-normal distribution for the small bubbles and to decay with an exponential tail for large bubbles. Then, and starting from the general Boltzmann equation, they derive a set of conservation equations for the average bubble volume and void fraction for these two groups yielding a system of four equations with four unknowns. Breakup and coalescence are included in their model. Another popular method used to solve the Boltzmann equation is the method of moments for which several versions are available. In the standard Method Of Moments (MOM) (Hulburt and Katz, 1964) the size distribution is determined through its moments. Conservation equations for these moments are obtained by formally taking the moments of the full Boltzmann equation. A main disadvantage of this early method of moments is that breakup and coalescence kernels need to have an easily tractable functional form in order to close the resulting integrals. This closure problem can be overcome by the Quadrature Method Of Moments (QMOM) which uses a quadrature approximation for the size distribution to obtain transport equations for the moments of the distribution. This method was originally proposed by McGraw (1997) in the context of aerosol dynamics and applied to bubbly flows in stirred reactors by Petitti et al. (2010).

A recent development on this field is the Direct Quadrature Method Of Moments (DQMOM) by Marchisio and Fox (2005) that distinguishes itself from QMOM by solving transport equations for the weights and abscissas of the quadrature rule directly instead of solving transport equations for the moments. DQMOM is applied to the bubbly flow in a stirred reactor in Buffo et al. (2010).

In this thesis, the multigroup approach presented in Carrica et al. (1999) is used. In this method, no assumption is made regarding the functional form of the number density distribution making the method applicable to a wide range of flow conditions. In the multigroup approach the size coordinate is discretized in groups within which the number density, bubble velocities, etc. are assumed to be constant. Therefore, each group is represented by a single bubble size for which conservation of number of bubbles and momentum are solved. The so called multigroup approach by Carrica et al. (1999) is named differently by other authors. In Chen et al. (2005b) bubble groups are referred as *bubble classes* and essentially the same multigroup methodology is given the name of *fixed pivot method* in Kumar and Ramkrishna (1996). In this work, the multigroup terminology is kept even when the discretization approach used follows the fixed pivot method by Kumar and Ramkrishna (1996).

This same approach is applied in Politano et al. (2003) for bubbly flows in vertical pipes and in Wang et al. (2005a) for bubble columns. The advantage of this method is that it provides detailed information for any arbitrarily shaped size distribution though it is clearly more computationally intensive than any of the methods mentioned before. Another numerical method very similar to the multigroup approach is the Multiple Size Group method (MUSIG) (see Frank et al., 2008, model implemented in ANSYS CFX). The MUSIG method can be seen as a particular case of the multigroup method used in this thesis. In the MUSIG method several sizes are grouped together and it is assumed that they have the same phase

velocity in order to reduce the number of momentum equations solved for the dispersed phase. Frank et al. (2008) applies the MUSIG method to the simulation of bubbly flows in vertical pipes in the context of nuclear power technology.

1.5 Contribution of this Thesis

This thesis makes two main contributions. First, the development of a new generation of two-phase flow code with a focus on ship hydrodynamics. Second, the modeling of the two-phase polydispersed bubbly flow around a real ship applying the latest available models and computational techniques. Not of less importance, this thesis identifies issues that need further study and modeling, and attempts to provide a path for future studies tackling the two-phase polydispersed bubbly flow around ships.

In the first main contribution, a two-phase code is developed as an extension of the single phase version of CFDShip-Iowa V4.5 (Huang et al., 2007, 2008, 2010) and is now available for use since release r009. CFDShip-Iowa V4.5 is a mature CFD code developed at the University of Iowa's Institute of Hydraulic Research (IIHR) and is capable of handling complex computations involving free surface flows (Carrica et al., 2007b), 6DOF large amplitude motions (Carrica et al., 2007a), fluid structure interaction (Paik et al., 2009) and fully discretized propellers (Castro et al., 2011; Carrica et al., 2010a). The development of the new two-phase capability into CFDShip-Iowa V4.5 pursues a final product that is accurate but at the same time both robust and efficient, in order to be able to perform computations involving the same level of complexity than those performed with the single phase version. The final objective is the development of a tool that, using state of the art models and numerical methods, would allow to perform simulations that include most of the relevant physics of the problem to add realism and represent better the conditions found in real world scenarios. Some of the main features of the tool developed in this thesis are

1. Capability to simulate polydispersed bubbly flows, *i.e.* the simulation of bubbly flows containing a continuous distribution in bubble sizes.

2. Two-way coupled. The dispersed bubbly phase is affected by the continuous liquid phase and vice versa, the bubbly phase affects the liquid phase.

3. Simulation of bubbly two-phase flows with free surface and air entrainment by wave breaking, spilling, etc.

4. Problems involving moving boundaries: 6DOF motions, control surfaces and propulsors.

5. Ability to handle high void fraction flows without loosing mass in either the continuous or dispersed phase.

6. Strong coupling between the continuous and dispersed phases. Robust and efficient.

7. Strong coupling between bubble sizes (coupled by breakup, coalescence, dissolution, etc.) guaranteeing mass conservation of the dispersed phase.

8. Carefully designed numerical methods minimize the number of floating point operations involved in order to reduce computational cost.

To the knowledge of the author, there are no other codes available to date that can perform the same type of computations involving free surface polydispersed bubbly flows, two-way coupled phases and on moving meshes that the two-phase version of CFDShip-Iowa V4.5 is capable of. It is for this reason that many of the above features required the development of novel numerical methods that solve issues never identified before or were sometimes neglected in the past. Original developments of this work include: a two-phase projection method for pressure-velocity coupling that implicitly treats void fraction changes with pressure (Section

4.4), a time splitting marching method for the Boltzmann transport equation that allows to apply different numerical methods for each of the different terms involved (Section 4.2), a very stable and robust algorithm that allows to handle dispersive forces that depend on the gradient of the number density (Section 4.8), a near wall integration of the number density suitable for overset codes that avoids an uncontrolled accumulation of gas in the small cells near the wall discretizing the boundary layer (Section 4.6.1) and a method to compute bubble radius that implicitly incorporates the surface tension induced pressure (Section 3.1.5). This work also implements state of the art numerical methods already available in the literature. Examples are the use of TVD schemes for the transport of number densities (Section 4.6) and the fixed pivot method (Section 2.3) for a mass conservative integration of the intergroup transfer terms. This thesis also identifies some of the issues found when using the fixed pivot method. This method is considered a standard in the literature but implementation details are not given. It is pointed out in this work that this method guarantees mass conservation of the dispersed phase only if the method is fully implicit. The implicit integration of the full Boltzmann equation is a very computational demanding task if not impossible for many applications. As a result, this work develops the time splitting marching scheme presented in Section 4.2. In addition, an in-depth analysis of the fixed pivot method is performed (Section 2.3) and modifications are proposed for the discretization of the smaller and larger bubble sizes that guarantees mass conservation. This analysis is original to this thesis and nowhere found in the literature.

In the second main contribution of this thesis, a study on the bubbly flow around the research vessel Athena is presented in Chapter 6. This computation is a new contribution by itself since it includes a polydispersed bubbly flow model, two-way coupled, with free surface, at full scale Reynolds number, with incoming waves and with a fully appended geometry. Athena R/V is chosen for these simulations since

today, this is probably the ship with the most comprehensive characterization of its bubbly field. In this study, the relative importance of the different intergroup transfer mechanisms involved is assessed. This is done by selectively enabling/disabling different terms in the Boltzmann equation and comparing the simulation results. In addition, the evolution of the bubbly field is followed along fluid streamlines in order to understand the source of different bubble sizes at the wake of the Athena. Finally, the computed results are compared against available experimental data.

A final computation of Athena is performed and this includes: fully appended geometry, discretized rotating propeller, free surface, full scale Reynolds number, breakup, coalescence and dissolution, incoming waves, oceanic background and bubble growth by rectified diffusion. This last computation is performed mostly as a demonstration of the simulation capability developed throughout this research.

This research also contributes in the revision of some modeling aspects and proposes a collision-like model for packing at high void fractions (Section 3.1.4), a turbulent shear stress breakup model (Section 3.3.2), a coalescence model for sea water (Section 3.2) and a model for bubble growth by rectified diffusion in the propeller based on lookup tables from Hsiao and Chahine (2005) (Section 3.10). The main purpose of these models is to point out sometimes neglected physics and models that need to be improved. The packing force model proposed in Section 3.1.4 clearly needs a more in depth research and more importantly, validation with experiments. Still, it points out the importance of a model of this nature in order to avoid the unphysical accumulation of air bubbles specially occurring at solid boundaries and the numerical issues associated with it. The model for coalescence in sea water proposed in Section 3.2 highlights the dependence of the coalescence efficiency with bubble radius experimentally observed in electrolyte solutions. Even when the model does not include the effect of other contaminants found in real sea water, it shows that the modeling of coalescence in sea water needs further

research. The breakup by velocity shear model proposed in Section 3.3.2 attempts to include the effect of unresolved turbulent shear. Later on, in Section 6.4.2.2, this model helps to asses the importance of breakup induced by shear in the boundary layer and from this study issues and possible modeling strategies are discussed. The model for bubble growth by rectified diffusion proposed in Section 3.10 is in its infancy, mainly because rectified diffusion modeling is in its infancy. However, the proposed model illustrates how new physics can be incorporated into the Eulerian framework of the Boltzmann transport equation.

Intergroup transfer by breakup and coalescence is validated in Chapter 5. This chapter also contributes with a convergence analysis (Section 5.2) with the number of bubble groups, a study on the dependence of the solution with the initial conditions in fresh water (Section 5.3) and in salt water (Section 5.7) and a detailed analysis of intergroup transfer budget and time scales.

CHAPTER 2
MATHEMATICAL DESCRIPTION OF POLYDISPERSED FLOWS

The term *polydispersed* refers to a multiphase system in which a *dispersed* phase (composed by separate individual units) is immersed in a main component termed *continuous* (in the sense that two points belonging to this component may be connected by a line entirely contained inside it). Moreover, the term dispersed usually denotes the fact that the total volume of dispersed phase per unit of total volume is small, an assumption often used in the formulation of models for polydispersed flows. However, this is not always the case and corrections accounting for this fact may apply. The suffix *poly* refers to the fact that the individual units composing the dispersed phase may have different sizes. The term polydispersed applies not only to bubbly flows but also to particles in a fluid (gas or liquid), drops in a gas (or even another liquid), etc. In bubbly flows the liquid phase is the *continuous phase* and the bubbly phase is the *dispersed phase*. In this work, subscripts c are used to denote the continuous phase variables and subscripts d are used to denote the dispersed phase variables.

In many works found in the literature an Eulerian/Lagrangian approach is used to describe polydispersed flows. In these methods the continuous phase is described in an Eulerian framework while the individual units conforming the dispersed phase are tracked independently in a Lagrangian fashion (see Xu et al., 2002; Apte et al., 2003a). However, the application of this method is not feasible for the simulation of typical bubbly flows found in engineering where a large number of bubbles makes their individual tracking not possible with the available computing power. Besides, the knowledge on each individual bubble trajectory in the system may result to be an over-detailed description for many engineering purposes where very often much less information is considered to be satisfactory.

As an alternative to describing each bubble individually, the system can be

characterized by its statistics. This approach is used in Eulerian/Eulerian formulations where both the continuous and dispersed phase are described in an Eulerian framework. In the statistical description of polydispersed flows a number density distribution $f(\boldsymbol{r}, \boldsymbol{\xi}, t)$ is used to describe the dispersed phase. This function is defined such that, the mean number of dispersed units (bubbles, drops, particles, etc) per unit volume located at position $\boldsymbol{r}$ and at time t with internal variables $\boldsymbol{\xi}$ in the range $(\boldsymbol{\xi}; \boldsymbol{\xi} + \mathrm{d}\boldsymbol{\xi})$ is $f(\boldsymbol{r}, \boldsymbol{\xi}, t)\,\mathrm{d}\boldsymbol{\xi}$. The internal variables contained in the vector $\boldsymbol{\xi}$ are those relevant for a particular application. For instance, in particulate flows the internal variables may be chosen to be the particle diameter D and the particle velocity $\boldsymbol{u}$ such that the mean number of particles per unit volume with diameter in the range $(D; D + \mathrm{d}D)$ and velocities in the *velocity volume* $\mathrm{d}^3\boldsymbol{u}$ is $f(\boldsymbol{r}, D, \boldsymbol{u}, t)\,\mathrm{d}D\,\mathrm{d}^3\boldsymbol{u}$. In the work by Carrica et al. (1999) on polydispersed bubbly flows, it is assumed that all the relevant internal variables of the problem can be computed in some way from the bubble mass and therefore the possible set of internal variables reduces to the bubble mass m only. This simplification assumes that all bubbles with the same volume $v(m)$ (which, knowing the gas density, can be computed from the bubble mass) have exactly the same mean diameter D, mean velocity $\boldsymbol{u}_d$ and interfacial area a_i. This approximation is particularly reasonable when bubbles are small and thus close to spherical (due to surface tension). In this case of spherical bubbles the relation between the bubble volume and the other internal variables is

$$D = \left(\frac{6}{\pi}\right)^{1/3} v(m,p)^{1/3} \tag{2.1}$$

$$a_i = (36\pi)^{1/3}\, v(m,p)^{1/3} \tag{2.2}$$

$$\boldsymbol{u}_d = \boldsymbol{u}_d(m) \tag{2.3}$$

where the bubble volume is a function not only of the bubble mass but also of the local pressure since this determines the dispersed phase density. For non-spherical

bubbles the above expressions may be taken as the definition of a characteristic diameter, interfacial area and velocity for a bubble of mass m.

Under these conditions, the bubbly phase is characterized by a number density distribution $f(m, \boldsymbol{r}, t)$ such that the mean number of bubbles per unit volume with masses within dm of mass m is $f(m, \boldsymbol{r}, t)\,\mathrm{d}m$. Hence, in the international system of units (SI), $f(m, \boldsymbol{r}, t)$ has units of $\mathrm{m}^{-3}\,\mathrm{Kg}$. The use of the mass m as the independent variable is advantageous for the simulation of flows around ships since this quantity is preserved under pressure changes, such as the large variations of hydrostatic pressure with depth. Therefore, while the size distribution does not change with pressure when expressed as a function of the bubble mass m, it does change when written in terms of the bubble diameter or volume (or any other geometrical measure). This simplifies the evolution equation for the number density since no additional terms accounting for the change in bubble size with gas density changes are needed (the derivation of these additional terms is shown in Morel et al. (2010)).

The bubble volume can be used instead of the bubble mass as the internal variable describing bubble size. However, the use of bubble mass or volume is equivalent only when the gas phase is assumed to be incompressible. As an example, Chen et al. (2005a) use the bubble volume instead of the bubble mass in their simulations of bubble columns.

Other quantities important in the context of two-phase flows can be obtained by taking different moments of the number density distribution:

Bubble number density, *i.e.* the total number of bubbles per unit volume

$$N(\boldsymbol{r}, t) = \int_0^\infty \mathrm{d}m\, f(m, \boldsymbol{r}, t) \tag{2.4}$$

Mass density, *i.e.* the mass of gas per unit volume

$$\varepsilon_m = \int_0^\infty \mathrm{d}m\, m f(m) \tag{2.5}$$

Gas volume fraction, or simply *void fraction i.e.* the volume of gas per unit of total volume

$$\alpha_d(\boldsymbol{r}, t) = \int_0^\infty \mathrm{d}m\, \frac{m}{\rho_d(m, \boldsymbol{r}, t)} f(m, \boldsymbol{r}, t) \tag{2.6}$$

where $\rho_d(m, \boldsymbol{r}, t)$ is the dispersed phase density at the location of interest. Note that the dispersed phase density is a function of location since it can change due to variations in pressure. In addition, it is also dependent on the bubble size m since for small bubbles the pressure inside them is affected by surface tension. The integrand in Eq. (2.6) is a useful quantity to show bubble size distributions and it will be referred as the *void fraction distribution*

$$\alpha_m(m, \boldsymbol{r}, t) = \frac{m}{\rho_d(m, \boldsymbol{r}, t)} f(m, \boldsymbol{r}, t) \tag{2.7}$$

Details in the bubble size distribution difficult to appreciate with the number density distribution become more evident when looking at the void fraction distribution. Notice that while the area under $f(m, \boldsymbol{r}, t)$ is the number density $N(\boldsymbol{r}, t)$, the area under $\alpha_m(m, \boldsymbol{r}, t)$ is the total gas void fraction $\alpha_d(\boldsymbol{r}, t)$.

2.1 The Boltzmann Equation

The evolution equation for the number density $f(m, \boldsymbol{r}, t)$ is developed inspired on the Boltzmann theory for dispersed gases by making the analogy of bubbles in a fluid with molecules in a gas. The Boltzmann equation was first established by Ludwig Boltzmann (1844-1906) in 1872 to describe the state of a dilute gas. The Boltzmann equation has been successfully applied not only to the description of

dispersed gases as originally conceived by Boltzmann, but also, with the appropriate extensions, to the study of neutron transport in nuclear reactors (Beckurts and Wirtz, 1964), crystal nucleation and growth (Singh and Ramkrishna, 1977), aerosol dynamics (McGraw, 1997), and radiative transport in planetary and stellar atmospheres (Collins II, 2003).

Even when the analogy between bubbles and gas molecules is quite crude, in the context of polydispersed bubbly flows, the Boltzmann equation essentially is a balance of bubble destruction and production due to breakup and coalescence inside a differential volume around a particular location in space (effects as bubble entrainment, dissolution and others are also considered). In addition to breakup and coalescence, bubbles can get in or out this volume by means of convective fluxes. This conservation equation was given the name of *Population Balance Equation* by the chemical engineering community (see for instance Chen et al., 2005a; Frank et al., 2005). In nuclear engineering this equation is called the *Boltzmann* transport equation in analogy with the Boltzmann equation for neutrons (see Guido-Lavalle et al., 1994; Lahey Jr. et al., 1992).

Historically, a Boltzmann-like equation was first applied in the context of crystal growth by Hulburt and Katz (1964) and later on by Singh and Ramkrishna (1977). In the context of bubbly flows these ideas were first applied by Achard (1978), Navarro-Valenti et al. (1991), Lahey Jr. et al. (1992), Guido-Lavalle et al. (1994) and Carrica et al. (1999).

The conservation equation for the number density distribution, i.e. the Boltzmann transport equation, can be written as (Guido-Lavalle et al., 1994)

$$\frac{\partial f(m,\boldsymbol{r},t)}{\partial t} + \nabla\cdot\left(\boldsymbol{u}_d(m,\boldsymbol{r},t)f(m,\boldsymbol{r},t)\right) + \frac{\partial}{\partial m}\left(\dot{m}f(m,\boldsymbol{r},t)\right) = \beta(m,\boldsymbol{r},t) + \chi(m,\boldsymbol{r},t) + S(m,\boldsymbol{r},t) \tag{2.8}$$

where β is the net source due to breakup, χ is the net source due to coalescence and S is a production term that in the simulation of ships is used to model the entrainment of bubbles due to wave breaking and spilling. The third term on the left hand side of Eq. (2.8) models the change in bubble mass due to dissolution and $\dot{m}$ is the rate at which gas is transfered from one single bubble to the surrounding water. Dissolution is an important process in the prediction of the bubbly wake behind a ship specially for small bubble sizes for which the ratio of interfacial area to volume is high. In addition, the surface tension induced pressure, higher for small bubbles, enhances the gas transfer from the bubbles into the surrounding water. The mass dissolution rate $\dot{m}$ in Eq. (2.8) can either be positive or negative being then possible for a bubble to increase or decrease in size as air is exchanged.

The breakup source can be split into two contributions

$$\beta(m, \boldsymbol{r}, t) = \beta^{+}(m, \boldsymbol{r}, t) - \beta^{-}(m, \boldsymbol{r}, t) \tag{2.9}$$

$$\beta^{+}(m, \boldsymbol{r}, t) = \int_{m}^{\infty} \mathrm{d}m' \; h(m, m') b(m') f(m', \boldsymbol{r}, t) \tag{2.10}$$

$$\beta^{-}(m, \boldsymbol{r}, t) = b(m) f(m, \boldsymbol{r}, t) \tag{2.11}$$

where β^{+} is the *birth term* due to the breakup of larger bubbles than m into bubbles of size m and β^{-} is the *death term* due to breakup of bubbles in size m. $b(m)$ is the kernel for breakup and gives the rate of bubble destruction due to breakup for bubbles of size m. The units of $b(m)$ are of 1/s. Bubbles of size m' break into smaller bubbles with a size distribution $h(m, m')$, the daughter bubble size distribution which has units of 1/Kg. Both, the breakup kernel $b(m)$ and the daughter bubble size distribution $h(m, m')$, are also functions of time and position since they depend on local flow conditions such as velocity gradients, turbulent dissipation, etc., even when this is not explicitly shown in Eqs. (2.9)-(2.11). The spatial and time dependences will be omitted for brevity from now on whenever doing so does not

cause confusion.

If n bubble fragments are produced per breakup event then the daughter bubble size distribution is normalized as (see Appendix A.1)

$$\int_0^{m'} \mathrm{d}m\, h(m, m') = n \tag{2.12}$$

Coalescence sources can also be split into births and deaths as

$$\chi(m) = \chi^+(m) - \chi^-(m) \tag{2.13}$$

then for births

$$\chi^+(m) = \frac{1}{2} \int_0^m \mathrm{d}m'\, Q(m - m', m') f(m - m') f(m') \tag{2.14}$$

and for deaths

$$\chi^-(m) = f(m) \int_0^\infty \mathrm{d}m'\, Q(m, m')\, f(m') \tag{2.15}$$

χ^+ represents the birth rate of bubbles within size m due to the coalescence between smaller bubbles with masses m' and $m - m'$ and χ^- represents the death term due to the coalescence of bubbles of size m with bubbles of any other size. $Q(m, m')$ is the coalescence kernel and it has units of m^3/s.

In the mathematical description of a polydispersed flow given by the Boltzmann equation, the breakup and coalescence kernels $b(m)$, $h(m, m')$ and $Q(m, m')$ are assumed to be given. The mathematical model itself does not provide closure relations for them and modeling is required. The modeling of these kernels is a challenging task that typically involves results from in depth theoretical analyses

and the careful design of experiments. The modeling of these kernels is discussed in Chapter 3.

2.2 Multigroup Approach

Equation (2.8) must be solved for every bubble size m. This can be accomplished using a multigroup approach where the basic idea is that bubble sizes between $m_{g-1/2}$ and $m_{g+1/2}$ can be represented by a single size m_g containing all bubbles in this range. This is sketched in Fig. 2.1

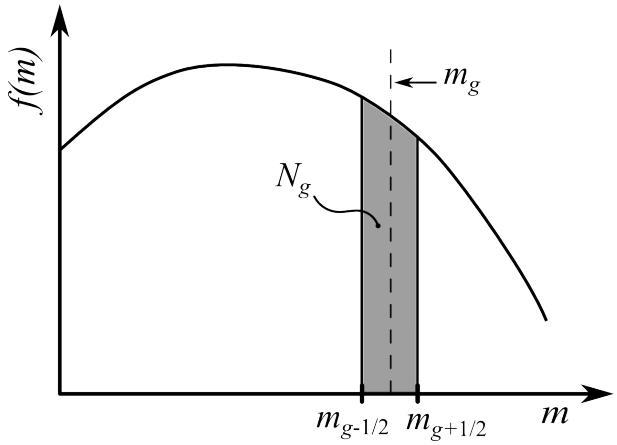

Figure 2.1: Multigroup approach. Bubbles in the interval ($m_{g-1/2}$; $m_{g+1/2}$) are represented with a single size m_g containing all bubbles in this range.

Then the range of bubble masses of interest is discretized into G groups ranging from a minimum bubble size m_1 to a maximum bubble size m_G. The half groups masses are defined as $m_{g+1/2} = (m_{g+1} + m_g)/2$ and the two boundaries are defined as $m_{1/2} = 0$ and $m_{G+1/2} = \infty$. Interval sizes at every group are computed as $\Delta m_g = m_{g+1/2} - m_{g-1/2}$.

Integration of Eq. (2.8) between $m_{g-1/2}$ and $m_{g+1/2}$ results in

$$\frac{\partial N_g}{\partial t} + \nabla \cdot \left(\boldsymbol{u}_g N_g \right) + F_{g+1/2} - F_{g-1/2} = \beta_g + \chi_g + S_g \tag{2.16}$$

where the g-group number density number is defined as

$$N_g(\boldsymbol{r},t) = \int_{m_{g-1/2}}^{m_{g+1/2}} \mathrm{d}m\, f(m,\boldsymbol{r},t) \tag{2.17}$$

And the g-group velocity is defined such that the flux of bubbles in the continuous and discrete versions are consistent

$$\boldsymbol{u}_g(\boldsymbol{r},t)N_g(\boldsymbol{r},t) = \int_{m_{g-1/2}}^{m_{g+1/2}} \mathrm{d}m\, \boldsymbol{u}_d(m,\boldsymbol{r},t)f(m,\boldsymbol{r},t) \tag{2.18}$$

β_g, χ_g and S_g are the breakup, coalescence and source terms in group g respectively and are defined analogously to N_g

$$\beta_g(\boldsymbol{r},t) = \int_{m_{g-1/2}}^{m_{g+1/2}} \mathrm{d}m\, \beta(m,\boldsymbol{r},t) \tag{2.19}$$

$$\chi_g(\boldsymbol{r},t) = \int_{m_{g-1/2}}^{m_{g+1/2}} \mathrm{d}m\, \chi(m,\boldsymbol{r},t) \tag{2.20}$$

$$S_g(\boldsymbol{r},t) = \int_{m_{g-1/2}}^{m_{g+1/2}} \mathrm{d}m\, S(m,\boldsymbol{r},t) \tag{2.21}$$

$$F_g(\boldsymbol{r},t) = \dot{m}_g\, f(m_g) \tag{2.22}$$

Since $\dot{m}$ is the rate at which a single bubble of mass m exchanges mass by dissolution with the surrounding fluid and $f(m)\,\mathrm{d}m$ is the number of bubbles per unit volume with mass m and within $\mathrm{d}m$, then $\dot{m}\, f(m)\,\mathrm{d}m = F(m)\,\mathrm{d}m$ is the rate of mass exchange between bubbles of mass m within $\mathrm{d}m$ and the surrounding fluid. If only gas dissolution is considered in Eq. (2.8), this equation is nothing but a one-dimensional convection equation for the number density in the m space with a *velocity* $\dot{m}$. In analogy with this one dimensional convection equation $F_g = F(m_g)$ is called

dissolution flux.

In the multigroup approach, the number density distribution is assumed to be a piecewise constant function in the bubble mass m. Therefore, if $\gamma_g(m)$ is a function defined to be one in $(m_{g-1/2};\ m_{g+1/2})$ an zero elsewhere, the number density distribution is approximated by

$$f(m, \boldsymbol{r}, t) = \sum_{g=1}^{G} f_g(\boldsymbol{r}, t)\gamma_g(m) \tag{2.23}$$

With this approximation, the discrete number density distribution f_g is determined in terms of the group-g number density N_g from its definition in Eq. (2.17)

$$f_g = \frac{N_g}{\Delta m_g} \tag{2.24}$$

Using the discrete approximation for the number density in Eq. (2.23), Eqs. (2.4) to (2.6) reduce to

$$N(\boldsymbol{r}, t) = \sum_{g=1}^{G} N_g(\boldsymbol{r}, t) \tag{2.25}$$

$$\varepsilon_m(\boldsymbol{r}, t) = \sum_{g=1}^{G} m_g N_g(\boldsymbol{r}, t) \tag{2.26}$$

$$\alpha_d(\boldsymbol{r}, t) = \sum_{g=1}^{G} \alpha_g = \sum_{g=1}^{G} \frac{m_g}{\rho_d(m_g, \boldsymbol{r}, t)} N_g(\boldsymbol{r}, t) \tag{2.27}$$

where the group-g void fraction is defined as

$$\alpha_g(\boldsymbol{r}, t) = = \frac{m_g}{\rho_d(m_g, \boldsymbol{r}, t)} N_g(\boldsymbol{r}, t) \tag{2.28}$$

It should be pointed out that Eqs. 2.25 and 2.26 follow, without any other approximation involved, directly from replacing the discrete number density in

Eq. (2.23) in the respective definitions in Eqs. 2.4 and 2.5. On the other hand, Eq. (2.27) is obtained by replacing Eq. (2.23) into the void fraction definition in Eq. (2.6) and using the midpoint rule on each of the discrete intervals $(m_{g-1/2};\, m_{g+1/2})$.

From its definition in Eq. (2.18), the group-g velocity is the mean dispersed phase velocity weighted with the number density distribution. An approximation for the group-g dispersed phase velocity is found by using the discrete number density distribution from Eq. (2.23) into Eq. (2.18), and applying the midpoint integration rule

$$\boldsymbol{u}_g(\boldsymbol{r}, t) = \boldsymbol{u}_d(m_g, \boldsymbol{r}, t) \tag{2.29}$$

i.e. the group-g velocity is approximated by the dispersed phase velocity for bubbles of mass m_g. Finally, the void fraction distribution defined in Eq. (2.7) is computed using the discrete number density distribution f_g in Eq. (2.24) and the group-g void fraction definition in Eq. (2.28)

$$\alpha_m(m_g) = \frac{m_g}{\rho_d(m_g)} f(m_g) = \frac{m_g}{\rho_d(m_g)} \frac{N_g}{\Delta m_g} = \frac{\alpha_g}{\Delta m_g} \tag{2.30}$$

In order to solve for the number densities N_g from Eq. (2.16) it is necessary to compute the group velocities $\boldsymbol{u}_g$ and to find an appropriate approximation for the intergroup transfer terms given by Eqs. (2.19)-(2.22). While this chapter deals with the numerical integration of the intergroup transfer terms, the mathematical model used to obtain the group velocities $\boldsymbol{u}_g$ is presented in Section 3.1.1 and the strategy to solve it numerically is presented in Section 4.5. The convective transport of N_g is discussed in Section 4.6.

2.3 Intergroup Transfer Discretization

In this section the numerical method used to discretize the intergroup transfer mechanisms in Eq. (2.16) is presented. The numerical strategy used to solve the full

Boltzmann equation coupled in both space and bubble size is described in Chapter 4. In that chapter a time-splitting strategy is presented which allows to solve intergroup transfer for every individual point in the domain independently of the bubble transport in space. In this regard intergroup transfer is solved as if every point was a separate homogeneous media problem with the local hydrodynamic conditions. It is for this reason that this section only deals with intergroup transfer and bubble transport is not considered without any loss of generality. If bubble transport and sources are not considered, then Eq. (2.8) reduces to

$$\begin{aligned}\frac{\partial f(m,t)}{\partial t} + \frac{\partial}{\partial m}\left(\dot{m} f(m,t)\right) = \\ \int_m^\infty \mathrm{d}m'\; h(m,m')b(m')f(m',t) - b(m)f(m,t) \\ + \frac{1}{2}\int_0^m \mathrm{d}m'\; Q(m-m',m')f(m-m')f(m') - f(m)\int_0^\infty \mathrm{d}m'\; Q(m,m')\, f(m')\end{aligned} \tag{2.31}$$

By construction, the Boltzmann Eq. (2.31) has the property that the intergroup transfer mechanisms of breakup and coalescence preserve mass (see Appendix A.2). This is consistent with the physical intuition that tells as that mass is preserved whenever a breakup or coalescence event occurs. On the other hand, dissolution preserves the total number of bubbles but not mass since gas is transfered between bubbles and the surrounding liquid. It is worth to mention also that Eq. (2.31) is an integro-differential equation. Then the evolution of a certain group will be strongly coupled to the number density in all the other groups. In addition, coalescence terms are very nonlinear since they involve the product of two number densities. This makes Eq. (2.31) very sensitive to numerical inaccuracies that ultimately, cause unphysical mass losses. It is desirable then to develop a numerical integration scheme that preserves mass. This requirement does not guarantee the accuracy of

the numerical method by itself but in practice it leads to a robust implementation that shows to provide accurate results.

In what follows, the fixed pivot method developed by Kumar and Ramkrishna (1996) is presented. Their method guarantees conservation of mass at every time step. From Kumar and Ramkrishna (1996) it is not clear what should be done with the first and last groups and if mass conservation is possible or not for them. It is shown in this work that for these groups at the boundaries there are two possibilities: either to conserve mass or number of bubbles. Preference is given to mass conservation.

2.3.1 Breakup

As done for its continuous counterpart $\beta(m)$ in Eq. (2.9), β_g can also be split in two contributions

$$\beta_g = \beta_g^+ - \beta_g^- \tag{2.32}$$

Using the approximation from Eq. (2.23) into Eq. (2.19), β_g^- is computed as

$$\begin{aligned}
\beta_g^-(\boldsymbol{r},t) &= \int_{m_{g-1/2}}^{m_{g+1/2}} \mathrm{d}m\, \beta^-(m,\boldsymbol{r},t) \\
&= \int_{m_{g-1/2}}^{m_{g+1/2}} \mathrm{d}m\, b(m,\boldsymbol{r},t)\, f(m,\boldsymbol{r},t) \\
&= \frac{N_g(\boldsymbol{r},t)}{\Delta m_g} \int_{m_{g-1/2}}^{m_{g+1/2}} \mathrm{d}m\, b(m,\boldsymbol{r},t) \\
&= N_g(\boldsymbol{r},t)\, \bar{b}_g(\boldsymbol{r},t)
\end{aligned} \tag{2.33}$$

where the fact that $f(m)$ is constant in $(m_{g-1/2};\, m_{g+1/2})$ is used to take it outside the

integral. In the last equality in Eq. (2.33) the mean breakup kernel is defined as

$$\bar{b}_g(\boldsymbol{r},t) = \frac{1}{\Delta m_g}\int_{m_{g-1/2}}^{m_{g+1/2}} \mathrm{d}m\, b(m,\boldsymbol{r},t) \tag{2.34}$$

This can be approximated using a midpoint integral rule as $\bar{b}_g(\boldsymbol{r},t) = b(m_g,\boldsymbol{r},t)$. Using this approximation, the breakup deaths are computed as

$$\beta_g^-(\boldsymbol{r},t) = b_g(\boldsymbol{r},t)\, N_g(\boldsymbol{r},t) \tag{2.35}$$

where $b_g = b(m_g)$. The evaluation of β^+ is somewhat more complex. The situation is illustrated in Fig. 2.2 where a bubble with mass $m_{g'}$ breaks into two fragments with sizes m and m''. The ideal situation (not sketched in the figure) would be one in which these fragments have masses m_g and $m_{g''}$ belonging to the mass stencil and this stencil to be such that $m_{g''} = m_g + m_{g''}$. In this case mass would be conserved exactly. For instance, this is the case if bubble masses are equally spaced. However, this situation is rare since in most applications, a non-uniform spacing is used in order to selectively refine the size discretization where needed. Therefore, as shown in Fig. 2.2, the bubble size m typically falls lets say somewhere inside an interval $(m_{g-1};\, m_g)$ and bubble with size m'' falls somewhere inside an interval $(m_{g''-1};\, m_{g''})$ (but not exactly at a given size m_g in the discretization).

Consider the fragment with mass m. The solution proposed by Kumar and Ramkrishna (1996) is to assign a fraction of this fragment to group $g-1$ and another fraction to group g such that the total mass is still m. Then if $a^+(m, m_{g-1})$ is the fraction assigned to group $g-1$ and $a^-(m, m_g)$ is the fraction assigned to group

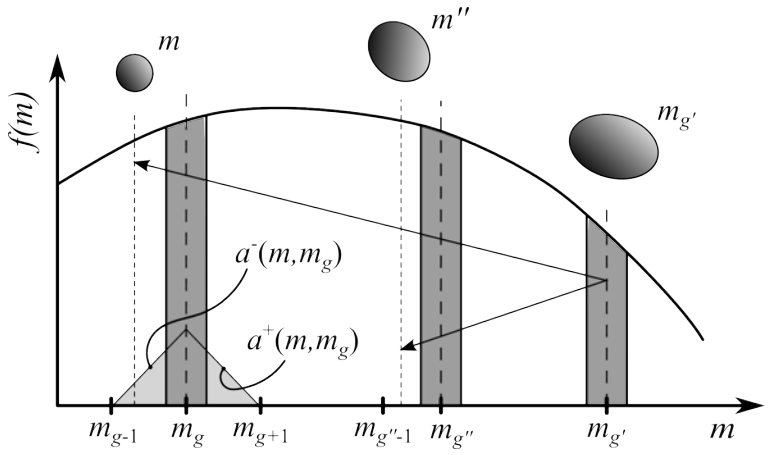

Figure 2.2: Breakup in the multigroup approach.

g, these have to satisfy the requirements

$$\begin{aligned} a^+(m, m_{g-1}) \;+\; a^-(m, m_g) &= 1 \quad \text{Number conservation} \\ m_{g-1}\, a^+(m, m_{g-1}) \;+\; m_g\, a^-(m, m_g) &= m \quad \text{Mass conservation} \end{aligned} \tag{2.36}$$

From Eq. (2.36) fractions a^- and a^+ can be solved

$$a^-(m, m_g) = \begin{cases} \dfrac{m - m_{g-1}}{m_g - m_{g-1}} & m \in (m_{g-1};\, m_g) \\ 0 & \text{Otherwise} \end{cases}$$

$$a^+(m, m_g) = \begin{cases} \dfrac{m_{g+1} - m}{m_{g+1} - m_g} & m \in (m_g;\, m_{g+1}) \\ 0 & \text{Otherwise} \end{cases}$$

Then $\Lambda(m, m_g) = a^-(m, m_g) + a^+(m, m_g)$ is a hat shaped function centered at m_g, see Fig. 2.2. Breakup events that contribute to births in group g are computed using these fractions as

$$\beta_g^+(m) = \beta^+(m)\, a^-(m, m_g) + \beta^+(m)\, a^+(m, m_g) = \beta^+(m)\, \Lambda(m, m_g) \tag{2.37}$$

hence $\beta_g^+(m)$ is computed by smoothing out the births on $(m_{g-1};\, m_{g+1})$ given by the original continuous $\beta(m)$. The effect of this smoothing will be to diffuse the size distribution in the variable m but this error will decrease as the discretization in m is refined. Moreover, this numerical diffusion can safely be neglected when compared to the usual uncertainties found in the breakup kernels. $\beta^+(m)$ can be computed in terms of N_g using the approximation in Eq. (2.23)

$$\beta^+(m) = \begin{cases} \displaystyle\sum_{g'=g}^{G} \bar{h}(m, m_{g'}) \bar{b}_{g'} N_{g'} & m \in (m_{g-1};\, m_g) \\ \displaystyle\sum_{g'=g+1}^{G} \bar{h}(m, m_{g'}) \bar{b}_{g'} N_{g'} & m \in (m_g;\, m_{g+1}) \end{cases} \tag{2.38}$$

where the mean breakup rate is already defined in Eq. (2.34) and the mean daughter bubble size distribution is computed weighting it with the breakup rate as

$$\bar{h}(m, m_{g'}) = \frac{\displaystyle\int_{m_{g'-1/2}}^{m_{g'+1/2}} \mathrm{d}m'\, b(m')\, h(m, m')}{\displaystyle\int_{m_{g'-1/2}}^{m_{g'+1/2}} \mathrm{d}m'\, b(m')} \tag{2.39}$$

As previously done with the mean breakup rate $\bar{b}_g$, the mean daughter bubble size distribution can be approximated using the midpoint rule to compute the integrals in Eq. (2.39) as

$$\bar{h}(m, m_{g'}) \approx \frac{\Delta m_{g'}\, b(m_{g'})\, h(m, m_{g'})}{\Delta m_{g'}\, b(m_{g'})} = h(m, m_{g'}) \tag{2.40}$$

Using these midpoint rule approximations to compute the mean breakup rate and daughter bubble size distribution, the breakup births source in Eq. (2.38) is

computed as

$$\beta^+(m) = \begin{cases} \sum_{g'=g}^{G} h(m, m_{g'}) b_{g'} N_{g'} & m \in (m_{g-1};\ m_g) \\ \sum_{g'=g+1}^{G} h(m, m_{g'}) b_{g'} N_{g'} & m \in (m_g;\ m_{g+1}) \end{cases} \tag{2.41}$$

Note that due to the weighting applied on $\beta^+(m)$ in Eq. (2.37), the contribution to births in group g is now expanded over the interval $(m_{g-1};\ m_{g+1})$. Hence the total number of births in group g is found by using Eq. (2.19) modified to account for this to

$$\beta_g^+ = \int_{m_{g-1}}^{m_{g+1}} \mathrm{d}m\, \beta_g^+(m) \tag{2.42}$$

with this, births in group g are computed as

$$\beta_g^+ = \sum_{g'=g}^{G} b_{g'} N_{g'} \int_{m_{g-1}}^{m_g} \mathrm{d}m\, a^-(m, m_g) h(m, m_{g'}) + \sum_{g'=g+1}^{G} b_{g'} N_{g'} \int_{m_g}^{m_{g+1}} \mathrm{d}m\, a^+(m, m_g) h(m, m_{g'}) \tag{2.43}$$

Equation (2.43) can be rewritten by defining the discrete daughter bubble size distribution $h_{g,g'}$

$$h_{g,g'} = \underbrace{\int_{m_{g-1}}^{m_g} \mathrm{d}m\, a^-(m, m_g) h(m, m_{g'})}_{h^I_{g,g'}} + \underbrace{\int_{m_g}^{m_{g+1}} \mathrm{d}m\, a^+(m, m_g) h(m, m_{g'})}_{h^{II}_{g,g'}} \tag{2.44}$$

where the integral $h^{II}_{g,g'}$ is set to be zero when $g = g'$ since this term is not present in the original Eq. (2.43). With this definition the births source is

$$\beta_g^+ = \sum_{g'=g}^{G} h_{g,g'} b_{g'} N_{g'} \tag{2.45}$$

Hence, if only breakup is considered, the discrete Boltzmann equation reads

$$\frac{\partial N_g}{\partial t} = \sum_{g'=g}^{G} h_{g,g'} b_{g'} N_{g'} - b_g N_g \tag{2.46}$$

Equation (2.46) can be written in matricial form by defining

$$\begin{aligned} \mathbf{B}^+_{g,g'} &= h_{g,g'} b_{g'} & \mathbf{B} &= \mathbf{B}^+ - \mathbf{B}^- \\ \mathbf{B}^-_{g,g'} &= b_g \delta_{g,g'} & \mathbf{N}_g &= N_g \end{aligned} \tag{2.47}$$

then

$$\frac{\partial \mathbf{N}}{\partial t} = \mathbf{B}^+ \cdot \mathbf{N} - \mathbf{B}^- \cdot \mathbf{N} = \mathbf{B} \cdot \mathbf{N} \tag{2.48}$$

where $\mathbf{B}^+$ is an upper triangular matrix, $\mathbf{B}^-$ is diagonal and thus $\mathbf{B}$ is upper triangular as well.

2.3.1.1 Conservation of mass and number of bubbles

Conservation of mass and number of bubbles can be analyzed for the discrete Boltzmann equation from Eq. (2.46). Equation (2.46) can be expanded in matricial form as

$$\frac{\partial}{\partial t}\begin{bmatrix} N_1 \\ N_2 \\ N_3 \\ \vdots \\ N_G \end{bmatrix} = \begin{bmatrix} h_{11}b_1N_1 & + & h_{12}b_2N_2 & + & h_{13}b_3N_3 & + & \dots & + & h_{1G}b_GN_G \\ 0 & + & h_{22}b_2N_2 & + & h_{23}b_3N_3 & + & \dots & + & h_{2G}b_GN_G \\ 0 & + & 0 & + & h_{33}b_3N_3 & + & \dots & + & h_{3G}b_GN_G \\ \vdots & + & \vdots & + & \vdots & & \ddots & & \vdots \\ 0 & + & 0 & + & 0 & + & \dots & + & h_{GG}b_GN_G \end{bmatrix} - \begin{bmatrix} b_1 N_1 \\ b_2 N_2 \\ b_3 N_3 \\ \vdots \\ b_G N_G \end{bmatrix} \tag{2.49}$$

The equation for the total number of bubbles is obtained by summing over g in Eq. (2.46) or equivalently, by summing over the columns of Eq. (2.49). The result is

$$\frac{\partial N}{\partial t} = \frac{\partial}{\partial t}\sum_{g=1}^{G} N_g = \sum_{g=1}^{G} b_g N_g \sum_{g'=1}^{g} h_{g',g} - \sum_{g=1}^{G} b_g N_g \tag{2.50}$$

The summation on $h_{g,g'}$ is nothing but the discrete version of Eq. (2.12). To satisfy the number of bubbles balance it must be required that

$$\sum_{g'=1}^{g} h_{g'g} = n \tag{2.51}$$

which simplifies Eq. (2.50) to

$$\frac{\partial N}{\partial t} = (n-1)\sum_{g=1}^{G} b_g N_g \tag{2.52}$$

which is the discrete counterpart of Eq. (A.24). The last summation in Eq. (2.52) is the total number of breakup events per unit of time (and per unit of volume). Then, this equation tells that if two bubbles are formed per breakup event ($n = 2$), one bubble is added to the system every time the breakup of a bubble occurs.

Similarly, the equation for total mass is obtained by first multiplying Eq. (2.46) by m_g and then summing over g. The result is

$$\frac{\partial \varepsilon_m}{\partial t} = \frac{\partial}{\partial t}\sum_{g=1}^{G} m_g N_g = \sum_{g=1}^{G} b_g N_g \sum_{g'=1}^{g} m_{g'} h_{g',g} - \sum_{g=1}^{G} b_g m_g N_g \tag{2.53}$$

Since mass is preserved under breakup events (see Appendix A.2), Eq. (2.53) must reduce to

$$\frac{\partial \varepsilon_m}{\partial t} = 0 \tag{2.54}$$

this is the case only if

$$\sum_{g'=1}^{g} m_{g'} h_{g',g} = m_g \tag{2.55}$$

which is the equivalent of the continuous counterpart in Eq. (A.2).

The discrete daughter bubble size distribution properties in Eqs. (2.51) and (2.55) can be shown to be valid for $h_{g,g'}$ computed according to Eq. (2.44). The proof consists in realizing that when performing the summations in Eqs. (2.51) and (2.55) the neighboring terms involving $h^I_{g',g}$ and $h^{II}_{g'-1,g}$ defined in Eq. (2.44) can be combined to form the contribution to the integrals in Eqs. (A.1) and (A.2) on the interval $(m_g; m_{g+1})$. However, this proof can be performed only for interior groups and not for the boundary groups at $g = 1$ and $g = G$.

Let's consider now the case for which $g = 1$ in Eqs. (2.51) and (2.55). From Eq. (2.51) it is found that $h_{11} = n$ while from Eq. (2.55) $h_{11} = 1$. This inconsistency is due to the fact that when $g = 1$ there is no $h^{II}_{0,1}$ to be combined with $h^I_{1,1}$. The same is true for any other g since $h^{II}_{0,g}$ is not defined. This inconsistency means that either mass or number of bubbles (or both) is not conserved at $g = 1$.

This problem is not present when $g = G$ since for this case the summation in Eq. (2.43) only goes over $g' = G$ and for the first term only. Hence there is no $h^{II}_{G,g}$ that needs to be combined with a $h^I_{G+1,g}$.

2.3.1.2 Boundary conditions

The discussion above about the non-conservation due to the discretization at $g = 1$ clearly shows that the fix pivot discretization by Kumar and Ramkrishna (1996) cannot preserve mass and number of bubbles simultaneously. The solution in this work is to give preference to mass conservation, *i.e.* to ensure that Eq. (2.55) is satisfied. With this Eq. (2.54) is satisfied exactly but Eq. (2.52) is not. However it can be shown that the error in Eq. (2.52) is $O(m_1)$.

In order to satisfy mass conservation it is necessary determine how to compute

$h^I_{1,g'}$ such that the discrete flux of mass due to particles born on $(0;\, m_1)$ equals to its continuous evaluation. Then it is required that

$$\underbrace{m_1 h^I_{1g'} b_{g'} N_{g'}}_{\text{Actual discrete mass flux}} = \underbrace{b_{g'} N_{g'} \int_0^{m_1} \mathrm{d}m\, m\, h(m, m_{g'})}_{\text{Continuous evaluation of } h(m,m')} \tag{2.56}$$

Then $h^I_{1g'}$ can be obtained from Eq. (2.56) as

$$h^I_{1g'} = \frac{1}{m_1} \int_0^{m_1} \mathrm{d}m\, m\, h(m, m_{g'}) \tag{2.57}$$

Actually this same result can be obtained by expanding Eq. (2.44). This shows that the method by Kumar and Ramkrishna (1996) naturally preserves mass in the breakup discretization as well. In particular, if $g' = 1$, then $h_{11} = 1$.

2.3.2 Coalescence

The coalescence deaths source can be computed from its definition in Eq. (2.15) using the discrete approximation of $f(m)$ in Eq. (2.23) and using the midpoint rule to compute each of the integrals on the intervals $(m_{g-1/2};\, m_{g+1/2})$. The result is

$$\chi^-(m) = f(m) \sum_{g'=1}^{G} N_{g'}\, Q(m, m_{g'}) \tag{2.58}$$

and χ^-_g is obtained by integrating this approximation for $\chi^-(m)$ on $(m_{g-1/2};\, m_{g+1/2})$

$$\chi^-_g = \int_{m_{g-1/2}}^{m_{g+1/2}} \mathrm{d}m\, \chi^-(m) = N_g \sum_{g'=1}^{G} N_{g'}\, Q_{gg'} \tag{2.59}$$

with $Q_{gg'} = Q(m_g, m_{g'})$ and once again the midpoint integration rule is used to integrate the coalescence kernel $Q(m, m')$ on m.

The discretization of coalescence births has a problem similar to the one found for breakup as illustrated in Fig. 2.3. If two bubbles of sizes $m_{g'}$ and $m_{g''}$ coalesce to form a larger bubble of size $m = m_{g'} + m_{g''}$, typically this size is not represented by any of the other group sizes m_g. An exception to this is the case in which a uniformly spaced grid in the mass coordinate is used. However, the mass coordinate is typically discretized with a non-uniform spacing in order to selectively refine the size discretization where needed.

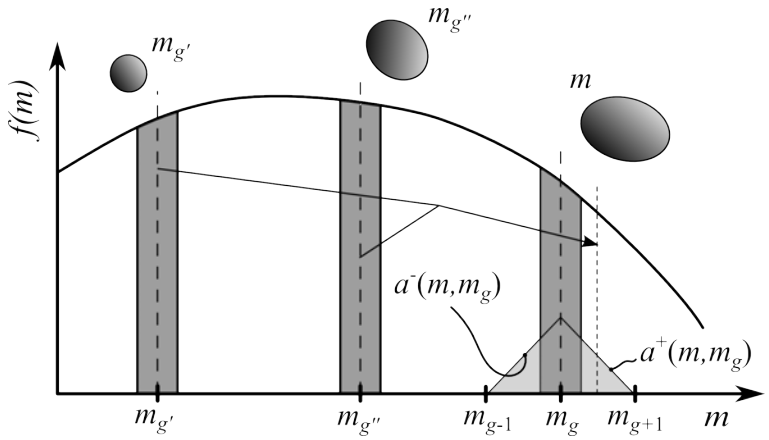

Figure 2.3: Coalescence in the multigroup approach.

Once more the solution is to use weights a^+ and a^- to find the contribution to births in a group g from neighboring births in $(m_{g-1};\, m_{g+1})$. Then

$$\chi_g^+ = \underbrace{\int_{m_{g-1}}^{m_g} \mathrm{d}m\, a^-(m, m_g)\, \chi^+(m)}_{T_I} + \underbrace{\int_{m_g}^{m_{g+1}} \mathrm{d}m\, a^+(m, m_g)\, \chi^+(m)}_{T_{II}} \tag{2.60}$$

$\chi^+(m)$ can be evaluated using the discrete approximation in Eq. (2.23) on $f(m')$ in Eq. (2.14) and using a midpoint rule to perform the resulting integrals on intervals

$(m_{g-1/2};\, m_{g+1/2})$. The result is

$$\chi^{+}(m) = \frac{1}{2} \sum_{g'=1}^{m_{g'}<m} f(m - m_{g'})\, N_{g'}\, Q(m - m_{g'},\, m_{g'}) \tag{2.61}$$

Now, the integration in Eq. (2.60) is carried out in two terms. In the first term, m belongs to the interval $(m_{g-1};\, m_g)$ and then the upper limit in Eq. (2.61) is $g' < g$. Similarly, for the second term in Eq. (2.60), the upper limit in Eq. (2.61) is $g' < g+1$.

Then for the first term

$$\begin{aligned} T_I &= \int_{m_{g-1}}^{m_g} \mathrm{d}m\, a^{-}(m, m_g)\, \chi^{+}(m) \\ &= \frac{1}{2} \sum_{g'=1}^{g'<g} N_{g'} \int_{m_{g-1}}^{m_g} \mathrm{d}m\, a^{-}(m, m_g)\, f(m - m_{g'})\, Q(m - m_{g'},\, m_{g'}) \\ &= \frac{1}{2} \sum_{g'=1}^{g'<g} N_{g'} \sum_{\substack{g'' \\ m_{g-1}<m_c<m_g}} a^{-}(m_c, m_g)\, N_{g''}\, Q_{g''g'} \end{aligned} \tag{2.62}$$

where $m_c = m_{g'} + m_{g''}$. Similarly for the second term

$$T_{II} = \int_{m_g}^{m_{g+1}} \mathrm{d}m\, a^{+}(m, m_g)\, \chi^{+}(m) = \frac{1}{2} \sum_{g'=1}^{g'<g+1} N_{g'} \sum_{\substack{g'' \\ m_g<m_c<m_{g+1}}} a^{+}(m_c, m_g)\, N_{g''}\, Q_{g''g'} \tag{2.63}$$

The final result for χ_g^{+} is

$$\chi_g^{+} = \frac{1}{2} \sum_{g'=1}^{g'\le g} \sum_{\substack{g''=1 \\ m_{g-1}<m_c<m_{g+1}}}^{G} \eta_g(m_c)\, Q_{g''g'}\, N_{g''}\, N_{g'} \tag{2.64}$$

with $\eta_g(m)$ defined as

$$\eta_g(m) = \begin{cases} \dfrac{m_{g+1} - m}{m_{g+1} - m_g} & m \in (m_g;\, m_{g+1}) \\ \dfrac{m - m_{g-1}}{m_g - m_{g-1}} & m \in (m_{g-1};\, m_g) \end{cases} \tag{2.65}$$

Since g'' in Eq. (2.64) runs over all groups, interactions between g' and g'' are counted twice and hence the factor 1/2. In order to save operations, *i.e.* computational work, the summation in Eq. (2.64) can modified in order to be carried only over pairs of sizes. This is possible since the kernel $Q(m, m')$ is symmetric. Then Eq. (2.64) is rewritten as

$$\chi_g^+ = \sum_{g'=1}^{g} \sum_{g''=g'}^{g} C^g_{g'g''}\, N_{g'}\, N_{g''} \tag{2.66}$$

with $C^g_{g'g''}$ defined as

$$C^g_{g'g''} = \begin{cases} \left(1 - \frac{1}{2}\delta_{g'g''}\right) \eta_g(m_c)\, Q_{g''g'} & m_{g-1} \le m \le m_{g+1},\ g' \le g'' \\ 0 & \text{otherwise} \end{cases} \tag{2.67}$$

the factor $\left(1 - \frac{1}{2}\delta_{g'g''}\right)$ is necessary in $C^g_{g'g''}$ since the factor 1/2 is still present in Eq. (2.64) when $g' = g''$

As with breakup, coalescence sources can be recast in matricial form defining the matrices

$$\begin{aligned} \mathbf{C}^+_{gg'}(\mathbf{N}) &= \sum_{g''=g'}^{g} C^g_{g'g''}\, N_{g''} \\ \mathbf{C}^-_{gg'}(\mathbf{N}) &= \delta_{gg'} \sum_{g''=1}^{G} Q_{gg''}\, N_{g''} \\ \mathbf{C}(\mathbf{N}) &= \mathbf{C}^+(\mathbf{N}) - \mathbf{C}^-(\mathbf{N}) \end{aligned} \tag{2.68}$$

and then if only coalescence is considered the discrete Boltzmann equation reduces to

$$\frac{\partial \mathbf{N}}{\partial t} = \mathbf{C}^{+}(\mathbf{N}) \cdot \mathbf{N} - \mathbf{C}^{-}(\mathbf{N}) \cdot \mathbf{N} = \mathbf{C}(\mathbf{N}) \cdot \mathbf{N} \tag{2.69}$$

Note that $\mathbf{C}^{+}$ and therefore $\mathbf{C}$ are lower diagonal matrices. Note also that in contrast to the breakup matrices defined in Eq. (2.47) the coalescence matrices are functions of the number density vector $\mathbf{N}$ and then the solution of the Boltzmann equation becomes non-linear in $\mathbf{N}$ even if the breakup and coalescence kernels do not depend on $\mathbf{N}$.

2.3.2.1 Boundary conditions

Similarly as with breakup where special care had to be taken for the first group, special care must be taken for the last group in the discretization of the coalescence terms. This is due to the fact that there exist coalescence events that result in a bubble size larger than the maximum size in group G. For instance, consider the case of small bubbles colliding onto a large bubble that belongs to group G, the group of bubbles with the largest size. This increases the mass of this bubble but it still remains in group G since this group includes all bubbles in $(m_{G-1/2}; \infty)$. However, in the multigroup approximation, all bubbles in this group have m_G only. Hence, mass is lost since the mass of this new bubble is larger than the mass of the group to which it is assigned.

The only way to remedy this situation is to modify the number of bubbles assigned to group G such that mass is preserved. Once more this does not preserve the number of bubbles, but it is assumed that this bubble size is at the end of the size distribution where boundary condition effects do not affect the rest of the solution.

Consider then the coalescence event between bubbles with masses in groups g' and g''. The rate at which mass is lost from these groups can be computed from

the respective contribution in Eq. (2.59)

$$\begin{aligned} \dot{m}_{g'} &= -m_{g'}\, Q_{g'g''} N_{g'} N_{g''} \\ \dot{m}_{g''} &= -m_{g''}\, Q_{g'g''} N_{g'} N_{g''} \end{aligned} \tag{2.70}$$

Then the total mass lost due to this coalescence event is

$$\dot{m}_{g'+g''} = -m_c\, Q_{g'g''} N_{g'} N_{g''} \tag{2.71}$$

where $m_c = m_{g'} + m_{g''}$. It is assumed that $m_c > m_G$ and then bubble births due to this coalescence event are assigned to group G. Consider now the rate at which mass is transfered to group G due to this coalescence. According to Eqs. (2.66) and (2.67) this contribution is

$$\dot{m}_G = +m_G \left(1 - \tfrac{1}{2}\delta_{g'g''}\right) \eta_G(m_c)\, Q_{g'g''} N_{g'} N_{g''} \tag{2.72}$$

In order for mass to be conserved it must be satisfied that $\dot{m}_G = -\dot{m}_{g'+g''}$. Then it is found that

$$\eta_G(m) = \frac{m}{m_G} \qquad \text{for } m > m_G \tag{2.73}$$

this expression is found to hold even for $g' = g''$. Note that since $m > m_G$ then $\eta_G > 1$ therefore having this factor the desired effect of assigning more bubbles to group G in order to preserve mass.

2.3.3 Dissolution

For dissolution it is necessary to find an approximation for the fluxes $F_{g-1/2}$ and $F_{g+1/2}$ in Eq. (2.16). The approach adopted here is the same as the one taken in Carrica et al. (1999): an upwind scheme where the dissolution mass rate $\dot{m}$ *convects* the number density distribution $f(m)$ along its *space coordinate* m. An

upwind convection scheme is the natural choice since the Boltzmann equation is hyperbolic in the mass dissolution term.

Thus fluxes are computed according to

$$\begin{aligned} F_{g+1/2} &= \dot{m}_{g+1/2} f_{g+1/2} \\ F_{g-1/2} &= \dot{m}_{g-1/2} f_{g-1/2} \end{aligned} \tag{2.74}$$

where $f_{g+1/2}$ and $f_{g-1/2}$ are computed using a first order upwind approximation

$$\begin{aligned} f_{g+1/2} &= \frac{N_{g+1/2}}{m_{g+1} - m_g} \\ f_{g-1/2} &= \frac{N_{g-1/2}}{m_g - m_{g-1}} \\ N_{g+1/2} &= \begin{cases} N_g & \dot{m}_{g+1/2} > 0 \\ N_{g+1} & \dot{m}_{g+1/2} < 0 \end{cases} \\ N_{g-1/2} &= \begin{cases} N_{g-1} & \dot{m}_{g-1/2} > 0 \\ N_g & \dot{m}_{g-1/2} < 0 \end{cases} \end{aligned} \tag{2.75}$$

A higher order approximation can be obtained by using high order TVD schemes to compute these fluxes. TVD schemes provide high order convection schemes and at the same time they avoid under and over shoots in the solution that could result in a non-physical negative number density distribution. It should be kept in mind, however, that most likely the physical models used for breakup, coalescence and dissolution in the Boltzmann equation introduce an uncertainty in the solution that does not justify the use of higher order schemes to reduce the numerical discretization error. Therefore, a first order approximation is considered to be accurate enough. Then, if only dissolution is considered, the discrete Boltzmann equation reads

$$\frac{\partial N_g}{\partial t} + a_{g,g-1} N_{g-1} + a_{g,g} N_g + a_{g,g+1} N_{g+1} = 0 \tag{2.76}$$

with discrete coefficients $a_{g,g'}$ computed according to

$$\begin{aligned} a_{g,g-1} &= -\frac{\dot{m}_{g-1/2}}{m_g - m_{g-1}} H(\dot{m}_{g-1/2}) \\ a_{g,g} &= \frac{\dot{m}_{g+1/2}}{m_{g+1} - m_g} H(\dot{m}_{g+1/2}) - \frac{\dot{m}_{g-1/2}}{m_g - m_{g-1}} \left[1 - H(\dot{m}_{g-1/2})\right] \\ a_{g,g+1} &= \frac{\dot{m}_{g+1/2}}{m_{g+1} - m_g} \left[1 - H(\dot{m}_{g+1/2})\right] \end{aligned} \tag{2.77}$$

where $H(x)$ is the Heaviside function. Similarly as with breakup and coalescence the discrete dissolution terms can also be written in matricial form by defining the dissolution matrix

$$\mathbf{D} = \begin{bmatrix} a_{1,1} & a_{1,2} & 0 & 0 & \dots & 0 \\ a_{2,1} & a_{2,2} & a_{2,3} & 0 & \dots & 0 \\ 0 & a_{3,2} & a_{3,3} & a_{3,4} & \dots & 0 \\ 0 & 0 & a_{4,3} & a_{4,4} & \dots & 0 \\ \vdots & \vdots & \vdots & \vdots & \ddots & \vdots \\ 0 & 0 & 0 & 0 & \dots & a_{G,G} \end{bmatrix} \tag{2.78}$$

Then if only dissolution is considered the discrete version of the Boltzmann equation is

$$\frac{\partial \mathbf{N}}{\partial t} + \mathbf{D} \cdot \mathbf{N} = 0 \tag{2.79}$$

where the dissolution matrix $\mathbf{D}$ is tridiagonal.

2.3.3.1 Boundary conditions

For dissolution the cases $g = 1$ and $g = G$ have to be considered separately. Lets consider the dissolution of one single bubble from its original size to its complete disappearance. Then according to Eq. (2.31) this bubble continuously goes across all masses until it reaches zero mass as it would happen with a real bubble. In contrast, in the discrete version of the Boltzmann equation the smallest a bubble can be is m_1. Lets consider this case first *i.e.* when $g = 1$. For this case $F_{g-1/2}$ actually

is the flux at $m = 0$ and hence $F_{g-1/2} = F_0 = 0$ (since $\dot{m} = 0$ for a zero-sized bubble). For this case, and considering only dissolution, the discrete Boltzman equation reduces to

$$\frac{\partial N_1}{\partial t} + F_{1+1/2} = 0 \tag{2.80}$$

Hence bubbles can be transfered from N_2 to N_1 due to dissolution of bubbles of size N_2 or vice versa if bubbles in group $g = 1$ are growing in size. But Eq. (2.80) does not consider the case of bubbles of mass m_1 dissolving into water. This is a consequence of approximating all bubbles contained in the interval $(0; m_{1+1/2})$ with a single size m_1. Therefore Eq. (2.80) must be modified to account for this.

The total mass of air per unit volume contained in bubbles of size N_1 is $m_1 N_1$. This bubbles are dissolved into water at a rate $\dot{m}_1 N_1$. Then if only this process is considered the mass of air contained in the first group changes in time according to

$$\frac{\partial (m_1 N_1)}{\partial t} = \dot{m}_1 N_1 \tag{2.81}$$

or equivalently, since m_1 does not change in time, the number of bubbles contained in the first group change according to

$$\frac{\partial N_1}{\partial t} = \frac{\dot{m}_1}{m_1} N_1 \tag{2.82}$$

This is the new term that must be added to Eq. (2.80). With these considerations Eq. (2.76) is modified to

$$\frac{\partial N_g}{\partial t} + a_{g,g-1} N_{g-1} + a_{g,g} N_g + a_{g,g+1} N_{g+1} = \frac{\dot{m}_1}{m_1} N_1 \left[1 - H(\dot{m}_1)\right] \delta_{1,g} \tag{2.83}$$

The Heaviside function is necessary since this additional term only accounts for dissolution of bubbles of mass m_1 when $\dot{m}_1 < 0$. When $\dot{m}_1 > 0$ bubbles grow into bubbles of mass m_2 and this is already accounted for by $F_{1+1/2}$. The matrix

coefficients when $g = 1$ in Eq. (2.77) are then modified to

$$\begin{aligned}
a_{g,g-1} &= 0 && \text{Dummy since } g-1=0 \\
a_{g,g} &= \frac{\dot{m}_{g+1/2}}{m_{g+1}-m_g} H(\dot{m}_{g+1/2}) - \frac{\dot{m}_1}{m_1}\left[1-H(\dot{m}_1)\right] && \text{Since } F_{1-1/2}=0 \\
a_{g,g+1} &= \frac{\dot{m}_{g+1/2}}{m_{g+1}-m_g}\left[1-H(\dot{m}_{g+1/2})\right] && \text{Same as an inner group}
\end{aligned} \tag{2.84}$$

When $g = G$ the upper limit of this group is $m_{G+1/2} = \infty$. Since physical size distributions will go to zero as the bubble size goes to infinity, or actually a finite large bubble size, $F_{G+1/2} = F_\infty = 0$. Then the coefficients in Eq. (2.77) are

$$\begin{aligned}
a_{g,g-1} &= -\frac{\dot{m}_{g-1/2}}{m_g-m_{g-1}} H(\dot{m}_{g-1/2}) && \text{Same as an inner group} \\
a_{g,g} &= -\frac{\dot{m}_{g-1/2}}{m_g-m_{g-1}}\left[1-H(\dot{m}_{g-1/2})\right] && \text{Since } F_\infty = 0 \\
a_{g,g+1} &= 0 && \text{Dummy}
\end{aligned} \tag{2.85}$$

2.3.4 Full System of Equations

The final system of equations considering together breakup, coalescence and dissolution reads

$$\frac{\partial \mathbf{N}}{\partial t} + \mathbf{D}\cdot\mathbf{N} = \mathbf{B}^+\cdot\mathbf{N} - \mathbf{B}^-\cdot\mathbf{N} + \mathbf{C}^+(\mathbf{N})\cdot\mathbf{N} - \mathbf{C}^-(\mathbf{N})\cdot\mathbf{N} \tag{2.86}$$

where the breakup matrices are defined in Eq. (2.47), the coalescence matrices in Eq. (2.68) and the dissolution matrix in Eq. (2.78). Modifications to the coefficients appearing in these matrices due to boundary conditions can be found for breakup in Eq. (2.57) for $g = 1$, for coalescence in Eq. (2.73) for $g = G$ and for dissolution in Eq. (2.84) for $g = 1$ and in Eq. (2.85) for $g = G$.

Matrices $\mathbf{B}^-$ and $\mathbf{C}^-$ that account for breakup and coalescence deaths respectively are diagonal. The births breakup matrix $\mathbf{B}^+$ is upper diagonal while the

births coalescence matrix $\mathbf{C}^+$ is lower diagonal. The dissolution matrix is tridiagonal. Therefore in general the system of equations in Eq. (2.86) will lead to a dense matrix. In addition the reader should recall the nonlinear dependence of the coalescence matrix on the solution vector $\mathbf{N}$ even when the coalescence kernels might not depend on it. In real life problems typical kernels will depend on the solution vector $\mathbf{N}$ most likely having a functional dependence on the dispersed phase void fraction α_d. Therefore all the the matrices in Eq. (2.86) generally depend on the solution vector $\mathbf{N}$, though the strongest non-linearity is due to coalescence interactions.

2.4 Derived Quantities

This section summarizes the derived quantities that can be obtained once the number density distribution is known and a few new ones are introduced. These quantities are used in the analysis of the simulations performed in Chapters 5 and 6. In addition, discrete versions are presented as well. These quantities can be obtained as a post-processing step after the solution is obtained.

2.4.1 Integral Quantities

Total number density and void fraction are computed as in Eqs. 2.4 and 2.6 respectively. For number density

$$N(\boldsymbol{r}, t) = \int_0^\infty \mathrm{d}m \; f(m, \boldsymbol{r}, t) \tag{2.4}$$

and for void fraction

$$\alpha_d(\boldsymbol{r}, t) = \int_0^\infty \mathrm{d}m \; \frac{m}{\rho_d(m, \boldsymbol{r}, t)} f(m, \boldsymbol{r}, t) \tag{2.6}$$

The discrete counterpart to these were presented in Eqs. 2.25 and 2.27

$$N(\boldsymbol{r},t) = \sum_{g=1}^{G} N_g(\boldsymbol{r},t) \tag{2.25}$$

$$\alpha_d(\boldsymbol{r},t) = \sum_{g=1}^{G} \alpha_g = \sum_{g=1}^{G} \frac{m_g}{\rho_d(m_g,\boldsymbol{r},t)} N_g(\boldsymbol{r},t) \tag{2.27}$$

More generally, the p-th moment of the number density distribution is defined as

$$Q_p(\boldsymbol{r},t) = \int_0^\infty \mathrm{d}m\, D(m)^p\, f(m,\boldsymbol{r},t) \tag{2.87}$$

From this, a series of mean diameters (or sizes in the case of non-spherical bubbles) that prove to be useful when analyzing polydisperse bubbly flows are defined as (from Brennen, 2005)

$$d_{pq} = \left(\frac{Q_p}{Q_q}\right)^{\frac{1}{p-q}} \tag{2.88}$$

with $p > q$. Common examples are the mean diameter d_{10} and the mass mean diameter d_{30}. In some bubble reactors where the interfacial area is important, the surface area mean diameter d_{20} may prove to be a more representative quantity. Another popular choice is the Sauter mean diameter d_{32} which is a measure of the ratio of the bubble volume to the bubble surface area.

The discrete approximation of the p-th moment is

$$Q_p(\boldsymbol{r},t) = \sum_{g=1}^{G} D_g^p N_g(\boldsymbol{r},t) \tag{2.89}$$

This approximation is then used in Eq. (2.88) to compute diameters d_{pq}.

2.4.2 Size Distributions

In addition to the number density distribution $f(m)$, size distributions can be presented in the form of a void fraction distribution as introduced in Eq. (2.7)

$$\alpha_m(m) = \frac{m}{\rho_d(m, \boldsymbol{r}, t)} f(m, \boldsymbol{r}, t) \tag{2.7}$$

In the continuum, size distributions can be recast in terms of another variable by means of a change of variables. For instance, the size distribution in radius is obtained as, with $m = \rho_d \, 4/3 \, \pi \, R^3$

$$f(R) = f(m) \left| \frac{\mathrm{d}m}{\mathrm{d}R} \right| = 3 \frac{m}{R} f(m) \tag{2.90}$$

Note that the above transformation is valid also for non-spherical bubbles as long as, as commented at the beginning of this chapter, the bubble radius is taken as a representative characteristic radius for bubbles of mass m.

If the size distribution in diameter is desired it can be obtained from the size distribution in radius as

$$f(D) = f(R) \left| \frac{\mathrm{d}R}{\mathrm{d}D} \right| = \frac{1}{2} f(R) \tag{2.91}$$

These changes of variables ensure that the integral of the number density distribution performed on any of these variables (either m, R or D) is always the total number density $N(\boldsymbol{r}, t)$. The same changes of variables performed in Eqs. 2.90 and 2.91 on the number density distribution can be applied to any distribution and in particular to the void fraction distribution in Eq. (2.7).

When computing size distributions from the discrete number density N_g instead, the following approximations can be used (which assume a constant $f(m)$ in

($m_{g-1/2}$; $m_{g+1/2}$) in accordance with the approximation in Eq. (2.23))

$$\begin{aligned} f(m_g) &= \frac{N_g}{\Delta m_g} \qquad & \alpha_m(m_g) &= \frac{\alpha_g}{\Delta m_g} \\ f(R_g) &= \frac{N_g}{\Delta R_g} \qquad & \alpha_R(R_g) &= \frac{\alpha_g}{\Delta R_g} \end{aligned} \tag{2.92}$$

An alternative to obtain $f(R)$ for instance, would be to compute first $f(m)$ as in Eq. (2.92) and then use the transformation given by Eq. (2.90). These two approximations for $f(R)$ are different but they should converge to a unique result as the discretization in sizes is refined.

The last group of the multigroup discretization, *i.e.* the one with $g = G$, contains, in theory, all bubble sizes between $m_{G-1/2}$ (or $R_{G-1/2}$) and ∞. This would mean that the interval size Δm_G (or ΔR_G) is infinity and according to Eq. (2.92) the estimated size distribution at $g = G$ would be zero even with a non-zero number density N_G. In order to come up with a finite approximation of the size distribution at $g = G$ reflecting the corresponding non-zero number density, a second order extrapolation is used to compute the G-th interval size. Therefore this is estimated as $\Delta m_G = 2\Delta m_{G-1} - \Delta m_{G-2}$ (or $\Delta R_G = 2\Delta R_{G-1} - \Delta R_{G-2}$).

It is important to note that while the interval sizes Δm_g are fixed given an initial size discretization, the interval sizes ΔR_g generally change in time and space since variations in pressure change the radius of the bubbles.

2.4.3 Intergroup Transfer Budget

In addition to the prediction of void fraction and size distributions, the modeling of polydispersed flows in the computer allows the modeler to carry a detailed analysis of the individual contributions to the Boltzmann equation made by the different multigroup transfer mechanisms (breakup, coalescence and dissolution in this work). This analysis is given the name of *intergroup transfer budget analysis* in this work in analogy to the energy budget for turbulent flows. In the budget

analysis the different source terms appearing in the Boltzmann equation are plotted together as a function of the bubble size. This section describes how these terms are obtained from the discrete solution.

Breakup and coalescence sources $\beta(m)$ and $\chi(m)$ in Eq. (2.8) are size distributions as well, giving the rate of change due to breakup and coalescence respectively for bubble sizes within dm of size m. These are computed with the same approximations in Eq. (2.92) used for the number density and void fraction distributions. For the sake of completeness the expressions used to compute them are given below

$$\begin{aligned} \beta^+(m_g) &= \frac{\beta_g^+}{\Delta m_g} \qquad & \beta^-(m_g) &= \frac{\beta_g^-}{\Delta m_g} \\ \chi^+(m_g) &= \frac{\chi_g^+}{\Delta m_g} \qquad & \chi^-(m_g) &= \frac{\chi_g^-}{\Delta m_g} \end{aligned} \tag{2.93}$$

with similar expressions to compute them in terms of the bubble radius R.

Another quantity of interest for the budget analysis is the dissolution rate. If only dissolution is considered and the bubble mass is a function of time $m(t)$ instead of an independent variable, the number density distribution $f(m)$ changes according to

$$\frac{\mathrm{d}f(m(t),t)}{\mathrm{d}t} = \frac{\dot{m}(m(t))}{m(t)} f(m(t),t) \tag{2.94}$$

this is the equivalent to a *Lagrangian* formulation in continuum mechanics since $f(m,t)$ is describing the number density of an initial population of bubbles as its mass changes with time. However, this population of bubbles remains the same as the original, meaning that the same bubbles are tracked as their mass changes with time. The *Eulerian* equivalent to Eq. (2.94) is, from Eq. (2.31), given by

$$\frac{\partial f(m,t)}{\partial t} + \frac{\partial}{\partial m}\left(\dot{m} f(m,t)\right) = 0 \tag{2.95}$$

where instead of following a given population of bubbles during its lifetime $f(m,t)$

describes the number density of the bubbles that at time t are going through mass m.

From the right hand side of the *Lagrangian* form in Eq. (2.94) the *dissolution rate density* is defined as

$$\dot{\mathcal{R}}_d(m) = -\frac{\dot{m}}{m} f(m) \tag{2.96}$$

and gives the dissolution rate per unit of volume for bubbles within dm of size m. The minus sign is added in order to define $\dot{\mathcal{R}}_d(m)$ as positive when bubbles dissolve into the surrounding water and as negative when gas dissolved in the water goes into the bubbles. From the *Eulerian* form in Eq. (2.31) the *dissolution source* is

$$\mathcal{D}(m) = -\frac{\partial}{\partial m}\left(\dot{m} f(m,t)\right) \tag{2.97}$$

and gives the rate of change of the number density due to dissolution. The physical meanings encoded in the *dissolution rate density* $\dot{\mathcal{R}}_d(m_g)$ and in the *dissolution source* $\mathcal{D}(m)$ are substantially different but confusion may arise given that they both give a dissolution rate. An example may help to clarify. Consider a case with a flat number density distribution, *i.e.* $f(m)$ is constant for all sizes (or at least within a range of bubble sizes). If, in addition, the bubble dissolution rate $\dot{m}$ is constant as well, then the dissolution source in Eq. (2.97) is zero. This does not mean that bubbles are not dissolving and, in fact, they are. This is reflected by the *dissolution rate density* $\dot{\mathcal{R}}_d(m)$ which is different from zero. The reason why the dissolution source is zero is because as bubbles of size m dissolve out of this size, larger bubbles dissolve into size m at the same rate (considering $\dot{m} < 0$ for instance). It is for this reason that the dissolution rate density $\dot{\mathcal{R}}_d(m)$ is preferred when performing the budget analysis. However, if the different components of the budget are going to be added in order to find the total rate of change, the term that must be considered is the dissolution source $\mathcal{D}(m)$ in Eq. (2.31)

The discrete version to Eq. (2.96) is simply obtained by using the discrete approximation to $f(m)$

$$\dot{\mathcal{R}}_d(m_g) = -\frac{\dot{m}(m_g)}{m_g} f(m_g) = -\frac{\dot{m}(m_g)}{m_g} \frac{N_g}{\Delta m_g} \tag{2.98}$$

2.4.4 Intergroup Transfer Frequencies

The budget analysis is a very powerful tool providing plenty of information on the relative importance of the several mechanisms controlling the final distribution in bubble sizes. However, a small or zero breakup source does not necessarily mean that breakup for that size is small or zero as well. Consider the source for breakup deaths $\beta^-(m)$. This is simply computed as the product of the breakup kernel with the number density distribution as reflected in Eq. (2.11). Therefore, this source can become zero either because breakup is zero or either because the population of bubbles at that size is zero. The second situation is quite common. Given that large bubbles are easily breakable by turbulence the breakup rate $b(m)$ is large. However, this large breakup causes large bubbles to quickly breakup into smaller ones and the number density becomes negligible at large sizes. Therefore the breakup source $\beta^-(m)$ becomes negligible as well. Still, breakup is strong at large sizes.

In order to have a quantity that would reflect the strength of the different intergroup transfer mechanisms independently of the number density, the intergroup transfer frequencies are introduced. For breakup, the breakup frequency $\omega_b(m)$ is simply given by the breakup rate $b(m)$. According to equation Eq. (2.11) this could be defined as $\omega_b(m) = \beta^-(m)/f(m) = b(m)$ and then the breakup frequency is the number of breakup events per unit of time per bubble. Coalescence and dissolution frequencies can be defined analogously, *i.e.* the number of events per unit of time per bubble. Inspired on this idea, intergroup transfer frequencies for

each mechanism are defined as

$$\omega_b(m) = \frac{\beta^-(m)}{f(m)} = b(m) \tag{2.99}$$

$$\omega_c(m) = \frac{\chi^-(m)}{f(m)} = \int_0^\infty \mathrm{d}m'\, Q(m,m')\, f(m') \tag{2.100}$$

$$\omega_d(m) = \frac{\dot{\mathcal{R}}_d(m)}{f(m)} = -\frac{\dot{m}_g}{m_g} \tag{2.101}$$

While the breakup and dissolution frequencies are almost independent of the size distribution, the coalescence frequency strongly depends on it. The discrete version of Eqs. (2.99)-(2.101) are

$$\omega_b(m_g) = b_g = \frac{\beta_g^-}{N_g} \tag{2.102}$$

$$\omega_c(m_g) = \frac{\chi_g^-}{N_g} = \sum_{g'=1}^{G} N_{g'}\, Q_{gg'} \tag{2.103}$$

$$\omega_d(m_g) = \frac{\dot{\mathcal{R}}_d(m_g)}{f(m_g)} = -\frac{\dot{m}_g}{m_g} \tag{2.104}$$

where it should be noted that the dissolution frequency $\omega_d(m)$ could become negative if gas dissolved in the water goes into the bubbles. However, dissolution into the water is the typical situation.

CHAPTER 3
POLYDISPERSED BUBBLY FLOW MODEL

The Boltzmann equation introduced in Chapter 2 together with the multigroup approach allows to compute the number density distribution at every point in space and time, provided that the group-g velocity $\boldsymbol{u}_g$ is available. In order to formulate a closed model for polydisperse flows a new set of equations must be provided to compute these velocities. In addition, the effect of the dispersed phase on the continuous phase must be considered.

This new set of equations is provided by the so called two-fluid model. In the two-fluid model the instantaneous local equations of motion for the liquid and gas phases are averaged to obtain conservation laws for the average hydrodynamics conditions of the fluid. This approach is similar to the one used to obtain the standard RANS equations in turbulence modeling. The two-fluid model equations can be obtained by several averaging procedures. In the pioneer work by Ishii (1975), the two-fluid equations are obtained by time-averaging the equations of motion. In Drew (1983) similar equations are obtained by using the concept of a phase field function first introduced in Drew (1971). The two-fluid formulation presented in this work is based on the more recent developments made by Drew and Lahey Jr. (1979); Drew (1983); Lahey Jr. et al. (1992); Drew and Passman (1999) and later on applied to the prediction of polydispersed bubbly flows around ships by Carrica et al. (1999) and Moraga et al. (2008).

In addition, this chapter presents the models used for: turbulence; breakup, coalescence and dissolution; air entrainment; oceanic background; rectified diffusion in the propeller. Together, these models close the mathematical description for polydispersed bubbly flows presented in this work.

3.1 Two Fluid Model

In the two-fluid model the presence of either the continuous or dispersed phase at a certain point in space and time is described statistically. The equations of motion for each phase are obtained by ensemble averaging the Navier-Stokes equations conditioned to be either in the continuous or dispersed phase. The result of this averaging process is (see Drew and Passman, 1999)

$$\frac{\partial \alpha_k \rho_k \boldsymbol{u}_k}{\partial t} + \nabla \cdot (\alpha_k \rho_k \boldsymbol{u}_k \otimes \boldsymbol{u}_k) = \nabla \cdot (\alpha_k \mathbf{T}_k) + \boldsymbol{M}_k - \alpha_k \rho_k \, g \, \hat{k} + \boldsymbol{u}_{ki}^m \Gamma_k \tag{3.1}$$

$$\frac{\partial \alpha_k \rho_k}{\partial t} + \nabla \cdot (\alpha_k \rho_k \boldsymbol{u}_k) = \Gamma_k \tag{3.2}$$

where the subindex $k = c$ or $k = g$ denotes the continuous phase or the gas group g respectively. α_k is the phase k void fraction, ρ_k is the phase density, $\boldsymbol{u}_k$ is the velocity of the phase k and $\mathbf{T}_k$ is the stress tensor of the phase k which already considers the additional mixing due to turbulence. $\boldsymbol{M}_k$ in Eq. (3.1) is the result from averaging the interfacial forces acting on the interface separating the two phases. In the conservation of mass Eq. (3.2) Γ_k is a source term that considers the mass transfer between phases (*e.g.*, dissolution). Similarly, the source term $\boldsymbol{u}_{ki}^m \Gamma_k$ in Eq. (3.1) considers the transfer of momentum between the phases due to this mass transfer. The term $-\alpha_k \rho_k \, g \, \hat{k}$ in Eq. (3.1) is the gravitational force acting in the $-z$ direction.

The stress tensor can be decomposed as

$$\mathbf{T}_k = -p_k \mathbb{I} + 2\mu_{eff,k} \nabla^s \boldsymbol{u}_k \tag{3.3}$$

where p_k is the phase k pressure and $\mu_{eff,k}$ is an effective viscosity that models the additional mixing due to turbulent fluctuations. $\mathbb{I}$ is the identity matrix and $\nabla^s \cdot = (\nabla \cdot + \nabla^\dagger \cdot)/2$ is the symmetric gradient operator.

Since at all times any point in space is occupied by one of these phases the void fractions satisfy

$$\begin{aligned} \alpha_d &= \sum_{g=1}^{G} \alpha_g \\ \alpha_c + \alpha_d &= 1 \end{aligned} \tag{3.4}$$

where α_d is the dispersed phase void fraction already defined in Eq. (2.6) and α_g is the group void fraction defined in Eq. (2.28).

3.1.1 Dispersed Phase

In the Bolzmann equation, Eq. (2.8), the dispersed phase is transported by the dispersed phase velocity $\boldsymbol{u}_d(m)$ which is a function of the bubble mass m. In the discrete multigroup version of this equation, Eq. (2.16),the group velocity $\boldsymbol{u}_g$ plays this rol. Therefore, in order for the model to be complete, a set of equations for the group velocities $\boldsymbol{u}_g$ must be formulated. These equations are the momentum conservation equations provided by the two-fluid model in Eq. (3.2) when $k = g$.

For the gas phase it can be assumed that inertia and shear stresses are negligible. The inertia of the bubbles is neglected given that the density of the surrounding liquid is much larger than that of gas, $\rho_d \ll \rho_c$. Moreover, the inertia of the gas is negligible in comparison to the effort that takes to accelerate the fluid surrounding the bubble. This effect is considered by an additional *virtual mass* force to be discussed later. Shear stresses in the dispersed phase are neglected given that bubbles are separate units and shear between them can only be transfered through the fluid. An additional viscous shear inside the bubbles is caused by recirculations inside them but this effect is confined inside the bubbles and does not contribute to the momentum balance between bubbles. In addition, it is assumed that the gas phase pressure can be approximated by the liquid pressure, *i.e.* $p_g \approx p_c$ for all

groups. With these assumptions Eq. (3.1) for group g simplifies to

$$0 = -\nabla\left(\alpha_g p_c\right) + \boldsymbol{M}_g - \alpha_g \rho_g \, g \, \hat{k} \tag{3.5}$$

In Drew and Passman (1999, §15.3.4), it is shown that concentration gradients contribute with an additional force proportional to the gradient of the continuous phase void fraction. Hence the momentum transfer term becomes

$$\boldsymbol{M}_g = p_g \nabla \alpha_g + \widetilde{\boldsymbol{M}}_g \approx p_c \nabla \alpha_g + \widetilde{\boldsymbol{M}}_g \tag{3.6}$$

where $\widetilde{\boldsymbol{M}}_g$ is the interfacial force evaluated without accounting for a gradient in the void fraction and the approximation $p_g \approx p_c$ was used in the last equality. It is usual practice to compute the interfacial force as a linear superposition of separate contributions. Hence this can be written as

$$\widetilde{\boldsymbol{M}}_g = \boldsymbol{M}_g^{VM} + \boldsymbol{M}_g^{D} + \boldsymbol{M}_g^{TD} + \boldsymbol{M}_g^{L} + \boldsymbol{M}_g^{P} \tag{3.7}$$

where these contributions are respectively the virtual mass, drag, turbulent dispersion, lift and packing. Other contributions like the Basset (Basset, 1888) and wall lubrication forces (Moraga et al., 2006; Lucas et al., 2007) are less important and therefore neglected in this work. The packing force accounts for the additional momentum transfer due to collisions between bubbles and is typically ignored by other researchers. This force plays a fundamental roll in wall bounded flows where bubbles tend to accumulate as they rise onto a wall. The models used to compute each of these contributions are described in Section 3.1.4.

Equation (3.5) can be rearranged by using Eq. (3.6)

$$-\alpha_g \nabla p_c + \widetilde{\boldsymbol{M}}_g - \alpha_g \rho_g \, g \, \hat{k} = 0 \tag{3.8}$$

Additionally, it is common practice to subtract the piezometric pressure when dealing with free surface flows. The piezometric pressure $\hat{p}_c$ is defined as

$$p_c = \hat{p}_c - \rho_c g z \tag{3.9}$$

and introducing this definition into Eq. (3.8) the final version of the gas momentum equation is obtained

$$-\alpha_g \nabla \hat{p}_c + \widetilde{\boldsymbol{M}}_g + \alpha_g \rho_c g \left(1 - \frac{\rho_g}{\rho_c}\right) \hat{k} = 0 \tag{3.10}$$

The gravitational term in Eq. (3.10) is no more than the buoyant force per unit volume minus the weight per unit volume and since $\rho_g \ll \rho_c$ this term will provide a net positive buoyant force on the bubbly phase.

3.1.2 Jump Conditions

Transfer of mass and momentum at the gas/liquid interface must satisfy mass and momentum conservation as well. This requirement is given by the jump conditions. When these jump conditions are ensemble averaged a new set of conditions suitable for a two-fluid model are obtained (Drew and Passman, 1999, §11.3). These are

$$\Gamma_c + \sum_{g=1}^{G} \Gamma_g = 0 \tag{3.11}$$

$$\boldsymbol{M}_c + \boldsymbol{u}_{ci}^m \Gamma_c + \sum_{g=1}^{G} \left(\boldsymbol{M}_g + \boldsymbol{u}_{gi}^m \Gamma_g\right) = \boldsymbol{m} \tag{3.12}$$

Equation Eq. (3.11) states the conservation of mass when there is mass transfer between phases. Similarly, Eq. (3.12) states the conservation of momentum, where $\boldsymbol{m}$ is the surface tension source.

3.1.3 Continuous Phase

In this work, bubbly flows are assumed to be adiabatic and isothermal, with no phase change. Therefore, the only mechanism of mass transfer considered is due to the dissolution of the air contained in the bubbles into the surrounding water. In this case the mass transfer rates Γ_g are very small and thus, according to Eq. (3.11), Γ_c is small as well. This mass transfer rate can then be neglected in the mass conservation equation Eq. (3.2) for the continuous phase. Then the mass conservation equation for the continuous phase is simplified as

$$\frac{\partial \alpha_c \rho_c}{\partial t} + \nabla \cdot (\alpha_c \rho_c \boldsymbol{u}_c) = 0 \tag{3.13}$$

If the surface tension source, together with the momentum transfer due to mass transfer, are neglected in Eq. (3.12), the interfacial force for the continuous phase can then be computed in term of the interfacial forces acting on the dispersed phase as

$$\boldsymbol{M}_c = -\sum_{g=1}^{G} \boldsymbol{M}_g \tag{3.14}$$

and using $\boldsymbol{M}_g$ from Eq. (3.6) $\boldsymbol{M}_c$ is

$$\boldsymbol{M}_c = -p_c \nabla \alpha_d - \sum_{g=1}^{G} \widetilde{\boldsymbol{M}}_g \tag{3.15}$$

The summation in this last equation can be simplified by using the group-g

momentum equation in Eq. (3.8)

$$\begin{aligned}\sum_{g=1}^{G} \widetilde{\boldsymbol{M}}_g &= \sum_{g=1}^{G} \left(\alpha_g \nabla p_c + \alpha_g \rho_g \, g \, \hat{k}\right) \\ &= \nabla p_c \sum_{g=1}^{G} \alpha_g + g \, \hat{k} \sum_{g=1}^{G} \alpha_g \rho_g \\ &\approx \alpha_d \nabla p_c + \rho_d \, g \, \hat{k} \sum_{g=1}^{G} \alpha_g \\ &= \alpha_d \nabla p_c + \alpha_d \rho_d \, g \, \hat{k}\end{aligned} \tag{3.16}$$

The approximation in the second to last line in Eq. (3.16) is that the group-g density equals the gas density at the given pressure, *i.e.* $\rho_g \approx \rho_d$. This is not true for small bubbles where surface tension causes the pressure and gas density inside them to increase but, since the contribution of small bubbles to the total void fraction is small, this is a reasonable approximation for the momentum balance. With this assumption Eq. (3.15) becomes

$$\boldsymbol{M}_c = -p_c \nabla \alpha_d - \sum_{g=1}^{G} \widetilde{\boldsymbol{M}}_g = -\nabla \left(\alpha_d p_c\right) - \alpha_d \rho_d \, g \, \hat{k} \tag{3.17}$$

This last expression can be used in Eq. (3.1) to combine the interfacial force term with the continuous phase stresses term. Then, using the definition for $\mathbf{T_c}$ in Eq. (3.3) and the condition $\alpha_c + \alpha_d = 1$, the momentum equation is rearranged as

$$\begin{aligned}\frac{\partial \alpha_c \rho_c \boldsymbol{u}_c}{\partial t} + \nabla \cdot \left(\alpha_c \rho_c \boldsymbol{u}_c \otimes \boldsymbol{u}_c\right) &= \nabla \cdot \left(\alpha_c \mathbf{T}_c\right) - \nabla \left(\alpha_d p_c\right) - \alpha_d \rho_d \, g \, \hat{k} - \alpha_c \rho_c \, g \, \hat{k} \\ &= -\nabla(\alpha_c \, p_c) + \nabla \cdot \left(2\alpha_c \mu_{\text{eff},c} \nabla^s \boldsymbol{u}_c\right) - \nabla \left(\alpha_d p_c\right) - \alpha_d \rho_d \, g \, \hat{k} - (1 - \alpha_d) \rho_c \, g \, \hat{k} \\ &= -\nabla p_c + \nabla \cdot \left(2\alpha_c \mu_{\text{eff},c} \nabla^s \boldsymbol{u}_c\right) + \alpha_d \rho_c \, g \left(1 - \frac{\rho_d}{\rho_c}\right) \hat{k} - \rho_c \, g \, \hat{k}\end{aligned} \tag{3.18}$$

Finally, the gravitational term can be eliminated by using instead the piezometric

pressure defined in Eq. (3.9)

$$\frac{\partial \alpha_c \rho_c \boldsymbol{u}_c}{\partial t} + \nabla \cdot (\alpha_c \rho_c \boldsymbol{u}_c \otimes \boldsymbol{u}_c) = -\nabla \hat{p}_c + \nabla \cdot (2\alpha_c \mu_{\text{eff},c} \nabla^s \boldsymbol{u}_c) + \alpha_d \rho_c \, g \left(1 - \frac{\rho_d}{\rho_c}\right) \hat{k} \quad (3.19)$$

The last term in Eq. (3.19) accounts for the buoyant force exerted by the bubbles on the liquid.

3.1.4 Interfacial Forces

As mentioned before the net interfacial force is typically assumed to be the linear superposition of individual contributions

$$\widetilde{\boldsymbol{M}}_g = \boldsymbol{M}_g^{VM} + \boldsymbol{M}_g^{D} + \boldsymbol{M}_g^{TD} + \boldsymbol{M}_g^{L} + \boldsymbol{M}_g^{P} \quad (3.20)$$

where the individual terms are the virtual mass, drag, turbulent dispersion, lift and packing respectively.

3.1.4.1 Drag

The momentum transfer due to drag is estimated using the expression for the drag force around a sphere

$$\boldsymbol{M}_g^{D} = -\alpha_g \rho_c C_D \frac{3}{8} \frac{\|\boldsymbol{u}_{r,g}\|}{R_g} \boldsymbol{u}_{r,g} \quad (3.21)$$

where $\boldsymbol{u}_{r,g}$ is the relative velocity defined as $\boldsymbol{u}_{r,g} = \boldsymbol{u}_g - \boldsymbol{u}_c$. The drag coefficient is that given by Tomiyama (1998) with a void fraction correction based on the work by Ishii and Zuber (1979) to include the effect of interaction between bubbles. For deformed bubbles in contaminated water the drag force may be expressed as (Moraga et al., 2008)

$$C_D = \frac{1}{\alpha_c} \max \left[\frac{24}{Re_g} (1 + 0.168 \, Re_g^{0.75}), \frac{8}{3} \frac{Eo_g}{Eo_g + 4} \right] \quad (3.22)$$

where the bubble Reynolds number Re_g is based on the bubble relative velocity $\boldsymbol{u}_{r,g}$ and the bubble diameter D_g, *i.e.* $Re_g = \|\boldsymbol{u}_{r,g}\| D_g / \nu_c$. The Eötvös number Eo_g is defined as

$$Eo_g = \frac{g(\rho_c - \rho_d) D_g^2}{\sigma} \tag{3.23}$$

where σ is the surface tension. The Eötvös number can be thought as the ratio of the buoyancy force and the surface tension force. Surface tension tends to keep the spherical shape of a bubble, while a higher buoyancy force causes a higher terminal velocity that departs a bubble from its spherical shape. Therefore, the Eötvös number can also be considered a measure of bubble deformation. This correction for bubble deformation is very significant for large bubble sizes.

Note that even when the expression for the drag force given by Eq. (3.21) resembles that for a spherical bubble, this is still valid for non-spherical bubbles due to the corrections added to the drag coefficient, that is made to be a function not only of the bubble Reynolds number but also of the Eötvös number. The bubble radius used for the computation of the Reynolds number is the equivalent radius of a sphere with the same volume than that of the bubble being considered.

$$R_g(\boldsymbol{r}, t) = \left(\frac{3}{4\pi} \frac{m_g}{\rho_g(\boldsymbol{r}, t)} \right)^{1/3} \tag{3.24}$$

where $\rho_g = \rho_d(m_g, \boldsymbol{r}, t)$ is the dispersed phase density inside the bubble and is a function of space and time since compressibility effects due to local pressure are considered by using an ideal gas law of the form

$$\rho_g(\boldsymbol{r}, t) = \rho_{d,0} \frac{p_g(\boldsymbol{r}, t)}{p_0} \tag{3.25}$$

where p_0 is a reference pressure, typically taken to be the atmospheric pressure, and $\rho_{d,0}$ is the dispersed phase density at this pressure. The pressure p_g in Eq. (3.25) is

the pressure inside a bubble of mass m_g and is computed using the Young-Laplace equation taking into account the contribution to pressure due to surface tension

$$p_g(\boldsymbol{r},t) = p_0 + \hat{p}_c(\boldsymbol{r},t) - \rho_c\, g\, z + \frac{2\sigma}{R_g(\boldsymbol{r},t)} \tag{3.26}$$

The contribution to pressure due to surface tension can be significant for small bubbles. Note that the pressure in Eq. (3.26) depends on the bubble radius which in turn depends on the pressure through Eq. (3.24). This justifies the use of the g-group subscript in Eqs. (3.24), (3.25) and (3.26) on the density ρ_g and pressure p_g inside a bubble of mass m_g. Therefore the bubble radius is not explicitly found from Eq. (3.24), but from solving a system of equations formed by Eqs. (3.24) to (3.26). This system of equations is solved in Section 3.1.5.

3.1.4.2 Virtual mass

The virtual mass force accounts for the acceleration of the fluid surrounding the bubble and it can be modeled as (Drew and Passman, 1999)

$$\boldsymbol{M}_g^{VM} = \alpha_g \rho_c C_{VM} \left[\left(\frac{\partial \boldsymbol{u}_c}{\partial t} + \boldsymbol{u}_c \cdot \nabla \boldsymbol{u}_c \right) - \left(\frac{\partial \boldsymbol{u}_g}{\partial t} + \boldsymbol{u}_g \cdot \nabla \boldsymbol{u}_g \right) \right] \tag{3.27}$$

where the virtual mass coefficient C_{VM} is taken to be 1/2, the theoretical value for dilute potential flow of spherical bubbles.

3.1.4.3 Lift

The lift force is modeled as

$$\boldsymbol{M}_g^{L} = -\alpha_g \rho_c C_L \boldsymbol{u}_{r,g} \times (\nabla \times \boldsymbol{u}_c) \tag{3.28}$$

this force is computed by ensemble averaging the lift force analytically obtained by solving the potential flow around a sphere submerged in a shear flow (Drew and

Lahey Jr., 1987, 1990). The analytical lift coefficient obtained with this model is $C_L = 1/2$ but experimentally it is found to vary for different experimental configurations. The value $C_L = 0.1$ is found for the upflow of spherical particles in a pipe (Lahey Jr. et al., 1993) and was used in previous simulations of ship flows (see Carrica et al., 1999; Moraga et al., 2008).

In Tomiyama et al. (2002) a correlation for the lift coefficient dependent on the bubble size is given as

$$C_L = \begin{cases} \min\left[0.288\tanh(0.121 Re_g), f(Eo_{h,g})\right] & \text{for } Eo_{h,g} < 4 \\ f(Eo_{h,g}) & \text{for } 4 \leq Eo_{h,g} < 10.7 \\ -029 & \text{for } Eo_{h,g} > 10.7 \end{cases} \tag{3.29}$$

where

$$f(Eo_{h,g}) = 0.00105\, Eo_{h,g}^3 - 0.0159\, Eo_{h,g}^2 - 0.0204\, Eo_{h,g} + 0.474 \tag{3.30}$$

where the Eötvös number is based on the maximum bubble horizontal dimension, $Eo_{h,g} = g(\rho_c - \rho_d)D_{h,g}^2/\sigma$. The ratio between the radius of an equivalent sphere with the same bubble mass to the maximum horizontal dimension is evaluated from the empirical correlation given by Wellek et al. (1966)

$$\left(\frac{2\,R_g}{D_{h,g}}\right)^3 = \frac{1}{1 + 0.163\, Eo_{h,g}^{0.757}} \tag{3.31}$$

The correlation given by Tomiyama et al. (2002) predicts a change in the sign of C_L at $D_g = 5.8$ mm in the air-water system. The popular value of $C_L = 0.1$ is attained for bubbles of about 2.6 mm. In Legendre and Magnaudet (1998) the lift force on a bubble is studied numerically and the limiting value $C_L = 1/2$ is obtained for high Reynolds numbers. Their prediction show a strong dependence of C_L on the bubble Reynolds number for low Reynolds numbers. In this work $C_L = 0.1$ is taken

in pursuit of simplicity and since this has been the commonly used value for ship flows. The lift coefficient given by Tomiyama et al. (2002) should be considered in future improvements to the model.

3.1.4.4 Turbulent dispersion

The turbulent dispersion is modeled in many works as an extra forcing term in the gas momentum equation (Carrica et al., 1999; Drew, 2001; Moraga et al., 2008; Lopez de Bertodano et al., 2004). For instance, Carrica et al. (1998) proposed to model the turbulent dispersion force as

$$\boldsymbol{M}_g^{TD} = -\rho_c \alpha_g \frac{3}{8} \frac{C_D \|\boldsymbol{u}_{r,g}\|}{R_g} \frac{\nu_t}{Sc_b} \frac{\nabla N_g}{N_g} \tag{3.32}$$

where ν_t is a turbulent viscosity obtained from a suitable turbulence model (two-phase turbulence modeling is discussed in Section 3.6) and Sc_b is the Schmidt number taken to be $Sc_b = 1.0$. This model is developed based on the idea that small bubbles should behave as fluid tracers. An approximation for the group velocity $\boldsymbol{u}_g$ can be found by only considering drag and turbulent dispersion in Eq. (3.10) and then taking the limit to small bubble radius. This leads to the result

$$\boldsymbol{u}_g = \boldsymbol{V}_{t\,g} - \frac{\nu_t}{Sc_b} \frac{\nabla N_g}{N_g} \tag{3.33}$$

where $\boldsymbol{V}_{t\,g}$ is the bubble terminal velocity. This velocity approximation is introduced into Eq. (2.16) for the number density transport and rearranged as

$$\frac{\partial N_g}{\partial t} + \nabla \cdot \left(\boldsymbol{V}_{t,g} N_g \right) = \nabla \cdot \left(\frac{\nu_t}{Sc_b} \nabla N_g \right) + \beta_g + \chi_g + S_g \tag{3.34}$$

Thus the model proposed by Carrica et al. (1998) predicts the right trend of small particles behaving as fluid tracers (Moraga et al., 2003). However, it was found in the present work (see Appendix B), that for bubble Reynolds $Re_g > 10$ the above

model does not have a unique solution. This was found to be responsible of numerical instabilities specially in highly turbulent regions as the boundary layer and the ship wake.

It is for this reason that in this work turbulent dispersion is not modeled as an extra momentum term in the dispersed phase momentum equations but as a diffusion in the number density transport equation. Based on these considerations Eq. (2.16) is modified to

$$\frac{\partial N_g}{\partial t} + \nabla \cdot \left(\boldsymbol{u}_g N_g \right) + F_{g+1/2} - F_{g-1/2} = \nabla \cdot \left(\frac{\nu_t}{Sc_b} \nabla N_g \right) + \beta_g + \chi_g + S_g \tag{3.35}$$

where the Schmidt number is taken to be $Sc_b = 1$ and the interfacial force for turbulent dispersion is set to $\boldsymbol{M}_g^{TD} = 0$.

3.1.4.5 Packing

In the mathematical description of polydispersed bubbly flows presented so far there is nothing preventing the void fraction from becoming larger than 100%. This poses a serious problem in wall bounded flows where void fraction builds up due to the accumulation of bubbles rising up towards the walls. In the real world this situation is far more complex than just the accumulation problem itself. In a turbulent boundary layer for instance, when bubbles start accumulating near a wall, the collision rate increases since a larger fraction of the volume is occupied by bubbles, they may coalescence due to this increased collision rate, and given the large turbulent fluctuations in the boundary layer they may breakup as well. To complete the picture, the situation can become even more complex as bubbles may actually form sheets of air underneath this wall that unsteadily break up into bubbles and recombine again to form new sheets or pockets of air.

Probably the first action to solve this problem would be to limit the void fraction to a given maximum value. This approach should be avoided since mass is lost in

the process and once the maximum void fraction is reached the solution is *frozen* at this void fraction unless something sweeps bubbles away from their location. A better approach than a hard imposed limit is to modify the gas velocity such that bubbles are taken away from a region of large void fraction. In this way the transport equation for the number density is not modified and mass is naturally preserved.

In Lucas et al. (2007) an extra force term is added based on the idea that bubbles deform elastically when they approach a wall. This model attempts to resolve a single elastic collision event with a wall and results in a very localized force. In vertical pipe flows it is customary to add a *wall lubrication force* in order to explain the formation of a void fraction peak close to the wall of the pipe (Antal et al., 1991). However, these are examples of models aiming to account for the collision and sometimes bouncing off of bubbles on a rigid boundary while in this work the interest is on a model that accounts for interaction between bubbles themselves by collision. In this regard, in the work by Kunz et al. (2007) it is assumed that bubbles that do not coalesce rebound and thus contribute to forces by collision. In the works by Gidaspow (1994) and Apte et al. (2003b) for particle flows, the repulsive force due to collisions between particles results from an effective collision pressure.

The models proposed by Kunz et al. (2007), Gidaspow (1994) and Apte et al. (2003b) all have in common that the repulsive force between bubbles is proportional to the gradient of the number density

$$\boldsymbol{M}_g \propto -\nabla N_g \tag{3.36}$$

where the minus sign indicates that bubbles move in the direction of lower number density since they are repelled by collisions with other bubbles. In this regard the collision model is similar to the turbulent dispersion force in Eq. (3.32) and therefore

is a dispersion type model. The functional dependence in Eq. (3.36) typically leads to numerical instabilities, given that any noise in the number density is amplified by the gradient operation and it feeds back with the resulting gas velocity in the number density transport equation.

The model by Kunz et al. (2007) is probably the first one addressing the dispersion of bubbles caused by collisions at high void fractions. However the model incorporates new adjustable constants that were found to be highly dependent on the particular problem. On the other hand, even when the models proposed for particle flows could be adapted to bubbly flows, these models cannot be applied directly as they are because the underlying physics are completely different.

Even after the aforementioned efforts, the accumulation of bubbles in a turbulent boundary layer is still an open problem to solve. To the knowledge of the author there is no experimental data on the subject nor any well accepted modeling strategy. Given this lack of experimental data, the objective in this work is simply to provide of a model based on physical grounds that would prevent an excessive accumulation of bubbles along wall boundaries but still at least conserve mass.

Following the developments made for particle flows, the packing force is modeled as (Gidaspow, 1994; Apte et al., 2003b)

$$\boldsymbol{M}_g^P = -\alpha_g \nabla \sigma_P(\alpha_d) \tag{3.37}$$

where σ_P models a *collision pressure* resulting from the collision between bubbles. A model of this nature, as in the work by Kunz et al. (2007), assumes that bubbles do not form sheets of air but remain as individual bubbles. For particle flows the collision pressure typically takes the form $\sigma_P(\alpha_d) \propto (\alpha_{\text{pkg}} - \alpha_d)^{-n}$, where α_{pkg} is a close packing void fraction and n is a positive exponent controlling the strength of the functional dependence of σ_P with void fraction. This functional form for σ_P

makes the packing force to increase as the void fraction approaches the packing void fraction α_{pkg}. With this model the maximum void fraction allowed is α_{pkg}. However, such a strong functional dependence together with a singular point at α_{pkg} leads to numerical instabilities that are typically solved by iterating on heavily relaxed equations, an intensive computational approach not applicable for the solution of large scale problems.

In order to avoid numerical instabilities the expression for $\sigma_P(\alpha_d)$ should be as smooth as possible, and without singular points. In this work an expression for the collision pressure is proposed based on the idea sketched in Fig. 3.1a.

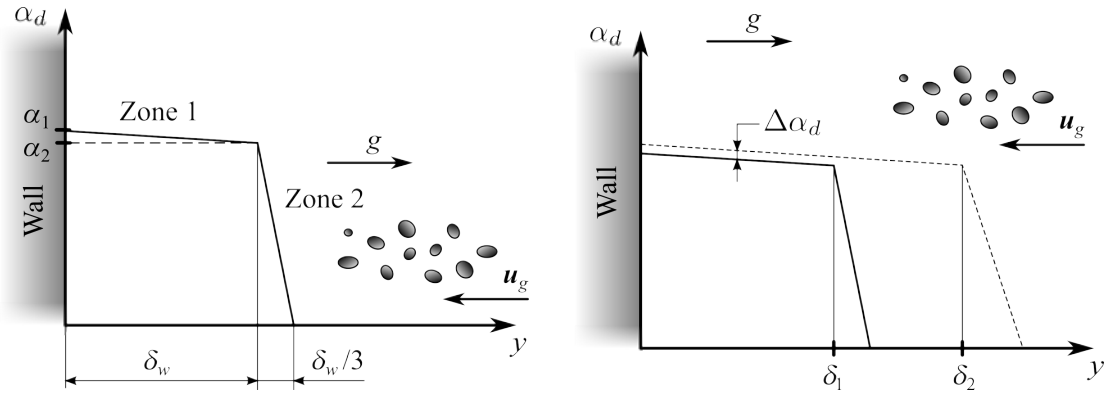

(a) Idealized void fraction profile when bubbles accumulate against a wall.

(b) Bubbly layer thickness increase as more bubbles arrive.

Figure 3.1: Accumulation of bubbles on a solid boundary and the bubble packing model.

In this figure the pull of gravity acts along the y axis. At $y = 0$ there is a wall and an initial mass of bubbles rises against it. After an initial transient bubbles accumulate at the wall with the assumed void fraction profile shown in Fig. 3.1a. Under this condition it is assumed that bubbles have zero velocity in the direction normal to the wall (and then a steady state can be reached in the normal direction

to the wall but still bubbles can be transported in the direction tangential to it). Therefore, the momentum balance in the y direction according to Eq. (3.10) reduces to

$$\rho_c g = \frac{\partial \sigma(\alpha_d)}{\partial y} = \beta(\alpha_d)\frac{\partial \alpha_d}{\partial y} \tag{3.38}$$

$$\beta(\alpha_d) = \frac{\mathrm{d}\sigma}{\mathrm{d}\alpha_d} \tag{3.39}$$

From this expression the gradient of the collision pressure can be obtained provided that the gradient of the void fraction profile is known (and vice versa)

$$\beta(\alpha_d) = \frac{\rho_c g}{\partial \alpha_d / \partial y} \tag{3.40}$$

The void fraction profile depicted in Fig. 3.1a exhibits two zones with different but constant void fraction gradients in each zone. In Zone 1 the profile is practically flat, corresponding to the layer where bubbles are closed packed. Zone 2 is a transition zone from the closed packing void fraction to zero void fraction. With this simplified profile Eq. (3.40) implies that function $\beta(\alpha_d)$ is constant in each zone with a large value in Zone 1 and a smaller value in Zone 2.

For a perfectly flat profile, *i.e.* one where $\partial\alpha/\partial y = 0$, the function $\beta(\alpha_d)$ must approach infinity according to Eq. (3.40). However, a finite (still large) gradient is required when solving the model numerically. In order to have a finite $\beta(\alpha_d)$ a non-zero but small gradient is allowed. Figure 3.1b sketches how the bubbly layer thickness would increase from thickness δ_1 to δ_2 as more bubbles reach the wall with the proposed model. Since the void fraction gradient in Zone 1 is close to zero, the bubbly layer thickness must increase in order to hold more bubbles as they approach the wall. In the model proposed in this section the function $\beta(\alpha_d)$ is set to be constant in each zone and thus, according to Eq. (3.38) the void fraction

gradient is fixed by the model inside each zone. Therefore, the bubbly layer grows with the same slope in both zones as depicted in Fig. 3.1b. Only the bubbly layer thickness changes. Given that the void fraction gradient in Zone 1 is not zero, but a small number, there is an increase of void fraction $\Delta\alpha_d$ in Zone 1. However, this increase in void fraction is negligible given the small void fraction gradient in Zone 1.

If α_1 is the maximum void fraction at the wall, the void fraction at the transition to Zone 2 is assumed to be $\alpha_2 = r\,\alpha_1 \approx \alpha_1$ with the ratio r a number close to one. If the transition from Zone 1 to 2 is assumed to be at $y = \delta_w$, the void fraction gradient inside Zone 1 is

$$\frac{\partial \alpha_d}{\partial y} = \frac{\alpha_1 - \alpha_2}{\delta_w} = \frac{\alpha_1(1-r)}{\delta_w} \tag{3.41}$$

In Zone 2 void fraction is assumed to go to zero in a thickness $\delta_w/3$. Then inside this zone the gradient is

$$\frac{\partial \alpha_d}{\partial y} = \frac{\alpha_2}{\delta_w/3} \approx \frac{\alpha_1}{\delta_w/3} \tag{3.42}$$

Therefore the collision pressure gradient is a step discontinuous function of the form

$$\beta(\alpha_d) = \begin{cases} \beta_1 = \dfrac{\rho_c\, g\, \delta_w}{\alpha_1(1-r)} & y < \delta_w \\ \beta_2 = \dfrac{\rho_c\, g\, \delta_w}{3\alpha_1} & y > \delta_w \end{cases} \tag{3.43}$$

For the simulations run in this thesis the coefficients of the model are set to $\delta_w = 1.0$ cm, $\alpha_1 = 0.3$ and $r = 0.99$. With this, the void fraction profile is practically flat if the void fraction is slightly larger than the assumed packing void fraction $\alpha_1 = 0.3$. Therefore r is not a physical parameter of the model but rather an artifact to have an almost zero gradient profile without incurring into numerical instabilities. In addition, parameters α_1 and δ_w are combined into one single parameter, the transition thickness gradient α_1/δ_w. This gradient could be determined from experiments.

As noted before, any discontinuities in the model for $\beta(\alpha_d)$, or equivalently $\sigma(\alpha_d)$, would result in numerical instabilities. To avoid this, the function $\beta(\alpha_d)$ is replaced by a smother version

$$\beta(\alpha_d) = \beta_1 + \frac{1}{2}\Big\{ \tanh\left[\gamma(\alpha_d - \alpha_1)\right] + 1\Big\}(\beta_1 - \beta_2) \tag{3.44}$$

where the new dimensionless parameter γ controlling the smoothness of the transition is set to $\gamma = 20.0$, the largest number with which the model is found to be stable. The numerical method used to integrate this model is key to avoid instabilities. The approach developed for this thesis is described in Section 4.8.

Assuming that the packing pressure model is a good representation of the underlying physics, still the proposed functional form in Eq. (3.44) is very simple depending only on the total void fraction. Moreover, the packing void fraction α_1 and the transition gradient α_1/δ_w are assumed to be constant for all flow conditions. In the context of turbulent boundary layers, it would be to expect that these two parameters depend on the local turbulent intensity or mixing. As the intensity of turbulent fluctuations increase bubbles cannot stay as closed packed as in a stationary flow. In addition, it would be to expect that the additional turbulent mixing would diffuse the transition zone (Zone 2 in Fig. 3.1a) and widen its thickness. Turbulent mixing is characterized by the turbulent viscosity ν_t (turbulence modeling is treated in Section 3.6) and thus a functional dependence of the packing void fraction and the transition gradient with it seems to be reasonable.

Another effect not considered in this very simplistic model, is that there is not a single packing void fraction in polydisperse flows. A closed packing void fraction can be obtained for different arrangements of hard spheres of the same size. However, in polydisperse bubbly flows, small bubbles can fill in the interstitial spaces left between larger bubbles. This situation is depicted in Fig. 3.2. Therefore,

a better model for the packing pressure might introduce a functional dependence with the size distribution $f(m)$ and, since void fraction can be obtained from $f(m)$, this model would replace the void fraction dependence with the number density $f(m)$. In other words, the simple dependence on an integral parameter (in this case the void fraction α_d) might need to be replaced by a more complex functional form on the full number density distribution.

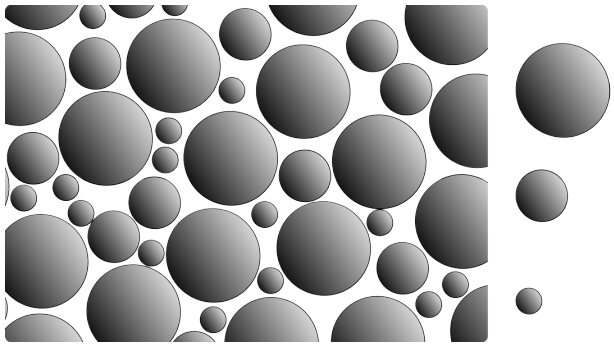

Figure 3.2: Packing of bubbles in a polydisperse bubbly flow. The example shows a polydisperse mixture with only three bubble sizes (shown on the right). Smaller bubbles take the interstitial spaces left by the larger ones.

The above discussion highlights weaknesses in the modeling of bubble packing and the possible functional dependences expected to be seen in a real flow situation. Clearly more research is needed in this matter, and experiments on bubbly turbulent layers are key for the better understanding of the problem and the development of more realistic models.

3.1.5 Bubble Radius

As explained before when introducing the drag force, the radius of a bubble with a mass m depends on the local pressure and also on the pressure induced by surface tension inside the bubble. This led to the system of Eqs. (3.24) to (3.26) here

summarized again for completeness

$$R_g = \left(\frac{3}{4\pi}\frac{m_g}{\rho_g}\right)^{1/3} \tag{3.24}$$

$$\rho_g = \rho_{d,0}\frac{p_g}{p_0} \tag{3.25}$$

$$p_g = p_0 + \widehat{p} - \rho_c\, g\, z + \frac{2\sigma}{R_g} \tag{3.26}$$

Notice then that according to Eq. (3.26) the pressure p_g is a function of the bubble radius R_g computed according to Eq. (3.24) which in turn depends on the pressure through the gas density computed according to Eq. (3.25). Therefore, to compute the bubble radius, this system of equations must be solved simultaneously for the variables R_g, ρ_g and p_g.

The density ρ_g in Eq. (3.24) can be put in terms of the bubble radius using Eqs. (3.25) and (3.26). This results in one single equation for R_g, and further algebraic manipulation leads to a third order degree polynomial on R_g

$$R_g^3\, p_0 + 2\,\sigma\, R_g^2 - \frac{3}{4\pi} m_g = 0 \tag{3.45}$$

with solution

$$\frac{R_g}{R_{0g}} = \Delta - \tilde{S}_p + \frac{\tilde{S}_p^2}{\Delta} \tag{3.46}$$

$$\Delta = \frac{1}{2^{1/3}}\left[1 - 2\tilde{S}_p^3 + \sqrt{1 - 4\tilde{S}_p^3}\right]^{1/3} \tag{3.47}$$

$$\tilde{S}_p = \frac{2}{3}\frac{\sigma/R_{0g}}{p_0} \tag{3.48}$$

where R_{0g} is the solution to this equation when $\sigma = 0$. The root of the polynomial in Eq. (3.45) is always real even when the squared root in Eq. (3.47) may become imaginary, as is the case for very small bubbles. The dimensionless parameter $\tilde{S}_p$ is a measure of the importance of surface tension in computing the bubble radius.

For $\tilde{S}_p \ll 1$, as it would happen for large bubbles, the effect of surface tension can be neglected. The squared root in Eq. (3.47) becomes imaginary at $\tilde{S}_p > \tilde{S}_{p\,\text{crit}} = (1/4)^{1/3} = 0.62996$ and thus Eqs. (3.46)-(3.48) have to be implemented with complex arithmetic. This may result in an expensive implementation considering that this operation is performed over every spatial grid point in the domain. To save computational work, three cases are considered. If $\tilde{S}_p < \tilde{S}_{p\,\text{crit}}$ then real arithmetic may be used. And if additionally $\tilde{S}_p < 0.5$ the computation of R_g can be simplified by expanding it on $\tilde{S}_p$ as

$$\frac{R_g}{R_{0g}} = 1 - \tilde{S}_p + \tilde{S}_p^2 - \frac{2}{3}\tilde{S}_p^3 \tag{3.49}$$

which is within 1.6% of the exact expression. Finally, the full expression for R_g in complex arithmetic is used for $\tilde{S}_p > \tilde{S}_{p\,\text{crit}}$.

The effect of this computation on the overall model comes into play when computing the bubble Reynolds number in Eq. (3.22), when computing intergroup transfer rates in Sections 3.2 through 3.4, and when computing the group-g or total void fraction in Eq. (2.27).

3.2 Coalescence Modeling

Bubble coalescence is a complex phenomenon where two or more bubbles merge to form a larger one. This process depends on the velocity field of the continuous phase, whether this is turbulent or not, and on the presence of impurities in the water and its chemical composition. A usual simplification is to consider only binary interactions, *i.e.* the coalescence between two bubbles. Coalescence can be described as a three steps process. First a collision between two bubbles must take place. This collision brings the two bubbles close to each other trapping a thin film of liquid between them. The second step is the thinning of this liquid film during which the bubbles must be in contact long enough to allow the liquid film between them to drain (Marrucci, 1969). Finally, film rupture occurs resulting in coalescence.

The above description suggests that the rate of coalescence is intimately related to the *collision rate*, the number of bubble collisions per unit of time (and volume). Whether a collision results in coalescence or not is given by the *coalescence efficiency*, the probability of coalescence once collision has occurred.

In analogy with particle collisions in a gas, the collision rate is estimated as

$$\mathcal{R}_{\text{coll}}(m, m') = T(m, m') f(m) f(m')\, dm\, dm' \tag{3.50}$$

where $T(m, m')$ is a kernel that allows to compute the collision rate per unit volume $\mathcal{R}_{\text{coll}}(m, m')$ between bubbles within dm of size m with bubbles within dm' of size m'. Not all collisions result in bubble coalescence. The fraction of collisions that result in an actual coalescence is given by the *coalescence efficiency* and therefore the coalescence rate is computed as the product of the collision rate with the coalescence efficiency $C(m, m')$

$$\mathcal{R}_{\text{coal}}(m, m') = \mathcal{R}_{\text{coll}}(m, m')\, C(m, m') \tag{3.51}$$

As suggested by its two arguments, the coalescence efficiency $C(m, m')$ is a function of the two participating bubble sizes. Alternatively, the rate of coalescence in Eq. (3.51) can be written as

$$\mathcal{R}_{\text{coal}}(m, m') = Q(m, m') f(m) f(m')\, dm\, dm' \tag{3.52}$$

where the coalescence kernel already introduced in Eqs. (2.14) and (2.15) is defined as the product of the collision kernel with the coalescence efficiency

$$Q(m, m') = T(m, m')\, C(m, m') \tag{3.53}$$

and allows to compute the rate of coalescence per unit volume between bubbles within dm of size m with bubbles within dm' of size m'.

The collision between two bubbles is caused by a non-zero relative velocity between them. In analogy with the RANS models for turbulence, the velocity of the bubbles, as well as the relative velocity between them, can be split into a mean velocity contribution, which is resolved by the computational grid, and into a turbulent fluctuation contribution, which is estimated from a suitable turbulence model. In addition, gradients in the velocity field may cause bubbles in a high velocity region to overtake bubbles in a slower velocity region (see Prince and Blanch, 1990a; Williams and Loyalka, 1991). This last mechanism was not implemented at the time this thesis was written but should be considered as a future improvement to the model since high velocity gradients may be encountered in some regions of the flow as it occurs along boundary layers.

Two coalescence models are implemented in this work: the model of Prince and Blanch (1990a) and the model of Lehr et al. (2002). The model of Prince and Blanch (1990a) has been used extensively in the past in a multitude of applications due to its general formulation and is widely accepted in the two-phase community. Similar models can be found in the works by Luo and Svendsen (1996b) and Wang et al. (2005a). Some of these models would include additional effects particular to specific applications. As an example, in Fu and Ishii (2003), a *wake entrainment* model is formulated for slug flows where bubbles can be accelerated into the strong wake behind a sphere cap shape bubble. Even though the model of Prince and Blanch (1990a) is preferred in this work due to its generality, the model by Lehr et al. (2002) is implemented as well to perform a validation of the multigroup transfer solver in Chapter 5 against computations originally performed by the authors of the model in their work.

3.2.1 Model of Prince and Blanch

This model was originally proposed in Prince and Blanch (1990a). The model considers that collisions may occur due to turbulent fluctuations, different bubble

velocities, and laminar shear. In this work only the contributions to the collision rate by turbulent fluctuations and different bubble velocities are considered. Collisions caused by velocity gradients should be taken into account in future improvements to the model. The model used in this work slightly differs from the one originally proposed in Prince and Blanch (1990a). Differences are highlighted accordingly throughout the presentation of the model.

The contribution to the collision rate caused by a difference in bubble velocities is estimated with the kernel proposed by Friedlander (1977)

$$T_u(m, m') = \pi\, u_r(m, m')\, (R_m + R_{m'})^2 \tag{3.54}$$

where R_m is the bubble radius for a bubble of mass m, $u_r(m, m')$ is the relative velocity between bubbles of sizes m and m' and $\pi\,(R_m + R_{m'})^2$ is the geometrical *cross section* of the collision. This model has extensively been used in the past by other authors (see Carrica et al., 1999; Wang et al., 2006; Frank et al., 2008). In Carrica et al. (1999) the additional contribution to relative velocities caused by velocity gradients in the dispersed phase is considered using the model by Williams and Loyalka (1991). If these velocity gradients are neglected a first order approximation for the relative velocity can be used, *i.e.* $u_r(m, m') = \|\boldsymbol{u}_d(m) - \boldsymbol{u}_d(m')\|$.

Collision due to the relative random motion induced by turbulent fluctuations is modeled as

$$T_t(m, m') = 1.41\, (R_m + R_{m'})^2\, \varepsilon^{1/3} \left(R_m^{2/3} + R_{m'}^{2/3}\right)^{1/2} \tag{3.55}$$

where ε is the local turbulent dissipation rate. In Prince and Blanch (1990a) the total collision rate is assumed to be the algebraic addition of the individual contributions in Eqs. (3.54) and (3.55). In addition, when the void fraction approaches a maximum compactness α_{cr}, the collision rate should become infinity since bubbles are more closely packed as void fraction increases. A correction for high void fractions of

the form $Y(\alpha) = \alpha_{\text{cr}}/(\alpha_{\text{cr}} - \alpha_d)$ is suggested by Ferziger and Kaper (1972) for dense gases and is used by Carrica et al. (1999) for bubbly flows[1].

Then the total collision kernel is computed as

$$T(m, m') = \frac{\alpha_{\text{cr}}}{\alpha_{\text{cr}} - \alpha_d} (T_u + T_t) \tag{3.56}$$

where $\alpha_{\text{cr}} = 1$ is used in this work since even when a close packing void fraction can be used for spherical bubbles, in a polydispersed flow smaller bubbles can occupy the interstitial spaces left between larger bubbles (see discussion on Section 3.1.4 about bubble packing).

In the model proposed by Prince and Blanch (1990a) the coalescence efficiency is estimated as

$$C(m, m') = e^{-t_{m,m'}/\tau_{m,m'}} \tag{3.57}$$

where $t_{m,m'}$ is the *coalescence time*, the time required to drain out the liquid film separating two bubbles. $\tau_{m,m'}$ is the *contact time*, which estimates for how long bubbles will be in the proximity of each other and depends on the bubble sizes and on the local hydrodynamic conditions. This is estimated as in Carrica et al. (1999) where in addition to a turbulent characteristic time as in the original work by Prince and Blanch (1990a) a characteristic time based on the relative velocity between bubbles and their sizes is considered. In Carrica et al. (1999) the turbulent characteristic time is estimated as[2]

$$\tau^t_{m,m'} = \frac{(R_{m'} + R_{m'})^{2/3}}{\varepsilon^{1/3}} \tag{3.58}$$

and defining a characteristic time computed with the relative velocity between

[1]The correction for compactness is not used in the original Prince and Blanch (1990a) model

[2]In Prince and Blanch (1990a) the equivalent radius from Chesters and Hofman (1982) is used as the characteristic length instead

bubbles as

$$\tau^{u}_{m,m'} = \frac{2(R_m + R_{m'})}{u_r(m,m')} \tag{3.59}$$

Carrica et al. (1999) estimate the contact time as

$$\tau_{m,m'} = \left(\frac{1}{\tau^{t}_{m,m'}} + \frac{1}{\tau^{u}_{m,m'}}\right)^{-1} = \frac{2(R_m + R_{m'})^{5/3}}{u_r(m,m')(R_m + R_{m'})^{2/3} + 2(R_m + R_{m'})\varepsilon^{1/3}} \tag{3.60}$$

Prince and Blanch (1990a) estimate the coalescence time as

$$t_{m,m'} = C_s \left(\frac{R^3_{m,m'}\rho_c}{16\sigma}\right)^{1/2} \ln\left(\frac{h_0}{h_f}\right) \tag{3.61}$$

This time is obtained from the solution of a simplified Navier-Stokes equation describing the thinning process of the liquid film between two bubbles (see Oolman and Blanch, 1986). This equation is then integrated between an initial thickness h_0 and a critical film thickness where rupture occurs h_f. These are estimated to be $h_0 = 10^{-4}$ m (Kirkpatrick and Lockett, 1974) and $h_f = 10^{-7}$ m (Thomas, 1981). For polydispersed bubbly flows, the equivalent radius $R_{m,m'}$ as introduced by Chesters and Hofman (1982) is used in Eq. (3.61). This is defined as

$$R_{m,m'} = 2\left(\frac{1}{R_m} + \frac{1}{R_{m'}}\right)^{-1} \tag{3.62}$$

If the two bubble radii are the same then the equivalent radius reduces to the radius of the bubbles *i.e.* $R_{m,m'} = R_m = R_{m'}$. Equation (3.61) can even be used to compute the burst time of a bubble hitting a free surface. For this case the equivalent radius is two times the bubble radius since the free surface is considered to have infinite radius.

The constant C_s in Eq. (3.61) was introduced by Carrica et al. (1999) to take into account the effect of dissolved salt in sea water which strongly inhibits coalescence by increasing the coalescence time. Differences between fresh and sea water are

discussed in Section 3.5 together with modeling strategies.

3.2.2 Model of Lehr et al.

In the work by Lehr et al. (2002) experiments are performed to determine under what conditions the collision between two bubbles results in coalescence or bouncing. Their experiments show that bubbles approaching with a relative velocity higher than a critical value bounce off while if their relative velocity is smaller than this critical value they coalesce. For distilled water and air they obtained for the critical relative velocity $u_{\text{crit}} = 0.08$ m/s.

Collisions are considered that arise either from turbulent fluctuations or from different bubble velocities. Both situations are considered in a characteristic velocity u' computed as

$$u'(m,m') = \max\left(1.782\ \varepsilon^{1/3}\sqrt{R_m^{2/3} + R_{m'}^{2/3}}, \|\boldsymbol{u}_m - \boldsymbol{u}_{m'}\|\right) \tag{3.63}$$

Considering a cross sectional area $\pi(R_m + R_{m'})^2$ for the collision frequency (as in Eq. (3.54)) and the characteristic velocity u' they propose

$$Q(m,m') = \pi(R_m + R_{m'})^2 \min(u', u_{\text{crit}}) \exp\left[-\left(\frac{\alpha_{\text{Max}}^{1/3}}{\alpha_d^{1/3}} - 1\right)^2\right] \tag{3.64}$$

where the last term was developed to reflect the limited range of the turbulent fluctuations and $\alpha_{\text{Max}} = 0.6$ is the maximum packing density of the bubbles.

3.3 Breakup Modeling

The breakup of fluid particles in turbulent dispersions, and in particular air bubbles in water, is influenced by the continuous phase hydrodynamics and interfacial interactions. Typically, breakup is described as the competition between external stresses or forces from the continuous phase attempting to destroy the fluid particle and the stabilizing surface tension and viscous stresses inside the

fluid particle stabilizing its shape. Therefore breakup is modeled to be a function of the continuous phase hydrodynamic conditions and of the fluid particle characteristics such as size, surface tension, etc. Several breakup mechanisms are reported in the literature: Turbulence induced breakup, shear induced breakup, and tip-streaming to mention the most popular. A good review on this subject is given by Liao and Lucas (2009).

Tip-streaming of bubbles considers the separation of very small bubbles from the tips of a parent bubble that is immersed in a shear flow. Tip-streaming is observed in the experiments separately performed by Grace (1982), De Bruijn (1991, 1993),Elemans et al. (1993) and Janssen et al. (1994) but it is described only qualitatively and not enough information is provided to construct a model based on their results. In Fu and Ishii (2003) a model for tip-streaming is provided for slug bubbles in pipes. The breakup regime described in Fu and Ishii (2003) is very particular to slug flows in pipes and their model is not directly applicable to ship flows.

Since not enough information for the development of a breakup model by tip-streaming is available, in this work only two breakup mechanisms are considered: turbulence induced breakup and shear induced breakup.

3.3.1 Turbulence Induced Breakup

Turbulence induced breakup is probably the most studied of the aforementioned mechanisms and several works on the subject are found in the literature (see for instance Prince and Blanch, 1990a; Luo and Svendsen, 1996a; Martínez-Bazán et al., 1999a,b; Lehr et al., 2002).

Being two of the latest models found in the literature, this work implements the models of Luo and Svendsen (1996a) and Lehr et al. (2002). The model of Luo and Svendsen (1996a) is probably the first model with no adjustable parameters and set the theoretical foundations still used today on the formulation of newer models.

Their model not only provides the breakup rate kernel but also the daughter bubble size distribution. However, besides its theoretical importance, recent studies reveal that the Luo and Svendsen (1996a) model significantly under predicts the rate of breakup. In the work by Wang et al. (2005a) the Luo and Svendsen (1996a) model is compared against other popular models available in the literature showing that the predicted breakup rate is always below estimations made with other models. In Chen et al. (2004, 2005b) this model is used for the simulation of bubble columns but the breakup rate is multiplied by a factor of ten in order to match their experimental results.

The more recent model proposed by Lehr et al. (2002) seems to correct for this under prediction and comparisons against experiments performed by the same authors of the model (reported in Lehr et al., 2002) and separately by Wang et al. (2005a) show favorable results at least for bubble columns. Figure 3.3 compares breakup rates predicted with the models of Luo and Svendsen (1996a) and Lehr et al. (2002) for a turbulence dissipation of $\varepsilon = 1\ \mathrm{m}^2/\mathrm{s}^3$. As shown in this figure, the Luo and Svendsen (1996a) breakup rate is always well bellow the Lehr et al. (2002) breakup rate. The same trend is observed at different turbulent dissipation rates.

In addition, Fig. 3.3 shows that no breakup occurs below certain bubble size (which is different for each model). This bubble size is the *maximum stable diameter* D_{Max} and for bubbles smaller than this size the stabilizing effect of surface tension is stronger than the turbulent fluctuations trying to break them and breakup does not occur. The maximum stable bubble diameter can be estimated from the relation given by Hinze (1955)

$$D_{Max} = C\frac{\sigma^{3/5}}{\varepsilon^{2/5}\rho_c^{3/5}} \tag{3.65}$$

In his experimental work with drops Hinze finds $C = 0.725$.

The maximum stable bubble diameter for the models of Luo and Svendsen (1996a) and Lehr et al. (2002) can be estimated by solving for the bubble diameter

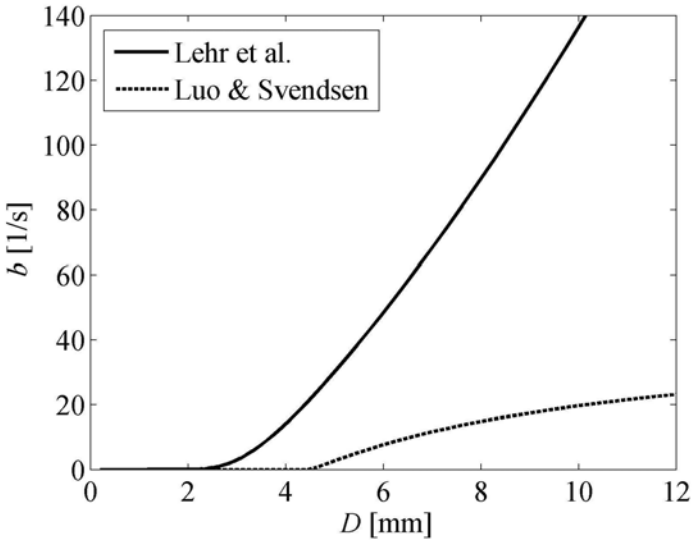

Figure 3.3: Breakup rates predicted by Luo and Svendsen (1996a) and Lehr et al. (2002) models. $\varepsilon = 1\ m^2/s^3$.

D_{Max} at which the breakup rate attains a small rate b_1. Therefore, the maximum stable bubble diameter is obtained from solving $b(D_{Max}, \varepsilon) = b_1$, which implicitly defines D_{Max} as a function of the turbulent dissipation ε. Figure 3.4 shows D_{Max} as a function of ε for the air-water system for the breakup models of Luo and Svendsen (1996a) and Lehr et al. (2002) together with Hinze's estimation. D_{Max} in this figure is solved for a breakup rate $b_1 = 0.1\ s^{-1}$. Figure 3.4 shows that the maximum stable bubble diameter predicted with Lehr et al. (2002) model closely follows the power law in Hinze's equation while the estimation made with Luo and Svendsen (1996a) model shows a power law behavior but with a significantly different exponent. Not only the power law trend predicted by Lehr et al. (2002) model is similar to that in Hinze's equation but also the order of magnitude of the predicted diameter is surprisingly close. The agreement of the Lehr et al. (2002) model with Hinze's correlation serves as indirect validation to the model and gives a stronger reliability to its predictions. The model of Luo and Svendsen (1996a), however, not only predicts a lower breakup rate, but Fig. 3.4 reveals that the

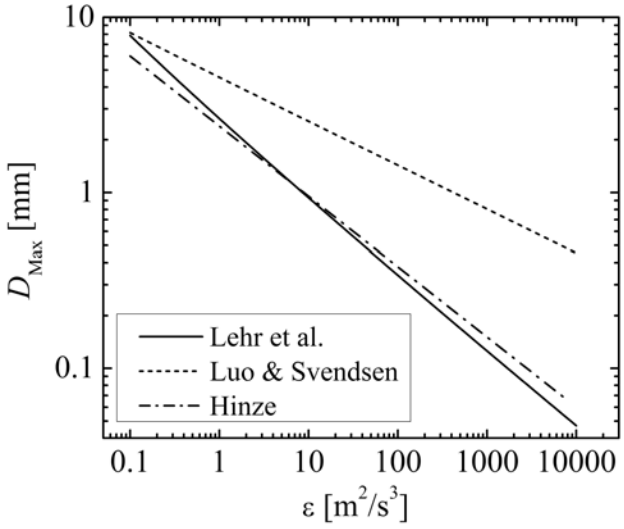

Figure 3.4: Maximum stable bubble diameter estimated from the models of Luo and Svendsen (1996a) and Lehr et al. (2002). Hinze's correlation is shown as well.

model predicts a larger D_{Max} as well. Some particular points may highlight the differences better: at a turbulent dissipation of $\varepsilon = 10000$ m^2/s^3 the model of Lehr et al. (2002) yields a maximum stable diameter $D_{Max} = 47\ \mu$m while the model of Luo and Svendsen (1996a) yields $D_{Max} = 453\ \mu$m and at $\varepsilon = 1$ m^2/s^3 Lehr et al. (2002) model gives $D_{Max} = 2.6$ mm while for the model of Luo and Svendsen (1996a) $D_{Max} = 4.5$ mm.

The models of Luo and Svendsen (1996a) and Lehr et al. (2002) exhibit differences on the predicted daughter bubble size distributions as well. These are shown in Fig. 3.5 as a function of the volumetric fraction f_v for several parent bubble sizes. The volumetric fraction f_v is defined as the ratio of the daughter bubble volume to the parent bubble volume and given that breakup preserves the total mass, daughter bubble size distributions are symmetric around $f_v = 0.5$.

The first observation to make is that while the Luo and Svendsen (1996a) model predicts a *U* shaped size distribution, the model by Lehr et al. (2002) predicts an *M*

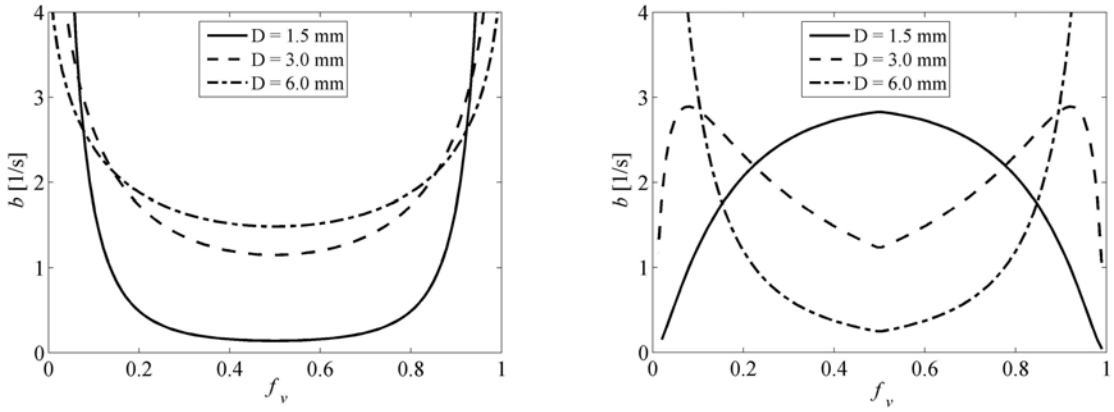

(a) Model of Luo and Svendsen

(b) Model of Lehr et al.

Figure 3.5: Predicted daughter bubble size distributions for $\varepsilon = 1$ m^2/s^3.

shaped size distribution. Two more main differences are observed. For the Luo and Svendsen (1996a) model the daughter bubble size distribution peaks at $f_v = 0$ (not shown with the scaling in Fig. 3.5 but the distribution reaches a finite value at $f_v = 0$ and $f_v = 1$) while the Lehr et al. (2002) distribution goes to zero for $f_v = 0$ (or $f_v = 1$). Physically, the energy required to tear a bubble from a given parent size increases as the daughter bubble becomes smaller due to fact that surface tension energy increases with larger curvatures. Therefore the trend should be a size distribution that goes to zero at $f_v = 0$ (or $f_v = 1$) as predicted by Lehr et al. (2002) model.

The second difference is that the peak at small sizes exhibited by the Luo and Svendsen (1996a) daughter bubble size distribution, becomes even higher for smaller parent bubbles. In other words, the U shaped size distribution becomes taller at $f_v = 0$ (or $f_v = 1$) and the bottom of this U goes lower. Therefore, the model of Luo and Svendsen (1996a) predicts that for smaller parent bubbles tearing off even smaller bubbles results to be an easier task. This trend is unphysical since tearing off smaller bubbles would require a larger amount of energy due to the increase in the surface tension energy. On the other hand, the model by Lehr et al.

(2002) transitions from an *M* shaped size distribution for large parent bubbles to a ∩ (*cap*) shaped size distribution for small parent bubbles. Therefore, for the Lehr et al. (2002) model, an equal-sized fracture is more energetically favorable than an uneven breakup when the parent bubble is small. This seems to be the right physical trend since tearing off a small bubble from an already small bubble would require a large amount of energy.

In Wang et al. (2003) a similar model to those proposed by Luo and Svendsen (1996a) and Lehr et al. (2002) is formulated. This model predicts breakup rates that are in close agreement with the predicted rates by Lehr et al. (2002) model. In addition, similar trends are predicted by both Lehr et al. (2002) and Wang et al. (2003) models for the daughter bubble size distribution. However, the Lehr et al. (2002) model offers of a closed mathematical expression for both breakup rate and daughter bubble size distribution facilitating its implementation in a computer code. Being that Lehr et al. (2002) model offers similar prediction capabilities than Wang et al. (2003) model and is of easier implementation, the model by Wang et al. (2003) was not implemented in this work. However, future research on breakup kernels may require the implementation of this and other models as well.

3.3.1.1 Model of Luo and Svendsen

In this model bubbles can breakup if the turbulent eddies from the continuous phase are energetic enough to counteract the stabilizing surface tension forces. This model provides not only the breakup frequency but also the daughter bubble size distribution.

In this model the breakup frequency is computed as

$$b(m) = 0.29\left(\frac{\varepsilon}{R_m^2}\right)^{1/3} \alpha_c \int_0^1 \mathrm{d}\chi \int_{\xi_{min}}^1 \mathrm{d}\xi \, \frac{(1+\xi)^2}{\xi^{11/3}} \, e^{-\chi_c(\chi,\xi)} \tag{3.66}$$

where $\chi_c(\chi, \xi)$ is the critical dimensionless energy for breakup, computed as

$$\chi_c(\chi, \xi) = \frac{1.89\, Z(\chi)\, \sigma}{\rho_c\, \varepsilon^{2/3}\, R_m^{5/3}\, \xi^{11/3}}$$
$$Z(\chi) = \chi^{2/3} + (1-\chi)^{2/3} - 1 \tag{3.67}$$

The lower limit in Eq. (3.66) is $\xi_{min} = \lambda_{min}/D_m$ and λ_{min} is taken to be the minimum size of the eddies in the inertial subrange of isotropic turbulence, λ_{is}. This is related to the microscale by $\lambda_{is}/\lambda_d \approx 11.4 - 31.4$. The value 11.4 is adopted in this work. The microscale is estimated as

$$\lambda_d = 12.56\, \frac{\nu^{3/4}}{\varepsilon^{1/4}} \tag{3.68}$$

The daughter bubble size distribution is also provided by Luo and Svendsen (1996a)

$$h(m, m') = \frac{2 \int_{\xi_{min}}^{1} \mathrm{d}\xi\, (1+\xi)^2\, \xi^{-11/3}\, e^{-\chi_c(\chi,\xi)}}{m' \int_0^1 \mathrm{d}\chi \int_{\xi_{min}}^{1} \mathrm{d}\xi\, (1+\xi)^2\, \xi^{-11/3}\, e^{-\chi_c(\chi,\xi)}} \tag{3.69}$$

3.3.1.2 Model of Lehr et al.

The model by Lehr et al. (2002) follows a similar derivation to that proposed by Luo and Svendsen (1996a). It adds a capillary constraint to avoid the unphysical breakup of very small bubbles and assumes that interfacial and inertial forces balance each other. Their model can be written in terms of a dimensionless bubble diameter defined as

$$D^* = D\, \varepsilon^{2/5} \left(\frac{\rho_c}{\sigma}\right)^{3/5} \tag{3.70}$$

and a time scale

$$T = \left(\frac{\sigma}{\rho_c}\right)^{2/5} \frac{1}{\varepsilon^{3/5}} \tag{3.71}$$

With these definitions, the breakup frequency is

$$b(m) = \frac{0.5\, {D_m^*}^{5/3}}{T} \exp\left(-\frac{\sqrt{2}}{{D_m^*}^3}\right) \tag{3.72}$$

and the daughter bubble size distribution

$$h(m,m') = \frac{1}{m'\sqrt{\pi}} \frac{\exp\left(-\frac{9}{4}\left[\ln(2^{2/5}D_m^*)\right]\right)}{\left\{1+\mathrm{erf}\left[\frac{3}{2}\ln(2^{1/15}D_{m'}^*)\right]\right\}} \tag{3.73}$$

3.3.2 Viscous Shear Breakup

Compared to the turbulent fluctuation breakup, the influence of viscous shear, shearing-off and surface instability in a turbulent flow are usually neglected and the corresponding theory and modeling are rare in literature.

Experimental studies include those by Grace (1982), De Bruijn (1991, 1993),Elemans et al. (1993), Janssen et al. (1994) and Müller-Fischer et al. (2008). In all of these studies two dimensionless parameters are defined: the viscosity ratio $\lambda = \mu_d/\mu_c$ and the dimensionless shear stress or capillary number $Ca = \mu_c \dot{\gamma} R/\sigma$, where $\dot{\gamma}$ is the shear rate. It is found that if the critical capillary number exceeds a critical value Ca_{crit}, breakup occurs. This critical capillary number is a function of the viscosity ratio only. For the air water system at 20 °C the viscosity ratio is $\lambda = 0.0183$ and the critical capillary number is found to be $Ca_{crit} \approx 1.3$ (Grace, 1982).

Several modes of breakup are found in the presence of shear. In Janssen et al. (1994), it is reported that for shear rates that are near critical, breakup occurs in two equisized fragments and a few much smaller satellite droplets. This is consistent with the observations in the studies made by Grace (1982) and by Elemans et al. (1993). Well above the critical shear stress droplets are elongated into a long cylindrical fluid thread which subsequently breaks into a series of fragments. The work by Grace (1982) is probably the most complete, providing the bubble burst

time, number of fragments and some daughter bubble size distributions.

Near the critical shear stress, when the bubble breaks in two equisized fragments and a few satellite bubbles, there is not enough experimental data reporting the size of these satellite bubbles. Besides, right after the critical capillary number is exceeded, bubbles elongate and break into bubbles of nearly equal sizes. Therefore, in this work the modeling will be simplified by assuming that breakup occurs into n equal sized bubbles. The number n of bubbles per breakup is obtained from the data reported by Grace (1982). The experimental data by Grace (1982) is fit for the viscosity ratio in the air water system

$$\begin{aligned} n &= 10^{-1.39x^2+3.88x+1.14} \\ x &= \log_{10}\left(\frac{Ca}{Ca_{crit}}\right) \end{aligned} \tag{3.74}$$

This fit is valid in the range $Ca/Ca_{crit} \in (1, 30)$.

With this model the bubble size distribution for shear breakup is written as

$$h(m, m') = n\delta\left(m - \frac{m'}{n}\right) \tag{3.75}$$

As proposed in Lo and Zhang (2009), the breakup frequency can be thought as inversely proportional to the burst time

$$b(m) = \frac{c_{vs}}{t_b} \tag{3.76}$$

where the viscous shear constant is taken to be $c_{vs} = 1.0$ in this work due to the lack of information to estimate its value. The burst time t_b can be obtained from the work by Grace (1982). Here the burst time is reported as the *reduced burst time*

$t^* = t_b\,\sigma/(D\mu_c)$. The fit to these data for the air water system viscosity ratio is

$$\begin{aligned} t^* &= \frac{t_b\sigma}{D\mu_c} = 10^{-0.61x+1.12} \\ x &= \log_{10}\left(\frac{Ca}{Ca_{crit}}\right) \end{aligned} \tag{3.77}$$

this fit being also only valid in the range $Ca/Ca_{crit} \in (1,\, 30)$.

All that remains in order to have a complete model is to specify how to compute the shear rate $\dot{\gamma}$ necessary to compute the capillary number Ca. In Carrica et al. (1999) this is directly computed by taking the norm of the velocity gradient. In Lo and Zhang (2009) it is pointed out that a different approach must be taken for turbulent flows and they propose to use the Kolmogorov shear rate

$$\dot{\gamma} = \sqrt{\frac{\varepsilon}{\nu_c}} \tag{3.78}$$

This shear rate is related to the velocity gradients at the Kolmogorov scale. However, the Kolmogorov scale may be smaller than the bubble size and the velocity gradients that should be considered are those in the scale range of the bubble size. The proposal in this work is to estimate a velocity gradient relevant to the bubble size scale.

From the turbulence model used in a RANS, code the turbulent kinetic energy k and the rate of dissipation ε or the rate of dissipation per unit turbulent kinetic energy ω are available. From these the following scales can be derived

$$u_0 = \sqrt{\frac{2}{3}k} \tag{3.79}$$

$$\ell_0 = C_\mu \frac{k^{3/2}}{\varepsilon} = \frac{k^{1/2}}{\omega} \tag{3.80}$$

$$\tau_0 = \frac{\ell_0}{u_0} \tag{3.81}$$

According to Pope (2000, §6.1.2) given an eddy size ℓ in the inertial subrange the characteristic velocity and time scales of that eddy can be formed by ε and ℓ

$$u(\ell) = u_0 \left(\frac{\ell}{\ell_0}\right)^{1/3} \tag{3.82}$$

$$\tau(\ell) = \tau_0 \left(\frac{\ell}{\ell_0}\right)^{2/3} \tag{3.83}$$

Then the characteristic turbulent shear rate corresponding to the bubble length scale $\ell = D$ is estimated as

$$\dot{\gamma}_t(D) = \frac{u(D)}{D} = \frac{u_0}{\ell_0}\left(\frac{\ell_0}{D}\right)^{2/3} \tag{3.84}$$

In regions of resolved velocity gradients it could happen that the explicitly computed velocity gradient $\dot{\gamma}_u = \|\nabla \boldsymbol{u}\|$ is larger than the modeled turbulent shear $\dot{\gamma}_t(D)$. To accommodate both of these situations the maximum of the two shears is taken

$$\dot{\gamma} = \max(\dot{\gamma}_t(D);\ \dot{\gamma}_u) \tag{3.85}$$

Finally, it must be observed that a bubble will breakup only if it resides long enough in the considered vortex of length scale D. Hence bubbles will be allowed to breakup only if $t_b < \tau(D)$.

3.4 Dissolution

The gas inside a bubble can diffuse and dissolve into the surrounding liquid. The mass transfer between the gas in the bubble and the surrounding liquid can be treated as a problem of forced convection around a sphere. The rate of mass transfer can then be written as

$$\dot{m} = 2\pi\, Sh\, \kappa\, R_m\, (C_\infty - C_0) \tag{3.86}$$

where κ is the diffusivity of air in water and Sh is the Sherwood number[3] which is the ratio of the mass transfer coefficient to the diffusive mass transfer coefficient. C_∞ and C_0 are the air concentrations far from and at the bubble's surface respectively. The Sherwood number is typically computed with correlations depending on the Reynolds number Re and the Schmidt number Sc. The correlation given by Whitaker (1972) has been verified over a wide range of Reynolds ($3.5 < Re < 7.6 \times 10^4$) and Schmidt numbers ($0.71 < Sc < 380$)

$$Sh = 2 + \left(0.4\, Re^{1/2} + 0.06\, Re^{2/3}\right) Sc^{0.4} \tag{3.87}$$

For Reynolds numbers $Re < 3.5$ the correlation given by Levich (1962) for high Schmidt numbers can be used

$$Sh = 2 + 0.997\, Pe_M^{1/3} \tag{3.88}$$

Where $Pe_M = Re\, Sc$ is the mass Peclet number and the limiting value of $Sh = 2$ corresponding to pure diffusion was added to the original expression given by Levich (1962) in order to include the case of very small Peclet numbers as it happens for small bubbles with almost zero terminal velocity. Concentrations are estimated using Henry's law. At the bubble surface, the total pressure inside the bubble is used

$$C_0 = H\left(\hat{p}_c - \rho_c\, g\, z + p_{\text{atm}} + \frac{2\sigma}{R_m}\right) \tag{3.89}$$

where H is the Henry constant. Far from the bubble's surface it is assumed that the concentration is that of equilibrium at the atmospheric pressure *i.e.*

$$C_\infty = H\, p_{\text{atm}} \tag{3.90}$$

[3] also called the mass transfer Nusselt number

3.5 Modeling Considerations for Sea Water

In the present study it is of interest to understand and quantify how the different thermophysical properties of sea water affect the mechanisms of breakup and coalescence, in order to apply the necessary corrections.

Sea water composition is reported in Dickson and Goyet (1992, §5). On average, sea water in the world's oceans has a salinity of about $S = 35$ (35 g/L or 580 mM[4]). This is about 35 grams per liter of dissolved salts, predominantly sodium chloride.

Sodium chloride in water forms an electrolyte solution *i.e.* it dissolves into its component ions Na^+ and Cl^-. It has been found that inorganic electrolytes have no significant effect on bubble breakup (see Walter and Blanch, 1986). The negligible effect of electrolytes on bubble breakup is attributed to the small effect they have on surface tension. At 20 °C surface tension increases only by less than 1% when changing salinity from $S = 0$ to $S = 30$ (Sharqawy et al., 2010). Therefore it can be assumed that breakup in sea water can be approximated with the models for distilled water. However, a shift toward smaller bubble sizes has been observed in experimental facilities when switching from fresh to salt water. Given the negligible effect inorganic salts have on surface tension this shift to smaller sizes is attributed to a lower coalescence rate. In support of this experiments show a sharp transition in the coalescence efficiency when a critical salt concentration c_t is reached for a broad variety of electrolyte solutions (see Craig et al., 1993; Tsang et al., 2004; Christenson et al., 2008). This decrease in efficiency is explained by an abrupt increase in the coalescence time once the critical concentration is reached (see Marrucci, 1969; Prince and Blanch, 1990b). Based on these observations Carrica et al. (1999) introduced the constant $C_s = 10^3$ in Eq. (3.61) to account for the increase in the coalescence time. Given the lack of experimental evidence, Carrica et al. (1999) fix the value of the constant C_s to an arbitrarily large number just to account

[4]mM stands for millimolar, a unit of concentration. For table salt 100 mM ≈ 6.04 g/L

for the almost complete inhibition of coalescence observed in sea water. In addition, this assumes that the coalescence time increases by the same factor for all bubble sizes and it shows no dependence on salt concentration.

Prince and Blanch (1990b) propose a model for the transition concentration c_t. In their model, the inhibition of coalescence is attributed to Marangoni stresses and hence the parameter $\partial\sigma/\partial c$, the surface tension gradient with salt concentration, comes into play. They derive the following expression for the transition concentration

$$c_t = 1.18\nu\left(\frac{B\sigma}{R}\right)^{1/2}\tilde{R}_g T\left(\frac{\partial\sigma}{\partial c}\right)^{-2} \tag{3.91}$$

where B is the retarded van der Waals coefficient, σ the surface tension, R the bubble radius, $\tilde{R}_g$ the universal constant of gases and T is the fluid temperature. Their result compares favorably well with experimental data.

According to Eq. (3.91), the model by Prince and Blanch (1990a) predicts a dependence of the critical concentration with bubble radius that scales as $c_t \sim R^{-1/2}$. Experimental results from Tsang et al. (2004) show a stronger dependence that scales as $c_t \sim R^{-1.2}$. Based on these experimental results Chan and Tsang (2005) formulate a new model for the critical concentration which shows a scaling of the form $c_t \sim R^{-1}$. Even though there is a significant difference in the reported exponents for the scaling of the critical salt concentration, all these studies show the same trend: the critical salt concentration decreases as the bubble radius increases and it does it with a power law of the form $c_t \sim R^{-n}$ with $0.5 \lesssim n \lesssim 1.2$. Although all of these results are equally valid, here the theoretically derived result by Prince and Blanch (1990a) is used. There is no particular reason to chose from the model by Prince and Blanch (1990b) or Chan and Tsang (2005) since more research on this subject is necessary to confirm one model or the other. The objective at this stage is to include an approximation for the bubble size dependence of the coalescence time.

If temperature and salt concentration are assumed fixed Eq. (3.91) can be rewrit-

ten as

$$c_t(R) = c_{t0}\left(\frac{R_0}{R}\right)^{1/2} \tag{3.92}$$

where c_{t0} is the transition concentration at the reference radius R_0. From Prince and Blanch (1990b) reference values can be taken as $c_{t0} = 175$ mM for $R_0 = 1.8$ mm. Similar values are reported in Christenson et al. (2008). The model proposed here then consists in making the constant C_s in Eq. (3.61) to be a function of the bubble radius through the use of Eq. (3.92)

$$C_s(R_{m,m'}) = \begin{cases} 1 & S < c_t(R_{m,m'}) \\ 1000 & S > c_t(R_{m,m'}) \end{cases} \tag{3.93}$$

where the equivalent radius $R_{m,m'}$ defined in Eq. (3.62) is used instead. The above expression leads to an abrupt transition in the coalescence time with salt concentration and even though this is observed in the experimental works of Craig et al. (1993), Tsang et al. (2004) and Christenson et al. (2008) the transition observed in these experiments is somewhat smoother. A smoother functional form in Eq. (3.93) could be chosen but for the sake of simplicity a step function is used instead.

The expression in Eq. (3.93) is equivalent to

$$C_s(R_{m,m'}) = \begin{cases} 1 & R_{m,m'} < R_t \\ 1000 & R_{m,m'} > R_t \end{cases} \tag{3.94}$$

where R_t is the transition radius computed from $c_t(R_t) = S$ in Eq. (3.92) resulting in $R_t = 0.16$ mm. Therefore, according to this model, coalescence is strongly inhibited only between bubbles with an equivalent radius larger than the transitional radius R_t and bubbles smaller than R_t are left to coalesce as they would in fresh water. Moreover, given that the equivalent radius $R_{m,m'}$ defined in Eq. (3.62) is used,

coalescence between a bubble with radius R much smaller than a larger one with radius R' is not inhibited whenever $R \lesssim R_t/2$ (the limit $R' \to \infty$ is taken in Eq. (3.62)).

3.6 Turbulence Modeling

Several turbulence models have been proposed for the modeling of two-phase flows. Two-equation turbulence models for two-phase flows have been developed in the past as an extension to the k-ε model. This approach is taken in the works by Elghobashi and Abou-Arab (1983), Lahey Jr. et al. (1993), Lopez de Bertodano et al. (1994), Lahey Jr. and Drew (2001) and Troshko and Hassan (2001a) where small variations exist between them mainly in how the effect of the bubble induced turbulence is taken into account. The presence of bubbles in a main liquid phase can either suppress or produce turbulent kinetic energy depending on the relation of bubble size to turbulent scales. In Kataoka et al. (1993) a turbulence model is developed in order to account for these effects. How the presence of bubbles modifies the logarithmic law of the wall is studied in Troshko and Hassan (2001b).

In this work a two-phase k-ω blended model is implemented. In the k-ω model of turbulence originally developed by Wilcox (1988) the two parameters describing the local turbulent field are the turbulent kinetic energy k and the rate of dissipation per unit turbulent kinetic energy ω. In the k-ω blended model developed by Menter (1994) the k-ω model of Wilcox (1988) is used near walls and the k-ε model elsewhere.

A k-ω model counterpart to a two-phase k-ε model can be found by following the procedure in Menter (1994) where the equation for ω is obtained by the formal substitution $\varepsilon = \beta^* \omega k$ into the equation for ε.

The resulting two-phase k-ω blended model , first presented in Moraga et al.

(2008), reads

$$\alpha_c \frac{Dk}{Dt} = \alpha_c \mathbf{T}_c^{Re} : \nabla \boldsymbol{u}_c + \nabla \cdot [\alpha_c(\nu_c + \sigma_k \nu_t)\nabla k] - \alpha_c \beta^* \omega k \tag{3.95}$$

$$\alpha_c \frac{D\omega}{Dt} = \alpha_c \gamma \frac{\omega}{k} \mathbf{T}_c^{Re} : \nabla \boldsymbol{u}_c + \nabla \cdot [\alpha_c(\nu_c + \sigma_\omega \nu_t)\nabla \omega] - \alpha_c \beta \omega^2 + 2\alpha_c(1 - F_1)\frac{\sigma_{\omega 2}}{\omega}\nabla \omega \cdot \nabla k \tag{3.96}$$

where $\mathbf{T}_c^{Re}$ is the Reynolds stress tensor computed as $\mathbf{T}_c^{Re} = 2\,\nu_t\,\nabla^s \boldsymbol{u}_c$. The turbulent viscosity is modeled as the superposition of two effects. The first one is the *shear induced* turbulence modeled by the *k-ω* turbulent viscosity

$$\nu_{SI} = C_\mu \frac{k^2}{\varepsilon} \tag{3.97}$$

and the second effect is the *bubble induced* turbulence here predicted using the multigroup version of the model proposed by Sato et al. (1981a,b)

$$\nu_{BI} = 1.2 \sum_{g=1}^{G} R_g \alpha_g \|\boldsymbol{u}_{r,g}\| \tag{3.98}$$

Hence, the turbulent viscosity is modeled by

$$\nu_t = \nu_{SI} + \nu_{BI} \tag{3.99}$$

The model coefficients used in the above model of turbulence are assumed to be the same as in the original single phase version.

The model proposed by Kataoka et al. (1993), which is claimed to reproduce not only the bubble induced turbulence but also turbulence suppression, should be considered as a future improvement to the model presented here.

3.7 Free Surface Tracking: Single Phase Level Set

For problems involving a free surface as it is the case for the flow around a ship, a mathematical description and numerical method must be provided to describe the position of the free surface. In this work the two-phase model for polydispersed bubbly flows is implemented in the code CFDShip-Iowa V4.5 (see Chapter 4 for details). In CFDShip-Iowa V4.5 the position of the free surface is described by a single-phase level set method as presented in Carrica et al. (2007b). In contrast to the standard level set, the single-phase level set is concerned with the solution of the flow field in the denser field only (water for ship applications). Some of its advantages are that the interface remains sharp, computations are performed within a fluid with uniform properties and minor computations are required in the lighter phase (air). A brief description of this method is given in this section in order to complete the presentation of the full mathematical model used to describe polydispersed bubbly flows with free surface and to introduce the level set function used later on in the model. However, the reader is referred to Carrica et al. (2007b) for further details.

In the level set method the location of the free surface given by the zero level set of a function $\phi(\boldsymbol{r})$ known as the level set function. At any given spatial location $\boldsymbol{r}$ the function $\phi(\boldsymbol{r})$ provides the minimum distance to the free surface. This distance is arbitrarily made to be positive in the water side and negative in the air side. Since the free surface is a material interface, the level set function follows the equation

$$\frac{\partial \phi}{\partial t} + \boldsymbol{u}_c \cdot \nabla \phi = 0 \tag{3.100}$$

The level set transport given by Eq. (3.100) generally does not preserve the signed distance function property of the level set function. Therefore, the level set function needs to be reinitialized periodically, typically after each time step. One of

the attractive features of the level set method is that given that the level set function is a signed distance function, the normal to the free surface can be computed as

$$\hat{\boldsymbol{n}} = -\nabla\phi \tag{3.101}$$

3.8 Entrainment Modeling

The entrainment of air through the free surface is of great interest for ship hydrodynamics due to its implications for stealth capabilities, drag reduction and cavitation on the propellers. It is also important on the design of spillways and other civil hydraulics structures. Air entrainment is characterized by a large amount of bubbles being formed and for a highly turbulent and unstable air/water interface where a wide range of length scales span from surface tension and turbulence dominated scales (in the order of micrometers) to the macroscopic scale of the problem (several meters for ship applications). These factors make prohibitive the use of DNS-like approaches to simulate this phenomenon and therefore, a model for air entrainment that does not require the resolution of all these small scale features is needed.

In ship flows, entrainment of air into the liquid phase is observed at the breaking/spilling waves at the bow, at the contact line between the free surface and the hull of the ship and at the highly aerated and turbulent stern. In the past, the location and strength of the entrainment was set by the user (Carrica et al., 1998). This required certain level of experience from the modeler. Recently, with the advent of the so called sub-grid scale models (Moraga et al., 2008; Ma et al., 2010a) input from an experienced user is avoided by attempting to automatically predict the strength, location and size distribution of the entrainment source.

In the model developed by Moraga et al. (2008) air entrainment is predicted at locations where the component of the velocity normal to the surface is higher

than a certain threshold value related to the terminal velocity of the bubbles. This model was found to provide reasonable qualitative agreement with the observed entrainment locations in cases of ships moving through calm water (see Moraga et al., 2008). In this work this model was tested in cases with incoming heading waves and it was observed that an unphysical prediction of the entrainment locations resulted as the normal velocity is non-zero and specially high at the crest and trough of the wave.

In the recent work by Ma et al. (2010a,b), a new model is developed based on the idea that air is entrained at locations where the resolved velocity field creates suction flow pulling bubbles down into the water. This model can essentially be applied to either steady or unsteady situations like those in ship flows with incoming waves and is therefore implemented in this work.

In early modeling of entrainment when the free surface was defined as one of the boundaries of the computational domain, the entrainment was imposed as a flux boundary condition on this boundary (see Carrica et al., 1998). Later on, with the advent of the level set method, this approach was replaced by the use of a volumetric source instead (see Moraga et al., 2008). This is the volumetric source $S(m, \boldsymbol{r}, t)$ in Eq. (2.8).

In this work the entrainment source is separated in the form

$$S(m, \boldsymbol{r}, t) = S_0 \, D^{\text{ent}}(m) \, E(\boldsymbol{r}, t) \, \Lambda(\alpha_d) \tag{3.102}$$

where $E(\boldsymbol{r}, t)$ is a function that detects the entrainment spatial locations and relative strength, $D^{\text{ent}}(m)$ is the entrainment size distribution, S_0 is an adjustable constant that controls the overall entrainment strength and $\Lambda(\alpha_d)$ is a function that limits the entrainment of air at locations with high void fraction.

In the model developed by Ma et al. (2010a,b, 2011) the function $E(\boldsymbol{r}, t)$ is

computed as

$$E(\mathbf{r},t) = \begin{cases} \dfrac{\partial u_n}{\partial \hat{n}} \dfrac{k}{g\,\phi_{\text{ent}}\,\bar{v}_{\text{ent}}} & \text{for } \dfrac{\partial u_n}{\partial \hat{n}} > 0,\ \phi < \phi_{\text{ent}} \\ 0 & \text{otherwise} \end{cases} \tag{3.103}$$

where g is the acceleration of gravity, $\bar{v}_{\text{ent}}$ is the mean entrained bubble volume computed from the number density distribution $f(R)$ as

$$\bar{v}_{\text{ent}} = \frac{1}{N} \int_0^\infty \mathrm{d}R\, \frac{4}{3}\pi R^3 f(R) \tag{3.104}$$

and ϕ_{ent} is an entrainment depth over which the source will be active. The distance to the surface is given by the level set function ϕ defined in Section 3.7. $\partial u_n/\partial \hat{n}$ is the derivative in the direction normal to the free surface of the normal component of the continuous phase velocity. The normal component of the continuous phase velocity is computed as $u_n = \boldsymbol{u}_c \cdot \hat{n}$ and thus

$$\frac{\partial u_n}{\partial \hat{n}} = \nabla u_n \cdot \hat{\boldsymbol{n}} = \nabla\left(\boldsymbol{u}_c \cdot \hat{\boldsymbol{n}}\right) \cdot \hat{\boldsymbol{n}} \tag{3.105}$$

where $\hat{\boldsymbol{n}}$ is the normal to the free surface computed according to Eq. (3.101).

There is no model available for the size distribution $D^{\text{ent}}(m)$ and in this work is obtained from the experimental data taken by Johansen et al. (2010). The group entrainment source is obtained according to Eq. (2.21) as

$$S_g(\boldsymbol{r},t) = \int_{m_{g-1/2}}^{m_{g+1/2}} \mathrm{d}m\, S(m,\boldsymbol{r},t) = S_0\, D_g^{\text{ent}}\, E(\boldsymbol{r},t)\, \Lambda(\alpha_d) \tag{3.106}$$

and the group size distribution is obtained from the experimental number density

distribution provided by Johansen et al. (2010) as

$$D_g^{\text{ent}} = \frac{1}{N} \int_{m_{g-1/2}}^{m_{g+1/2}} \mathrm{d}m \, f(m) \tag{3.107}$$

The source strength S_0 is an adjustable parameter of the model, set such that the void fraction levels in the simulation resemble those found in the experiments. The parameter ϕ_{ent} in Eq. (3.103) is set such that when the volumetric source is active, it does in a region a few nodes thick (around 5 nodes should suffice).

This work adds a functional dependence of the entrainment source with void fraction encapsulated in the term $\Lambda(\alpha_d)$. The role of this term is to avoid an unphysical entrainment of bubbles in regions with large void fractions. This term is modeled assuming that the air entrainment rate should be proportional to the available volume fraction of water. Since this fraction is given by α_c a first approximation is to make $\Lambda(\alpha_d)$ proportional to α_c or $\Lambda(\alpha_d) = \alpha_c = 1 - \alpha_d$. A term like this would easily allow the model to reach 100% void fractions while in reality air entrainment should probably stop, for instance, at a closed packing void fraction. Since there is not a unique close packing void fraction for polydispersed flows (see discussion about packing in Section 3.1.4) and no further experimental information is available, this work assumes a packing void fraction of $\alpha_{\text{crit}} = 0.3$. The model is then written as

$$\Lambda(\alpha_d) = \max\left(0, \frac{\alpha_c - (1 - \alpha_{\text{crit}})}{\alpha_{\text{crit}}}\right) \tag{3.108}$$

With this model for $\Lambda(\alpha_d)$ there is no air entrainment at void fractions larger than 30% and it linearly increases to its maximum value at $\alpha_d = 0$. However, special care must be taken with this term since void fraction could still reach unphysical values in only one time step of the numerical procedure if the functional dependence with α_d is not treated implicitly. Details on the numerical algorithm used to integrate

this term are given in Section 4.7.

3.9 Oceanic Background

The previous section describes a model for the entrainment of bubbles due to wave breaking. In addition to this source, bubbles may already be present in the ocean. One important source of bubbles in the ocean is the entrainment of air due to wind-induced breaking waves. To include this oceanic background of bubbles the model presented in this work uses the experimental data of Melville et al. (1995) to impose their measured background as an inlet boundary condition for the simulation of ships. Moreover, this same background is used as an initial condition for those computations involving an oceanic background. The measurements by Melville et al. (1995) were taken in the North Atlantic between Wood Hole and Bermuda for 12.7 m/s average wind speeds. Their results show a void fraction that fits well a z^{-n} power law with n between 2.5 and 3. In this work the void fraction background is computed from the following fit

$$\alpha(z) = \begin{cases} 1.0 \times 10^{-4} & z < 0.5 \text{ m} \\ \dfrac{1.8 \times 10^{-5}}{(0.1 + z)^3 (1 - 0.098\, z)} & 0.5 \text{ m} < z < 7.5 \text{ m} \\ 1.54 \times 10^{-7} & z > 7.5 \text{ m} \end{cases} \tag{3.109}$$

Since Melville et al. (1995) only provide void fraction for 0.5 m $< z <$ 7.5 m, this is assumed to be constant outside this range. Void fractions for $z <$ 0.5 m and $z >$ 7.5 m continuously extend the previous fit.

In addition to the void fraction profile with depth, Melville et al. (1995) provide bubble size distribution measurements taken at a depth of 0.5 m off the entrance to Buzzards Bay, Massachusetts, in winds of 8 m/s and significant wave heights of 0.5 m. Since their data only spans the range 70 μm $< R <$ 500 μm, it is assumed that

there are no background bubbles with $R > 500$ μm and that the size distribution linearly goes to zero for $R < 70$ μm. The following fit is used

$$f^{\text{bkg}}(R) = \begin{cases} 3.05 \times 10^{7}\ R & R < 70\ \mu\text{m} \\ 4.0 \times 10^{15}\ R^{-3.4} & 70\ \mu\text{m} < R < 500\ \mu\text{m} \\ 0 & R > 500\ \mu\text{m} \end{cases} \tag{3.110}$$

furthermore, the above size distribution is assumed to be constant with depth.

It must be noted that this model does not consider the entrainment of bubbles through the free surface due to wave-induced breaking and therefore background bubbles continuously disappear as they are allowed to escape through the free surface and dissolve as they move to the end of the computational domain.

Since the size distribution is assumed to be constant with depth, the oceanic background number density distribution is a function of the bubble radius R and depth ϕ that can be separated as

$$f(R, \phi) = N(\phi)\ D^{\text{bkg}}(R) \tag{3.111}$$

where $N(\phi)$ is the total number density as defined in Eq. (2.4) and the level set function ϕ is used as a measure of depth. $D^{\text{bkg}}(R)$ is the normalized size distribution computed from the fit in Eq. (3.110) as

$$D^{\text{bkg}}(R) = \frac{f^{\text{bkg}}(R)}{\int_0^\infty \mathrm{d}R\ f^{\text{bkg}}(R)} \tag{3.112}$$

Void fraction can be computed from the number density distribution in Eq.

(3.111) to obtain the relation between $N(\phi)$ and the void fraction $\alpha(\phi)$ in Eq. (3.109)

$$\alpha(\phi) = \int_0^\infty \mathrm{d}R\, v(R)\, f^{\mathrm{bkg}}(R) = N(\phi) \int_0^\infty \mathrm{d}R\, v(R)\, D^{\mathrm{bkg}}(R) = N(\phi)\, \bar{v}_{\mathrm{bkg}} \tag{3.113}$$

$$\bar{v}_{\mathrm{bkg}} = \int_0^\infty \mathrm{d}R\, v(R)\, D^{\mathrm{bkg}}(R) \tag{3.114}$$

where $\bar{v}_{\mathrm{bkg}}$ is the oceanic background mean bubble volume. From the above equation $N(\phi)$ is computed as

$$N(\phi) = \frac{\alpha(\phi)}{\bar{v}_{\mathrm{bkg}}} \tag{3.115}$$

With this, the background number density distribution is completely defined with Equations (3.111), (3.112) and (3.115).

Both, the inlet boundary condition and the initial condition, are imposed in terms of the group number densities N_g. These are simply computed as

$$N_g(\phi) = \int_{R_{g-1/2}}^{R_{g+1/2}} \mathrm{d}R\, f(R,\phi) = N(\phi)\, D_g^{\mathrm{bkg}} \tag{3.116}$$

$$D_g^{\mathrm{bkg}} = \int_{R_{g-1/2}}^{R_{g+1/2}} \mathrm{d}R\, D^{\mathrm{bkg}}(R) \tag{3.117}$$

3.10 Bubble Growth by Rectified Diffusion

One of the potential sources of bubbles in the wake of a ship is the release of air caused by the propellers. The water flowing around a ship contains not only bubbles entrained by wave breaking at the free surface but also microscopic size bubbles already present in the ocean's water (see the previous section on oceanic background).

As described in Section 3.4, the air dissolved in the water may transfer from

(causing bubble dissolution) or into (causing bubble growth) a bubble depending on the local pressure (controlling the concentration of air at the air/water interface through Henry's law) and equilibrium concentration away from the bubble. This process is dominated by diffusion and may be enhanced by convective mass transfer. The situation described in Section 3.4 is for steady or quasi-steady bubble sizes. When bubbles encounter the ship's propeller, they may undergo violent pressure changes that induce explosive growth, collapse and non-linear oscillations with periods in the order of 10 μsec – 200 μsec (see Hsiao and Chahine, 2005). The non-linear nature of the process causes highly asymmetric oscillations in size and concentration profiles ultimately responsible for the cumulative transfer of gas into the bubbles. This mechanism of mass transfer into the bubbles is known as *rectified diffusion* and is considerably more effective than the simple mass transfer by diffusion introduced in Section 3.4. Under these conditions the assumption of a quasi-steady bubble size implied in Section 3.4 is no longer valid. Moreover, the time steps required to resolve such high frequency oscillations are not practical in real CFD applications and modeling is needed.

As an early attempt to provide of a modeling strategy this work uses results from simulations performed by Raju et al. (2009) in order to develop a model of rectified diffusion that can be embedded into and Eulerian framework and solved with the time steps of a practical CFD computation.

In Raju et al. (2009) the modification of an incoming bubble nuclei population due to the presence of a rotating propeller is modeled using a combined Eulerian-Lagrangian approach: fluid equations are solved in an Eulerian framework while bubbles are tracked in a Lagrangian fashion. In their Lagrangian model the Rayleigh-Plesset equations describing the bubble dynamics are solved coupled together with a gas diffusion model. For their study they consider the five-bladed, controllable pitch DTMB propeller model P5168 with a design advance ratio of

$J = 1.27$ and a diameter of 0.403 m. In their study a uniform field of incoming bubbles of a given radius are placed upstream the propeller and are left to evolve as they go through the propeller. Then, the bubble size distribution is obtained at a plane 0.9 diameters downstream the propeller plane. Since in their model bubbles do not interact with each other in any way, they are able to construct transfer tables providing the bubble size distribution downstream the propeller for input bubbles of a given radius. The normalized (the integral over all sizes is one) size distribution for the monodispersed bubbly flow of bubbles with mass m' upstream the propeller can be written in terms of the Dirac delta function as

$$P_{\text{ups}}(m) = \delta(m - m') \tag{3.118}$$

After these bubbles go through the propeller some of them remain with the same size while a fraction $f_{\text{rd}}(m')$ grows to bubble sizes m with a probability $\tilde{P}(m, m')$. Therefore, the normalized size distribution downstream the propeller can be written as

$$P_{\text{dwn}}(m) = (1 - f_{\text{rd}}(m))\,\delta(m - m') + \tilde{P}(m, m') \tag{3.119}$$

Since $\tilde{P}(m, m')\mathrm{d}m$ is the probability of bubbles with mass m' to grow into a bubble within $\mathrm{d}m$ of mass m, the integral over m is the rectified fraction $f_{\text{rd}}(m')$

$$\int_m^\infty \mathrm{d}m\, \tilde{P}(m, m') = f_{\text{rd}}(m') \tag{3.120}$$

This is consistent with Eq. (3.119) where $\int_0^\infty \mathrm{d}m\, P_{\text{dwn}}(m) = 1$.

The size distribution $\tilde{P}(m, m')$ can be used as a transfer function or kernel to compute the fraction of bubbles growing from a size m' to a size m. The model presented in this work applies the transformation given by $\tilde{P}(m, m')$ inside a model disk with the dimensions of the propeller. In order to have a smooth transition

between the upstream and downstream planes of this propeller disk the transformation is applied in the time it takes the local fluid to go through it. In this manner, if δ_p is the propeller disk thickness and U_p is the magnitude of the local velocity, the time it takes a bubble to cross the propeller disk is $\tau_p = \delta_p / U_p$. As with bubble breakup and coalescence, source terms describing the *birth* and *death* of bubbles for a given size can be written and added to the right hand size of the Boltzmann equation in Eq. (2.8). Bubbles can be *born* by rectified diffusion as smaller bubbles grow to this size. This is described by a *birth* term expressed as

$$\mathcal{R}^{+}(m) = \frac{1}{\tau_p} \int_0^m \mathrm{d}m' \, f(m') \, \tilde{P}(m, m') \tag{3.121}$$

Similarly, bubbles can be removed from a given size as they gain mass. The fraction of bubbles growing from size m to any other size is $f_{\mathrm{rd}}(m)$ and thus *deaths* are given by

$$\mathcal{R}^{-}(m) = \frac{f(m)}{\tau_p} f_{\mathrm{rd}}(m) \tag{3.122}$$

It should be noted that given that gas is transfered from the liquid phase into the bubbles the process changes the total mass contained in the bubbly phase. However, the total number of bubbles is preserved. It can be shown that the above model preserves the number of bubbles.

3.10.1 Discrete Form

The discrete form of the source terms in Eqs. (3.121) and (3.122) is obtained by using the discrete form of the number density distribution in Eq. (2.23) and

performing the integration on the interval $(m_{g-1/2};\, m_{g+1/2})$ around m_g. The result is

$$\mathcal{R}_g^+ = \frac{1}{\tau_p} \sum_{g'=1}^{g} \tilde{P}_{g,g'}\, N_{g'} \tag{3.123}$$

$$\mathcal{R}_g^- = \frac{N_g}{\tau_p} f_{\mathrm{rd},g} \tag{3.124}$$

where it was defined

$$\tilde{P}_{g,g'} = \int_{m_{g-1/2}}^{m_{g+1/2}} \mathrm{d}m\, \tilde{P}(m, m_{g'}) \tag{3.125}$$

$$f_{\mathrm{rd},g} = f_{\mathrm{rd}}(m_g) \tag{3.126}$$

The contribution from group g into itself is moved from Eq. (3.123) into Eq. (3.124) rewriting the rectified diffusion sources as

$$\mathcal{R}_g^+ = \frac{1}{\tau_p} \sum_{g'=1}^{g-1} T_{g,g'}\, N_{g'} \tag{3.127}$$

$$\mathcal{R}_g^- = \frac{N_g}{\tau_p} (1 - T_{g,g}) \tag{3.128}$$

where the discrete transfer function $T_{g,g'}$ is defined as

$$T_{g,g'} = \begin{cases} \tilde{P}_{g,g'} & \text{for } g \neq g' \\ 1 - f_{\mathrm{rd},g} + \tilde{P}_{g,g} & \text{for } g = g' \end{cases} \tag{3.129}$$

and thus $T_{g,g'}$ represents the probability of a bubble with size in group g' growing to a size in group g. For $g = g'$ it gives the probability to stay in the same group. For instance, large bubbles are not as susceptible to rectified diffusion as small bubbles are, and the transfer function becomes $T_{g,g'} = \delta_{g,g'}$, the Kronecker delta.

From Raju et al. (2009) the transfer function $T_{g,g'}$ is obtained for several loading

conditions and cavitation numbers. Loading is expressed by the advance coefficient defined as $J = U_\infty / n D_p$ with U_∞ the incoming velocity into the propeller, n the propeller rotational speed in RPS and D_p the diameter of the propeller. The cavitation number is defined as $Ca = (p - p_v)/(1/2\rho_c U_\infty^2)$ where p_v is the vapor pressure and p is the hydrostatic pressure at the center of the propeller. Raju et al. (2009) actually provide the discrete transfer function $T_{g,g'}$ discretizing the input sizes g' in nine groups and the resulting groups g in twenty-five groups. For the model presented here the discretization in g' and g must be the same. In the computations performed for Athena in Chapter 6 fifteen groups are used with bubbles sizes summarized in Table 6.3. The data provided by Raju et al. (2009) is then interpolated to obtain a 15×15 transfer function $T_{g,g'}$. Figure 3.6 shows the transfer function used for Athena's computations. Two curves for two different incoming bubble sizes

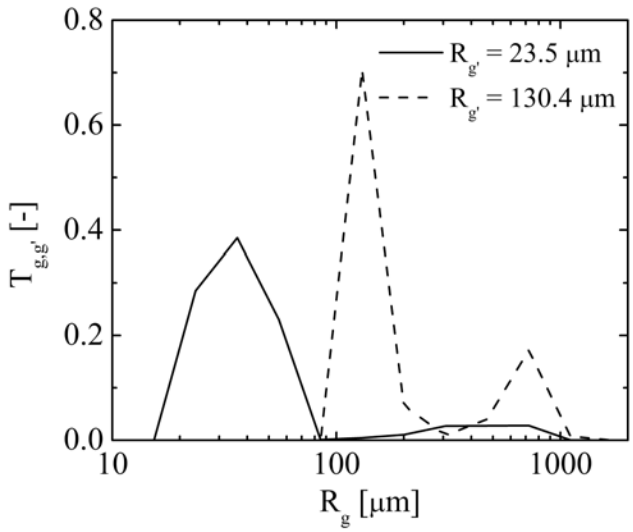

Figure 3.6: Discrete transfer function obtained for fifteen groups from simulations performed by Raju et al. (2009)

are shown. These curves exhibit two domes: the first dome is located around the

original bubble size while the second one is centered at 400 μm for $R_{g'} = 23.5$ μm and at 700 μm for $R_{g'} = 130.4$ μm making evident the growth in bubble size.

3.10.2 Limitations and Known Problems of the Model

Several limitations in the model can be identified at this very early stage of its development:

1. The model by Hsiao and Chahine (2005) does not solve for breakup or coalescence which can be significant near the propeller blades. Moreover, bubbles can breakup/coalesce as they go through the propeller in the model just presented. This is by no means a way to include this coupling but rather a simplification under the assumption that rectified diffusion dominates inside the disk.

2. The transfer function is assumed to be uniform inside the propeller disk *i.e.* it contains no spatial dependence. In reality, several factors contribute to the spatial dependence in $T(R, R')$: the incoming velocity field into the propeller is non uniform since it is located inside the ship's boundary layer. This locally changes the effective advance coefficient of the propeller. Another factor is that hydrostatic pressure makes the local cavitation number to change with depth.

3. Even if these factors are included in the model, the particular geometry of interest must be used to obtain the transfer function $T(R, R')$.

As pointed out in assertion 3, the geometry of Athena's propeller must be used if this transfer function is to be used for Athena's computations. However, simulations of the type presented in Raju et al. (2009) only include the DTMB P5168 propeller and computations are not available for Athena's propeller. Nevertheless,

the results from Raju et al. (2009) are used to construct a transfer function for Athena's computations in order to illustrate the modeling strategy.

3.11 Dimensionless Equations

This section summarizes the complete system of equations comprising the full polydispersed model for bubbly flows. The equations are nondimensionalized using a characteristic length scale L_0 and velocity scale U_0. For ship applications these are frequently chosen as the ship's length and cruise velocity. The mass of the bubbles is adimensionalized using the characteristic length L_0 and the gas density at standard conditions for temperature and pressure (STP) $\rho_{d,0}$. Therefore, dimensionless variables are defined as

$$\begin{aligned}
\boldsymbol{u}_c^* &= \frac{\boldsymbol{u}_c}{U_0} & k^* &= \frac{k}{U_0^2} & \rho_d^* &= \frac{\rho_d}{\rho_c} \\
p_c^* &= \frac{p_c}{\rho_c U_0^2} & \varepsilon^* &= \frac{\varepsilon}{U_0^3/L_0} & R^* &= \frac{R}{L_0} \\
N_g^* &= \frac{N_g}{1/L_0^3} & \omega^* &= \frac{\omega}{U_0/L_0} & m^* &= \frac{m}{\rho_{d,0}\, L_0^3} = \rho_d^*\, \frac{4}{3}\pi R^{*3} \\
\boldsymbol{u}_g^* &= \frac{\boldsymbol{u}_g}{U_0} & \nu_t^* &= \frac{\nu_t}{U_0\, L_0} & \boldsymbol{r}^* &= \frac{\boldsymbol{r}}{L_0}, \quad t^* = \frac{t}{L_0/U_0}
\end{aligned} \tag{3.130}$$

The corresponding dimensionless equations then are

Continuous Phase Momentum Equation

From Eq. (3.19)

$$\frac{\partial \alpha_c \boldsymbol{u}_c^*}{\partial t^*} + \nabla^*\cdot(\alpha_c \boldsymbol{u}_c^* \otimes \boldsymbol{u}_c^*) = -\nabla^* \hat{p}_c^* + \nabla^*\cdot\left[2\alpha_c\left(\frac{1}{Re} + \nu_t^*\right)\nabla^{s*}\boldsymbol{u}_c^*\right] + \frac{\alpha_d}{Fr^2}\left(1 - \pi_\rho \rho_d^*\right)\hat{k} \tag{3.131}$$

where, as with its single phase counterpart, Re is the Reynolds number. The Froude number Fr results from imposing the boundary condition for the pressure at the

free surface ($p(\phi = 0) = p_{\text{atm}}$). Reynolds and Froude numbers are defined as

$$Re = \frac{U_0 L_0}{\nu}, \qquad Fr = \frac{U_0}{\sqrt{g L_0}} \tag{3.132}$$

The new parameter in this equation is the ratio between the densities of the two phases

$$\pi_\rho = \frac{\rho_{d,0}}{\rho_c} \tag{3.133}$$

and $\rho_d^* = \rho_d / \rho_{d,0}$ is the dimensionless dispersed phase density. With the fluid at rest and at STP $\rho_d^* = 1$. The asterisk superscript on top of the nabla operators in Eq. (3.131) is used to denote the fact that they operate on the dimensionless coordinates $\boldsymbol{r}^*$.

Continuous Phase Continuity Equation

From Eq. (3.13)

$$\frac{\partial \alpha_c}{\partial t^*} + \nabla^* \cdot (\alpha_c \boldsymbol{u}_c^*) = 0 \tag{3.134}$$

Group$-g$ Number Density Equation

From Eq. (3.34)

$$\frac{\partial N_g^*}{\partial t^*} + \nabla^* \cdot \left(\boldsymbol{u}_g^* N_g^* \right) + F_{g+1/2}^* - F_{g-1/2}^* = \nabla^* \cdot \left(\frac{\nu_t^*}{Sc_b} \nabla^* N_g^* \right) + \beta_g^* + \chi_g^* + S_g^* \tag{3.135}$$

Group$-g$ Dispersed Phase Momentum Equation

From the dispersed phase momentum Eq. (3.10) and the interfacial forces in Eqs. (3.21), (3.27), (3.28) and (3.37)

$$\begin{aligned} C_{VM} \left[\left(\frac{\partial \boldsymbol{u}_g^*}{\partial t^*} + \left(\boldsymbol{u}_g^* \cdot \nabla^* \right) \boldsymbol{u}_g^* \right) - \left(\frac{\partial \boldsymbol{u}_c^*}{\partial t^*} + \left(\boldsymbol{u}_c^* \cdot \nabla^* \right) \boldsymbol{u}_c^* \right) \right] + \widehat{C}_{D,g}^* \left\| \boldsymbol{u}_{r,g}^* \right\| \boldsymbol{u}_{r,g}^* = \\ - \nabla^* \hat{p}_c^* + \left(1 - \pi_\rho \rho_d^* \right) \frac{\hat{k}}{Fr^2} - C_L \, \boldsymbol{u}_{r,g}^* \times \nabla^* \times \boldsymbol{u}_c^* - \nabla^* \sigma_P^* \end{aligned} \tag{3.136}$$

where $\widehat{C}_{D,g}$ is defined as

$$\widehat{C}_{D,g} = \frac{3}{8}\frac{C_D(Re_g)}{R_g} \tag{3.137}$$

and its dimensionless form is

$$\widehat{C}^*_{D,g} = \frac{3}{8}\frac{C_D(Re_g)}{R^*_g} \tag{3.138}$$

The bubble Reynolds number Re_g is computed in terms of the dimensionless variables as

$$Re_g = \frac{\|\boldsymbol{u}_{r,g}\|\, D_g}{\nu_c} = Re\, \|\boldsymbol{u}^*_{r,g}\|\, D^*_g \tag{3.139}$$

Turbulence Model Equations

From Eqs. (3.95) and (3.96)

$$\alpha_c \frac{Dk^*}{Dt^*} = \quad 2\alpha_c \nu^*_t \nabla^{s*}\boldsymbol{u}^*_c : \nabla^{s*}\boldsymbol{u}^*_c + \nabla^*\cdot\left(\frac{\alpha_c}{Pe_k}\nabla^* k^*\right) - \alpha_c\, \beta^*\, \omega^*\, k^* \tag{3.140}$$

$$\alpha_c \frac{D\omega^*}{Dt^*} = 2\alpha_c \gamma \frac{\omega^*}{k^*}\nu^*_t \nabla^{s*}\boldsymbol{u}^*_c : \nabla^{s*}\boldsymbol{u}^*_c + \nabla^*\cdot\left(\frac{\alpha_c}{Pe_\omega}\nabla^* \omega^*\right) - \alpha_c\, \beta\, \omega^{*2} + 2\alpha_c(1-F_1)\frac{\sigma_{\omega 2}}{\omega^*}\nabla^*\omega^*\cdot\nabla^* k^* \tag{3.141}$$

where the Péclet numbers are defined as

$$Pe_k = \frac{U_0\, L_0}{\nu_c + \sigma_k \nu_t} = \frac{1}{1/Re + \sigma_k \nu^*_t}\,, \qquad Pe_\omega = \frac{U_0\, L_0}{\nu_c + \sigma_\omega \nu_t} = \frac{1}{1/Re + \sigma_\omega \nu^*_t} \tag{3.142}$$

and it should be recalled from Eq. (3.95) that β^* is a numerical constant of the model and not a dimensionless variable. Both β and β^* are two different numerical constants and do not have units even before the adimensionalization process.

In addition to the already introduced Reynolds Re, Froude Fr and density ratio π_ρ numbers, other dimensionless numbers arise from the two-phase model. In those expressions involving surface tension the adimensionalization results in a new parameter, the Weber number We_L. For instance, the dimensionless counter-

part of Eq. (3.26) is

$$p_g^* = \frac{p_g}{\rho_c \, U_0^2} = Eu + \hat{p}_c^* - \frac{z^*}{Fr^2} + \frac{2}{R_g^* \, We_L} \tag{3.143}$$

In addition, this example shows that in expressions involving the reference pressure (taken to be the atmospheric pressure p_{atm} for most simulations) a new dimensionless number appears, the Euler number Eu. These two dimensionless numbers are defined as

$$We_L = \frac{\rho_c U_0^2 \, L_0}{\sigma}, \qquad Eu = \frac{p_{\text{atm}}}{\rho_c U_0^2} \tag{3.144}$$

The Weber number can be thought as a measure of the relative importance of the fluid's inertia compared to its surface tension. The Euler number can be thought as a measure of the relative importance of the stagnation pressure compared to the atmospheric or reference pressure.

The model for dissolution of air in water, Section 3.4, introduces two new dimensionless numbers. These are the Schmidt number Sc and the dimensionless equilibrium concentration C_∞^* defined as

$$Sc = \frac{\nu_c}{\kappa}, \qquad C_\infty^* = \frac{C_\infty}{\rho_{d,0}} \equiv H^* = \frac{H \, p_{\text{atm}}}{\rho_{d,0}} \tag{3.145}$$

Note that the dimensionless dissolved gas concentration at equilibrium and the dimensionless Henry constant are two equivalent dimensionless numbers.

Table 3.1 summarizes the dimensionless numbers of the polydispersed bubbly flow model.

From this point on, and for the sake of simplicity, the asterisk subscript will be omitted from dimensionless equations unless otherwise specified.

Table 3.1: Dimensionless numbers of the polydispersed bubbly flow model

Parameter	Definition
Reynolds number	$Re = \frac{U_0 L_0}{\nu}$
Froude number	$Fr = \frac{U_0}{\sqrt{g L_0}}$
Density ratio	$\pi_\rho = \frac{\rho_{d,0}}{\rho_c}$
Weber number	$We_L = \frac{\rho_c U_0^2 L_0}{\sigma}$
Euler number	$Eu = \frac{p_{\text{atm}}}{\rho_c U_0^2}$
Schmidt number	$Sc = \frac{\nu_c}{\kappa}$
Dimensionless equilibrium concentration	$C_\infty^* = \frac{C_\infty}{\rho_{d,0}}$

CHAPTER 4
NUMERICAL METHODS AND IMPLEMENTATION

Chapters 2 and 3 describe the full mathematical model for polydispersed bubbly flows. In addition, the multigroup approach used to discretize the Boltzmann equation in the bubble size coordinate is introduced in Section 2.2.

This chapter describes the implementation details and numerical methods used to incorporate this model into the code CFDShip-Iowa V4.5. CFDShip-Iowa V4.5 is a computational fluid dynamics (CFD) software developed at The University of Iowa's Institute of Hydraulic Research (IIHR). The program solves the incompressible Reynolds Averaged Navier-Stokes (RANS) equations and allows to handle free surface flows using a single phase level set method. More details are given in the next section.

Many of the numerical methods presented in this chapter are developed to solve particular problems found when dealing with the full model for polydispersed bubbly flows, and constitute original contributions of this PhD thesis. One of the original goals of this PhD thesis is the implementation of the full model presented throughout Chapters 2 and 3 into CFDShip-Iowa V4.5. CFDShip-Iowa V4.5 has been applied successfully to many complex ship hydrodynamics problems of interest as those including large amplitude ship motions and self-propulsion with discretized propellers. The challenge for this PhD thesis is to incorporate the full polydispersed model into CFDShip-Iowa V4.5 without affecting its robustness and to provide a two-phase version of the code that can run the same complex situations that the single phase version can run.

The time splitting approach presented in Section 4.2 is proposed to efficiently and accurately solve the coupling in space and bubble sizes of the Boltzmann equation. The projection method proposed in Section 4.4 solves the strong coupling between pressure and void fraction given that for ship flows the change in gas den-

sity with pressure is considered. Section 4.6 presents the numerical schemes used to transport number densities and the near wall integration approach proposed to avoid the build up of void fraction in the first computational cells discretizing the boundary layer. Taking advantage of the time splitting approach, Section 4.7 presents an iterative method to integrate the non-linear dependence of the air entrainment source with void fraction. Finally, Section 4.8 presents a stable iterative method used to integrate forces in the group-g momentum equations that depend on the gradient of the number density. All the above numerical methods/schemes are original contributions of this PhD thesis.

4.1 CFDShip-Iowa V4.5

CFDShip-Iowa V4.5 uses multiblock structured body-fitted grids with overset gridding capability to model complex geometries and perform local refinement where needed. CFDShip-Iowa V4.5 solves the URANS/DES equations in the liquid phase with free surface using a single-phase level set approach (Carrica et al., 2007b). Turbulence modeling is performed with a blended k-ω model (Menter, 1994) and it has DES capabilities as well (Xing et al., 2007). Wall functions are implemented for full scale simulations (Bhushan et al., 2009; Castro et al., 2011). The multi-block dynamic overset grid capability allows to perform computations with large amplitude motions in objects with six degrees of freedom (6DOF) (Carrica et al., 2007a, 2010a). Overset interpolation coefficients are obtained with SUGGAR (Noack, 2005). The governing equations are discretized using a control volume/finite differences approach and time marching is performed with a second order backward difference formula (BDF2). The convection terms are discretized using a 2^{nd} or hybrid $2^{nd}/4^{th}$ order upwind or TVD schemes (Ismail et al., 2010). Either Projection (Bell et al., 1991) or PISO (Issa, 1986) are used for pressure-velocity coupling and PETSc (Balay et al., 2009, 2008, 1997) is used to solve the resulting pressure Poisson equation. CFDShip-Iowa V4.5 has also been successfully used

in problems involving fluid structure interaction (Paik et al., 2009), ship exhaust plumes (Huang et al., 2010), broaching (Carrica et al., 2008) and self propulsion with discretized propellers (Carrica et al., 2010a; Castro et al., 2011). Scalability in large scale computations is assessed in (Carrica et al., 2010b).

In this chapter, only details related to the solution of the multiphase problem are discussed. The reader interested in any of the CFDShip-Iowa V4.5 particulars is referred to the citations mentioned above.

4.2 Time Splitting

4.2.1 The Problem

In the multigroup approach presented in Section 2.2, the number density distribution $f(m, \boldsymbol{r}, t)$ is represented by its discrete counterparts, the group-g number densities N_g. These are solved from the multigroup Boltzmann equation for each group shown in Eq. (2.16). This set of equations is not only coupled in space due to transport, but also in bubble size through the intergroup transfer terms. As described in Section 2.3.4, the discretization of these terms typically leads to a system of equations where every group is coupled with all the other groups. Therefore, if the spatial domain is discretized in $\mathrm{N_{nod}}$ computational nodes and G groups are used to discretize the bubble sizes, the resolution of the Boltzmann equation requires to solve a system with $G \times \mathrm{N_{nod}}$ unknowns, provided the group-g velocities and continuous phase variables are given. Actually, the full model requires to solve for seven variables in the continuous phase ($\boldsymbol{u}_c = (u_c, v_c, w_c)$, p_c, ϕ, k_c, ω_c) and $4 \times G$ variables in the dispersed phase ($G \times (\boldsymbol{u}_g = (u_g, v_g, w_g), N_g)$). To exemplify the situation, consider the simulation of the bubbly flow around Athena with discretized propeller presented in Chapter 6. In this case $\mathrm{N_{nod}} = 25 \times 10^6$ and $G = 15$ adding up to a total of 1.68 billion of unknowns. Given the very large size of the problem it is not even imaginable to conceive a numerical scheme where all these variables are solved simultaneously. However, there are clear natural

divisions of the problem that can be made: the continuous phase variables can be solved separately using the last available void fraction, the group-g velocities can be solved using the last available void fraction and number densities and finally the Boltzmann transport equation can be solved using the last available group-g velocities and continuous phase variables. If needed, iterations can be performed on this strategy to attain the convergence of the overall system. In this way, the problem is reduced to solve separately the continuous phase momentum and mass conservation equations (Section 4.4), the group-g momentum equations (Section 4.5) and finally the Boltzmann equation. As previously mentioned, the resolution of the Boltzmann equation by itself involves $G \times \mathrm{N_{nod}}$ equations ($G \times N_g$). In the case of the Athena vessel treated in Chapter 6 this involves 375 million unknowns. The discrete version of the Boltzmann equation obtained using the multigroup approach is given in Eq. (2.16). This is rewritten here using the intergroup transfer matrices derived in Section 2.3 and summarized in Section 2.3.4

$$\frac{\partial N_g}{\partial t} + \nabla \cdot \left(\boldsymbol{u}_g N_g \right) + a_{g,g-1} N_{g-1} + a_{g,g} N_g + a_{g,g+1} N_{g+1} = \sum_{g'=g}^{G} \mathbf{B}^{+}_{g,g'} N_{g'} - \mathbf{B}^{-}_{g,g} N_g + \sum_{g'=1}^{g} \mathbf{C}^{+}_{g,g'} N_{g'} - \mathbf{C}^{-}_{g,g} N_g + S_g \quad \forall\, g = 1 \ldots G \tag{4.1}$$

A possible iterative scheme to solve this system of equations is to solve Eq. (4.1) consecutively for each group sending the unknowns from previous iterations to the right hand side. Therefore, if k is the iteration number, the g-th group is solved from

$$\frac{\partial N^k_g}{\partial t} + \nabla \cdot \left(\boldsymbol{u}_g N^k_g \right) + \left(\mathbf{B}^{-}_{g,g} + \mathbf{C}^{-}_{g,g} + a_{g,g} \right) N^k_g = -a_{g,g-1} N^{k-1}_{g-1} - a_{g,g+1} N^{k-1}_{g+1} + \sum_{g'=g}^{G} \mathbf{B}^{+}_{g,g'} N^{k-1}_{g'} + \sum_{g'=1}^{g} \mathbf{C}^{+}_{g,g'} N^{k-1}_{g'} + S^k_g \quad \forall\, g = 1 \ldots G \tag{4.2}$$

Once an appropriate discretization scheme for the temporal derivative and

convection term in Eq. (4.2) (these are described in Section 4.6) are used, each group-g equation becomes a linear system of equations with N_{nod} unknowns where the matrix of the system is formed by all those terms to the left of the equal sign in Eq. (4.2) and the right hand side of the system is formed by all those terms to the right of the equal sign in Eq. (4.2). This strategy is sketched in Fig. 4.1.

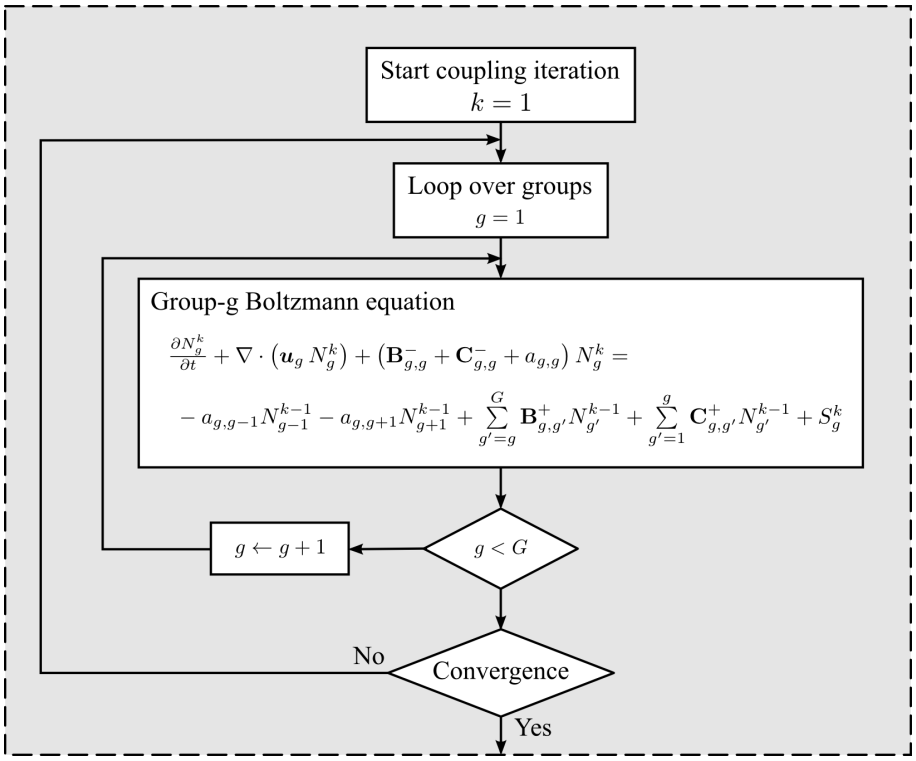

Figure 4.1: Iterative scheme solving each group-g number density in sequence.

A major disadvantage of this approach is the high computational cost involved. From the flow chart in Fig. 4.1 it is clear that the matrix of the system and the intergroup transfer matrices need to be computed at every iteration. Intergroup transfer typically requires a few iterations to converge and the number of iterations may increase at particular points in the domain, specially those with high void fractions and high turbulence levels. On the other hand, a poor convergence of

the intergroup transfer terms severely affects the conservation of mass and number of bubbles. The reason for this is that in the fixed pivot method from Kumar and Ramkrishna (1996) the conservation of mass and number of bubbles is guaranteed by computing births and deaths (in either breakup or coalescence) using the same time instance of the number density N_g. When using the scheme in Fig. 4.1 deaths are computed with densities at iteration k while births are computed *explicitly* with densities at iteration $k-1$. It was observed that small differences in densities at iterations k and $k-1$ severely affect the conservation of mass and number of bubbles. It could be argued that this problem can easily be solved by using iteration $k-1$ for both, births and deaths. However, this approach is explicit by nature and it becomes unstable very easily. The number of iterations required to reach convergence together with the fact that the matrix of the system must be computed with each iteration, makes prohibitive the application of this scheme to the solution of the problems presented in this work.

Another disadvantage of the iterative scheme depicted in Fig. 4.1 is that it tries to solve at once several different couplings taking place in the equations: transport (Section 4.6), intergroup transfer (this section), packing (Section 4.8) and entrainment (Section 4.7). These couplings are very different in nature, with different spatial and temporal dynamics, and thus require very different strategies to successfully solve them. It is for the above reasons that, in addition to its high computational cost, the strategy sketched in Fig. 4.1 is very prone to numerical instabilities and to the divergence of the system of equations. It is therefore necessary to device another strategy.

4.2.2 The Proposed Solution

To solve the system of equations resulting from the discretization of the Boltzmann equation, this work proposes to split the underlying physics involved in time. This is, while physically bubbles transport as they breakup, coalesce and dis-

solve all in one single continuous time process, the strategy proposed here is to split these processes in time. Therefore, bubbles first change their size distribution by intergroup transfer to an intermediate stage, and from there, they are transported to the next time step. This strategy is sketched in Fig. 4.2 where also the entrainment source is split in time. Then, bubbles are entrained and the solution evolves from time instance t_n to an intermediate stage t^*. From there, they breakup, coalesce and dissolve to stage t^{**} and finally, bubbles are transported to time instance t_{n+1}. All processes occur in one single time step $\delta t = t_{n+1} - t_n$. Note that the intermediate time stages t^* and t^{**} are fictitious and they do not really fall on the time line in Fig. 4.2.

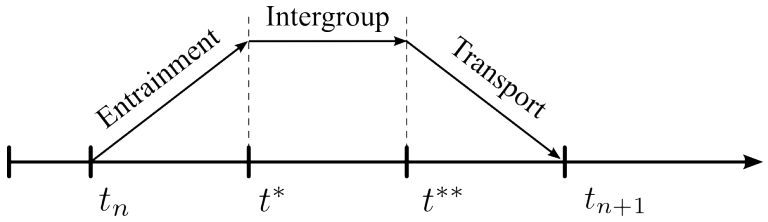

Figure 4.2: Time splitting strategy for the numerical resolution of the Boltzmann equation.

Given an arbitrary field f, the following approximation is used for time derivatives inside CFDShip-Iowa V4.5 to advance the solution from t_n to t_{n+1}

$$\left.\frac{\partial f}{\partial t}\right|_{t=t_{n+1}} = \frac{1}{\delta t}\left(w_{n+1}f^{n+1} + w_n f^n + w_{n-1}f^{n-1}\right) \tag{4.3}$$

where the weight coefficients w_{n+1}, w_n and w_{n-1} determine the time marching scheme, one of Implicit Euler (IE, for which $w_{n+1} = 1$, $w_n = -1$ and $w_{n-1} = 0$) or second order backward difference formula (BDF2, for which $w_{n+1} = 3/2$, $w_n = -2$ and $w_{n-1} = 1/2$). The order in which time splitting is performed cannot be

arbitrary. As shown in Fig. 4.2, bubble transport is the last stage of the time splitting procedure. The reason for this is that when using a BDF2 scheme, the intermediate solution at t_n must be computed consistently with the rest of the scheme to attain a second order time marching scheme. Otherwise, not only that the scheme is not second order in time, but also, the discrete marching method is inconsistent with the original continuous equations (in the sense that they do not converge to the continuous solution of the system as $\delta t \to 0$). To attain a time marching scheme that is second order in time, the solution at stage t_n is computed as

$$N_g^{**,n} = -\frac{1}{w_n}\left[N_g^{**} - (1 + w_n) N_g^n\right] \tag{4.4}$$

this pseudo time instance is used in Eq. (4.3) as the solution at t_n.

Using the approximation in Eq. (4.3) for the time derivative in the transport stage and an IE for the entrainment and intergroup transfer stages, the time splitting strategy reduces to Procedure 4.1.

To show the consistency of the overall scheme, the equations in Procedure 4.1 for each stage are added together. The result of this operation is

$$\frac{1}{\delta t}\left(w_{n+1} N_g^{n+1} + w_n N_g^n + w_{n-1} N_g^{n-1}\right) + \nabla \cdot (\boldsymbol{u}_g^{n+1} N_g^{n+1}) = \nabla \cdot \left(D_g^{n+1} \nabla N_g^{n+1}\right) + S_g^* + G_g^{**} \tag{4.5}$$

and therefore the overall scheme is second order accurate in time when S_g^* and G_g^{**} are both zero, and it is first order accurate in the entrainment and intergroup transfer sources since these are evaluated at stages t^* and t^{**} respectively, and not at the time instance t_{n+1}. A second order accuracy in time in the transport stage is desired since first order accurate time marching schemes introduce additional phase errors and therefore spurious numerical dispersion. For the IE scheme (with $w_{n+1} = 1$, $w_n = -1$ and $w_{n-1} = 0$) the intermediate stage reduces to $N_g^{**,n} = N_g^{**}$ and therefore to the result from the previous stage. For the BDF2 scheme (with $w_{n+1} =$

Procedure 4.1 Time splitting of the Boltzmann equation.

for $i_{\text{nod}} = 1$ **to** N_{nod} **do**

Solve N_g^* from: $\quad \dfrac{1}{\delta t}\left(\mathbf{N}^* - \mathbf{N}^n\right) = \mathbf{S}(\alpha_d^*)$

end for

for $i_{\text{nod}} = 1$ **to** N_{nod} **do**

Solve N_g^{**} from: $\quad \dfrac{1}{\delta t}\left(\mathbf{N}^{**} - \mathbf{N}^*\right) = \mathbf{G}(\mathbf{N}^{**})$

With $\quad \mathbf{G}(\mathbf{N}^{**}) = (\mathbf{B} + \mathbf{C}(\mathbf{N}^{**})) \cdot \mathbf{N}^{**} - \mathbf{D} \cdot \mathbf{N}^{**}$

This is Eq. (2.86).

end for

for $g = 1$ **to** G **do**

Solve N_g^{n+1} from:

$$\frac{1}{\delta t}\left(w_{n+1}N_g^{n+1} + w_n N_g^{**,n} + w_{n-1}N_g^{n-1}\right) + \nabla \cdot (\boldsymbol{u}_g^{n+1}N_g^{n+1}) = \nabla \cdot \left(D_g^{n+1}\nabla N_g^{n+1}\right)$$

Or, using Eq. (4.4),

$$\frac{1}{\delta t}\left(w_{n+1}N_g^{n+1} - N_g^{**} + (1 + w_n)\, N_g^n + w_{n-1}N_g^{n-1}\right) + \nabla \cdot (\boldsymbol{u}_g^{n+1}N_g^{n+1}) = \nabla \cdot \left(D_g^{n+1}\nabla N_g^{n+1}\right)$$

This is Eq. (4.63) with no intergroup transfer or sources.

end for

$3/2$, $w_n = -2$ and $w_{n-1} = 1/2$) the intermediate stage reduces to $N_g^{**,n} = 1/2(N_g^{**} + N_g^n)$ and therefore the algebraic mean between N_g^{**} and N_g^n must be used in order to attain second order accuracy in time.

One main advantage of the time splitting procedure is that different couplings can be solved separately at each stage. In the entrainment stage the nonlinear dependence of the entrainment source with void fraction ($\Lambda(\alpha_d)$ in Eq. (3.102)) is solved. The intergroup transfer stage solves the coupling between sizes due to breakup, coalescence and dissolution. The transport stage solves the spatial coupling due to bubble transport by convection and due to turbulent dispersion

and packing. Therefore, in this time splitting strategy the problem is split in three parts where $\mathrm{N_{nod}}$ entrainment problems are solved (Section 4.7), $\mathrm{N_{nod}}$ intergroup transfer problems are solved each involving a $G \times G$ nonlinear system coupling, at each location, the G group sizes and finally, G transport problems are solved each involving an $\mathrm{N_{nod}}$ matrix system coupling each N_g in space (Sections 4.8 and 4.6).

4.2.3 Guaranteeing Mass Conservation

An additional advantage of the time splitting procedure is that, when solving the intergroup transfer pseudo-time step, the intergroup transfer coefficients for all groups at that location are available. This allows, if needed, to make corrections to these coefficients to ensure mass conservation of the dispersed phase. This is the case with the breakup terms in the discrete Boltzmann equation. The condition for the discrete daughter bubble size distribution $h_{g,g'}$ in Eq. (2.55) holds only if the integrations in Eq. (2.44) are performed exactly. However, these integrations are performed numerically using a midpoint rule to save computational time (since the midpoint rule only requires one evaluation of the integrand) and Eq. (2.44) does not hold any more due to the truncation error in the numerical integration. Therefore, mass is not preserved any longer. To fix this problem, and since all the coefficients $h_{g,g'}$ are available in the local intergroup solver, the discrete daughter bubble size distribution is renormalized to make it satisfy Eq. (2.55). Then, if the approximate daughter bubble size distribution $\tilde{h}_{g,g'}$ is defined as (*i.e.* by using the midpoint rule in Eq. (2.44))

$$\begin{aligned}\tilde{h}_{g,g'} &= a^-(m_{g-1/2}, m_g)h(m_{g-1/2}, m_{g'})\,(m_g - m_{g-1}) \\ &\quad + a^+(m_{g+1/2}, m_g)h(m_{g+1/2}, m_{g'})\,(m_{g+1} - m_g) \\ &= \frac{1}{2}h(m_{g-1/2}, m_{g'})\,(m_g - m_{g-1}) + \frac{1}{2}h(m_{g+1/2}, m_{g'})\,(m_{g+1} - m_g)\end{aligned} \tag{4.6}$$

where the last equality holds due to the fact that $a^-(m_{g-1/2}, m_g) = a^+(m_{g+1/2}, m_g) = 1/2$, the discrete daughter size distribution is computed as

$$h_{gg'} = m_{g'} \frac{\tilde{h}_{gg'}}{\sum_{k=1}^{g'} m_k \tilde{h}_{kg'}} \tag{4.7}$$

and therefore Eq. (2.55) holds and mass is preserved exactly.

4.2.4 Solving the Intergroup Transfer System

After an implicit Euler time marching scheme is used in Eq. (2.86), finding the solution at time t_{n+1} reduces to find the solution to the non-linear matrix system given by

$$\begin{aligned} &\mathbf{M}(\mathbf{N}^{n+1}) \cdot \mathbf{N}^{n+1} = \mathbf{R} \\ &\mathbf{M}(\mathbf{N}) = \frac{1}{\delta t}\mathbb{I} + \mathbf{D} - \mathbf{B} - \mathbf{C}(\mathbf{N}) \\ &\mathbf{R} = \frac{\mathbf{N}^{**}}{\delta t} \end{aligned} \tag{4.8}$$

This system is solved by applying a succession of backward and forward substitution stages. The matrix of the system $\mathbf{M}$ is updated after every backward and forward substitution stage inside a Picard iteration loop. This is shown in Procedure 4.2. After the backward and forward substitution stages, a convergence test is performed (against a predefined tolerance ε). If convergence is not reached the iteration ends at the maximum number of iterations MaxIters. This procedure is inspired by the fact that if only breakup (coalescence) is considered, the matrix $\mathbf{M}$ is upper (lower) triangular and it can be solved with only one backward (forward) substitution stage. Experience shows that, when considering breakup, coalescence and dissolution together, this procedure typically converges in about two iterations (using a convergence tolerance of $\varepsilon = 10^{-6}$), making it highly efficient.

Procedure 4.2 Solving the non-linear multigroup transfer system.

While:
Recompute $\mathbf{M} = \mathbf{M}(\mathbf{N}^{n+1,k-1})$
for $g = G$ **to** 1 **do**

$$N_g^{n+1,k} = \frac{1}{\mathbf{M}_{g,g}} \left(\mathbf{R}_g - \sum_{g'=g+1}^{G} \mathbf{M}(\mathbf{N}^{n+1,k-1})_{g,g'} N_{g'}^{n+1,k} \right)$$

end for
Recompute $\mathbf{M} = \mathbf{M}(\mathbf{N}^{n+1,k})$
for $g = 1$ **to** G **do**

$$N_g^{n+1,k+1} = \frac{1}{\mathbf{M}_{g,g}} \left(\mathbf{R}_g - \sum_{g'=1}^{g-1} \mathbf{M}(\mathbf{N}^{n+1,k})_{g,g'} N_{g'}^{n+1,k+1} \right)$$

end for
Compute error: $E^{k+1} = \max_{g=1...G} \left(\frac{N_g^{n+1,k+1} - N_g^{n+1,k}}{N_g^{n+1,k+1}} \right)$
if $E^{k+1} < \varepsilon \Rightarrow$ leave while
$k \leftarrow k + 2$
until $k <$ MaxIters

4.2.5 Full Dispersed Phase Solver

To finalize this section, Fig. 4.3 shows the flow chart of the dispersed phase solver implemented. This flow chart also shows how the dispersed phase momentum solver is integrated. Gas momentum equations are solved before the Boltzmann solver and involve the resolution of G matrix systems of $\mathrm{N_{nod}}$ unknowns each coupling velocities in space (Section 4.5). In addition, this schematic also shows that intergroup transfer by rectified diffusion is solved in a separate stage of the time splitting procedure.

4.3 Global Coupling Strategy

The time-splitting strategy presented in the previous section allows to solve the Boltzmann equation in space and separately in bubble sizes. In this way,

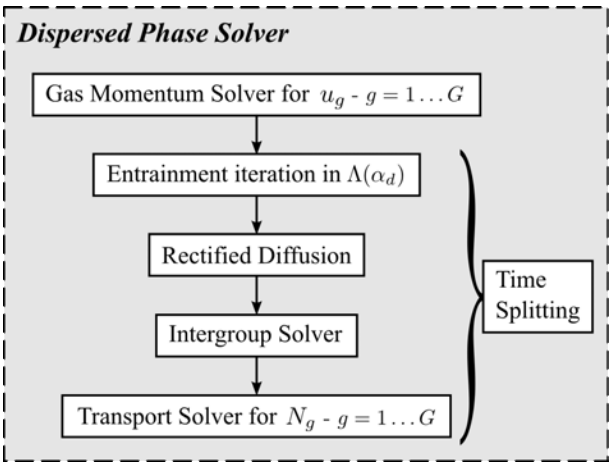

Figure 4.3: Dispersed phase solver. Time splitting allows to solve for each physics in a succession of separate steps.

numerical methods specific to each coupling (space and size) can be used and an excessive number of non-linear iterations can be avoided. It was also mentioned in the previous section that the solution of the continuous phase momentum and mass conservation equations can naturally be separated from the dispersed phase solution and coupled together inside a Picard iteration loop. The full coupling strategy used in CFDShip-Iowa V4.5 is shown in Fig. 4.4.

This is a modification to the procedure described in Huang et al. (2008) for the single-phase solver to include the dispersed bubbly phase. In CFDShip-Iowa V4.5, the fluid equations are solved at each time step inside a non-linear Picard iteration loop. The non-linear iterations loop runs with index n in Fig. 4.4. Inside this loop, each solver is called in sequence: the k-ω turbulence model equations are solved first, followed by the level set solver and finally the momentum and mass equations are solved together using a projection method (see Section 4.4). Additional calls to the 6DOF motions solver (Carrica et al., 2007a, 2010a) and SUGGAR (Noack, 2005) are performed to treat cases with predicted (and/or imposed) motions. The dispersed phase solver is included in this strategy as an additional block in this

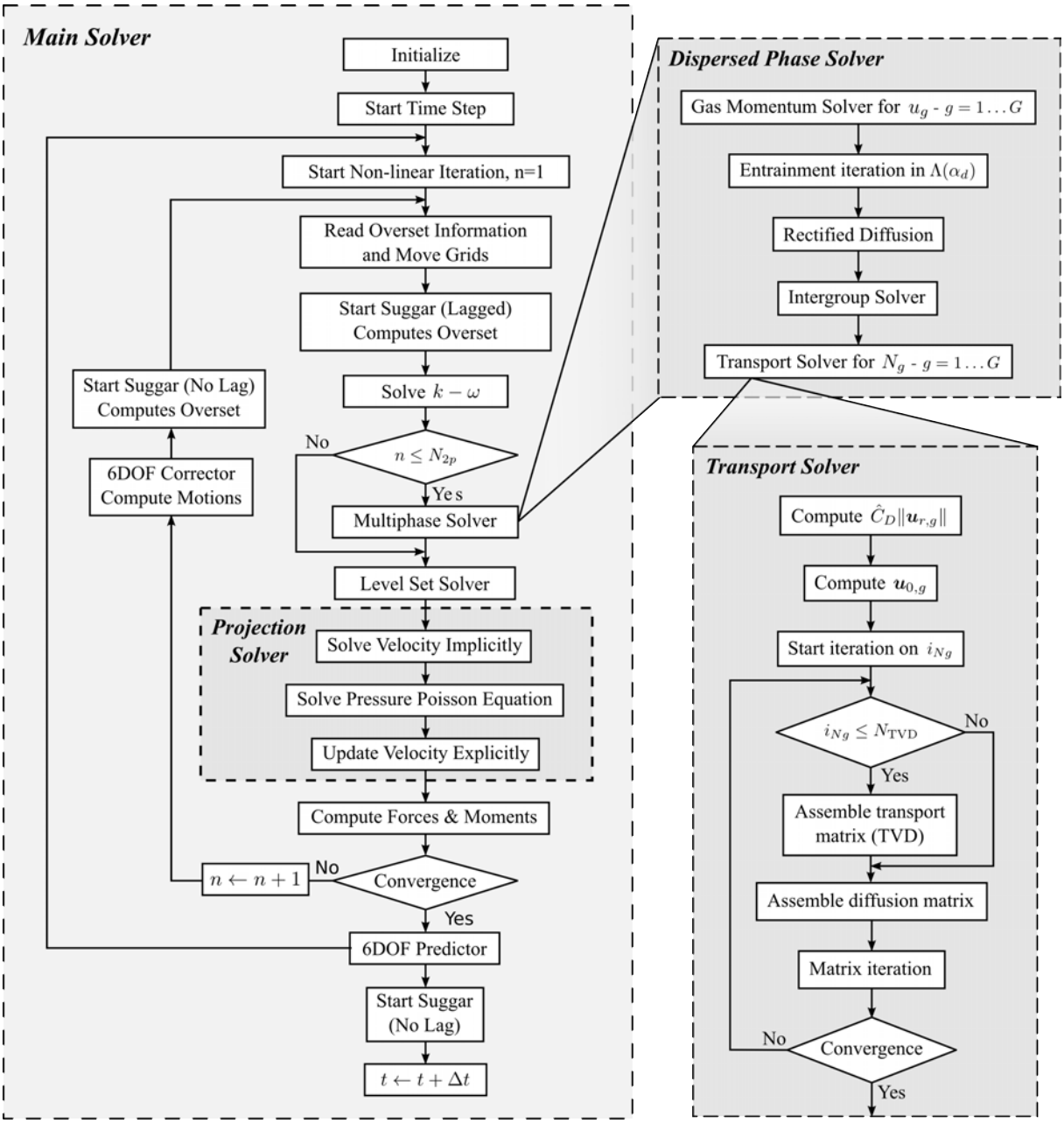

Figure 4.4: CFDShip-Iowa V4.5 flow chart showing how the multiphase capability is added to the main solver.

sequence of solvers' calls, as shown in Fig. 4.4. Since the dispersed phase solver is a very computationally intensive block in the overall multiphase solver, the number of times this is called inside the non-linear iteration loop is limited to N_{2p}. Typically,

$N_{2p} = 1$ is more than enough for most ship applications. However, the total void fraction α_d is computed in each non-linear iteration since pressure and void fraction are implicitly coupled in the projection block. The two-phase projection method shown in Fig. 4.4 is one of the contributions of this thesis and is described in Section 4.4. In the dispersed phase solver shown in Fig. 4.4 (shown separately in Fig. 4.3), the gas momentum equations for each group are solved first in sequence. After that, in a sequence of time-splitting stages (Section 4.2), entrainment (Section 4.7), rectified diffusion, transport (Section 4.6) and intergroup transfer (Section 4.2) are solved. The transport solver requires an additional iterative loop solving for the non-linear coupling introduced by the packing force introduced in Section 3.1.4. The iterative procedure used in the transport solver is included in Fig. 4.4 and is discussed in detail in Section 4.8.

The remainder of this chapter covers each of the separate blocks conforming the full polydispersed solver for bubbly flows.

4.4 Pressure-Velocity Coupling

The single phase version of CFDShip-Iowa V4.5 provides two pressure-velocity coupling schemes: PISO (Issa, 1986) and projection (Bell et al., 1991). In this work the projection method by Bell et al. (1991) is extended to two phase flows. Two schemes were developed and are referred as Scheme I and Scheme II. Scheme I was originally developed first and it is found to be unstable under certain conditions. Scheme II improves Scheme I by implicitly treating the existing coupling between pressure and void fraction (since the dispersed phase is compressible).

The next two sections derive these schemes in detail and a last section shows an example case where Scheme I is unstable while Scheme II is not.

4.4.1 Scheme I

Conservation of mass and momentum for the continuous phase in Equations (3.131) and (3.134) can be rewritten as

$$\frac{\partial \alpha_c \boldsymbol{u}_c}{\partial t} + \nabla \hat{p}_c = \boldsymbol{V}(\boldsymbol{u}_c, \alpha_c) \tag{4.9}$$

$$\begin{aligned} \boldsymbol{V}(\boldsymbol{u}_c, \alpha_c) = &- \nabla \cdot (\alpha_c \boldsymbol{u}_c \otimes \boldsymbol{u}_c) \\ &+ \nabla \cdot \left[2\alpha_c \left(\frac{1}{Re} + \nu_t \right) \nabla^s \boldsymbol{u}_c \right] + \frac{\alpha_d}{Fr^2} \left(1 - \pi_\rho \rho_d \right) \hat{k} \end{aligned} \tag{4.10}$$

$$\frac{\partial \alpha_c}{\partial t} + \nabla \cdot (\alpha_c \boldsymbol{u}_c) = 0 \tag{4.11}$$

First a velocity $\boldsymbol{u}_c^{*1}$ that does not satisfy the continuity equation is solved with an implicit time stepping scheme from Eq. (4.9)

$$\frac{1}{\delta t}(w_n \alpha_c^n \boldsymbol{u}_c^* + w_{n-1} \alpha_c^{n-1} \boldsymbol{u}_c^{n-1} + w_{n-2} \alpha_c^{n-2} \boldsymbol{u}_c^{n-2}) + \nabla \hat{p}_c^{n-1} = \boldsymbol{V}(\boldsymbol{u}_c^*, \alpha_c^n) \tag{4.12}$$

As described in Section 4.3 transport and intergroup transfer on the dispersed phase are solved before the continuous phase computations take place. Therefore, the void fraction at the current time step α_c^n in Eq. (4.12) is already available for use. The time derivative in Eq. (4.9) is discretized using the scheme in Eq. (4.3) where the weights w_n, w_{n-1} and w_{n-2} determine the time stepping scheme, one of Implicit Euler (IE, for which $w_n = 1$, $w_{n-1} = -1$ and $w_{n-2} = 0$) or second order backward difference formula (BDF2, for which $w_n = 3/2$, $w_{n-1} = -2$ and $w_{n-2} = 1/2$). In contrast to its approximation the desired velocity $\boldsymbol{u}_c^n$ at the time step n satisfies Eq. (4.12) but with pressure $\hat{p}_c^n$ instead of $\hat{p}_c^{n-1}$. The idea behind the projection method is to solve for velocity and pressure separately and then apply a correction to the velocity such that it satisfies mass conservation. This is accomplished by replacing

[1] The asterisk on the predicted velocity $\boldsymbol{u}_c^*$ should not be confused with the asterisk used on the dimensionless equations in Section 3.11

$\boldsymbol{u}_c^n$ in $\boldsymbol{V}(\boldsymbol{u}_c^n, \alpha_c)$ with $\boldsymbol{u}_c^*$ on the momentum equation for $\boldsymbol{u}_c^n$

$$\frac{1}{\delta t}(w_n \alpha_c^n \boldsymbol{u}_c^n + w_{n-1}\alpha_c^{n-1}\boldsymbol{u}_c^{n-1} + w_{n-2}\alpha_c^{n-2}\boldsymbol{u}_c^{n-2}) + \nabla \hat{p}_c^n = \boldsymbol{V}(\boldsymbol{u}_c^*, \alpha_c) \tag{4.13}$$

$\boldsymbol{V}(\boldsymbol{u}_c^*, \alpha_c)$ in Eq. (4.13) can be eliminated by using Eq. (4.12)

$$\frac{w_n}{\delta t}\alpha_c^n \boldsymbol{u}_c^n + \nabla \hat{p}_c^n = \boldsymbol{V}(\boldsymbol{u}_c^*, \alpha_c) - \frac{1}{\delta t}(w_{n-1}\alpha_c^{n-1}\boldsymbol{u}_c^{n-1} + w_{n-2}\alpha_c^{n-2}\boldsymbol{u}_c^{n-2}) = \hat{\boldsymbol{u}} \tag{4.14}$$

$$\hat{\boldsymbol{u}} = \nabla \hat{p}_c^{n-1} + \frac{w_n}{\delta t}\alpha_c^n \boldsymbol{u}_c^* \tag{4.15}$$

An equation for pressure is obtained by taking the divergence at both sides of Eq. (4.14) and using the mass conservation in Eq. (4.11). The result is

$$\nabla^2 \hat{p}_c^n = \nabla \cdot \hat{\boldsymbol{u}} + \frac{w_n}{\delta t} \left.\frac{\partial \alpha_c}{\partial t}\right|_{t=t_n} \tag{4.16}$$

where the partial derivative of the continuous phase void fraction with respect to time is approximated with a first order backward difference formula and an ALE[2] term is included in order to account for cases with moving meshes

$$\left.\frac{\partial \alpha_c}{\partial t}\right|_{t=t_n} = \frac{\alpha_c^n - \alpha_c^{n-1}}{\delta t} - \boldsymbol{w} \cdot \nabla \alpha_c^n \tag{4.17}$$

where $\boldsymbol{w}$ is the mesh velocity.

Once the pressure $\hat{p}_c^n$ is solved the velocity $\boldsymbol{u}_c^n$ can explicitly be updated from Eq. (4.15) as

$$\boldsymbol{u}_c^n = \frac{\delta t}{w_n\, \alpha_c^n}(\hat{\boldsymbol{u}} - \nabla \hat{p}_c^n) \tag{4.18}$$

In summary, the two-phase version of the projection method reads as

- Solve for a predicted velocity $\boldsymbol{u}_c^*$ using Eq. (4.12)

[2] ALE stands for Arbitrary Lagrangian Eulerian formulation.

- Compute $\hat{\boldsymbol{u}}$ with Eq. (4.15)
- Solve for the pressure $\hat{p}_c^n$ from Eq. (4.16)
- Explicitly compute $\boldsymbol{u}_c^n$, Eq. (4.18)

Scheme I shows to be stable for many practical cases. However, when the solution is highly unsteady the above scheme may fail. The key observation is to notice that even when the continuous phase is incompressible, the two-fluid model allows for the propagation of void fraction waves due to the compressibility of the dispersed phase (see Eq. (3.25)). The compressibility of the dispersed phase allows for changes in bubble size with pressure and thus in void fraction. These changes in void fraction are coupled to the continuous phase through the continuity equation Eq. (4.11). Therefore, the instability of Scheme I is due to the fact that these void fraction changes are essentially driven by pressure and they are fed back to the pressure by explicitly computing the time derivative of the void fraction on the right hand side of the pressure Poisson equation Eq. (4.16). In the following section a new scheme is developed where the void fraction time derivative in Eq. (4.16) is treated implicitly in order to solve this stability problem.

4.4.2 Scheme II

As described above, the instability of Scheme I is due to the explicit treatment of the functional dependence of the void fraction with pressure. Therefore, in Scheme II this problem is solved by implicitly coupling pressure with void fraction when solving the pressure Poisson equation. The result is a projection scheme for two-phase flows that not only couples velocity and pressure but also void fraction implicitly.

Having identified the functional dependence of void fraction with pressure, the key is to write its temporal derivative in terms of the pressure's time derivative and substitute it into Eq. (4.16).

If surface tension tension is neglected in Eq. (2.6), void fraction can be rewritten in terms of the mass density ε_m defined in Eq. (2.5) as

$$\alpha_d(\boldsymbol{r},t) = \int_0^\infty \mathrm{d}m \, \frac{m}{\rho_d(m,\boldsymbol{r},t)} f(m,\boldsymbol{r},t) \approx \frac{1}{\rho_d(\boldsymbol{r},t)} \int_0^\infty \mathrm{d}m \, m f(m,\boldsymbol{r},t) = \frac{\varepsilon_m}{\rho_d} \tag{4.19}$$

$$\varepsilon_m(\boldsymbol{r},t) = \int_0^\infty \mathrm{d}m \, m f(m,\boldsymbol{r},t) \tag{2.5}$$

Equation (4.19) shows that there will be two contributions to the time derivative of the void fraction. The first one is caused by changes in ε_m which are directly related to the number density distribution $f(m)$. Therefore, as the number density distribution is transported and changes due to intergroup transfer mechanisms the void fraction changes accordingly. The second contribution is the one responsible for the instability of Scheme I. This comes from the functional dependence of the gas density with total pressure as shown in Eq. (3.25). Neglecting surface tension in Eqs. (3.25) and (3.26) gas density and total pressure are computed as

$$\rho_d(\boldsymbol{r},t) = \rho_{d,0} \frac{p_c(\boldsymbol{r},t)}{p_0} \tag{4.20}$$

$$p_c(\boldsymbol{r},t) = p_0 + \hat{p}_c(\boldsymbol{r},t) - \rho_c \, g \, z \tag{4.21}$$

Taking the temporal derivative of the void fraction in Eq. (4.19) this is recast in terms of the temporal derivatives of the mass density ε_m and the gas density ρ_d as

$$\frac{\partial \alpha_d}{\partial t} = \frac{1}{\rho_d} \frac{\partial \varepsilon_m}{\partial t} - \frac{\varepsilon_m}{\rho_d^2} \frac{\partial \rho_d}{\partial t} = \frac{1}{\rho_d} \frac{\partial \varepsilon_m}{\partial t} - \frac{\alpha_d}{\rho_d} \frac{\partial \rho_d}{\partial t} \tag{4.22}$$

while the temporal derivative of the gas density can be recast in terms of the

temporal derivative of the piezometric pressure from Eqs. (4.20) and (4.21) as

$$\frac{\partial \rho_d}{\partial t} = \frac{\rho_d}{p_c}\frac{\partial \hat{p}_c}{\partial t} \tag{4.23}$$

Finally, the substitution of the gas density temporal derivative from Eq. (4.23) into Eq. (4.22) leads to the desired result

$$\frac{\partial \alpha_d}{\partial t} = \gamma - \beta\frac{\partial \hat{p}_c}{\partial t} \tag{4.24}$$

with

$$\beta = \frac{\alpha_d}{p_c} \tag{4.25}$$

$$\gamma = \frac{1}{\rho_d}\frac{\partial \varepsilon_m}{\partial t} \tag{4.26}$$

Note that β and γ are not constants but functions of space and time.

The void fraction time derivative in Eq. (4.16) can now be recast into a pressure time derivative using Eq. (4.24) and by noticing that $\partial\alpha_c/\partial t = -\partial\alpha_d/\partial t$. This leads to a new version of the pressure Poisson equation for two-phase flows where now the time derivative of the pressure is involved

$$\tilde{\beta}\ \left.\frac{\partial \hat{p}_c}{\partial t}\right|_{t=t_n} - \nabla^2 \hat{p}_c^n = S \tag{4.27}$$

where

$$\tilde{\beta} = \frac{w_n}{\delta t}\frac{\alpha_d^n}{p_c^{n-1}} \tag{4.28}$$

$$S = -\nabla\cdot\hat{\boldsymbol{u}} + \left.\frac{w_n}{\delta t\,\rho_d}\ \frac{\partial \varepsilon_m}{\partial t}\right|_{t=t_n} \tag{4.29}$$

The new temporal dependence in Eq. (4.27) is a result of the wave like nature

of the two-fluid model when the dispersed phase is compressible even when the continuous phase is not. In general, for the applications at hand and the time steps involved, void fraction waves are not resolved. However, if the numerical scheme does not offer a strong enough coupling to handle these waves it may become unstable as it occurs with Scheme I.

Equation (4.27) is solved in time by discretizing the pressure time derivative using a first order Euler scheme and by recalling that for problems involving moving meshes an ALE term must be added when computing time derivatives

$$\tilde{\beta}\,\frac{\hat{p}_c^n}{\delta t} - \nabla^2 \hat{p}_c^n = \tilde{\beta}\,\frac{\hat{p}_c^{n-1}}{\delta t} + \tilde{\beta}\,\boldsymbol{w}\cdot\nabla\hat{p}_c^{n-1} + S \tag{4.30}$$

$$S = -\nabla\cdot\hat{\boldsymbol{u}} + \frac{w_n}{\delta t\,\rho_d}\left(\frac{\varepsilon_m^n - \varepsilon_m^{n-1}}{\delta t} - \boldsymbol{w}\cdot\nabla\varepsilon_m^n\right) \tag{4.31}$$

Comparing with Eq. (4.16) the void fraction time derivative on the right hand side is now replaced by a mass density time derivative and the strong dependence of the void fraction with pressure is implicitly treated in the pressure time derivative. When discretizing Eq. (4.30) in space, the time derivative term adds a positive contribution to the diagonal elements of the matrix of the system and makes these equations more diagonally dominant and thus more stable. Since $\tilde{\beta} > 0$, this new term basically opposes to changes in pressure therefore stabilizing the system.

The full system of equations for the two-fluid model makes all variables to be coupled together with each other and therefore the mass density, as any other variable in the system, depends on the total pressure. However, mass density lacks the strong dependence with pressure present in the void fraction. The difference is that pressure is directly involved in the computation of the total void fraction when computing bubble volumes. Therefore, the explicit computation of the time derivative of the mass density on the right hand side of Eq. (4.30) does not introduce numerical instabilities as it occurs when computing the time derivative of the void

fraction on the right side of equation Eq. (4.16).

In summary, the new implicit two-phase projection method involves the following steps:

- Solve for a predicted velocity $\boldsymbol{u}_c^*$ using Eq. (4.12)
- Compute $\hat{\boldsymbol{u}}$ with Eq. (4.15)
- Solve for the pressure $\hat{p}_c^n$ from Eq. (4.30)
- Explicitly compute $\boldsymbol{u}_c^n$, Eq. (4.18)

Note that the only difference with Scheme I is in the pressure Poisson equation now involving the pressure time derivative. All other steps remain unchanged.

4.4.3 Example Case: Self-Propelled Athena with Heading Waves

This section presents an example case in which Scheme I fails while Scheme II is stable. In this example the bubbly flow around the self-propelled Athena is computed. For the particulars of the ship and details in the case setup the reader is referred to Chapter 6. In this section only a few details about the computation are given for the sake of completeness. The computations of the self-propelled Athena are performed on a mesh with 25 million grid points and is composed of 36 overset blocks, see Fig. 6.3. The time step is set to $\delta t = 3.3 \times 10^{-4}$ to accurately resolve the time scales introduced by the propeller. The case is assumed to have a symmetry along the half-plane of the ship and hence only half of the geometry is modeled. The grid system includes the fully appended Athena plus the rotating discretized propeller. The Reynolds and Froude numbers are $Re = 2.53 \times 10^8$ and $Fr = 0.252$ respectively. The simulation includes incoming waves of wave length $\lambda = 35.2$ m. Fifteen groups are used to discretize the Boltzmann equation in bubbles sizes with radii spanning from 10 μm to 4 mm on a logarithmically spaced stencil.

Figure 4.5 shows the results from these computations using the projection Schemes presented in this section. On top, Fig. 4.5a, the simulation results us-

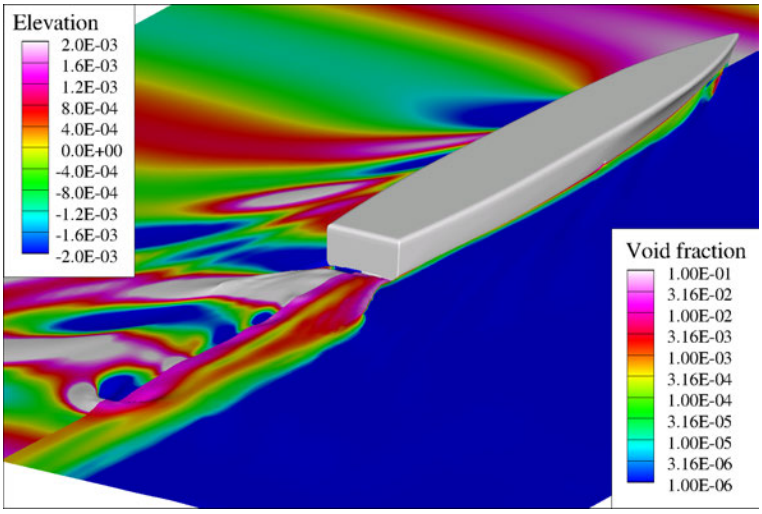

(a) Scheme I

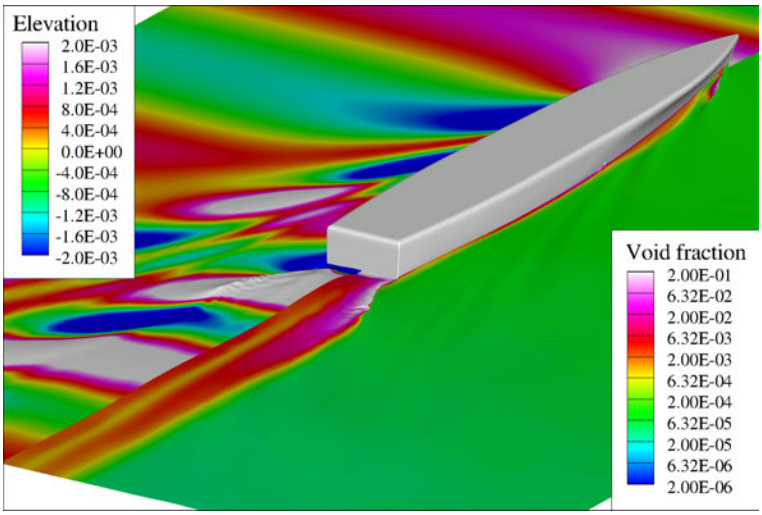

(b) Scheme II

Figure 4.5: Self-propelled Athena with heading waves.

ing Scheme I are shown. In this computation a non-physical wave is formed at the wake of the Athena. In this region the void fraction is larger than in the rest of the domain and Scheme I decouples pressure from void fraction. The computed pres-

sures have a very strong impact on the free surface elevations and these manifest as the very large and unphysical waves traveling downstream seen in Fig. 4.5a.

Figure 4.5b shows the computational results obtained using Scheme II. The spurious waves observed when using Scheme I are completely eliminated. It should be noticed that the void fraction scale in Fig. 4.5b is for larger void fractions than that in Fig. 4.5a. The reason for this is that the latest version of the code allows to handle much larger void fractions and the void fraction at the stern is matched with experimental data in the simulation run with Scheme II. In addition, the case shown in Fig. 4.5b is run with an oceanic background of bubbles (see Section 3.9) making the computation even a harder test for coupling Scheme II. This is why the free surface in Fig. 4.5b has a green color, corresponding to a void fraction of about 10^{-4} at the free surface.

4.5 Dispersed Phase Momentum Equation

The dispersed phase momentum equation is in general drag dominated, meaning that the most relevant interfacial momentum term is the drag force. Moreover, for ship applications, simulations are carried out with the ship immersed on a large enough background in order to impose incoming and outgoing flow boundary conditions. On a large region of this background the flow is nearly inviscid and the pressure field is close to hydrostatic. Inside this region, the gas relative velocity departs very little from the bubble terminal velocity and the gas velocity is simply the algebraic composition of this terminal velocity and the liquid velocity. Even when the group relative velocity may practically remain fixed to the terminal velocity for that group size, changes in the continuous phase velocity with time imply a change in the total gas velocity which is $\boldsymbol{u}_g = \boldsymbol{u}_c + \boldsymbol{u}_{r,g}$. Therefore, when solving Eq. (3.136) a few iterations are required to attain convergence even in simple cases where the relative velocity does not change in time. For this reason, the gas momentum equations are written in terms of the relative velocity $\boldsymbol{u}_{r,g}$ instead.

Doing so, the convergence to the solution of these equations is improved and the computational cost is reduced. Another advantage of solving the gas momentum equations in terms of the relative velocity is that, on solid boundaries, it is more natural to impose boundary conditions to the relative velocity $\boldsymbol{u}_{r,g}$ than to the total gas velocity $\boldsymbol{u}_g$. The adequate boundary conditions on a solid boundary for the gas relative velocity are

$$\begin{aligned} u_{r,n} &= \boldsymbol{u}_r \cdot \hat{n} = 0 \\ \frac{\partial \boldsymbol{u}_{r,t}}{\partial \hat{n}} &= 0 \end{aligned} \tag{4.32}$$

where $\hat{n}$ is the normal to the solid boundary. Hence, the normal component of the relative velocity, $u_{r,n}$, is zero and the gradient of the tangential relative velocity, $\boldsymbol{u}_{r,t}$, in the direction normal to the wall, is zero as well. The first condition imposes the physical requirement that bubbles cannot go through solid boundaries. Since the fluid velocity at a solid boundary is the wall velocity $\boldsymbol{u}_w$, this condition is equivalent to

$$u_{g,n} = \boldsymbol{u}_g \cdot \hat{n} = \boldsymbol{u}_w \cdot \hat{n} \tag{4.33}$$

The second boundary condition in Eq. (4.32) allows bubbles to have a non-zero slip velocity at the wall and is easily implemented when solving for the relative velocity $\boldsymbol{u}_r$. If the total gas velocity $\boldsymbol{u}_g$ is solved instead the above boundary condition would be

$$\frac{\partial \boldsymbol{u}_{g,t}}{\partial \hat{n}} = \frac{\partial \boldsymbol{u}_{c,t}}{\partial \hat{n}} \tag{4.34}$$

requiring this to compute the continuous phase velocity gradient at the wall and thus making the implementation more difficult.

It is for the aforementioned reasons that the disperse phase momentum equation in Eq. (3.136) is written in terms of the relative velocity. Making the formal change of variables $\boldsymbol{u}_g = \boldsymbol{u}_c + \boldsymbol{u}_{r,g}$ in Eq. (3.136) the equation for the relative velocity is

obtained as

$$C_{VM}\left(\frac{\partial \boldsymbol{u}_{r,g}}{\partial t}+\left(\boldsymbol{u}_g\cdot\nabla\right)\boldsymbol{u}_{r,g}\right)+\widehat{C}_{D,g}\left\|\boldsymbol{u}_{r,g}\right\|\boldsymbol{u}_{r,g}=-\nabla\hat{p}_c+g\left(1-\frac{\rho_g}{\rho_c}\right)\hat{k} \\ -C_{VM}\left(\boldsymbol{u}_{r,g}\cdot\nabla\right)\boldsymbol{u}_c-C_L\,\boldsymbol{u}_{r,g}\times\nabla\times\boldsymbol{u}_c-\nabla\sigma_P \tag{4.35}$$

where $\widehat{C}_{D,g}$ is defined as

$$\widehat{C}_{D,g}=\frac{3}{8}\frac{C_D(Re_g)}{R_g} \tag{4.36}$$

The resulting equation contains a convection term of the relative velocity $\boldsymbol{u}_{r,g}$ with the total gas velocity $\boldsymbol{u}_g$. Since, as mentioned above, this equation is drag dominated, a first order upwind scheme for the discretization of this convection term is considered to be accurate enough. For the same reason, an implicit Euler scheme is considered to be accurate enough to discretize the temporal derivative. In addition, the use of these first order schemes contributes to the robustness of the gas momentum solver. Equation 4.35 is written such that all the terms on the left hand side are assembled in a matrix and the terms on the right hand side are treated as sources. The spatial gradients on the right hand side of Eq. (4.35) are discretized using central differences. Equation (4.35) is highly non-linear due to the convection and drag terms coupling the components of the group-g velocity vector. A Picard iteration procedure is used to solve the non-linear system of equations resulting from the discretization of Eq. (4.35).

4.6 Number Density Transport

One of the time splitting stages is the transport of the group-g number densities according to the equation

$$\frac{\partial N_g}{\partial t}+\nabla\cdot\left(\boldsymbol{u}_g\,N_g\right)=\nabla\cdot\left(D_g\nabla N_g\right) \tag{4.37}$$

To avoid an excessive numerical diffusion of the computed solution, high or-

der convection schemes must be used to discretize the number density transport equation. However, classic high order linear schemes may introduce spurious oscillations (wiggles) at some locations in the domain and the solution may become negative. This poses a serious problem given that, since the group-g number density represents the number of bubbles per unit volume for a given group size, this quantity must remain positive throughout the computation. To avoid this problem, TVD (Total Variation Diminishing) convection schemes are used to transport the number densities. TVD schemes do not ensure the positiveness of the number densities in the general three-dimensional case, but they have proven to perform very well in this regard. To preserve the positiveness of the solution, TVD schemes introduce a non-linear dependence of the discretization coefficients with the computed solution. Therefore, even when the number density transport equation is linear in the convection term, its discretization using a TVD scheme leads to a non-linear system of equations. This forces to compute the matrix of the system in each non-linear iteration making its resolution more computationally demanding than when using linear schemes. This problem is treated in Section 4.8. The implementation of TVD schemes on non-orthogonal grids for CFDShip-Iowa V4.5 is discussed in Ismail et al. (2010). The temporal discretization the number density transport equations follows Eq. (4.3), allowing to selectively choose using either and implicit Euler (first order) or second order backward difference time stepping scheme.

4.6.1 Near Wall Integration

In simulations involving solid boundaries, grids are refined in the direction normal to the wall in order to accurately resolve the boundary layer velocity gradients occurring there. As an example, in the simulations of Athena presented in Chapter 6, even when wall functions are being used, grid spacing near the wall is about 94 μm. This length is very small when compared to the 47 m in length of

the ship. In wall bounded flows, bubbles tend to accumulate on the walls as they rise against them. The packing force presented in Section 3.1.4 attempts to account for this effect. However, since the volume of the cells close to a wall is so small, these cells may fill up with gas in only one single iteration of the number density transport solver. Then, the void fraction reaches levels larger than 100% causing the divergence of the multiphase solver. The original idea to solve this problem is to merge cells in the direction normal to the wall in order to end up with a larger volume cell that takes longer to be filled up with gas. Still, the equations for the continuous phase are solved in the original mesh. The implementation of this method in an overset code like CFDShip-Iowa V4.5 where one of the overset blocks might overlap on top of one of these enlarged elements becomes quite difficult. In addition, the number of cells to be merged may vary along a boundary layer as the refinement changes and this brings additional problems in the implementation since the stencil then changes as well. To solve this problem, a more suitable method for overset codes is devised that mimics the original idea of merging cells in the direction normal to the wall. The method consists in adding a large diffusivity in the region close to the wall into the diffusion term in Eq. (4.37). This diffusivity, however, must be anisotropic to only act in the direction normal to the wall. In this way, the number density is automatically averaged in the direction normal to the wall and since there is no diffusion in the tangential direction it has no effect on the tangential transport. Therefore, the diffusion coefficient in Eq. (4.37) is composed of three contributions in this work: the turbulent dispersion diffusivity ν_t/Sc_b (Section 3.1.4, Eq. (3.35)), the packing diffusivity D_g^p (Section 4.8) and the wall integration diffusivity D^W. An anisotropic diffusion in the direction normal to the wall can be described mathematically by using a diffusivity tensor $\mathbf{D}^W$ instead of a single scalar diffusivity D^W. Given the outgoing normal to the solid boundary $\hat{\boldsymbol{n}}_s$, this tensor is

written as $\mathbf{D}^W_{i,j} = D^W \hat{n}_{s,i} \hat{n}_{s,j}$. Then flux caused by this diffusivity is

$$\boldsymbol{F}^W_{g,i} = \mathbf{D}^W_{i,j} \frac{\partial N_g}{\partial x_j} = D^W \hat{n}_{s,i} \frac{\partial N_g}{\partial \hat{n}} \tag{4.38}$$

where the Einstein summation convention is used. In vectorial notation this is

$$\boldsymbol{F}^W_g = D^W \hat{\boldsymbol{n}}_s \frac{\partial N_g}{\partial \hat{n}} \tag{4.39}$$

and therefore this flux is in the direction of the normal to the wall only and is proportional to the gradient of the number density in the direction normal to the wall. This is the desired effect. If δ_w is the desired wall integration distance and d_w is the actual distance to the wall, the diffusivity D^W is set to a large number for $d_w < \delta_w$ and to zero for $d_w > \delta_w$. An almost zero number density gradient can be attained by using a sufficiently large diffusivity D^W. It should be noticed that since the diffusive term in Eq. (4.37) is conservative, the number of bubbles is automatically preserved under this wall integration procedure.

In CFDShip-Iowa V4.5 the governing equations are transformed from the physical domain in Cartesian coordinates (x, y, z) into the computational domain in non-orthogonal curvilinear coordinates (ξ, η, ζ) (Thompson et al., 1985). A partial transformation is used in which only the independent variables are transformed while the velocity vectors are left in the original Cartesian coordinates. In the computational domain the computational cells are cubic with sides of unit length. The generalized transformation is fully characterized by its metric, represented by the geometric coefficients b^j_i and the Jacobian of the transformation J. These are

defined in Thompson et al. (1985) as

$$b_l^i = \varepsilon_{l,m,n} \frac{\partial x_m}{\partial \xi_j} \frac{\partial x_n}{\partial \xi_k}, \quad \text{with } i, j, k \text{ running cyclically} \tag{4.40}$$

$$J = \begin{vmatrix} x_\xi & x_\eta & x_\zeta \\ y_\xi & y_\eta & y_\zeta \\ z_\xi & z_\eta & z_\zeta \end{vmatrix} \tag{4.41}$$

where once again the summation convection is used.

After the transformation to the general curvilinear coordinates (ξ, η, ζ) the diffusion term (with an isotropic diffusivity D^W to simplify the presentation) in Eq. (4.37) is written as

$$\nabla \cdot \left(D^W \nabla N_g \right) = \frac{1}{J} \frac{\partial}{\partial \xi_i} \left(D^W \, e^{i,j} \, \frac{\partial N_g}{\partial \xi_j} \right), \quad \text{with } e^{i,j} = \frac{b_k^i \, b_k^j}{J} \tag{4.42}$$

and therefore the contravariant diffusion flux in the ξ_i direction is

$$\breve{\boldsymbol{F}}_{g,i}^W = D^W \, e^{i,j} \, \frac{\partial N_g}{\partial \xi_j} \tag{4.43}$$

It should be kept in mind that the final objective of the normal wall diffusion is to average the number density in the direction normal to the wall, not to have a real normal diffusion. Therefore, and without any loss of generality, assuming that the wall is normal to the ξ_i direction, the contravariant flux in Eq. (4.43) is replaced by

$$\breve{\boldsymbol{F}}_{g,i}^W = D^W \, e^{i,i} \, \frac{\partial N_g}{\partial \xi_i} \tag{4.44}$$

where the summation convection is not used. In this way the diffusive flux only acts exactly in the direction normal to the wall and convection in the tangential

direction is not affected. As commented before, the wall integration diffusivity is non-zero only inside a layer of thickness δ_w close to the wall. In addition, it should be noticed that since diffusive fluxes are the same but with different signs for contiguous cells, the method is naturally conservative. For the simulations of Athena presented in Chapter 6 the wall integration thickness is set to be $\delta_w = 1.0\,\text{cm}$. This is a very small thickness when compared to Athena's length $L_0 = 47\,\text{m}$.

4.7 Air Entrainment Source Integration

The entrainment source must be integrated in time with care since, locally, it may reach high peaks in which, if treated explicitly, the dispersed phase void fraction may become higher than the critical void fraction α_{crit} in Eq. (3.108) or even higher than 100%.

In the time splitting strategy discussed in Section 4.2, the non-linear dependence of the entrainment source with void fraction can be solved locally for every point in the computational domain by considering the discrete transport equation for N_g when only the entrainment source is included. This equation is

$$\frac{\partial N_g}{\partial t} = S_g(\boldsymbol{r}, t) = S_0\, D_g^{\text{ent}}\, E(\boldsymbol{r}, t)\, \Lambda(\alpha_d) \tag{4.45}$$

An approximate time evolution equation for the void fraction α_d can be obtained by multiplying on both sides of Eq. (4.45) by the group-g bubble volume v_g and

summing over all groups. The result is

$$\begin{aligned}\sum_{g=1}^{G} v_g \frac{\partial N_g}{\partial t} \approx \frac{\partial \sum_{g=1}^{G} v_g N_g}{\partial t} = \frac{\partial \alpha_d}{\partial t} &= \sum_{g=1}^{G} v_g S_g \\ &= \sum_{g=1}^{G} v_g S_0 D_g^{\text{ent}} E(\boldsymbol{r}, t) \Lambda(\alpha_d) \\ &= S_0 E(\boldsymbol{r}, t) \Lambda(\alpha_d) \sum_{g=1}^{G} v_g D_g^{\text{ent}} \\ &= S_0 E(\boldsymbol{r}, t) \Lambda(\alpha_d) \bar{v}_{\text{ent}}\end{aligned} \tag{4.46}$$

where the mean entrained bubble volume $\bar{v}_{\text{ent}}$ is defined in Eq. (3.104). The approximation made in Eq. (4.46) is that changes in v_g with time can be neglected. Typically v_g changes with variations in pressure. To simplify notation, Eq. (4.46) is rewritten as

$$\frac{\partial \alpha_d}{\partial t} = \widetilde{S}(\boldsymbol{r}, t) \Lambda(\alpha_d) \tag{4.47}$$

with

$$\widetilde{S}(\boldsymbol{r}, t) = S_0 \bar{v}_{\text{ent}} E(\boldsymbol{r}, t) \tag{4.48}$$

Consider the situation depicted in Fig. 4.6. In this figure the solid line represents

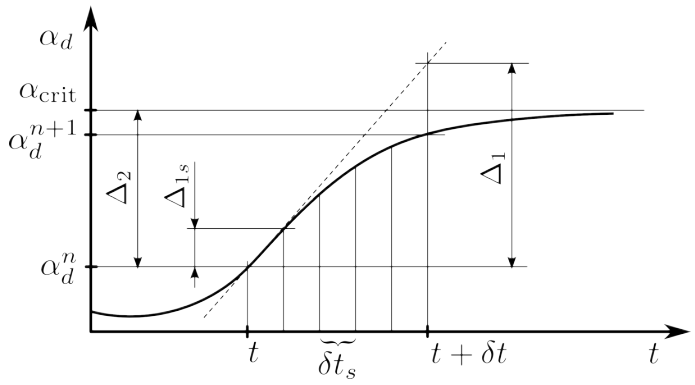

Figure 4.6: Entrainment source integration from t_n to t_{n+1}.

the solution to Eq. (4.47) if this is solved exactly. Since the functional dependence in $\Lambda(\alpha_d)$ makes the entrainment source to decrease to zero as the void fraction approaches α_{crit}, the void fraction approaches α_{crit} asymptotically and it never passes it. The dashed line is tangent to the solid curve at $t = t_n$ and represents the solution that would be obtained with an explicit Euler scheme. The situation in Fig. 4.6 is the one that the method in this chapter tries to avoid: void fraction going beyond α_{crit} (or even beyond 100%) due to an explicit treatment of the entrainment source dependence with void fraction.

Equation 4.47 can be solved with an implicit Euler scheme using any iterative scheme. In this work, the non-linear coupling in Eq. (4.47) is solved using a sub-time stepping approach. The idea is sketched in Fig. 4.6. This method simply uses a time step δt_s smaller than the time step δt used for the complete simulation. In this section, a method devised to compute an appropriate sub-time step δt_s is described. Figure 4.6 shows several variations (Δ's) in void fraction. Δ_1 is the void fraction change that is obtained using and explicit Euler scheme. This is

$$\Delta_1 = \delta t \, \widetilde{S} \, \Lambda(\alpha_d^n) \tag{4.49}$$

Δ_2 is the maximum variation that void fraction can undergo in the current time step

$$\Delta_2 = \alpha_{\text{crit}} - \alpha_d^n \tag{4.50}$$

Finally, Δ_{1s} is a *desired* maximum variation in void fraction in one sub-time step of duration δt_s.

In the method presented in this work, the desired variation in void fraction Δ_{1s} is set to be a fraction of the maximum possible variation Δ_2. Then

$$\Delta_{1s} = \frac{\Delta_2}{n_1} \tag{4.51}$$

where n_1 is a fixed parameter of the integration method. A smaller n_1 results in a more accurate integration but more expensive computationally since more sub-time steps are needed. In this work this is set to be $n_1 = 10$. On the other hand, the desired variation at time $t = t_n$ can be computed as

$$\Delta_{1s} = \delta t_s \widetilde{S}\, \Lambda(\alpha_d^n) \tag{4.52}$$

where the sub-time step δt_s is a fraction of the time step δt, *i.e.* $\delta t_s = \delta t / n_s$. Equations (4.51) and (4.52) can be made to be equal to find

$$\frac{\Delta_2}{n_1} = \frac{\delta t}{n_s} \widetilde{S}\, \Lambda(\alpha_d^n) = \frac{\Delta_1}{n_s} \tag{4.53}$$

from where the number of sub-time steps is obtained as

$$n_s = n_1 \frac{\Delta_1}{\Delta_2} \tag{4.54}$$

In a computer implementation, the number of sub-time steps n_s is cast to an integer. In regions of low entrainment, it may occur that this number is zero since no sub-time steps are required to accurately integrate the entrainment source and the time step δt is enough. To avoid having $n_s = 0$ Eq. (4.54) is changed to

$$n_s = n_1 \frac{\Delta_1}{\Delta_2} + 1 \tag{4.55}$$

where the final result stored in n_s is cast to an integer.

Once the number of sub-time steps n_s is found, Eq. (4.45) is integrated using an explicit Euler scheme with a time step δt_s and updating the void fraction at each sub-time step. This procedure is carried out for every point in the computational domain separately. Procedure 4.3 below summarizes the method

Procedure 4.3 Integration of the entrainment source.

for $i_{\text{nod}} = 1$ **to** N_{nod} **do**

Compute n_s and δt_s, Eq. (4.55)

for $i_s = 1$ **to** n_s **do**

$$N_g^{n+i_s/n_s} = N_g^{n+(i_s-1)/n_s} + \delta t_s \, S_0 \, D_g^{\text{ent}} \, E(\boldsymbol{r}, t_{n+1}) \, \Lambda(\alpha_d^{n+(i_s-1)/n_s})$$

$$N_g^{n+(i_s-1)/n_s} = N_g^{n+i_s/n_s}$$

Compute void fraction $\alpha_d^{n+i_s/n_s}$

end for

end for

4.8 Treatment of Forces with Number Density Gradients

Some of the interfacial forces in the two-fluid model are proportional to the spatial gradient of the group-g number density or to the gradient of the dispersed phase void fraction. For instance, if the model of Carrica et al. (1999) in Eq. (3.32) is used for the turbulent dispersion force, this is

$$\boldsymbol{M}_g^{TD} = -\rho_c \alpha_g \frac{3}{8} \frac{C_D \|\boldsymbol{u}_{r,g}\|}{R_g} \frac{\nu_t}{Sc_b} \frac{\nabla N_g}{N_g} \tag{3.32}$$

Another example is the packing force in Eq. (3.37) which can be written as

$$\boldsymbol{M}_g^P = -\alpha_g \nabla \sigma_P(\alpha_d) = -\alpha_g \, \beta(\alpha_d) \, \nabla \alpha_d, \quad \text{with } \beta(\alpha_d) = \frac{d\sigma}{d\alpha_d} \tag{4.56}$$

Since these forces depend on the number density, ideally, number density and gas velocity must be solved together inside an iterative loop until convergence is attained. However, it is found that even when iterations are performed, the number density decouples from the gas velocity and eventually the system diverges. The

reason for this instability is that small perturbations in the number density are significantly amplified by the gradient operation. These amplified perturbations are introduced into the gas momentum equations through the interfacial forces resulting in a transport velocity containing some level of perturbation as well. When this velocity is fed back into the transport equation for the number density, these perturbations amplify even further. This feedback continues until the final divergence of the system. In this section a numerical method that avoids this decoupling of the number density from the gas velocity is devised.

Using Eq. (2.27) and neglecting the gradient of the bubble volume, the packing force can be written as

$$\boldsymbol{M}_g^P = -\beta \sum_{g=1}^{G} v_g \nabla N_g, \quad v_g = \frac{m_g}{\rho_g(\mathbf{r}, t)} \tag{4.57}$$

This force can be bundled together with the turbulent dispersion force in one single gradient term by defining an effective diffusivity D_g as

$$\boldsymbol{M}_g^G = \boldsymbol{M}_g^{TD} + \boldsymbol{M}_g^P = -\widehat{C}_{D,g} \left\| \boldsymbol{u}_{r,g} \right\| D_g \frac{\nabla N_g}{N_g} - \beta \sum_{g' \neq g} V_{g'} \nabla N_{g'} \tag{4.58}$$

$$D_g = \frac{\nu_t}{Sc_b} + D_g^P \tag{4.59}$$

$$D_g^P = \frac{\beta \alpha_g}{\widehat{C}_{D,g} \left\| \boldsymbol{u}_{r,g} \right\|} \tag{4.60}$$

The key of the method proposed in this section is to realize that, by looking at Eq. (4.58), perturbations in the group-g velocity are introduced by perturbations in the number density gradient through the term $-D_g \nabla N_g / N_g$. Note that this term has units of velocity. With this idea in mind, a new pseudo velocity is defined by subtracting this term from the resulting group-g velocity. This velocity is defined

for each group as

$$\boldsymbol{u}_{0,g} = \boldsymbol{u}_g + D_g \frac{\nabla N_g}{N_g} \tag{4.61}$$

Consider the more general case in which turbulent dispersion is modeled as an additional interfacial force in the group-g momentum equation. In this case the transport equation for N_g is purely convective

$$\frac{\partial N_g}{\partial t} + \nabla \cdot \left(\boldsymbol{u}_g N_g \right) = 0 \tag{4.62}$$

Using the pseudo velocity defined in Eq. (4.61) into Eq. (4.62) the following equation results

$$\frac{\partial N_g}{\partial t} + \nabla \cdot \left(\boldsymbol{u}_{0,g} N_g \right) = \nabla \cdot \left(D_g \nabla N_g \right) \tag{4.63}$$

In this way the unstabilizing gradient term in the interfacial force is introduced into a very stabilizing diffusion term for the number density equation. The algorithm, referred herein as *pseudo transport velocity scheme* (STV), can be summarized as follows

- Solve for $\boldsymbol{u}_g$ from the original momentum equation in Eq. (4.35).
- Compute the pseudo velocity $\boldsymbol{u}_{0,g}$ from Eq. (4.61).
- Compute the total diffusivity D_g from Eq. (4.59).
- Solve for the number density N_g using the modified transport equation in Eq. (4.63).

Picard iterations may be applied over this procedure to attain convergence. It is very important to notice that the mathematical model is not changed, only the way in which the equations are solved is changed. Also notice that the group-g momentum equation remains the same.

4.8.1 1D Test Case

In order to test the new scheme a problem in which bubbles are transported towards a wall and let accumulate was solved. This is a 1D problem that can be enunciated as follows

$$\frac{\partial \alpha}{\partial t} + \frac{\partial}{\partial x}(u\alpha) = 0$$
$$C_D\, u = g - \frac{d\sigma}{dx}, \quad C_D = 1,\, g = 1$$
$$\alpha = 0, \quad \text{at } x = 0$$
$$\frac{\partial \alpha}{\partial x} = 0, \quad \text{at } x = 1$$
$$u = 0, \quad \text{at } x = 0$$
$$\alpha = 0.2, \quad \text{at } t = 0$$

The collision pressure used in this example is

$$\sigma(\alpha) = \frac{\alpha_c}{\alpha_c - \alpha} \tag{4.64}$$

with $\alpha_c = 0.74$.

To differentiate it from the STV scheme proposed in this section, the approach of solving the group-g velocity and using it directly to transport the corresponding number density is referred as *classic transport scheme* (CT).

Then, given an initially uniform distribution of bubbles, these are convected in the direction of increasing x until they find a wall at $x = 1$. There are no bubbles coming into the domain at $x = 0$ since the dispersed phase velocity and the void fraction are set to be zero as boundary conditions. The initial population of bubbles is transported to the right and ultimately accumulates at the wall. This problem is solved with a simple first order upwind scheme in space and an implicit Euler scheme in time, which is enough for the purposes of testing the new numerical

scheme. The problem was then solved with the CT and STV schemes.

Figure 4.7 shows the computed solution when using the classic scheme for several temporal instances. It is observed that the computed solution is not smooth and becomes unstable in an early stage before accumulation at the wall. The time step used is $\delta t = 5 \times 10^{-4}$ and the mesh size is $h = 0.01$ resulting in a Courant number of $C = 0.05$. Figure 4.8 shows the solution when computed with the STV

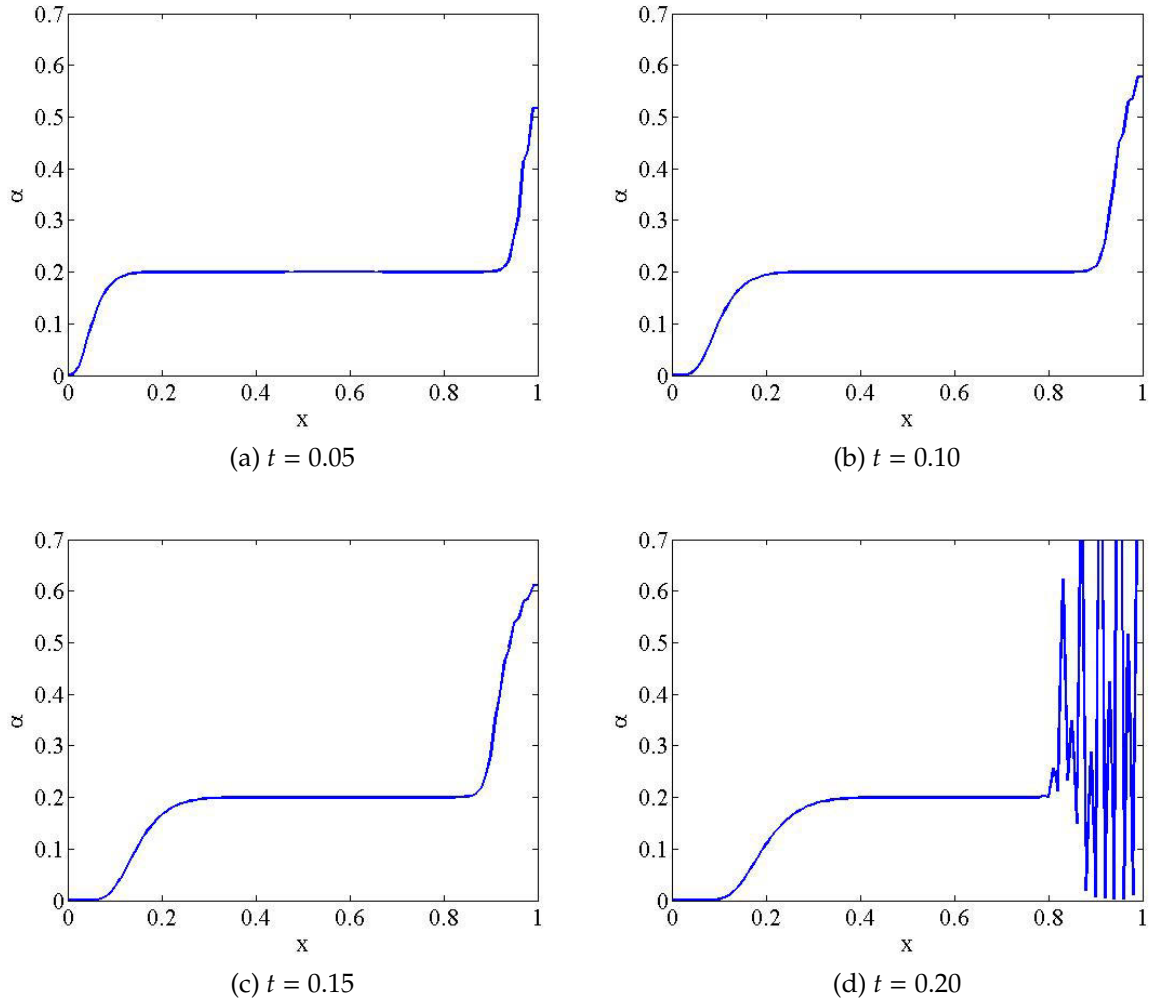

(a) $t = 0.05$ (b) $t = 0.10$

(c) $t = 0.15$ (d) $t = 0.20$

Figure 4.7: Time evolution of the solution computed with the CT scheme

scheme. This solution is smooth for all times and reaches the steady state without any instability. The time step used is $\delta t = 0.01$ and the mesh size is $h = 0.001$ resulting in a Courant number of $C = 10$. The reader should notice the large

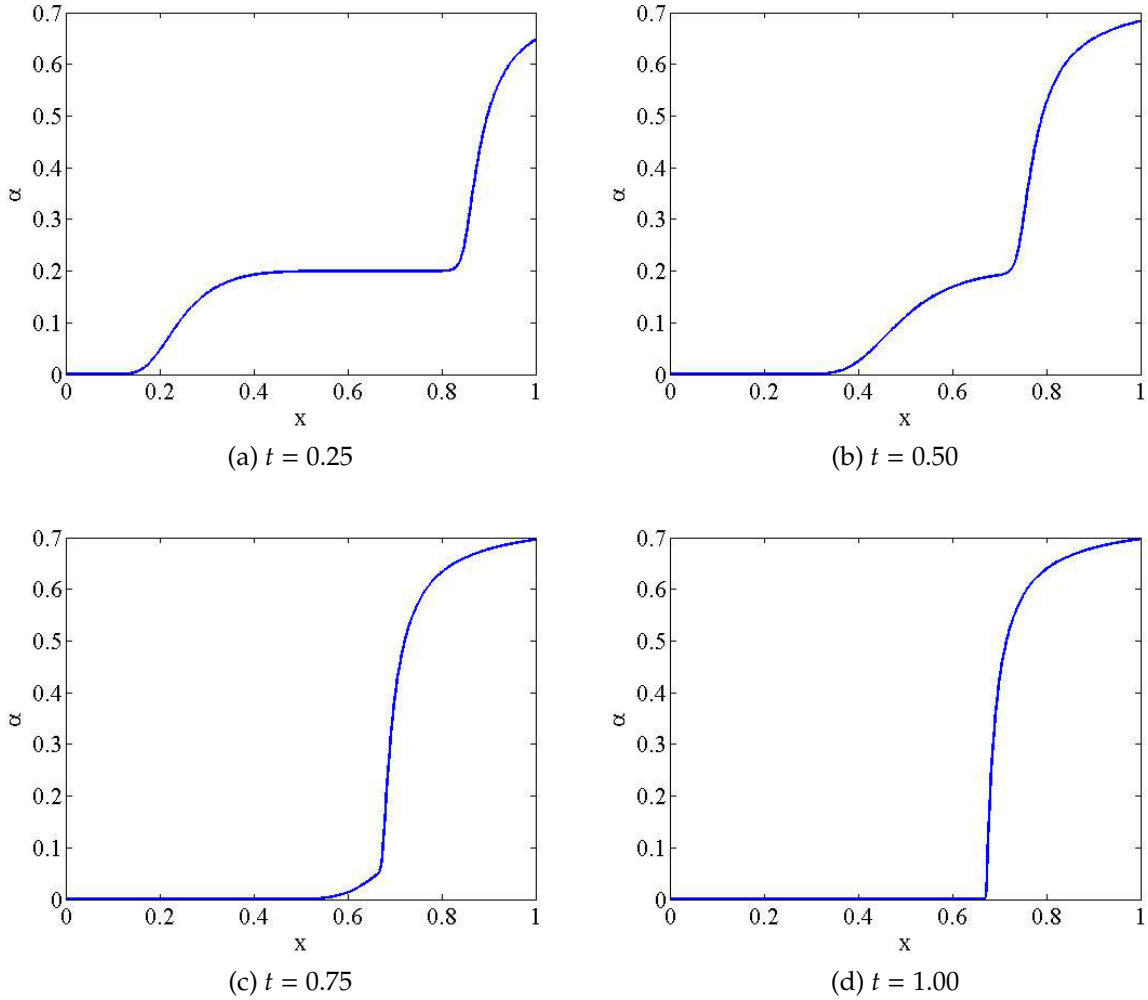

(a) $t = 0.25$ (b) $t = 0.50$

(c) $t = 0.75$ (d) $t = 1.00$

Figure 4.8: Time evolution of the solution computed with the STV scheme

difference in Courant numbers for the two cases. Even when the Courant number is as small as 0.05 the CT scheme is unstable while the STV scheme allows for very large Courant numbers without showing any instability.

4.8.2 Implementation in CFDShip-Iowa V4.5

Since the packing force couples both, the group-g velocity and the group-g number density, for all groups, the corresponding gas momentum and number density transport equations should be solved inside an iterative procedure until convergence is reached. This procedure would require not only to iterate in the number density transport equations but also in the gas momentum equations simultaneously and for all groups. The computational cost for such an approach is prohibitive for the applications presented in this thesis and an alternative iterative scheme must be devised. To lower the computational cost the number of floating point operations needs to be reduced. However, the final coupling must be strong enough to ensure the system of equations stability. The method presented in this work proposes to compute the group-g velocities only once. However, the packing diffusivity D_g^p is iterated inside the number density transport solver to ensure the stabilizing effect it has in the STV scheme on the packing force. The group-g momentum equations have a slower dynamics and as long as the number density profiles are smooth and well converged, they do not offer additional difficulties.

The transport solver implemented in CFDShip-Iowa V4.5 is sketched in Fig. 4.9. According to Eq. (4.60), D_g^p depends on the dispersed phase void fraction α_d trough the functional form in $\beta(\alpha_d)$, on the group-g void fraction α_g and on the product $\widehat{C}_{D,g} \left\| \boldsymbol{u}_{r,g} \right\|$. This last product remains constant once the group-g velocities are computed. Therefore, this is computed first in Fig. 4.9 before the transport solver starts iterating (loop on i_{N_g}). Since the group-g velocity $\boldsymbol{u}_g$ is kept constant inside the transport solver main loop, the group-g pseudo velocity $\boldsymbol{u}_{0,g}$ must be computed outside the iteration loop as well in order to use a consistent number density gradient in Eq. (4.61) with the one used to compute the original velocity $\boldsymbol{u}_g$. Therefore, in Fig. 4.9, the pseudo velocity $\boldsymbol{u}_{0,g}$ is computed outside the main iteration loop. Updating the pseudo velocity inside the iteration loop leads to an

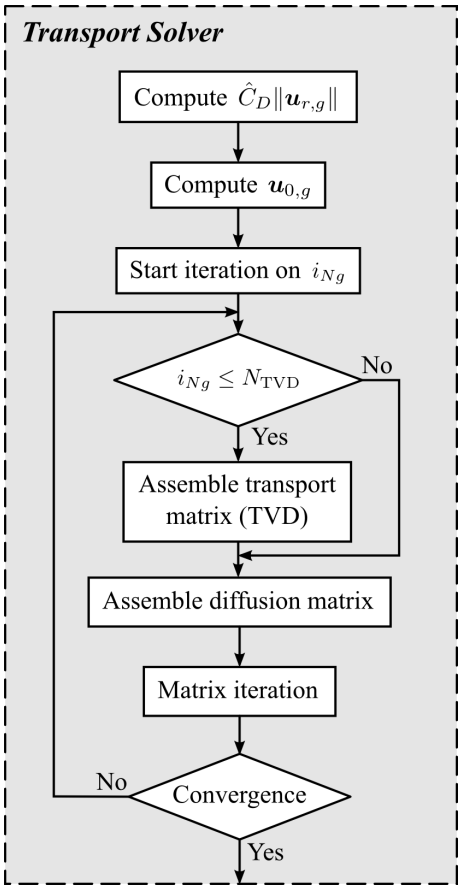

Figure 4.9: Iterative scheme for the number density transport as implemented in CFDShip-Iowa V4.5.

unstable scheme. Inside the iteration loop the matrix of the system is computed as two separate components: the transport term (discretized by TVD) and the diffusive term. The diffusive part of the matrix is assembled every time since D_g^P is updated as the computation evolves. The transport component of the matrix is non-linear since TVD schemes are used. However, it was found that the number of times the TVD matrix is computed can be limited to reduce the computational cost without appreciably affecting the TVD transport scheme properties. Actually, in all computations performed in Chapter 6 $N_{\mathrm{TVD}} = 1$ and no differences were noted in comparison with fully iterated matrices. This is due to the fact that for the small time steps used in the computations the solution at t_n is a good approximation to

compute the TVD matrix at t_{n+1}. The maximum number of TVD matrix evaluations N_{TVD} might need to be changed for larger time steps. Finally, once the matrix is assembled, an ADI-like iteration for all three spatial directions is performed. The iteration continues until convergence is attained.

CHAPTER 5
POLYDISPERSED MODEL VALIDATION

One of the main objectives of this chapter is to perform a validation of the implemented polydispersed model for bubbly flows. In addition, the problems solved in this section provide of some insight that help to understand the physics involved in polydispersed bubbly flows. Not only size distributions are studied but also budget analyses are performed as well, to help understand how breakup and coalescence balance each other. The study is complemented with the analysis of breakup and coalescence frequencies (introduced in Eqs. (2.99) and (2.100)). Overall, this study tells about the numbers involved, orders of magnitude, and provides an excellent exercise for the modeler looking to get familiar with the physics of the problem.

The full model for polydispersed bubbly flows, presented throughout Chapters 2, 3 and 4, basically has two fundamental components: A Boltzmann equation solver that solves for the number density distribution function $f(m, \boldsymbol{r}, t)$ and a modified CFD solver for the continuous phase that accounts for the presence of a dispersed phase, the bubbles. This chapter validates the Boltzmann solver.

The validation is twofold. It validates not only the physics introduced by the breakup and coalescence kernels presented in Sections 3.2 and 3.3 but also the correct implementation of the multigroup solver. Comparisons are performed not only against experimental data but also against computations previously performed by other authors. In addition to this validation, this chapter presents a comparative study of the breakup and coalescence models presented in Sections 3.2 and 3.3. The results from this comparison are later on used to decide what kernels to use in future simulations. Finally, it is shown that for salt water the solution depends on the initial conditions, a problem not observed in simulations for fresh water.

5.1 Study Case

The ideal physical situation that would allow to perform this validation would be that of a box with an homogeneous and steady turbulent field that perfectly mixes a given initial population of bubbles and with zero mean velocities. Given that the bubbles are kept under continuous motion and mixing by this turbulent field, they eventually distribute uniformly across the box and the number density distribution results to be independent of the spatial coordinates. If this initial population of bubbles is left to evolve in this turbulent field for long enough eventually breakup and coalescence reach a steady state in which the number density distribution does not change in time.

In order to simulate this ideal box is not necessary to solve for the continuous phase since it is known a priory that the continuous phase velocity is zero. If for this ideal experiment turbulent dissipation is available then the equations of the turbulence model do not need to be solved either since turbulence dissipation can be specified as a constant parameter. Then, the only equation that needs to be solved is the Boltzmann equation but only in the bubble size since the homogeneity of the problem eliminates the spatial dependence of the solution.

Therefore, this problem is fully specified by providing: the components of the two-phase mixture, the turbulence dissipation ε, which for this problem fully specifies the turbulent field[1], and the initial number density distribution. By specifying the initial number density distribution, the void fraction is automatically specified as well.

Such ideal experimental conditions do not exist in practice though certain experimental configurations can provide of a close enough approximation. One of these configurations is a stirred reactor. A stirred reactor consists of a vessel containing

[1]This is not entirely true since a second parameter needs to be specified in order to describe a homogeneous turbulent field with a two-equation model. Why the current models for breakup and coalescence do not need the specification of this second parameter is discussed in Section 6.4.3.

a main fluid continuously agitated by a rotating turbine. Bubbles are introduced into the vessel by means of some sort of sparger. Depending on the relative size between the turbine diameter and the vessel cross section some areas of the reactor can be considered homogeneous and in local equilibrium. Configurations of this type are used in the experiments by Alves et al. (2002), Hu et al. (2005) and Laakkonen et al. (2005) to cite just a few.

Another popular configuration is the bubble column. In a bubble column bubbles are introduced at the bottom of a column containing a main fluid with the aid of a sparger. There are no active elements as it is the case with stirred reactors but the buoyant action of the bubbles cause the circulation of the main fluid. An additional forced circulation of the main fluid may be induced with the aid of an external pump. Bubble columns are used in the experiments by Grienberger (1992),Wang et al. (2001) and Colella et al. (1999) to mention some examples. The flow in a bubble column is typically inhomogeneous. However, if the turbulent mixing is strong enough, homogeneity could be assumed along the column's cross section. In addition, equilibrium between breakup and coalescence could be attained at a certain height of the bubble column after the bubbles traveled a certain distance upwards. This situation is clearly illustrated in the experimental data by Wang et al. (2001). Under these conditions, the experiment approximates the bubbly flow in the steady homogeneous box.

In this work the experimental data by Grienberger (1992) is used to validate the polydispersed model presented in this thesis. This work is chosen not only because it provides a good data set for validation, but also because other authors (see Lehr et al., 2002; Wang et al., 2005a; Bayraktar et al., 2011) have used this experimental work to validate their own models and implementations. Therefore, in this thesis comparisons are made not only against the experimental data by Grienberger (1992) but also against the numerical results reported in Lehr et al. (2002) and Wang

et al. (2005a). Comparisons against the numerical results presented in Bayraktar et al. (2011) are not performed since this work became available on-line after the validation in this thesis was performed.

In the work by Lehr et al. (2002), new breakup and coalescence models are proposed and the experimental data set from Grienberger (1992) is used to validate them. These models were already introduced in Sections 3.3.1.1 and 3.2.2. As in this thesis, the Boltzmann equation is used to describe the polydispersed bubbly flow but, instead of using a multigroup approach to discretize it, a different numerical approximation is proposed in which a lognormal size distribution is assumed for small bubbles and an exponential tail is assumed for large bubbles. In their work the dissipation rate is estimated as the ratio of the energy introduced by the buoyant gas and the mass of the liquid phase in the bubble column

$$\varepsilon = \frac{j_g g \rho_c (1 - \alpha_d)}{\rho_c (1 - \alpha_d)} = j_g g \tag{5.1}$$

where j_g denotes the superficial gas velocity which is a quantity available from the experiments and g is the acceleration of gravity.

Similarly, in Wang et al. (2005a) the authors compare several models for breakup and coalescence including the models by Lehr et al. (2002) and Luo and Svendsen (1996a) and their own (Wang et al., 2003, 2005b) against the experimental data from Grienberger (1992). Wang et al. use, as in this thesis, the fixed pivot method developed by Kumar and Ramkrishna (1996) to solve the Boltzmann equation in the bubble sizes. The turbulence dissipation rate used in their work was obtained from a CFD simulation of the bubble column and size distributions are reported for the values of dissipation and void fraction computed at radial positions $r/R = 0$ and $r/R = 0.5$ with R the bubble column radius. In this work the data at $r/R = 0$ is used for comparison since their simulations provide almost indistinguishable

profiles at these two locations.

Table 5.1 summarizes the values of turbulence dissipation and void fraction for the cases considered. There are two experimental conditions, cases A and B. In addition, different estimations for ε and α_d are considered by Lehr et al. and by Wang et al., resulting in a total of four set of simulations.

Table 5.1: Values of turbulence dissipation and void fraction for the four validation cases

		ε [m^2/s^3]	α_d [−]
Lehr	Case A	0.785	0.2
	Case B	0.196	0.08
Wang	Case A	1.35	0.33
	Case B	0.232	0.095

It should be mentioned that dissolution is not included in any of the simulations presented in this chapter and thus the original mass prescribed with the initial condition is conserved. This fact was verified to be true in all of the simulations performed.

5.2 Convergence Study

In order to assess the number of groups to be used in the comparisons against the available experimental data and simulations from other authors, a convergence study is first performed. Moreover, this convergence study gives a first approximation on the number of groups to be used in polydispersed simulations.

The convergence study is performed on case B using the parameters used by Lehr et al. *i.e.* $\varepsilon = 0.196$ and $\alpha_d = 0.08$. Both breakup and coalescence models from

Lehr et al. (2002) are used. The minimum and maximum bubble sizes adopted are $R_1 = 0.05$ mm and $R_G = 12.0$ mm, respectively. Simulations are run with 11, 21, 41 and 61 group sizes uniformly discretizing the radius coordinate. The reader should recall from Section 2.2 that in this work the Boltzmann equation is discretized in the bubble mass. Therefore, while the discretization is uniform in the bubble radius, it is not in the bubble mass. The time step used in the simulations is $\delta t = 0.01$ sec. The convergence of the time marching scheme was not studied since a steady state solution was pursued. However, the time step is chosen to accurately resolve the evolution with time of the Sauter diameter and total number density. At time $t = 0$ a monodispersed size distribution with bubbles of radius $R = 6.025$ mm is imposed (this is $N_g = \alpha_d / m_g$ for $g = G/2 + 1$ and zero everywhere else).

Figure 5.1 shows the size distributions obtained using different grid sizes. Size

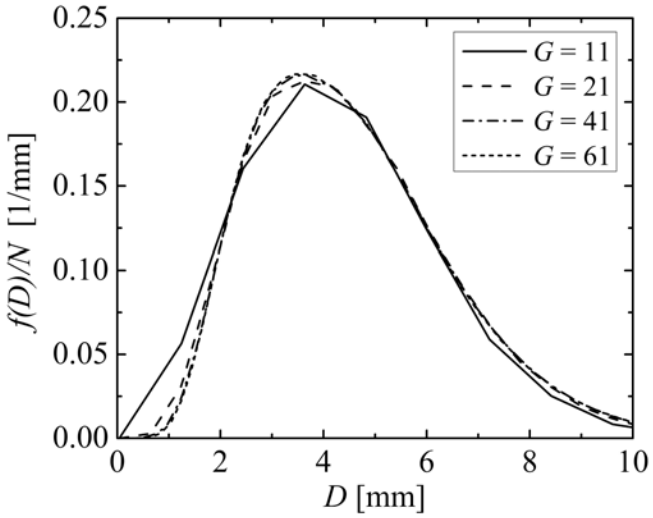

Figure 5.1: Size distribution convergence with the number of groups

distributions are shown as the number density distribution $f(R)$ normalized with

the total number density N. Therefore the area under the curves in Fig. 5.1 is one. As the number of groups used in the simulation is increased the solution approaches the continuous solution of the problem. Solutions computed with 40 and 60 groups practically lie on top of each other and are almost indistinguishable in Fig. 5.1.

The Sauter diameter d_{32} (defined in Eq. (2.88)) and the total number density are shown in Fig. 5.2. They both reach a steady state condition after $t \approx 3$ sec. Sauter diameters are $d_{32} = 6.118$ mm and $d_{32} = 6.128$ mm at $G = 41$ and $G = 61$ respectively differing only in 0.16%. Number densities are $N = 1.021 \times 10^6$ and $N = 1.018 \times 10^6$ at $G = 41$ and $G = 61$ respectively differing in 0.28%.

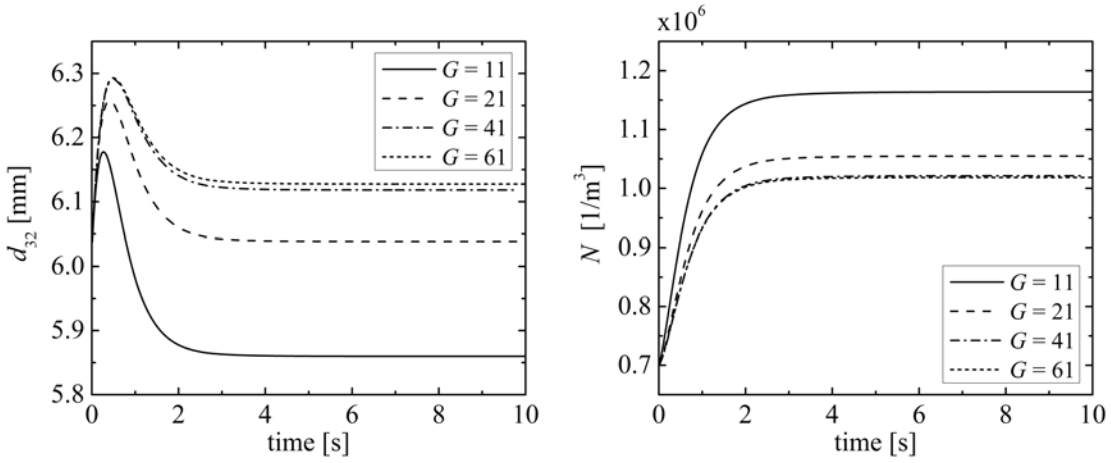

(a) Sauter diamter d_{32}.

(b) Total number density.

Figure 5.2: Sauter diameter and number density convergence with the number of groups.

Given the small difference in the solutions computed with 41 and 61 groups the computations presented in the rest of this chapter are performed with $G = 41$.

5.3 Dependence with the Initial Conditions

Since comparisons with the available data in the literature are performed for the final steady state, it is of interest to assess the existence of a unique solution or at least show with an example that this is the case. Then, case B with the parameters used by Lehr et al. (2002) is run, this time with a fixed number of groups $G = 41$ and variable initial conditions. Once again, the initial condition consists of a monodispersed distribution of bubbles. According to Fig. 3.4 the maximum stable bubble diameter for this turbulence dissipation ($\varepsilon = 0.196$ m^2/s^3) is around $D_{\text{Max}} \approx 5$ mm. In order to have three different initial transients, one where bubbles initially mainly coalesce, one where they initially mainly breakup and another one close to equilibrium, the initial monodispersed distributions are centered at $D_0 = 2.14$ mm, $D_0 = 6.025$ mm and $D_0 = 12.0$ mm, *i.e.* below, close to and above D_{Max}, respectively.

The time evolution of the Sauter mean diameter d_{32} and the total number density N are shown in Fig. 5.3. In all cases the Sauter diameter evolves to an equilibrium Sauter diameter of $d_{32} = 6.11$ mm and the number density goes to $N = 1.02 \times 10^6$ m^{-3}. However, the time evolution for d_{32} and N changes according to the initial condition. For an initial distribution of large bubbles breakup dominates the initial transient and the size distribution shifts towards smaller sizes making the Sauter diameter d_{32} to decrease. Conversely, for an initial distribution of small bubbles, coalescence dominates the initial transient and the distribution shifts towards larger sizes making d_{32} to increase. Note that the dynamics is slower for the case initially controlled by coalescence indicating that at this void fraction coalescence is weaker than breakup.

For the total number density the situation is analogous but it is inverted. For an initial distribution of large bubbles N starts increasing as bubbles breakup and generate more but smaller bubbles. On the contrary with an initial distribution of

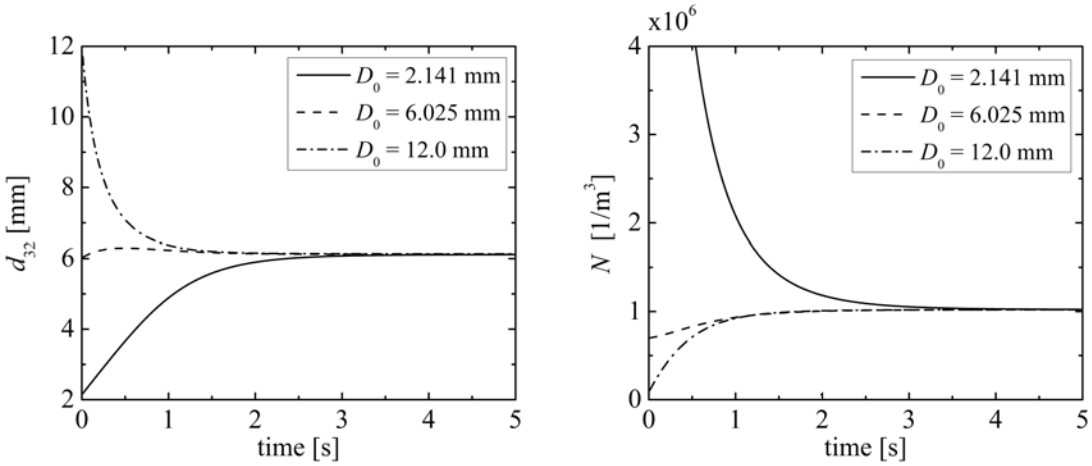

(a) Sauter diamter d_{32}.

(b) Total number density.

Figure 5.3: Sauter mean diameter and number density dependence with the initial condition.

small bubbles N starts decreasing as bubbles are lost when they coalesce to form larger bubbles. In either case the total mass of air and the total void fraction do not change with time.

5.4 Comparison with Previous Works

Figure 5.4 compares the computations performed for this thesis with the numerical results from Lehr et al. (2002) and from Wang et al. (2005a). In all cases a steady state was reached where breakup and coalescence balance each other. Also shown in Fig. 5.4 is the experimental data from Grienberger (1992). These computations were performed with the exact same models for breakup and coalescence presented by Lehr et al. (2002). In Wang et al. (2005a) several models are tested but the results used here are those where Wang et al. (2005a) use the models by Lehr et al. (2002) for both breakup and coalescence. In this regard, all the computations are consistent.

While the experimental data for case A has a peak at about $D \approx 2.0$ mm, case

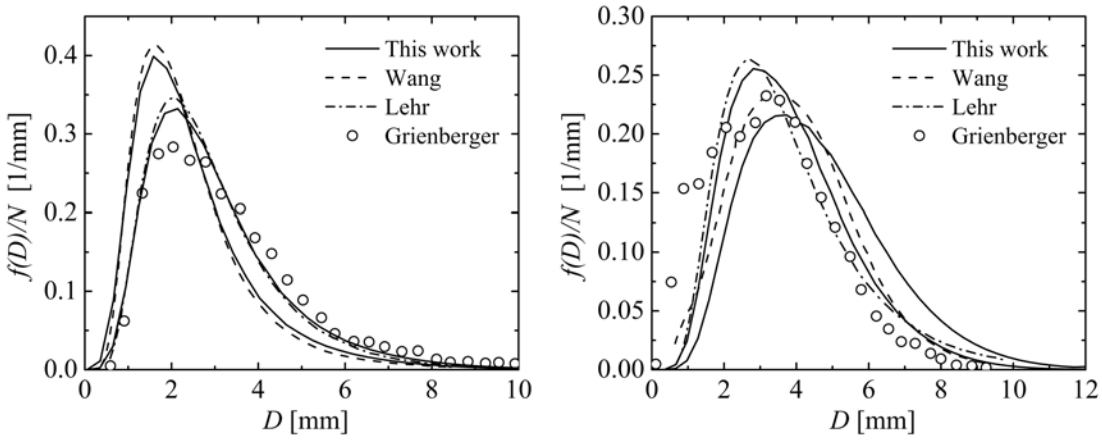

(a) Case A.

(b) Case B.

Figure 5.4: Comparison against the experimental results from Grienberger (1992) and previously performed computations by Lehr et al. (2002) and by Wang et al. (2005a).

B peaks around $D \approx 3.0$ mm. The reason for this is that the stronger turbulence in case A can split smaller bubbles. Even when the void fraction is higher for case A, and this would increase the rate of coalescence, breakup is still strong enough to shift the size distribution towards smaller sizes. Also, case B exhibits a wider distribution than case A.

These trends are well predicted by all the simulation results shown in Fig. 5.4, including the simulations results from this thesis. It is important not only to compare against the experimental data from Grienberger (1992) by also against the simulation results by Lehr et al. (2002) and Wang et al. (2005a). For both, case A and case B, Wang et al. (2005a) use a higher estimated value of the turbulence dissipation ε. This causes the size distribution in case A to shift toward smaller sizes, a trend that the computation from this thesis is able to reproduce. More interestingly for case B, Wang et al. (2005a) use not only a higher turbulence dissipation but also a higher void fraction. This causes the size distribution to shift towards larger sizes

instead even when the turbulence is stronger, showing that for case B coalescence plays a more important role than it does for case A. This trend is well captured by the computations performed in this work.

Even though the agreement with the computations performed by Lehr et al. (2002) is satisfactory, a perfect matching is not expected since Lehr et al. (2002) uses a completely different numerical discretization scheme to solve the Boltzmann equation. On the other hand, a perfect matching with the computations performed by Wang et al. (2005a) is not expected either since in their discretization in bubbles sizes they only use $G = 30$ groups distributed logarithmically while in this work there are $G = 41$ groups distributed uniformly.

5.5 Prince and Blanch Coalescence Kernel

In the model for coalescence presented by Lehr et al. (2002) the coalescence efficiency is a function that depends only on the local void fraction (see Eq. (3.64)). The model presented by Prince and Blanch (1990a) is more general in this regard since it considers the turbulent time scales ($\tau_{m,m'}$ in Eq. (3.57)) versus the time it takes for the liquid film between the two bubbles to drain out ($t_{m,m'}$ in Eq. (3.57)). It is then of interest to compare this two models and to study how Prince and Blanch (1990a) model performs for the cases being considered in this chapter.

The comparison is made for case A using the parameters estimated by Lehr et al. (see Table 5.1). Then two simulations are performed. Both of them use the breakup model by Lehr et al. (2002). In one the coalescence model by Lehr et al. (2002) is used. The simulation results for this case are already shown and validated in Fig. 5.4a. In the second simulation the coalescence model by Prince and Blanch (1990a) is used.

In the figures that follow different curves have a legend of the form A + B where A refers to the breakup model and B refers to the coalescence model. The abbreviations used are as follows: L for Lehr et al., PB for Prince and Blanch and

LS for Luo and Svendsen.

Figure 5.5 compares the size distributions obtained using the coalescence models by Lehr et al. (2002) and Prince and Blanch (1990a), together with the computational results by Lehr et al. (2002) and the experimental data from Grienberger (1992). Prince and Blanch (1990a) model predicts a size distribution slightly shifted to larger sizes in comparison with the size distribution obtained with Lehr et al. (2002) model. This seems to indicate that the model by Prince and Blanch (1990a) predicts a somewhat larger coalescence rate. However the difference is small and the solution obtained using Prince and Blanch (1990a) model can be considered to be as accurate as the one predicted with Lehr et al. (2002) model.

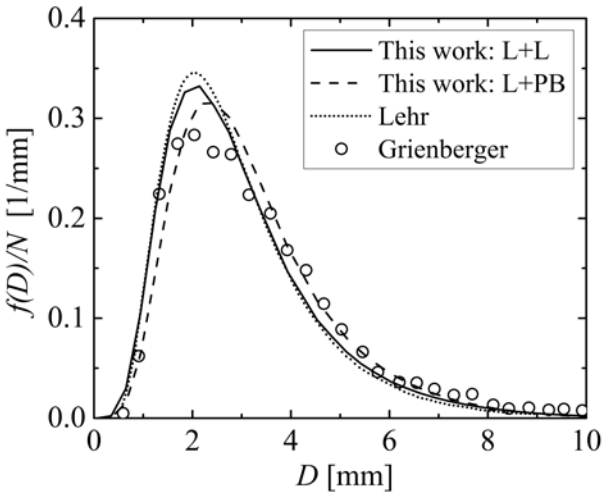

Figure 5.5: Size distributions obtained using the coalescence models by Lehr et al. (2002) and Prince and Blanch (1990a). The breakup model by Lehr et al. (2002) is used in both cases.

Breakup rates are shown in Fig. 5.6. Both, deaths and births are shown. As with the size distributions, the differences using either model are small. It should be noted that birth rates almost double death rates since two bubbles are generated per breakup event. More accurately, the area under the births curve exactly doubles

the area under the deaths curve.

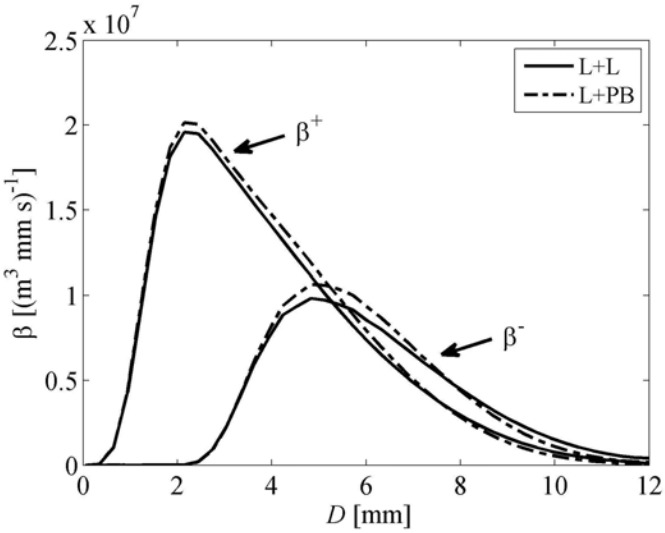

Figure 5.6: Breakup rates obtained with Lehr et al. (2002) and Prince and Blanch (1990a) coalescence models.

Coalescence rates are shown in Fig. 5.7. Once again deaths and births are shown. For the model by Prince and Blanch (1990a) rates are split in turbulent and relative velocity contributions χ_t and χ_u, respectively, as in Eq. (3.56).

The turbulence induced coalescence is shown to be the dominant contribution though the relative velocities contribution has the same order of magnitude and could not be neglected. Both contributions must be considered. Since two bubbles are lost to form only one bubble on each coalescence event, the area under the deaths curve is exactly twice the area under the births curve. This is the reason why deaths almost double births in magnitude.

Figure 5.8 shows the predicted Sauter diameters. The predicted Sauter diameters are d_{32} = 4.778 mm for the model by Lehr et al. (2002) and d_{32} = 4.79 mm for the model by Prince and Blanch (1990a) differing only in 0.25 %.

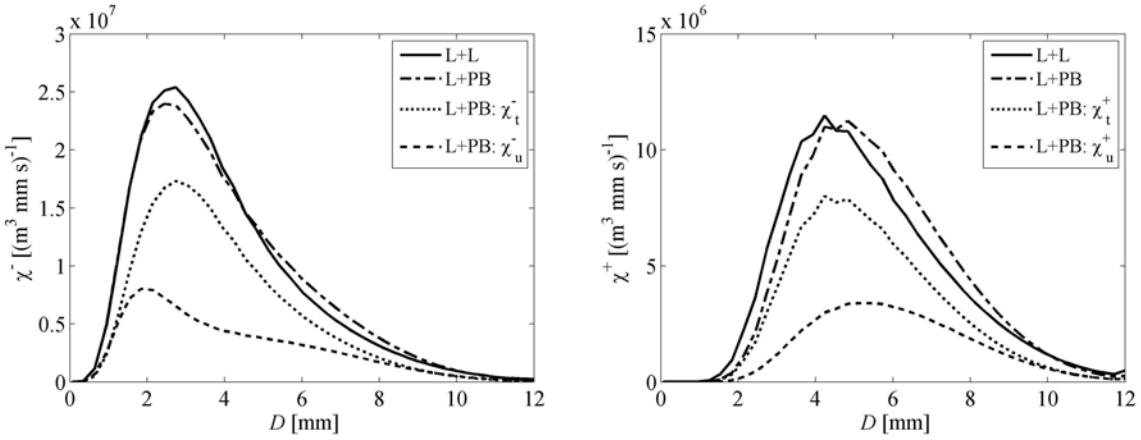

(a) Deaths. (b) Births.

Figure 5.7: Coalescence rates obtained with Lehr et al. (2002) and Prince and Blanch (1990a) coalescence models.

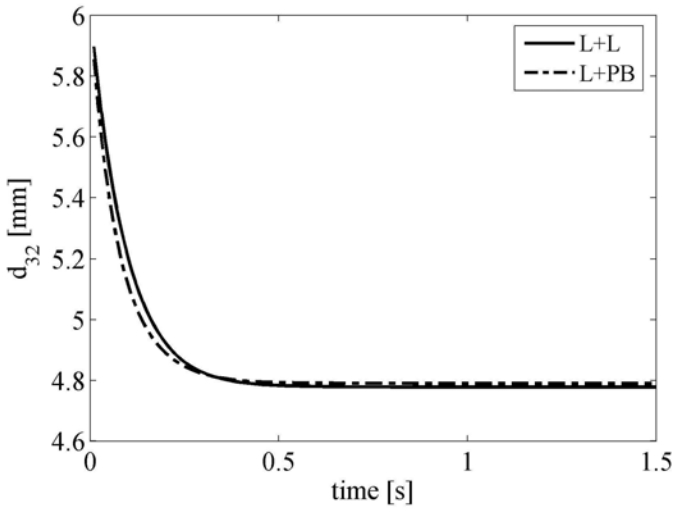

Figure 5.8: Sauter diameter. Predictions using the coalescence models of Lehr et al. (2002) and Prince and Blanch (1990a).

Breakup and coalescence frequencies as defined by Eqs. (2.99) and (2.100) are shown in Fig. 5.9. Recall that from Eq. (2.99) the breakup frequency is nothing but the breakup rate. Figure 5.9 shows that the model by Prince and Blanch (1990a)

predicts a higher value of the coalescence frequency than the model by Lehr et al. (2002). This explains the slight shift towards larger sizes of the size distribution predicted with the model by Prince and Blanch (1990a).

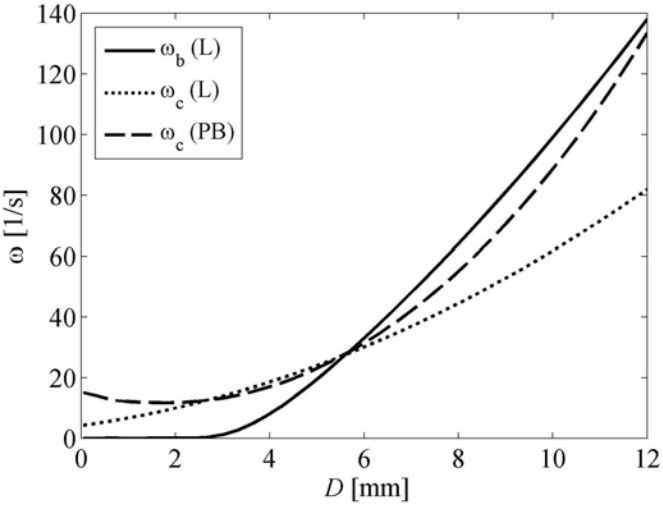

Figure 5.9: Breakup and coalescence frequencies obtained with Lehr et al. (2002) and Prince and Blanch (1990a) coalescence models.

It is shown with these comparisons that the coalescence model by Prince and Blanch (1990a) performs as well as the model by Lehr et al. (2002) for the case presented. The model by Prince and Blanch (1990a) is preferred in this work since it is more general than the model by Lehr et al. (2002) and also because is more widely accepted and used in the literature. Therefore, the Prince and Blanch (1990a) coalescence model is used for the simulation of the bubbly flow around the research vessel Athena in Chapter 6.

5.6 Luo and Svendsen Breakup Kernel

This section compares the predictions obtained with two different breakup models: the model by Luo and Svendsen (1996a) and the model by Lehr et al. (2002).

Similarly as it was done in the comparison of coalescence models in the previous section, the two breakup models are compared on case A with the turbulence dissipation estimated by Lehr et al. (2002). Two predictions are obtained, one with the breakup model by Lehr et al. (2002) and the other one with the breakup model by Luo and Svendsen (1996a). In both cases the coalescence model by Lehr et al. (2002) is used.

Figure 5.10 shows the size distribution obtained with both models together with the computed results by Lehr et al. (2002) and the experimental data from Grienberger (1992). The difference between the predicted results is quite evident. The model by Luo and Svendsen (1996a) predicts much larger bubbles sizes than the model by Lehr et al. (2002).

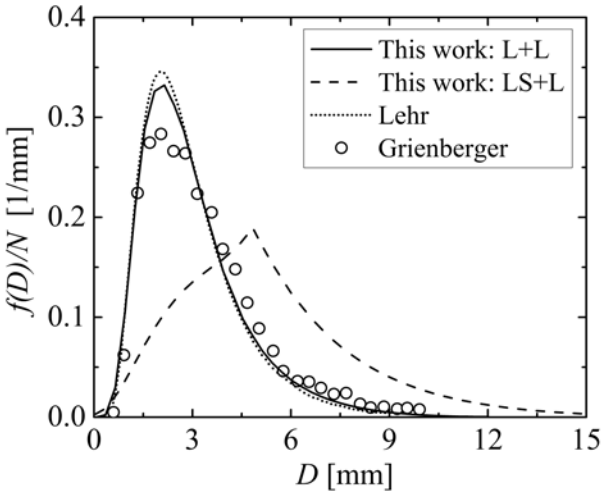

Figure 5.10: Size distributions obtained using the breakup models of Lehr et al. (2002) and Luo and Svendsen (1996a).

Given the large disparity in the size distributions the predicted Sauter diameters are significantly different as well. As mentioned before the model by Lehr et al. (2002) gives d_{32} = 4.778 mm. The model by Luo and Svendsen (1996a) predicts a

much larger Sauter diameter, d_{32} = 8.21 mm. This large disparity can also be seen in Fig. 5.11.

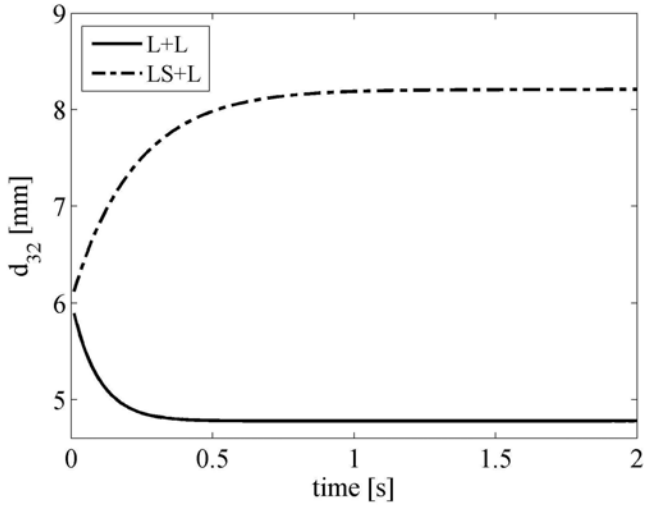

Figure 5.11: Sauter diameters obtained using the breakup models of Lehr et al. (2002) and Luo and Svendsen (1996a).

The reason for such a large disparity in the predictions was mentioned before in Section 3.3.1 and is illustrated in Fig. 3.3. The model by Luo and Svendsen (1996a) predicts a much lower breakup rate than the model by Lehr et al. (2002). This fact was previously observed by other authors. In Chen et al. (2004, 2005b) the model by Luo and Svendsen (1996a) is used in their simulations but they need to multiply the breakup kernel by a factor of ten in order to match their results with experimental measurements. In Wang et al. (2005a) several breakup models are evaluated and it is pointed out that the model by Luo and Svendsen (1996a) underestimates breakup rates. The reader is referred to Section 3.3.1 for a more in depth discussion about this.

Breakup and coalescence rates are shown in Fig. 5.12. In Fig. 5.12a the breakup

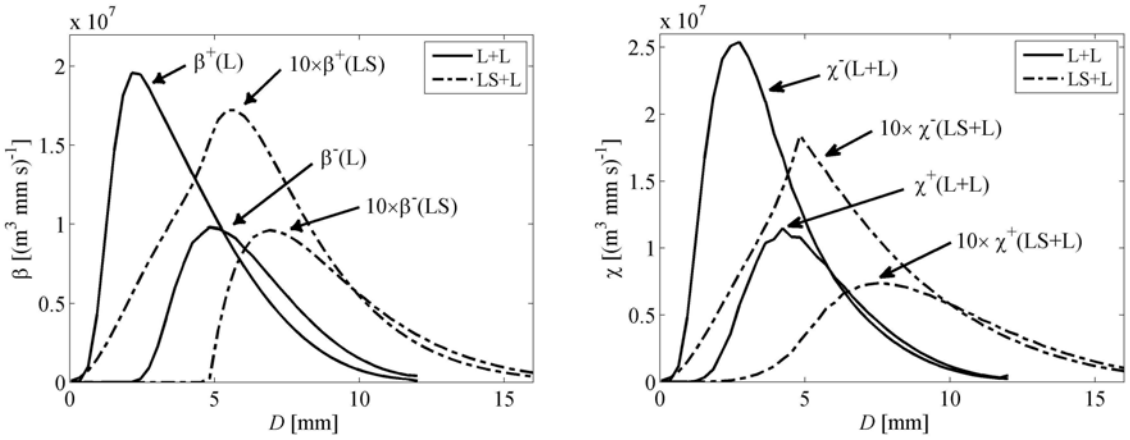

(a) Breakup. (b) Coalescence.

Figure 5.12: Breakup and coalescence rates obtained using the breakup models of Lehr et al. (2002) and Luo and Svendsen (1996a).

rates predicted with Luo and Svendsen (1996a) model are multiplied by a factor of ten in order to show them on the same scale with the breakup rates predicted with Lehr et al. (2002) model. Note that after scaling by a factor of ten, the breakup rates predicted with the models of Luo and Svendsen (1996a) and Lehr et al. (2002) are similar, in agreement with the observation made by Chen et al. (2004, 2005b).

Fig. 5.12 shows that breakup deaths are zero for bubbles sizes $D \lesssim 5$ mm and that this transition is quite sharp. This explains the abrupt change of slope in the predicted size distribution in Fig. 5.10 with Luo and Svendsen (1996a) model.

Coalescence rates are shown in Fig. 5.12b. Coalescence rates are also multiplied by a factor of ten for the predictions using Luo and Svendsen (1996a) model. This seems to contradict the results from Section 5.5 where it was shown that coalescence rates predicted with Lehr et al. (2002) and Prince and Blanch (1990a) models are very similar. The reason for the lower coalescence rates in Fig. 5.12b is that in steady state coalescence rates balance breakup rates and since these are ten time smaller so are the coalescence rates.

Finally, Fig. 5.13 shows the breakup and coalescence frequencies. The dif-

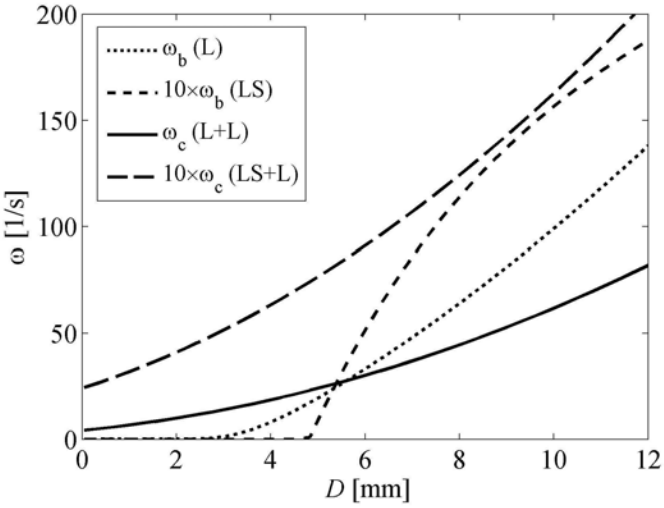

Figure 5.13: Breakup and coalescence frequencies obtained with the breakup models of Lehr et al. (2002) and Luo and Svendsen (1996a).

ferences between breakup models are clear: Luo and Svendsen (1996a) model predicts rates almost ten times smaller than Lehr et al. (2002) model and it has a sharp transition to zero at $D \approx 5$ mm while Lehr et al. (2002) model goes to zero smoothly. Coalescence rates do not match even when the Lehr et al. (2002) model for coalescence is used in both cases. As explained above the reason for this is that coalescence rates balance breakup rates in the steady state. In addition, the coalescence frequency is a function of the number density distribution and, from Fig. 5.10, the predicted size distributions are substantially different for both models.

5.7 Salt Water

In Section 5.3 it was shown than the steady state solution does not depend on the initial condition. The main reason for this is that for fresh water coalescence is possible at all sizes. With breakup, however, bubbles smaller than the maximum

stable diameter D_{Max} do not break, see Fig. 3.4 and the accompanying discussion. Therefore, if there is an excess of bubbles smaller than D_{Max} that breaks the balance between breakup births and coalescence, these bubbles coalesce forming larger bubbles. If there is an excess of large bubbles, larger than D_{Max}, then breakup takes them to smaller sizes. Eventually breakup and coalescence balance each other for all sizes.

For salt water the situation is different. Coalescence is highly inhibited in salt water. Lets consider a case in which coalescence can be neglected. In this case a bubble originally smaller than D_{Max} stays at this size since no breakup or coalescence occur. Therefore, for this case, the steady state solution depends on the initial condition since any size distribution below D_{Max} remains unchanged. If the modification to the Prince and Blanch (1990a) coalescence model presented in Section 3.5 is used to model coalescence in salt water, then coalescence is highly inhibited only for sizes larger than a transitional diameter D_t while for sizes smaller than D_t bubbles coalesce as they would in fresh water.

Lets consider once again case A in Table 5.1 with the parameters used by Lehr et al. (2002). For this case $\varepsilon = 0.785$ and from Fig. 3.5 the maximum stable diameter is $D_{\text{Max}} \approx 2.9$ mm. From Section 3.5 the transitional diameter is $D_t \approx 0.32$ mm for the salt concentrations in sea water. This means that any size distribution of bubbles that is originally located between the transitional diameter D_t and the maximum stable diameter D_{Max} remains unaltered since no breakup or coalescence occur in that region (or at least coalescence can be neglected).

To exemplify this situation, case A with the parameters used by Lehr et al. (2002) is simulated. The breakup model by Lehr et al. (2002) and the coalescence model by Prince and Blanch (1990a) with the modifications for salt water presented in Section 3.5 are used. The solution is started from a monodispersed size distribution centered at three different diameters. A diameter $D_0 = 7.54 \times 10^{-2}$ mm, below D_t,

a diameter D_0 = 0.775 mm, between D_t and D_{Max} and a diameter D_0 = 12.0 mm above D_{Max}.

The computed Sauter diameters with these three initial conditions are shown in Fig. 5.14. As expected from the above explanation when $D_t < D_0 < D_{\text{Max}}$ there

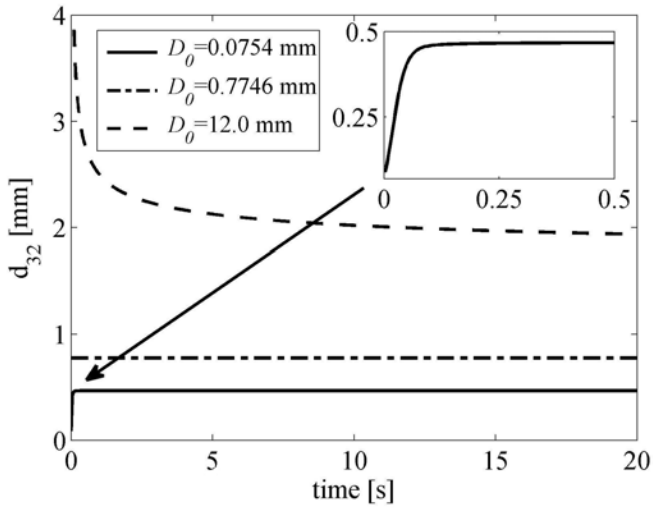

Figure 5.14: Sauter diameter obtained for salt water when the solution is initialized with different initial conditions.

is no breakup or coalescence and the size distribution remains the same. Thus the Sauter diameter is constant in time.

When the initial condition is located below D_t coalescence takes place until all bubbles smaller than D_t coalesce giving rise to bubbles larger than D_t. This can be seen in Fig. 5.15 where the time evolution of the size distribution for this case is shown. This is why d_{32} initially increases in Fig. 5.14.

Finally, when $D_0 > D_{\text{Max}}$, bubbles breakup up until no bubbles larger than D_{Max} are present. This can be observed in the size distribution time evolution shown in Fig. 5.16, and in Fig. 5.14, where d_{32} decreases with time.

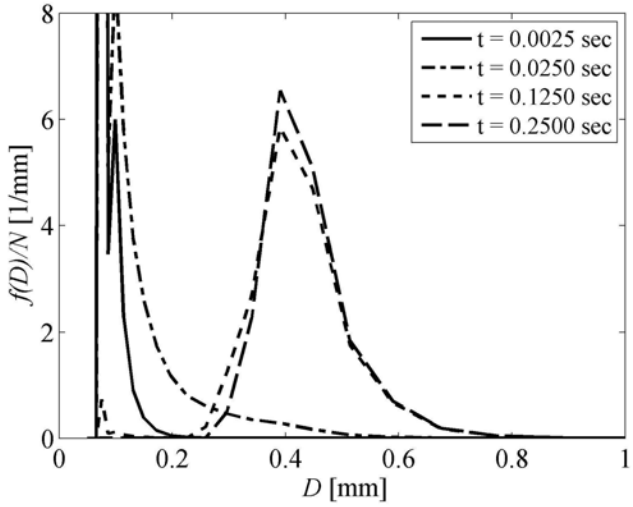

Figure 5.15: Size distribution time evolution in salt water when the initial condition is a monodispersed size distribution centered at $D_0 = 7.542 \times 10^{-2}$ mm.

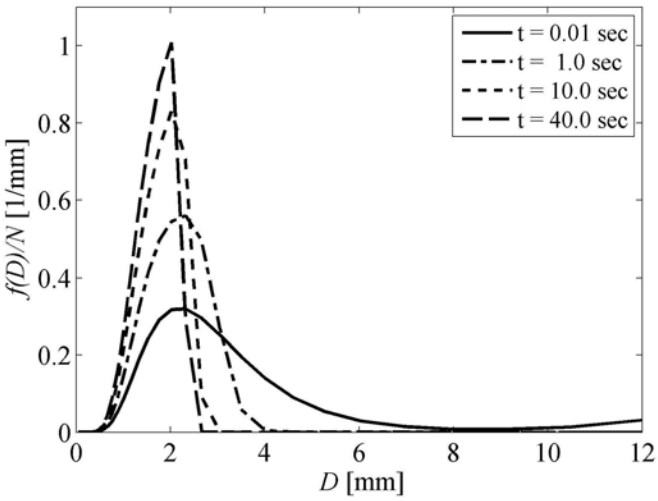

Figure 5.16: Size distribution time evolution in salt water when the initial condition is a monodispersed size distribution centered at $D_0 = 12.0$ mm.

CHAPTER 6
ATHENA R/V

The US Navy research vessel Athena II R/V is a decommissioned PG-84 Asheville-class patrol gunboat transformed into a high-speed research vessel in 1976. The waterline length of the Athena is $L = 47$ m, and propelled by a gas turbine it can reach maximum speeds of 18 m/s (35 knots). The Athena II R/V is fitted with a skeg, starboard and port roll stabilizers and a compound masker system to entrain bubbles and reduce the ship's radiated noise. The masker is a ring fitted around the hull at approximately $x/L = 0.45$. A 3D view of its geometry not including the propellers can be seen in Fig. 6.1.

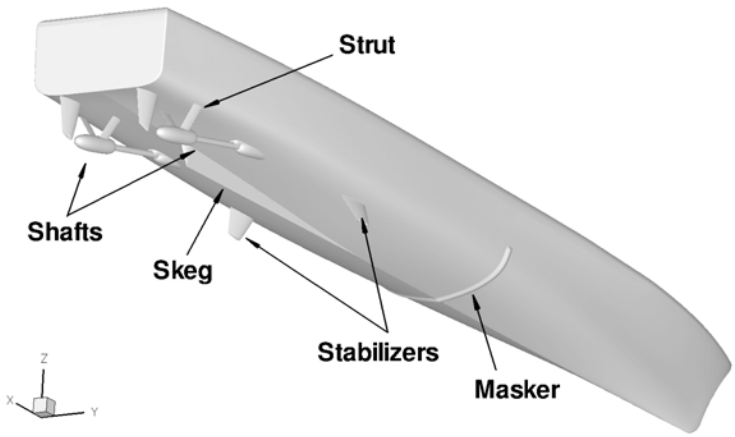

Figure 6.1: Athena II R/V geometry. Propellers are omitted.

This chapter presents the results from three set of simulations. In Section 6.4 a single phase computation (*i.e.* the bubbly field is not simulated) of the self-propelled Athena R/V is presented. The results from this simulation are used to analyze the turbulent field and velocity profiles in the boundary layer which in turn, are responsible for the breakup of bubbles in the boundary layer. The

analysis of the computed solution allows to assess the importance of breakup in the boundary layer and serves to identify some modeling deficiencies. The remaining two simulations model the polydispersed bubbly flow around Athena. In Section 6.5.1, a first set of simulations is carried out using a body force model for the propellers in order to save in computational cost. In these simulations, different intergroup transfer mechanisms are selectively enabled/disabled in order to asses their relative importance. In Section 6.5.2, a third and last simulation performed for this thesis includes the rotating propellers and Athena is in self-propelled condition *i.e.* , the resulting thrust from the propellers (which is a result from the computation) balances the ship's resistance. This last computation is mainly used to assess the code robustness and efficiency and as a test for the new developed two-phase capability.

All simulations presented in this thesis are performed in full scale. The author would like to stress the importance of performing these simulations in full scale in order to have a more realistic prediction of the turbulent field around the ship which, in turn, directly affects the intergroup transfer mechanisms and turbulent mixing or dispersion. It was customary in the past to perform these simulations with the liquid phase in model scale and to scale turbulent quantities to full scale in the dispersed phase equations (see Carrica et al., 1998, 1999; Moraga et al., 2008). Recently added capabilities to CFDShip-Iowa V4.5 allow to perform simulations in full scale (Bhushan et al., 2009; Castro et al., 2011) and with discretized propellers (Carrica et al., 2010a; Castro et al., 2011).

6.1 Summary of Experiments

To the knowledge of the author, the only experimental campaigns to date where near field two-phase measurements were carried out on the full scale Athena II R/V are the ones by Terril and Fu (2008) (see also Terril et al., 2005), Jeon et al. (2008) and Johansen et al. (2010).

In the experiment performed by Terril and Fu (2008) an array of twelve conductivity probes is used to measure void fraction at the stern of Athena II R/V. Measurements were performed during the May 2004 campaign at different depths and lateral positions for speeds ranging from 1 to 6.6 m/s (2 to 12.8 knots). These measurements revealed the presence of a sharp decrease on the gas volume fraction with depth, separating the recirculating region above the transom corner with the boundary layer developed by the hull. Optical sizing measurements performed with a shadowgraph technique below the hull line at the transom, in regions of low gas volume fraction, resulted in a peak in the number density distribution for bubbles at around 15 μm in radius.

In the measurements performed by Jeon et al. (2008), a defocussing DPIV (DDPIV) is used. The experiment took place during the same May 2004 campaign at two locations: nearby St. Charles Bay and the Gulf of Mexico with higher salinity water. Measurements were taken at two locations, one near the port propeller and the other near the centerline. Data was taken at night since the camera used cannot distinguish between bubbles illuminated by sun light or by laser. Void faction and size distributions are reported. Their experiments reveal higher void fractions when measuring in St. Charles Bay which has lower salinity waters. Bubble sizes were found to be generally larger in the bay. This is expected since coalescence is inhibited as salt concentration increases.

The experimental campaign by Johansen et al. (2010) took place in the week of April 20 to 24, 2009. The measurements were performed using double tipped optical local phase-detection sapphire probes. Measurements were taken downstream of the bow breaking wave, the aerator masker and in the highly ventilated transom stern flow, for velocities ranging from 3.1 to 6.2 m/s (6 to 12 knots). Probes made from polished 375 μm and 390 μm sapphire rods by RBI in Meylan, France are used. In addition the authors manufactured a smaller probe from a 125 μm sapphire fiber.

A double dome shape size distribution is found at the stern at depths below 0.5 m with peaks at bubble radius of 80 μm and 800 μm.

6.2 Geometry and Grids

The computations of Athena presented in this work are performed on the fully appended geometry including: skeg, masker, stabilizers, struts and propeller shafts and rudders. Symmetry along the y-axis allows to model half of the geometry and save computational work. The full system of grids, not including the propellers, is shown in Fig. 6.2 and consists of 21 blocks. This grid system is used in the

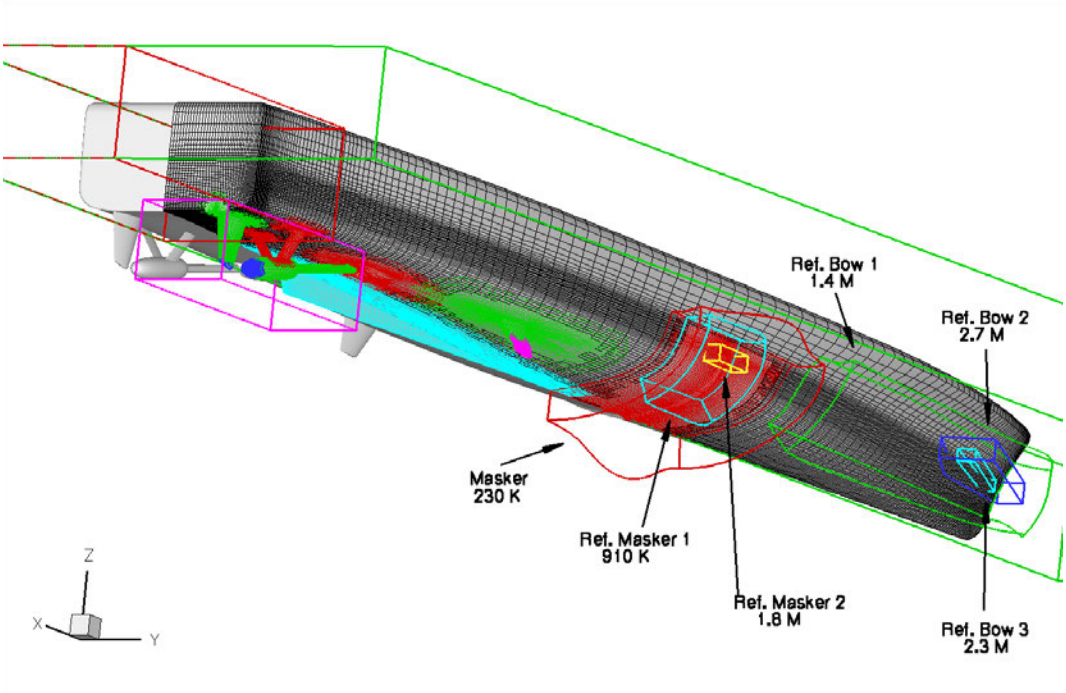

Figure 6.2: Mesh system used in the computation of the Athena II R/V.

computations of Athena where the propeller is modeled with a body force using the Hough and Ordway (1964) load distribution. Refinement blocks are located at the bow and masker to resolve in fine detail the breaking waves that occur there.

Three levels of refinement are used at the bow, with a total of 6.3 millions of nodes. At the masker, three levels of refinement are used as well, with a total of 2.9 millions of nodes. A high level of refinement is used in these zones to test the sub-grid air entrainment model by Ma et al. (2010a). Being this a sub-grid scale model, a high level of resolution is needed to capture plunging waves as required by the model. Additional refinement blocks are also located at the stern. The complete mesh system is formed by a total of 19.15 million grid points.

The mesh system used in the computations of the self-propelled Athena with discretized propeller is shown in Fig. 6.3. This mesh system is the same used for

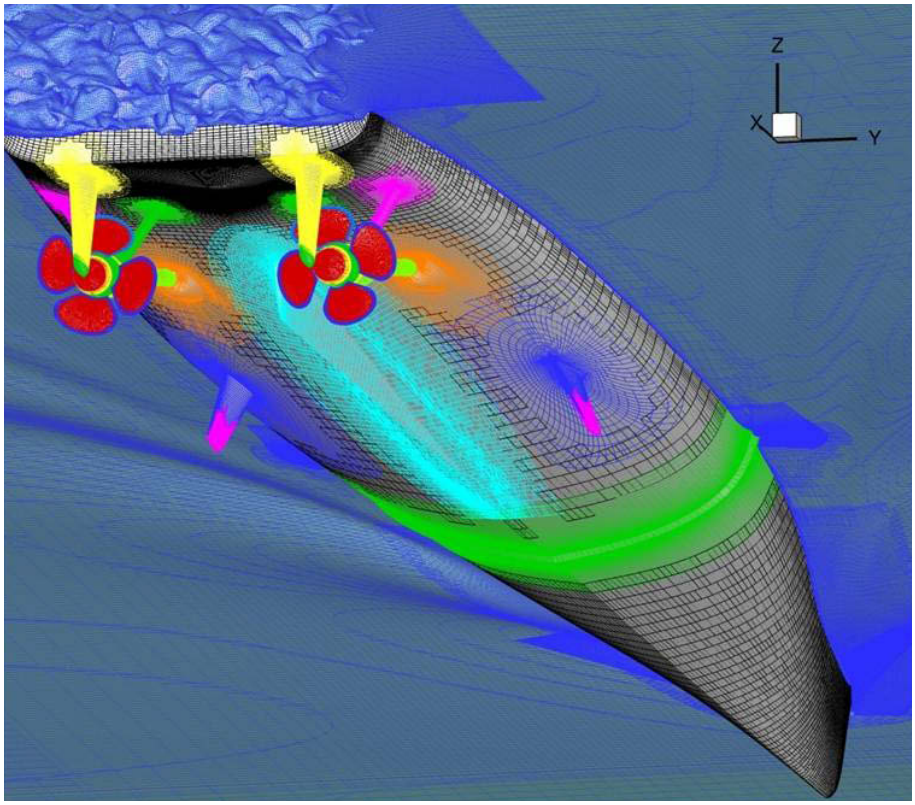

Figure 6.3: Mesh system used in the computation of the self propelled Athena.

the computations of Athena with body force model to which the propeller mesh

system is added. The particulars of this system are summarized in Table 6.1. The

Table 6.1: Grid system for the self-propelled computations of Athena

Grid	Points	Processors	Rotates with propeller
Bare hull	998,448	18	No
Bow refinement 1	1,363,096	24	No
Bow refinement 2	2,701,851	48	No
Bow refinement 3	2,253,411	40	No
Rudder body	341,138	6	No
Rudder cap	114,840	2	No
Skeg	229,653	4	No
Stabilizer body	232,050	4	No
Stabilizer cap	115,412	2	No
Shaft collar	114,660	2	No
Shaft	337,155	6	No
Shaft cap	115,425	2	No
Propeller background	453,951	8	No
Hub	336,960	6	No
Propeller blade tip	$4 \times 337,881$	4×6	Yes
Propeller blade. Pressure side.	$4 \times 112,896$	4×2	Yes
Propeller blade. Suction side.	$4 \times 112,896$	4×2	Yes
Propeller refinement	894,596	16	No
Strut port	115,169	2	No
Strut starboard	115,169	2	No
Masker	229,878	4	No
Masker refinement 1	910,616	16	No
Masker refinement 2	1,804,971	32	No
Stern refinement	4,001,500	72	No
Free surface ref.	1,608,750	42	No
Background	994,653	18	No
Total	22,638,044	416	

full system, including the discretized propeller, contains a total of 22.64 million nodes, in 35 blocks, distributed among 416 processors. In addition, the overset solver, SUGGAR (Noack, 2005), is run with 4 processes spanning 32 processors

(due to memory requirements). In total, the computation uses 448 processors. The additional mesh system of the propeller is shown between horizontal lines in Table 6.1. The mesh system for Athena without the discretized propeller is exactly the same presented in Table 6.1 but without the mesh system for the propeller. Moreover, given that motions are not computed in the computation without propeller, every block in the system is distributed in half of the processors shown in Table 6.1. Therefore, the computation not including the propeller is distributed among 174 processors and the overset solver is not called at runtime (overset information is computed as a pre-processing step).

6.3 Conditions Used in the Simulations

The conditions for the simulations are set to match those of the experiments performed by Johansen et al. (2010), i.e. the simulations are performed in full scale. It is important to perform the simulations in full scale in order to have a more realistic prediction of the turbulent field since this finally determines the breakup and coalescence rates. Moreover, the correct prediction of the turbulent field reproduces the turbulent mixing of bubbles (or turbulent dispersion) more accurately. From the conditions of the experiment, the ship cruise velocity is set to $U_0 = 5.4$ m/s. From Johansen et al. (2010) it is known that the ship encountered small amplitude heading waves with a wavelength $\lambda = 35.2$ m. Therefore, incoming waves are imposed at the inlet of the domain to match the wave length observed in the experiments. The periodic encounter of the ship with the waves induces a periodic wave breaking at the bow which in turn produces a periodic entrainment of bubbles. Since this was observed in the experiment, the incoming waves boundary condition seeks to match the experimental observations. Using the above cruise velocity and Athena's length as the reference velocity and length scales respectively, the Froude and Reynolds numbers are Fr = 0.252 and Re = 2.53×10^8, respectively.

6.4 Breakup in Athena's Boundary Layer

This section presents a study on the magnitude of the turbulent quantities in the boundary layer of Athena R/V and on the potential for breakup and generation of small bubbles in the boundary layer. The study is performed on a single phase solution, *i.e.* no bubbles are present, since it is assumed that the turbulent field does not suffer significant changes in the presence of bubbles. A single phase solution is computed for the fully appended Athena with discretized propeller and with the conditions described in Section 6.3 and the mesh system presented in Section 6.2. Velocity profiles and turbulence dissipation profiles are analyzed in order to determine the potential for breakup by shear and turbulence, respectively, in the boundary layer. Velocity and turbulence dissipation are a direct result from computations performed with CFDShip-Iowa V4.5 which, as described in Section 4.1, uses a k-ω blended turbulence model.

In fluid flows around complex geometries such as the hull of a ship, the boundary layer can vary significantly from point to point on the ship's surface. In order to carry out an ordered analysis of this boundary layer, it is desirable to find a small set of parameters describing the processes involved such that, analyzing a few cases with these parameters spanning their range of possible values, would cover most of the flow conditions around the hull.

One of the most relevant quantities in boundary layer flows is the boundary layer thickness. The thickness of the boundary layer is directly related with the velocity gradients in it: the thinner boundary layer the higher the velocity gradients are. Similarly, a direct relation exists between velocity gradients and the wall shear stress: a higher velocity gradient implies a higher wall shear stress. This is the reason why, in boundary layer theory, the wall shear stress τ_w plays an essential role and is used to form dimensionless groups describing the problem. A velocity scale is formed as $u_\tau = \sqrt{\tau_w/\rho}$ and a length scale is formed as $\delta_\tau = \nu/u_\tau$, where ρ

and ν are, respectively, the density and kinematic viscosity of the fluid. Using these velocity and length scales the variables of the problem can be non-dimensionalized as

$$y^+ = \frac{y}{\delta_\tau} = \frac{u_\tau y}{\nu} \tag{6.1}$$

$$u^+ = \frac{u}{u_\tau} \tag{6.2}$$

$$\varepsilon^+ = \frac{\varepsilon}{u_\tau^3/\delta_\tau} = \frac{\nu\varepsilon}{u_\tau^4} \tag{6.3}$$

where y is used to denote the distance normal to the wall and u (at least in this section) is the velocity component tangent to the wall. These non-dimensionalizations are of paramount importance since they allow to collapse different boundary layer profiles that may have different velocities and thicknesses into one single universal profile. Of particular importance is the logarithmic law of wall

$$u^+ = \frac{1}{\kappa} \ln y^+ + B \tag{6.4}$$

where $\kappa = 0.41$ is the Kármán constant and $B \approx 5.1$ for smooth surfaces.

Note that the boundary layer length scale δ_τ is inversely proportional to the wall shear stress τ_w and thus, the higher the wall shear stress, the thinner the boundary layer characteristic length. In addition, the velocity gradient at the wall is $du/dy = \tau_w/\mu$, with μ the fluid's dynamic viscosity. Therefore, a higher wall shear stress is an indicative of higher velocity shears in the boundary layer.

The above discussion highlights the importance of the wall shear stress τ_w as a parameter used to identify the boundary layer strength and thickness. Therefore, this parameter is chosen to be used as a metric to characterize the boundary layer strength at different locations along the hull of Athena.

6.4.1 Frictional Resistance and Wall Shear Stress

This section quickly shows the existing relation between the frictional resistance coefficient C_f (to be defined in what follows) and a mean wall shear stress. The frictional resistance coefficient C_f is standard when reporting frictional resistance for ships and reference values for Athena can be found in the literature. A direct relation between frictional resistance and mean wall shear allows to compute a reference wall shear stress from validated values of frictional resistance. Wall shear stresses at different locations along the hull can then be compared against this mean value to classify them as stronger or weaker boundary layers.

From computations performed with CFDShip-Iowa V4.5 the frictional resistance coefficient C_f is obtained. This is defined as

$$C_f = \frac{F_{f,x}}{1/2\ \rho\ U_0^2\ S_0} \tag{6.5}$$

where $F_{f,x}$ is the frictional drag force and the subscript x is used since the drag force is assumed to act in the x-coordinate direction. U_0 is a reference velocity taken to be the ship's cruise speed and S_0 is the hull's wetted area when the ship is at rest. The frictional force is computed as the surface integral of the wall shear stress along the hull

$$F_{f,x} = \int_{\partial\Omega} \mathrm{d}^2\boldsymbol{r}\ \tau_{w,x} \tag{6.6}$$

where $\tau_{w,x}$ is the x component of the wall shear stress and $\partial\Omega$ denotes the ship's surface. Equation (6.6) can be written in terms of a mean wall shear $\bar{\tau}_w$ as

$$F_{f,x} = S_0 \bar{\tau}_w \tag{6.7}$$

where $\bar{\tau}_w$ was defined as

$$\bar{\tau}_w = \frac{1}{S_0} \int_{\partial\Omega} \mathrm{d}^2\boldsymbol{r}\ \tau_{w,x} \tag{6.8}$$

With these definitions, the frictional resistance coefficient can be written as

$$C_f = 2\frac{\bar{\tau}_w}{\rho U_0^2} = 2\bar{\tau}_w^* \tag{6.9}$$

where the asterisk on $\bar{\tau}_w$, as in Section 3.11, is used to denote the dimensionless wall shear stress. Then, the frictional resistance coefficient is twice the dimensionless mean wall shear stress. The asterisk is omitted from now and the wall shear τ_w is understood to be dimensionless unless explicitly stated otherwise.

In order to analyze Athena's boundary layer, a single phase computation is carried out and wall shear stresses along the hull are computed and analyzed. The computation is performed for the fully appended Athena at fixed sinkage and trim with discretized propeller. Reynolds and Froude numbers are computed at full scale based on Athena's length $L_0 = 47$ m and cruise speed of $U_0 = 5.4$ m/s resulting in $Re = 2.53 \times 10^8$ and $Fr = 0.252$. Since the computation is carried out at full scale, wall functions are used and the walls are assumed to be smooth. The predicted frictional resistance is $C_f = 1.825 \times 10^{-3}$. This result is in agreement with the computations reported by Bhushan et al. (2009) and with the ITTC 1957 frictional line[1]. Then, from Eq. (6.9), the expected wall shear values along the hull would be around $\bar{\tau}_w = 9 \times 10^{-4}$.

Figure 6.4 shows Athena's hull colored with the magnitude of the wall shear stress. The gaps on the hull are are a rendering artifact due to the use of overset grids. This figure shows that the shear stress along the hull spans values that go from 5.0×10^{-4}, about half of $\bar{\tau}_w$, to 2.0×10^{-2}, about twenty times $\bar{\tau}_w$. Wall shear stresses are higher at appendages like the stabilizers and rudders since a new boundary layer starts to develop at the leading edge. Wall shear is significantly higher on the propeller blades since these move at a much higher velocity than the ship with respect to the surrounding water. Low shear is observed at the stern of

[1] $C_f = 0.075/(\log_{10}(Re) - 2)^2$

the ship where the boundary layer is the thickest and in separation zones on the rudder and struts.

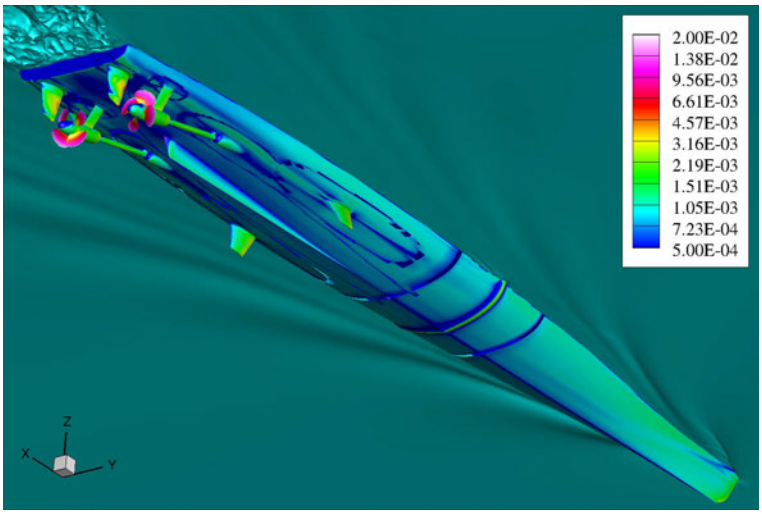

Figure 6.4: Athena's hull colored with wall shear stress. Dimensionless.

6.4.2 Boundary Layer Profiles

Four locations along Athena's hull were selected to study breakup in the boundary layer. Based on the above discussions, these locations were selected in order to span the range of wall shear stresses shown in Fig. 6.4. In this way, the selected boundary layers have different thicknesses and span different ranges of velocity gradients and turbulent dissipations. From these locations a line is extended outwards normal to the hull and solution variables are extracted to perform the analysis. Figure 6.5 shows the four selected locations with spheres in magenta along with the extracted lines normal to the wall shown in black.

Table 6.2 summarizes wall shear stresses at these locations. Wall shear stresses at locations 1 and 2 are very close to the mean wall shear stress $\bar{\tau}_w$ and thus these locations are thought to represent the mean boundary layer flow along the hull.

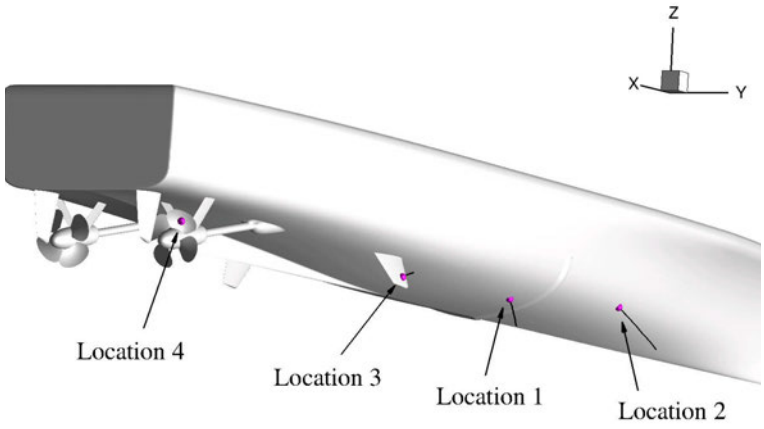

Figure 6.5: Sample boundary layer locations on Athena's hull.

Location 3 is positioned on the stabilizer. Here the wall shear stress increases since a new boundary layer starts to develop from the leading edge of the stabilizer. At this location the shear stress is twice the mean wall shear stress. At location 4, on a propeller blade, the wall shear stress is about eight times the mean wall shear stress. This is due to the high rotational velocity of the propeller blades. At this location, since the propeller is rotating, the wall velocity is subtracted before performing the analysis on the velocity profile. In addition, Table 6.2 also summarizes the distances to the first node from the wall, y_1, and y^+. For these four locations, y^+ is well inside the range of validity for wall functions to work properly. It is important to observe that the wall spacing at the propeller blades is significantly smaller to attain a proper value of y^+ that allows the use of wall functions. Locations with $\tau_w < \bar{\tau}_w$, like at stern with a wide boundary layer, are not analyzed since breakup at these locations is not as strong.

Profiles of velocity u^+ and turbulence dissipation ε^+ are shown in Fig. 6.6. As expected, the velocity follows the universal logarithmic law of the wall for $y^+ \lesssim 500$. The dimensionless turbulence dissipation ε^+ obeys a universal law as well. This

Table 6.2: Wall shear stresses (dimensionless) at the selected locations along with y^+ and distance to the first computational node from the wall y_1.

Location	τ_w [-]	y^+ [-]	y_1 [μm]
1	9.21×10^{-4}	30.58	186.6
2	1.00×10^{-3}	24.00	140.3
3	2.00×10^{-3}	33.93	140.4
4	8.13×10^{-3}	22.88	47.0

law is of the form $\varepsilon \sim y^{+-1}$, (see Wilcox, 2006).

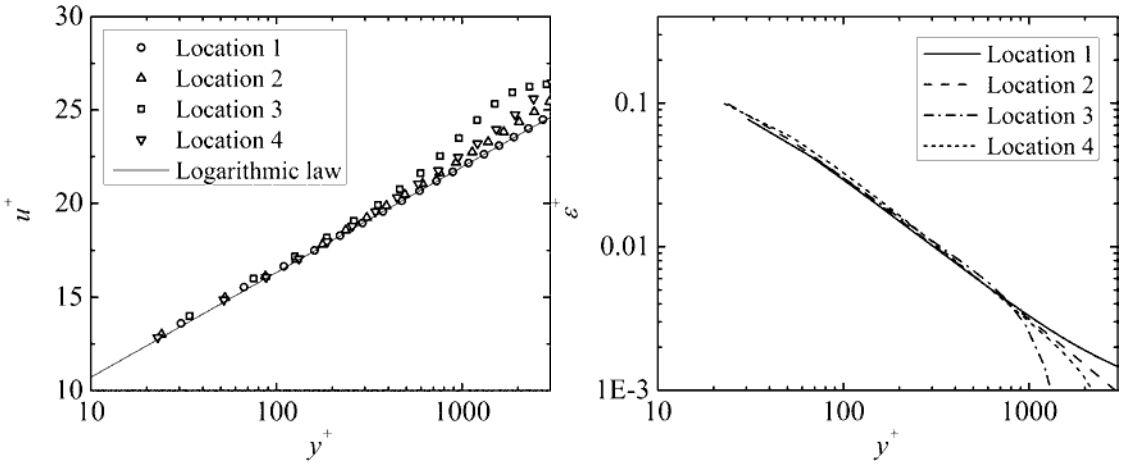

(a) Velocity.

(b) Turbulence dissipation.

Figure 6.6: Boundary layer profiles

6.4.2.1 Turbulence dissipation profiles and breakup by turbulence

Turbulence dissipation, this time with units, is shown in Fig. 6.7. Even though the non-dimensionalization in Fig. 6.6b makes all curves to fall into one single curve, Fig. 6.7 shows that these profiles are substantially different from each other.

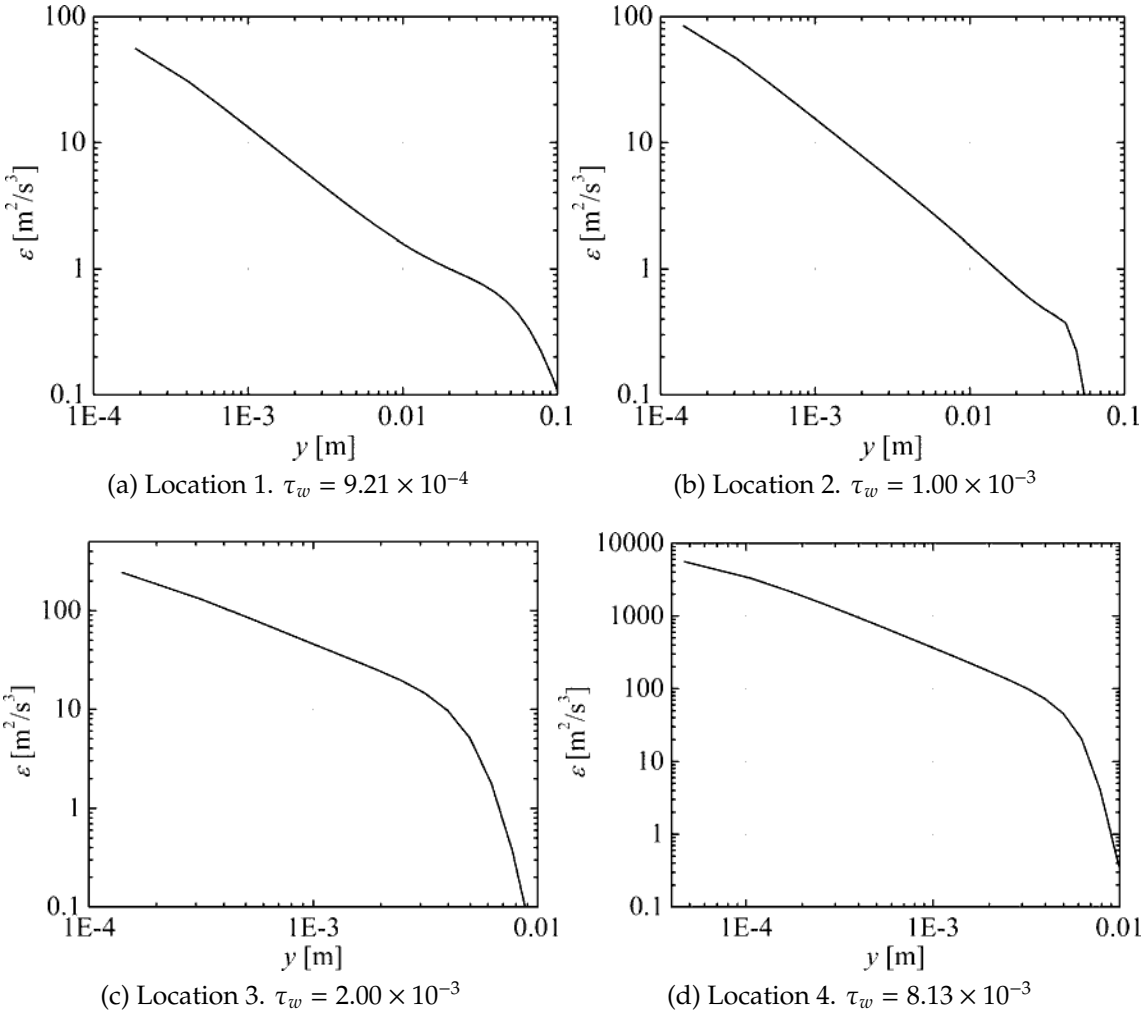

(a) Location 1. $\tau_w = 9.21 \times 10^{-4}$

(b) Location 2. $\tau_w = 1.00 \times 10^{-3}$

(c) Location 3. $\tau_w = 2.00 \times 10^{-3}$

(d) Location 4. $\tau_w = 8.13 \times 10^{-3}$

Figure 6.7: Turbulence dissipation profiles at the four selected locations.

In all locations $\varepsilon \sim y^{-1}$ inside the log layer though the reader should be aware of the different scaling used in the axes. Turbulence dissipation at locations 1 and 2 are similar as expected since the wall shear stresses at these locations are similar. Still, wall stress at location 2 is higher and thus the slightly higher dissipation and thiner boundary layer. As the wall shear stress increases turbulence dissipation increases and boundary layer thickness decreases. At location 3, with a wall shear about twice the mean shear, dissipation reaches values higher than 100 m^2/s^3 while at locations 1 and 2 dissipation is always below this number. At location 4, on one

of the propeller blades, turbulence dissipation reaches even higher values, up to above 5000 m^2/s^3.

In order to have an idea of what these turbulence levels mean, the reader is referred back to Fig. 3.4 in Section 3.3.1, where the maximum stable diameter is shown as a function of turbulence dissipation. Some of the values predicted with the model by Lehr et al. (2002) are: at $\varepsilon = 1$ m^2/s^3, $D = 2.6$ mm at $\varepsilon = 100$ m^2/s^3, $D = 330$ μm and at $\varepsilon = 5000$ m^2/s^3, $D = 63$ μm. This shows that in most of the boundary layer around the hull the breakup of bubbles with a diameter below 300 μm does not occur. Another observation is that breakup in the boundary layer of the propeller blades is a good candidate for the generation of small bubbles.

At this point, the following observation should be made. Let us take location 2 as an example and lets say a bubble with $R = 3$ mm is on the wall and thus its center is located at $y = 3$ mm. At its center, and from Fig. 6.7b, $\varepsilon = 5$ m^2/s^3, on its side opposite to the wall, $\varepsilon = 2.5$ m^2/s^3 and next to the wall, dissipation reaches $\varepsilon \approx 100$ m^2/s^3. Therefore, this bubble is exposed to a highly inhomogeneous turbulent field. Not only inhomogeneous but also highly anisotropic. The models presented in Section 3.3 for bubble breakup by turbulence assume both homogeneity and isotropy of the turbulent field. No models that correct for this situation are known to the author; in this work the models for breakup in Section 3.3 are assumed to be applicable.

6.4.2.2 Velocity gradient profiles and breakup by shear

Figure 6.8 shows velocity gradients at the four selected boundary layer locations. These velocity gradients are the *resolved velocity gradients* obtained by taking the gradient of the velocity vector. As expected, higher velocity gradients are attained at locations with a higher wall shear stress.

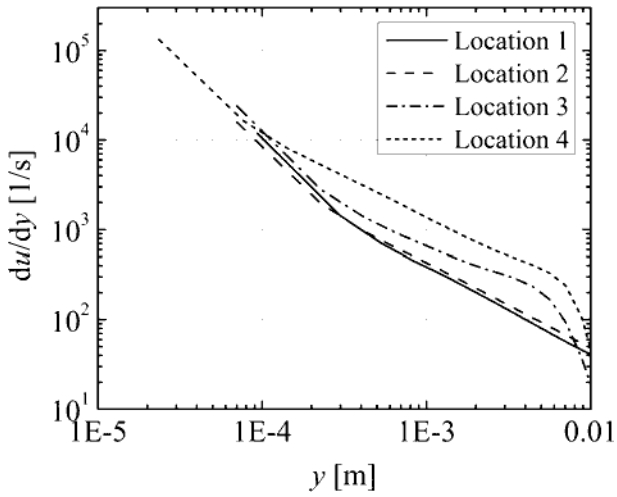

Figure 6.8: Velocity gradients in the boundary layer.

The capillary number introduced in Section 3.3.2 is computed as

$$Ca = \frac{\mu_c \dot{\gamma} R}{\sigma} \tag{6.10}$$

and then, given a fixed resolved shear rate $\dot{\gamma}_u = \mathrm{d}u/\mathrm{d}y$ the capillary number increases linearly with the bubble radius. Thus, larger bubbles are easier to break than small ones.

The modeled part of the velocity gradient, as presented in Section 3.3.2, depends on the local level of turbulence and on the relevant turbulent length scale which is taken to be the bubble diameter. The estimate for the turbulent shear in Eq. (3.84) can be rewritten in terms of the bubble diameter and turbulence dissipation only as

$$\dot{\gamma}_t = \frac{u(D)}{D} = \frac{(2/3)^{1/2}}{C_\mu^{1/3}} \frac{\varepsilon^{1/3}}{D^{2/3}} = 1.822 \frac{\varepsilon^{1/3}}{D^{2/3}} \tag{6.11}$$

and using the definition for the capillary number in Eq. (6.10) the turbulent contri-

bution to the capillary number is

$$Ca_t = 1.148\frac{\mu_c}{\sigma}(\varepsilon R)^{1/3} \tag{6.12}$$

which for a fixed dissipation increases with $R^{1/3}$.

Figure 6.9 shows the capillary number as a function of the bubble radius computed with both, the resolved and modeled shears.

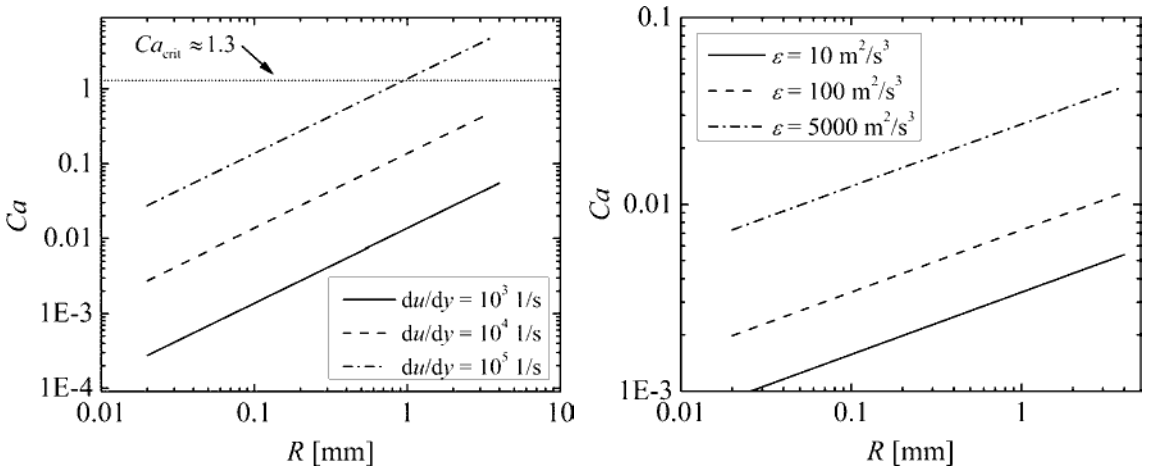

(a) Capillary number computed with a given resolved velocity gradient.

(b) Capillary number computed with the modeled shear given a turbulence dissipation.

Figure 6.9: Capillary number as a function of bubble radius

The values used for $\mathrm{d}u/\mathrm{d}y$ and ε are taken to represent the range of values in Figures 6.8 and 6.7 respectively. According to the experimental data taken by Grace (1982), the critical shear for the air water system would be $Ca_{\text{crit}} \approx 1.3$. A lower value of about $Ca_{\text{crit}} \approx 0.5$ is reported for tip streaming by the same author though no experiments are available for sea water (nor for fresh water) that would allow to develop a complete model. According to the proposed estimate for the modeled turbulent shear it can be concluded from Fig. 6.9b, that turbulent shear does not

induce the breakup of bubbles even for the high dissipation rates observed at the boundary layer of the propeller blades. The author would like to point out that the proposed estimate for turbulent shear in Eq. (6.11) is by no means assumed to be accurate but rather an estimation of the order of magnitude. Still, Fig. 6.9b shows that even if this estimate is multiplied by a factor of ten, turbulent shear would not be strong enough to induce breakup of bubbles in the boundary layer. On the other hand, Fig. 6.9a shows that breakup by resolved shear is possible but only with velocity gradients as high as $\mathrm{d}u/\mathrm{d}y \approx 10^5$ s^{-1}. These gradients are observed at the propeller blades in Fig. 6.8 for location 4. However, a velocity gradient of $\mathrm{d}u/\mathrm{d}y \approx 10^5$ s^{-1} is reached at location 4 at a distance of $y = 30$ μm, while from Fig. 6.9a a bubble can be split by this gradient if it is of about 1 mm in radius or larger. Therefore, even if a bubble is right next to the wall this large gradient strong enough to break it would only act in about 1.5% of the bubble's diameter. It is not clear to the author whether this situation would induce the breakup of a bubble or not and even if this is the case, there is no experimental data on a similar situation that would give any support to the model.

Another way to show the same information contained in Fig. 6.9, is to compute the capillary number as a function of the distance to the wall for several bubble radii. This is shown in Figures 6.10a and 6.10b for locations 1 and 4 respectively.

If location 1 is taken to represent the mean boundary layer flow on Athena's hull, then it is concluded from Fig. 6.10a that shear will not induce bubble breakup in most of Athena's boundary layer. Figure 6.10b shows that the high shear rate at the boundary layer of a propeller blade would be powerful enough to break a large bubble with $D = 5$ mm but once again, this high shear would only act in a portion of the bubble that represents only 2% of its diameter.

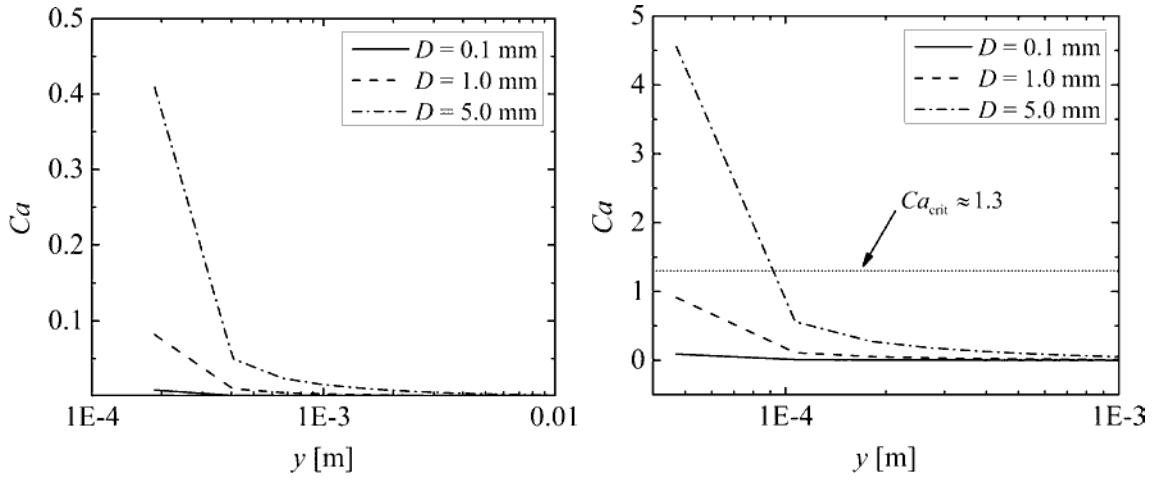

(a) Location 1 (b) Location 4

Figure 6.10: Capillary number in the boundary layer for different bubble diameters.

6.4.3 Breakup Modeling Issues in the Boundary Layer

The above exposition leads to the conclusion that breakup by shear at the boundary layer of Athena, and according to the proposed models, most likely does not occur. It should be noted, however, that the estimates in the above discussion are based on experimental data where only breakup by pure viscous shear occurs. The situation in a turbulent boundary layer (and generally in any shear driven turbulent field) is far more complex than this and Fig. 6.11 attempts to illustrate the idea.

In this figure a bubble is exposed to a shear rate $\dot{\gamma}$ for which the capillary number Ca is below the critical value to induce bubble breakup. Under this condition, the bubble affinely deforms to a steady state shape (provided the shear is imposed for long enough) and the amount of deformation depends on the magnitude of the shear stress (Elemans et al., 1993). Once the bubble has become highly extended, small distortions (known as Rayleigh distortions), start to develop along the deformed bubble and, depending on the viscosity ratio, one distortion wavelength

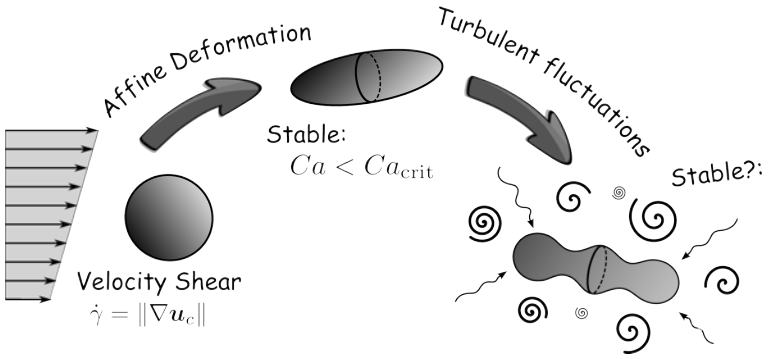

Figure 6.11: Nonlinear coupling of shear induced deformations with turbulent fluctuations on the breakup of bubbles.

turns out to be dominant and ultimately causes the bubble breakup (Elemans et al., 1993). These distortions are depicted in the last stage in Fig. 6.11. In a boundary layer, these distortions may couple with the induced fluctuations by turbulence. This highly non-linear interaction between shear and turbulence could eventually induce the breakup of bubbles even when the separate effects could not be strong enough to induce it. In addition, it is uncertain if these Rayleigh distortions could eventually *resonate* with any of the length scales of the turbulent fluctuations. Not only the interaction between these two effects set a challenge for the modeling of breakup in the boundary layer, but also the highly inhomogeneous and anisotropic turbulent field with boundary layer thicknesses in the order of the bubble diameters present in the bubbly field.

Another issue in the modeling of breakup in the boundary layer is related with the turbulent scales present. A characteristic turbulent length can be estimated from the modeled values of turbulent kinetic energy k and turbulence dissipation ε as $\ell_0 = C_\mu k^{3/2}/\varepsilon$ (this is Eq. (3.80)). This scale is characteristic of the largest eddies in the turbulent energy spectrum and typically falls right before the energy spectrum decay with Kolmogorov's 5/3 law (see §6.5.3 in Pope (2000) where this length,

called L in the reference, is used in a model spectrum to characterize the largest scales). The characteristic length ℓ_0 is computed at the four selected boundary layer locations and is shown in Fig. 6.12.

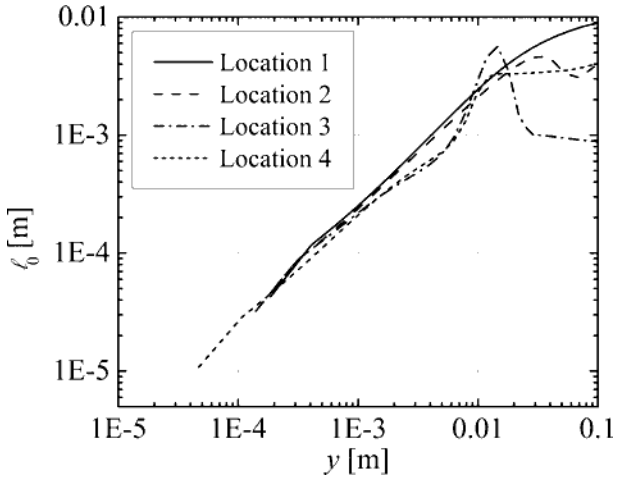

Figure 6.12: Turbulent length scale ℓ_0 in the boundary layer.

As expected, since ℓ_0 is a characteristic length of the largest eddies, $\ell_0 < y$ inside the log layer and $\ell_0 \propto y$ in agreement with the boundary layer theory. From Fig. 6.12, for $y = 1$ mm for instance, $\ell_0 \approx 0.2$ mm. This would mean that a bubble with a diameter of $D = 2$ mm laying on the wall would be exposed to a turbulent field containing a continuum of eddy sizes ranging from the Kolmogorov scale to a length of about $\ell_0 \approx 0.2$ mm. Therefore, the bubble size in this case is larger than the maximum eddy size in the surrounding turbulent field. This situation is not considered in modern turbulence induced breakup models, which typically assume that bubbles are immersed in a turbulent field containing all eddy sizes between the Kolmogorov scale and eddy sizes larger than the bubble diameter. This assumption is made in the works by Lehr et al. (2002) and by Luo and Svendsen (1996a) where the breakup kernel is computed from the frequencies of arriving

eddies $\omega(D,\lambda)$, with λ the eddy size, and the probability that collision leads to breakup $P(\lambda, D, D')$. The total breakup kernel is then obtained by integrating the contributions from different eddy sizes over all sizes from a minimum eddy size $\lambda_{\min}$ (which is different for each model and the reader is referred to the original references for the details) to the bubble diameter D

$$b(D)\,h(D',D) = \int_{\lambda_{\min}}^{D} d\lambda\,\omega(D,\lambda)\,P(\lambda,D,D') \tag{6.13}$$

In order to correct for the fact that the full spectrum of eddy sizes is composed by eddies smaller than the bubble size diameter, these models should be modified to

$$b(D)\,h(D',D) = \int_{\lambda_{\min}}^{\min(D,\ell_0)} d\lambda\,\omega(D,\lambda)\,P(\lambda,D,D') \tag{6.14}$$

and therefore the modified model would predict a lower breakup rate for the same turbulence dissipation, if no other effects like the non-linear coupling between shear and turbulence are considered. Still, the above proposal does not include a correction for the highly inhomogeneous turbulence in the boundary layer. It should be noted that for the above mentioned models the turbulent field is completely defined by specifying the turbulence dissipation ε while typically at least two parameters are needed to describe an homogeneous turbulent field (as done in two-equations turbulence models). With the proposed modification, since ℓ_0 depends on both the dissipation and the turbulent kinetic energy, the breakup kernels would then become dependent of two parameters, k and ε.

The above discussion identifies a series of weaknesses in the model of breakup inside a boundary layer. To the knowledge of the author, there is no work, either theoretical or experimental, studying the plausible non-linear interaction between shear and turbulence that might lead to additional breakup in the boundary layer.

Corrections accounting for cases where turbulence scales are smaller than the bubble size or for the large inhomogeneity of the turbulence field are not found in the literature either.

6.5 Bubbly Flow Around Athena

This section presents two different set of simulations. In the first set the propeller is modeled using a body force model while in the second set the propeller is fully discretized by the grid system. Since no motions are computed for the first case, and therefore is less computationally intensive, this case is used to test the influence of different intergroup transfer terms by selectively enabling/disabling them in a series of different simulations. The second case includes the prediction of the propeller rotational speed needed to attain the self-propulsion point and is therefore highly computationally intensive due to the additional work necessary to compute new overset interpolations at each time step and in addition it uses a smaller time step to resolve the propeller dynamics.

However, for both the body force and discretized propeller models, the main parameters defining these simulations are the same and differences are highlighted accordingly in the respective sections. Conditions are set as commented in Section 6.3 according to the conditions of the experiment carried out by Johansen et al. (2010), with a cruise speed of $U_0 = 5.4$ m/s resulting in Reynolds and Froude numbers $Re = 2.53 \times 10^8$ and $Fr = 0.252$, respectively. Incoming waves with wave length $\lambda = 35.2$ m and amplitude $a = 5$ cm are imposed as a boundary condition at the inlet of the computational domain. The addition of the bubbly phase introduces the new dimensionless numbers summarized in Table 3.1. Taking the air density at STP $\rho_{d,0} = 1.204$ Kgr/m^3, the water density $\rho_c = 1024.93$ Kgr/m^3 (from Sharqawy et al. (2010), at a salinity $S = 35$ g/L and temperature $T = 20\,^{\circ}C$)[2], the surface tension

[2]For fresh water at the same temperature $\rho_c = 998.207$ Kgr/m^3 being a 2.64% lower than that for sea water.

σ = 73.5 mN/m, the atmospheric pressure p_{atm} = 101.325 kPa, the diffusivity of air in water $\kappa = 2 \times 10^9$ m^2/s and the Henry constant $H = 2.38 \times 10^{-4}$ g/Nm, the additional dimensionless numbers for the two-phase computation are: the density ratio $\pi_\rho = 1.17 \times 10^{-3}$, the Weber number $We_L = 1.91 \times 10^7$, the Euler number $Eu = 3.39$, the Schmidt number $Sc = 500.0$ and the dimensionless equilibrium concentration $C^*_\infty = 0.02$.

The discretization in bubble sizes is set to span the complete range observed in the experiment. The size distribution measured at the bow of the Athena by Johansen et al. (2010) is used as the size distribution for the entrainment model. The measured number density distribution reported by Johansen et al. (2010) is first fitted to a power law of the form $f(R) = b\, R^a$, with R the bubble radius and the exponent $a = -2.35$. The maximum reported bubble radius is R = 2.5 mm and therefore the entrainment bubble size distribution is assumed to be zero for larger radii. Measurements by Terril and Fu (2008) report a number density distribution that peaks at about $R \approx 15$ μm. Then the entrainment size distribution is assumed to linearly go to zero for smaller bubbles and therefore it also exhibits a peak at $R = 15$ μm.

The range of interest, defined for bubbles with radius between 10 μm and 4 mm, is then discretized in 15 group sizes uniformly distributed on a logarithmic scale. These are summarized in Table 6.3 along with the group-g size distribution D_g^{ent} and the dimensionless radius and bubble mass. The group-g entrainment size distribution is computed as described in Section 3.8.

The entrainment depth in Eq. (3.103) is set to ϕ_{ent} = 10 cm to ensure that the region near the free surface where the model activates is well resolved by the grid. The near wall integration distance introduced in Section 4.6.1 is set to δ_w = 1 cm.

According to the results from Chapter 5, the model of Lehr et al. (2002) is used for the prediction of turbulence induced breakup and the model of Prince and

Table 6.3: Bubble size discretization in groups and entrainment size distribution.

Group	**Radius** [μm]	**Radius** [$-$]	m_g [-]	D_g^{ent}
1	10.00	2.13×10^{-7}	4.03×10^{-20}	3.13×10^{-1}
2	15.34	3.26×10^{-7}	1.46×10^{-19}	2.90×10^{-1}
3	23.54	5.01×10^{-7}	5.26×10^{-19}	1.75×10^{-1}
4	36.11	7.68×10^{-7}	1.90×10^{-18}	9.80×10^{-2}
5	55.39	1.18×10^{-6}	6.86×10^{-18}	5.50×10^{-2}
6	84.98	1.81×10^{-6}	2.48×10^{-17}	3.09×10^{-2}
7	130.37	2.77×10^{-6}	8.94×10^{-17}	1.73×10^{-2}
8	200.00	4.26×10^{-6}	3.23×10^{-16}	9.72×10^{-3}
9	306.83	6.53×10^{-6}	1.17×10^{-15}	5.45×10^{-3}
10	470.71	1.00×10^{-5}	4.21×10^{-15}	3.06×10^{-3}
11	722.13	1.54×10^{-5}	1.52×10^{-14}	1.72×10^{-3}
12	1107.84	2.36×10^{-5}	5.49×10^{-14}	9.64×10^{-4}
13	1699.55	3.62×10^{-5}	1.98×10^{-13}	5.41×10^{-4}
14	2607.35	5.55×10^{-5}	7.15×10^{-13}	9.38×10^{-5}
15	4000.00	8.51×10^{-5}	2.58×10^{-12}	0.00

Blanch (1990a) (implemented as presented in Section 3.2, including both turbulent fluctuations and relative velocity terms) for the estimation of bubble coalescence. The modification for coalescence modeling in sea water proposed in Section 3.5 is used as well.

The RANS equations of motion for the fluid are solved together with the two-phase k-ω blended model for turbulence presented in Section 3.6.

6.5.1 Effect of different intergroup transfer mechanisms

This section presents the set of simulations performed on Athena's full geometry including all appendages as presented in Section 6.2 but where the propeller is not included as part of the geometry but rather its effects are considered using a body force model. The propeller model uses the well known load distribution of Hough and Ordway (1964) with zero loading at the root and the tip. The ship is fixed at

even keel condition and thus is not allowed to move. Given these conditions, there are no motions that need to be predicted as part of the computation for this case. Therefore, the overset information is computed only once as a preprocessing step and it does not need to be updated during the computation. The time step used is rather large given that the turbulence model averages out the smallest scales and is set to $\delta t = 0.005$ and thus 200 time steps are needed per ship length (with units $\delta t = 43.52$ ms). Since no motions (and then overset information) are computed and the time step is rather large, it is feasible to run this case several times with slightly different conditions and perform comparisons. First, the entrainment strength S_0 (see Section 3.8) is calibrated to adjust the amount of void fraction at the stern with the available experimental results and several runs are needed. The procedure to adjust this constant is iterative, and S_0 is estimated for each new run considering a linear relation between the constant and the void fraction level at the stern. The relation between void fraction levels and S_0 is not linear since the entrainment depends on the void fraction. However, this estimation allows to converge to a value of S_0 after a few iterations (each iteration consisting of a new run of the complete case). Applying this procedure the entrainment constant is found to be $S_0 = 0.9$ for the full model including intergroup transfer and is kept unchanged for all the simulations presented herein.

Once the entrainment strength S_0 that adjusts the void fraction at the stern is found, five additional cases are run completing a total of six different cases. In the first five cases the effect of the different intergroup transfer mechanisms on the overall solution is investigated by selectively enabling/disabling them. The different cases run and the labels used to identify them (in parenthesis) from now on are: with no intergroup transfer (None), with breakup only (B), with coalescence only (C), with breakup and coalescence (BC) and with breakup, coalescence and dissolution (BCD). A final case (Full) includes all intergroup transfer mechanisms

(as with BCD) and adds the oceanic background model from Section 3.9 and the bubble growth by rectified diffusion in the propeller from Section 3.10.

For the given conditions, Froude number specifically, the solution exhibits a wet transom and vortices are shed at the stern coupled with an unsteady motion of the free surface. Moreover, the solution exhibits additional oscillations due to the imposed incoming waves. To analyze the computed bubbly flow, the solution is averaged over four wave encounter periods. For the imposed wave length the encounter period is $T_e = 0.316$ and over four encounter periods Athena travels 1.264 ship lengths. Therefore, in what follows, all the results are presented in terms of mean quantities.

6.5.1.1 Three-dimensional solution

Before analyzing the solution at specific spatial locations, the overall three-dimensional two-phase solution is inspected. Figure 6.13 shows the free surface colored with contours of total void fraction α_d. In this, and in all figures in this chapter where void fraction contours are shown, colors are distributed on a logarithmic scale given the wide range of values the void fraction can take owing to the fact that bubbles sizes span a wide range of scales as well. The bow and stern experimental locations where measurements were taken by Johansen et al. (2010) are shown in this figure as well. At these locations, Johansen et al. (2010) measured void fraction and bubble size distribution at several depths. To be more precise, the bow experimental location is at $(x;\ y) = (0.284;\ 0.0779)$ and the stern experimental location is at $(x;\ y) = (1.0106;\ 0.021)$. The main entrainment locations are also shown in Fig. 6.13. These are at the bow and masker breaking waves and at the highly aerated stern and shoulder waves. Colors in this figure show void fractions as high as 20%. However, some areas in the domain, specifically close to the transom corner at the stern and at the entrainment locations during some transients, the void fraction can be as high as 30% or even more. This illustrates

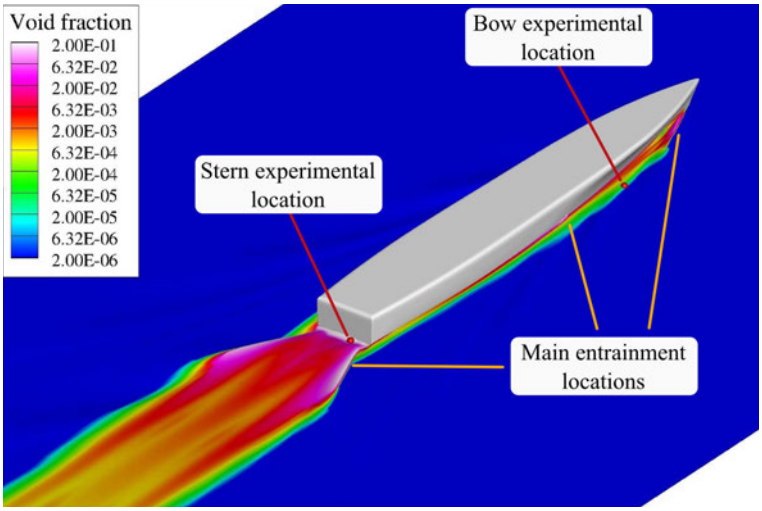

Figure 6.13: Free surface colored with total void fraction α_d for the BCD case. The bow and stern experimental locations from Johansen et al. (2010) are shown.

the robustness of the code at high void fractions in unsteady computations. While Fig. 6.13 shows mean void fraction, the actual solution is unsteady and the ship encounters incoming waves as it moves. These incoming waves cause the entrainment at the bow to be periodic with a period equal to the encounter period T_e. The unsteady breaking at the bow generates a periodic shedding of bubbles from this location that are further transported downstream.

The evolution and shape of the bubbly wake behind Athena is better appreciated in Fig. 6.14, where slices colored with void fraction are shown. Bubbles are entrained at the bow breaking wave and along the contact line. Depending on the size of these bubbles, some of them are pulled down the hull and transported downstream. In addition to the slices, Fig. 6.14 shows Athena's hull colored with void fraction from where the amount of gas around the hull can be appreciated. A depleted wake is observed downstream the stabilizers which is formed as the stabilizers act as an obstruction to the free flow of bubbles and it is reinforced by strong horse shoe vortices at their base. The last four slices before the stern of the ship show that as the boundary layer widens towards the stern, the bubbly wake

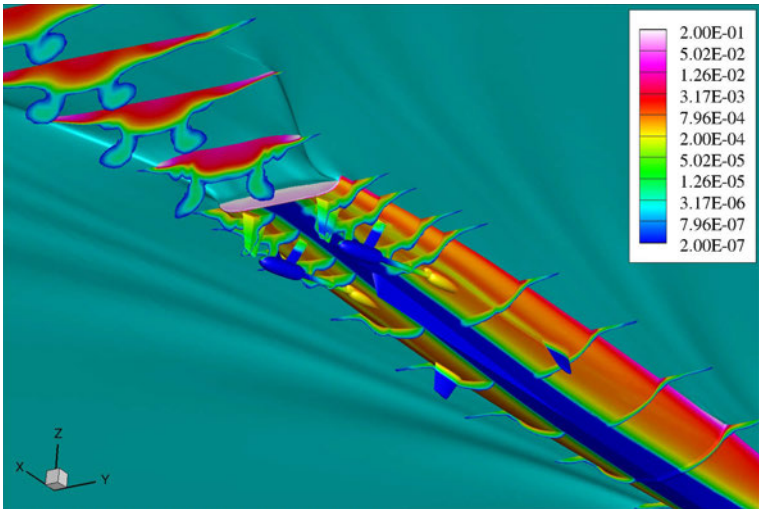

Figure 6.14: Slices colored with total void fraction showing the evolution of the bubbly phase around and behind Athena. Hull is colored with void fraction as well.

widens along with it. In addition, some of these bubbles are pushed down by vortices shed from the shaft mountings and later on sucked by the propeller inflow (the reader should recall that the action of the propellers in these simulations is considered with a body force model). At the stern, the void fraction is high near the free surface where air is entrained and a characteristic finger of bubbles is left behind the propellers wake.

Figure 6.15 shows the computed solution for the Full case which includes the oceanic background and rectified diffusion models. Free surface colored with void fraction is shown in Fig. 6.15a. The main difference observed with Fig. 6.13 is that, with the oceanic background, the void fraction is around $\alpha_d = 10^{-4}$ at the free surface while it is zero for the case with no background. Figure 6.15b shows slices colored with void fraction for this case. The coloring used for the void fraction in this figure is the same used in Fig. 6.14. Figure 6.14 shows that, on some areas of the hull, the deeper ones, the void fraction drops bellow 2×10^{-7} and these are colored in dark blue. This clearly shows how deep bubbles are pulled down the hull. In

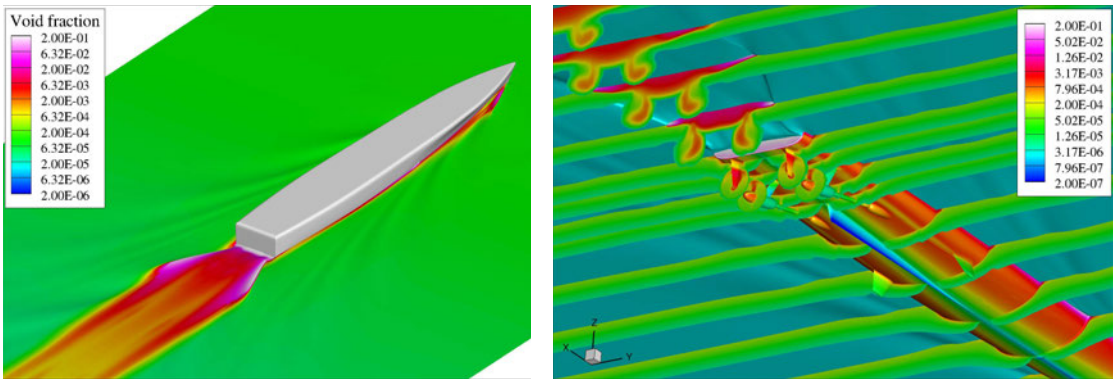

(a) Free surface colored with void fraction. (b) Slices and hull colored with void fraction.

Figure 6.15: Full case including oceanic background and rectified diffusion model.

Fig. 6.15b, these blue areas in Fig. 6.14 now are colored with other contour levels corresponding to higher void fraction levels. This extra void fraction is introduced by the imposed oceanic background.

Far to the sides of the ship slices show a layer of bubbles near the free surface corresponding to the oceanic background. The void fraction at the wake of the propellers is higher than in Fig. 6.14 due to growth by rectified diffusion of the bubbles going through the propellers. The rectified diffusion model does not change the number of bubbles that go through the propeller but, given that these bubbles grow in size, the void fraction increases. While the wake behind the propellers in Fig. 6.14 exhibits a finger shape, the bubbly wake behind the propellers in Fig. 6.15b exhibits a well defined circular shape covering the full area of the propellers. The difference is caused by the additional background of bubbles coming into the propellers which are affected by rectified diffusion as well. However, the contribution by bubbles from the boundary layer is stronger, and the finger is still noticeable inside the propeller wake. Moreover, the finger in Fig. 6.14 is stronger in Fig. 6.15b due to the growth of these bubbles by rectified diffusion.

6.5.1.2 Void Fraction Profiles

The resulting void fraction profiles with depth are shown in Fig. 6.16. This figure includes the experimental results from Johansen et al. (2010) (IIHR results) and from Terril and Fu (2008). Johansen et al. (2010) reports measurements taken with the ship going with and against the waves and these are labeled accordingly in Fig. 6.16. The same figure is shown with the void fraction in linear and logarithmic scale to highlight different features of the profile. This figure shows the results from three cases: None, BCD and Full. Full is not shown in Fig. 6.16a since it practically falls on top of the other two curves making the plot difficult to read. In addition, these figures include a vertical line indicating the position of the bottom of the transom. Both, the experiments and the simulations, see Fig. 6.16a, exhibit a

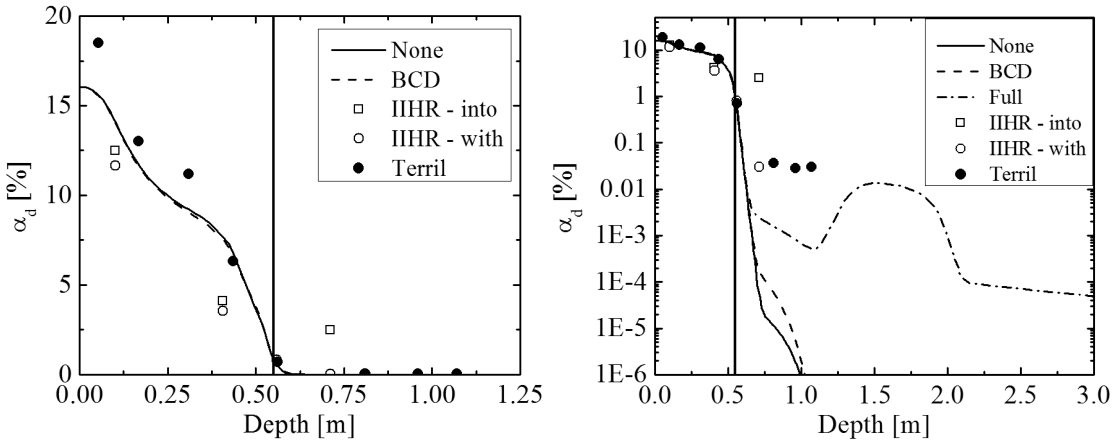

(a) Linear scale in void fraction.

(b) Logarithmic scale in void fraction.

Figure 6.16: Void fraction profile with depth at the stern experimental location.

void fraction profile with a maximum at the free surface and with a clear transition to low void fraction at the bottom of the transom. In the void fraction profile reported by Terril and Fu (2008) no filtering was applied to account for the fact that the free surface may cross their probe and thus they report a void fraction that

includes bubbles and also the fraction of the time their probe is in air. On the other hand, Johansen et al. (2010) do apply a filtering to account for void fraction in the two-phase mixture only. This is why the void fraction reported by Terril and Fu (2008) is higher than the one reported by Johansen et al. (2010). In this regard, since the void fraction predicted by the model is only due to bubbles, the measurements performed by Johansen et al. (2010) are more comparable with the results from the simulations. It should be noted that even when the void fraction level at the stern is adjusted by changing the value of the entrainment strength S_0, the shape of the profile and the sharp transition at the bottom of the stern are predicted by the model. Figure 6.16b highlights the differences between the predicted results with and without intergroup transfer and with the Full case. The predicted void fraction is noticeably higher when intergroup transfer is active for depths below 0.6 m. This difference is caused by an increased number of small bubbles created in breakup events. Figure 6.16b also shows the Full case including oceanic background and rectified diffusion at the propeller. Void fraction is higher for the Full case deep below the free surface due to the additional background bubbles. In addition, the void fraction increases at the depth of the propeller since bubbles going through the propeller grow in size by rectified diffusion and thus void fraction increases the expense of the air initially dissolved in the water. Figure 6.16b shows that the void fraction in the experiments is higher than the one predicted by the simulations at depths below the bottom of the stern. The reasons for this difference are unknown to the author though some possibilities are, but not limited to: inaccuracy of the entrainment model, underprediction of breakup in the boundary layer and oceanic background modeling. In addition, the uncertainty of these measurements should be reported as a result of the experiments. Experimental data acquisition at these depths is not easy due to the high speeds involved and the difficult to access area close to the propeller wake. Additional experimental work is needed to obtain a

more reliable experimental data set.

To better appreciate the difference in the predicted void fraction at the stern when enabling/disabling different models, Fig. 6.17 shows the void fraction profile for the B, C and BC cases normalized with the void fraction predicted without including any intergroup transfer mechanism.

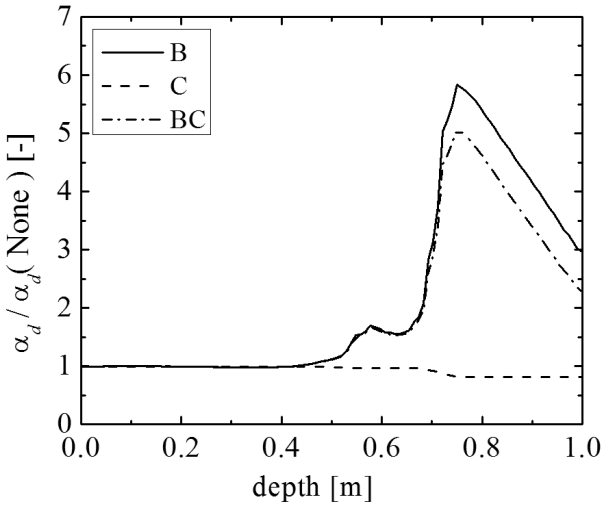

Figure 6.17: Void fraction profile with depth at the stern experimental location.

For depths below 0.5 m the predicted void fraction profiles are very similar and the quotient is close to one. At deeper depths the predicted void fraction profiles start to differ from each other. Figure 6.17 shows that void fraction is the highest when only breakup is active and that conversely, it is the lowest when only coalescence is considered alone. This is due to the fact that, even when the entrainment source is the same, breakup splits large bubbles into smaller bubbles that stay in the water longer. Terminal velocity is higher for large bubbles and therefore reach the free surface faster and escape from the domain. Conversely, coalescence generates larger bubbles from the coalescence of small bubbles and these larger bubbles, by the same buoyancy effect, leave the domain faster. The

difference is more noticeably at depths below the transom bottom since above the transom bottom the bubbly flows is mainly controlled by the entrainment source. Bellow the transom bottom the bubbly flow is conformed mostly by bubbles pulled down the hull from the entrainment regions and transported downstream. A difference can be observed as well between cases B and BC. In agreement with the above discussion, case BC predicts a lower void fraction than case B indicating that bubbles coalesce to form larger bubbles and leave the domain through the free surface.

Predicted void fraction at the experimental bow location is shown in Fig. 6.18 with and without intergroup transfer included. This figure compares the computed results with the measurements from Johansen et al. (2010). Ideally, the entrainment source strength S_0 would be adjusted to match the void fraction at this location and then the void fraction level at the stern would not need to be adjusted but it would be predicted. However, matching the void fraction at the bow would require such a large entrainment strength that void fraction would saturate at the packing void fraction α_{crit} (introduced for the entrainment model in Eq. (3.108)) in most of the rest of the domain. Is for this reason that the source strength is adjusted to match the void fraction at the stern instead.

This is a deficiency of the entrainment model and, as observed in Fig. 6.18, matching the void fraction at the stern largely underpredicts the void fraction at the bow. Due to the magnitude of this mismatch the predicted and measured void fractions are shown on two different scales off by a factor of 200.

6.5.1.3 Size Distribution

Figures 6.19, 6.23, 6.25, 6.27, 6.29 and 6.31 show the void fraction distribution $\alpha_R(R)$ (defined in Eq. (2.7) in terms of the mass variable, see Section 2.4.2 for details on the transformation of variables) at the stern experimental location as a function of depth. These distributions are normalized with the total void fraction α_d at

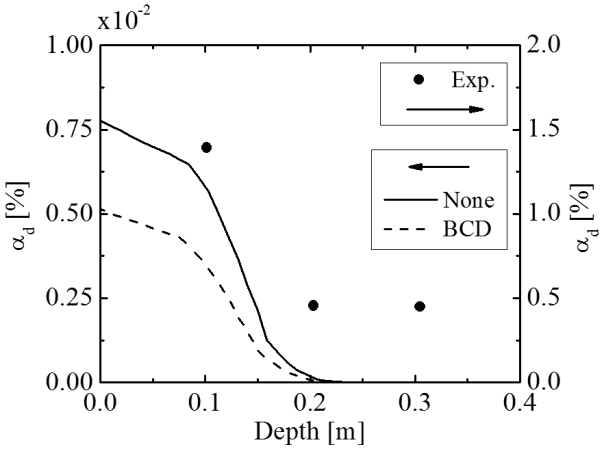

Figure 6.18: Void fraction profile with depth at the bow experimental location.

the particular depth such that the area under these curves is one. These figures show the size distribution predicted when activating/enabling different intergroup transfer terms. The analysis of these figures helps to understand the effect of separate contributions in the Boltzmann equation. In these figures the entrainment size distribution is shown in solid line with open circles as a reference. Recall that this entrainment size distribution is the result from the measurements at the bow location performed by Johansen et al. (2010). In addition, the reader should keep in mind that the bottom of the transom is located at a depth of 0.55 m, see Fig. 6.16.

Figure 6.19 shows the result when no intergroup transfer is used. However, the dispersed phase velocity is still a function of the bubble size. For depths above the transom bottom, $\phi \lesssim 0.5$, the size distribution is strongly determined by the entrainment size distribution due to the strong turbulent mixing at the stern. The size distribution continuously changes as the depth approaches the transom bottom, slowly shifting to smaller bubble sizes. In this region there are two competing effects: larger bubbles tend to escape the domain faster due to their higher terminal velocity, while turbulent mixing at the stern attempts to redistribute the entrained bubbles to deeper depths. The first effect makes the size

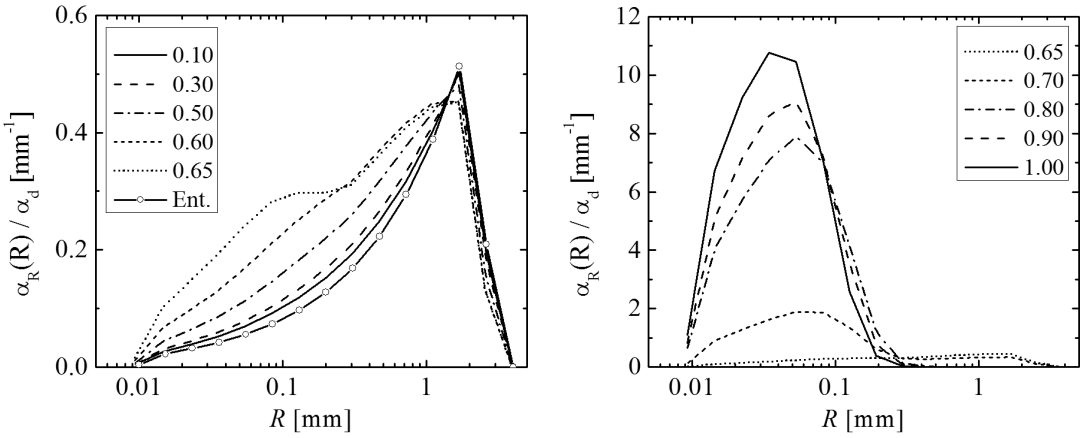

Figure 6.19: Size distribution at the stern. No intergroup transfer (None).

distribution to shift towards small bubble sizes, while the second effect attempts to maintain a well mixed bubbly flow with the entrained size distribution. Below the transom bottom, at depths between 0.6 and 0.7 m, the size distribution suffers a sudden change in shape since the flow also suffers a sudden transition from the highly mixed stern flow above the transom bottom to the boundary layer wake flow below the transom bottom. Therefore, at depths deeper than 0.6 m, the bubbly flow mainly comprises those bubbles transported within the boundary layer flow. These bubbles are entrained at some point through the free surface, are pulled down the hull and eventually get caught in the boundary layer flow and are transported downstream. Since large bubbles have a higher terminal velocity, it is more difficult to pull them down under the hull and therefore the majority of bubbles in the boundary layer flow are small bubbles. This is why the size distribution at the stern shifts to small sizes at depths within the boundary layer wake.

In order to support this idea of small bubbles caught under the hull and transported by the boundary layer flow, the solution is analyzed along a series of selected flow streamlines shown in Fig. 6.20. These streamlines follow the flow upstream

from experimental locations located at different depths and are computed with the mean continuous phase velocity. Four streamlines are computed and they cut the experimental location at different depths: Streamline 1 at 0.507 m, Streamline 2 at 0.545 m, Streamline 3 at 0.64 m and Streamline 4 at 0.74 m. Figure 6.20a shows a close up at the stern and Fig. 6.20b shows an overall view of Athena's bottom where the full trajectory of the streamlines from bow to stern can be seen. In addition, Fig. 6.20 also shows Athena's hull and mean free surface colored with total void fraction.

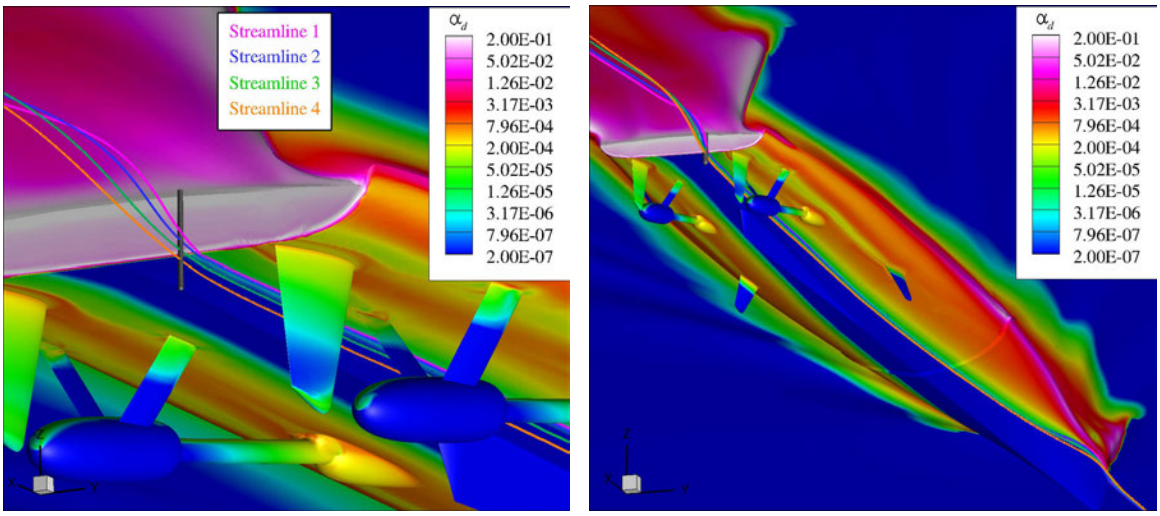

(a) Selected streamlines going through the experimental location (shown in a dark gray stick).

(b) Selected streamlines. Expanded view.

Figure 6.20: Streamlines following the flow upstream from the experimental location.

Total void fraction along Streamline 1 (the one closest to the hull) is shown in Fig. 6.21 for each different case. The location along the streamline is measured by the dimensionless x coordinate, with $x = 0.0$ at the bow and $x = 1.0$ at the stern of the ship. This figure shows that the amount of bubbles underneath the hull, *i.e.*

the void fraction, increases considerably when adding breakup to the case with no intergroup transfer. The reason for this increase in void fraction is that breakup generates small bubbles by splitting the large bubbles entrained at the free surface. While these large bubbles would quickly escape from the domain given their high terminal velocity, smaller bubbles are more easily sucked down the hull and mixed by the turbulent boundary layer. These bubbles therefore contribute to the larger void fraction observed in Fig. 6.21.

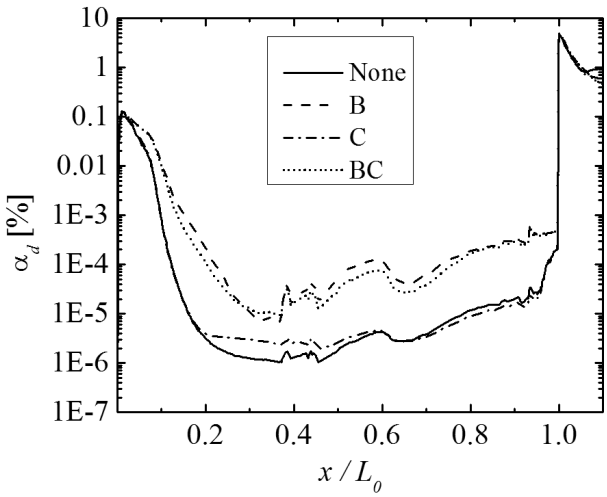

Figure 6.21: Total void fraction along Streamline 1 (the closest one to the hull) for each different case.

When coalescence is added to the case with breakup, *i.e.* the case labeled BC, the void fraction along Streamline 1 decreases slightly. This decrease is explained by the fact that the coalescence of small bubbles generates larger bubbles that leave the domain faster given their higher terminal velocity. When coalescence is activated only, the predicted void fraction along Streamline 1 is close to the one predicted with no intergroup transfer. Differences between these two do not seem to follow any particular explanation. Besides, these streamlines follow fluid particles, not

bubbles, and they could cross with the trajectories of bubbles of different sizes. This effect of fluid trajectories crossing with bubble trajectories could cause changes in the void fraction along a streamline that are difficult to explain without looking at the full three-dimensional solution.

Void fraction size distribution is extracted along each streamline and this is shown, normalized with the total void fraction, in Fig. 6.22 for the case with no intergroup transfer. In this figure each row shows the void fraction distribution on a different streamline, from Streamline 1 to 4, at different x locations ($x = 0$ at the bow, $x = 1$ at the stern and the experimental location is at $x = 1.0106$). The size distribution at $x = 1.01$ (at almost the experimental location) is highlighted with a thicker solid black line. The depth at the experimental location where the streamline goes through is shown with a label and an arrow pointing to the corresponding size distribution (the highlighted one). Streamline 1 is the one closest to the hull (it is at about 1 cm from the wall) and the one closest to the free surface. As the streamlines get away from the hull, they end at a deeper experimental location at the stern.

Figure 6.22 shows that for all streamlines, for $x < 1.0$, the size distribution continuously shifts to small sizes from the entrainment size distribution at the stern. This shift to small sizes is caused by the difference in terminal velocities for each size that effectively filters large bubbles as they escape the domain. The hull geometry is another factor that filters the size distribution as well since it represents an obstruction to the free flow of the bubbles. Size distributions for Streamlines 3 and 4 are only shown for $x > 0.3$ and $x > 0.5$, respectively, since void fraction before those locations is lower than 10^{-10}. For streamlines 1 and 2, when they reach the stern flow ($x > 1.0$), the size distribution changes abruptly to a size distribution close to the entrainment size distribution due to the strong mixing at the stern. For Streamline 4, below the transom bottom when it reaches the stern,

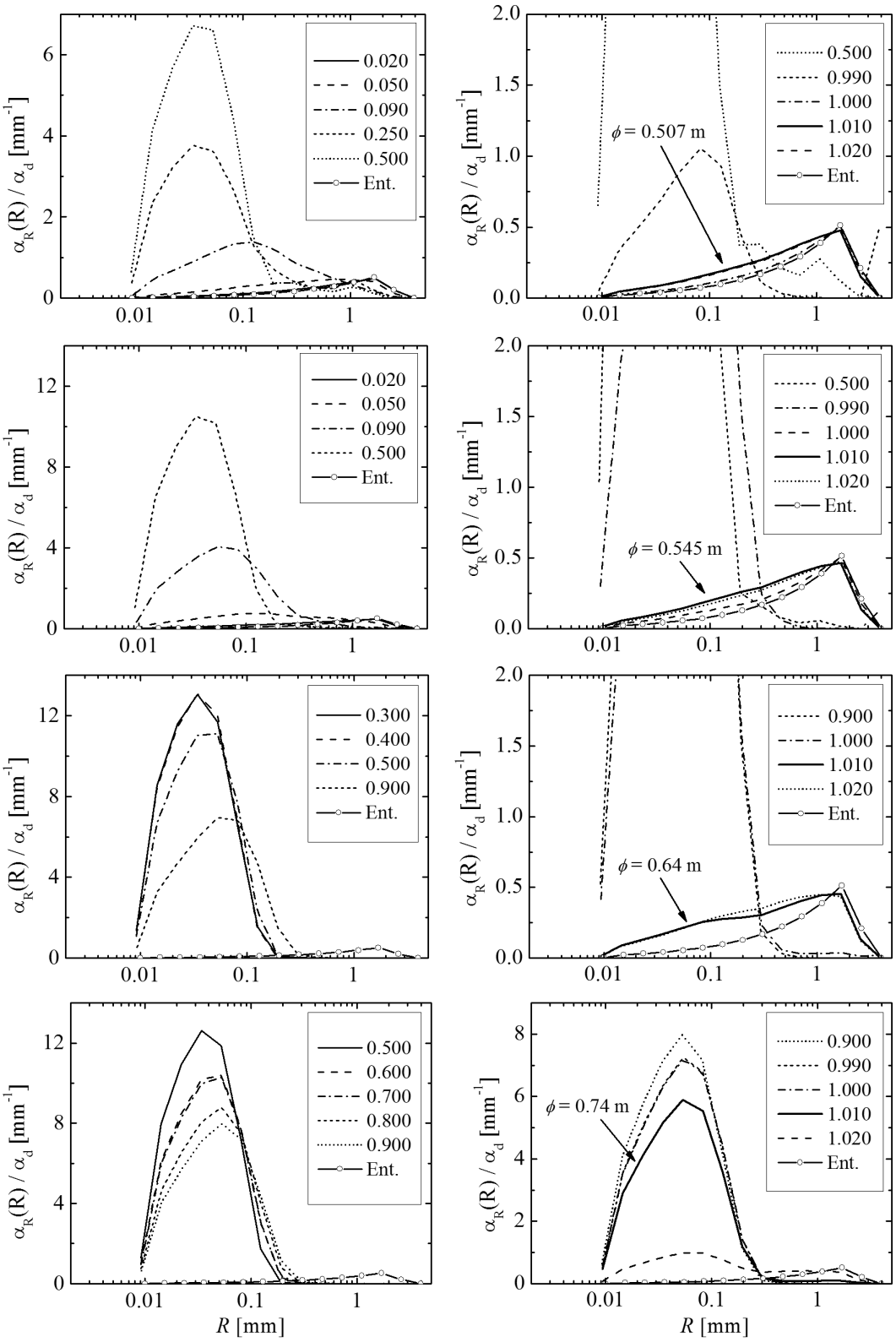

Figure 6.22: Size distribution along streamlines (None).

the size distribution remains the same as in the boundary layer flow. This verifies the hypothesis that these small bubbles at the stern come from below the hull of the ship transported by the boundary layer flow. Streamline 3 is at an intermediate depth where both flows, boundary layer flow and stern flow, meet and mix the two different contributions to the bubbly flow.

In what follows, the same analysis performed for the case with no intergroup transfer is carried out for the remaining cases: B, C, BC, BCD, and Full. Size distribution at the stern is analyzed together with size distribution along the streamlines to determine if the size distribution at the stern is influenced by bubbles coming from below the hull.

6.5.1.4 Size Distribution. Breakup Only

Figure 6.23 shows the size distribution at the stern experimental location when only breakup is enabled. This figure shows that above the bottom of the transom, $\phi \lesssim 0.6$ m, the large bubbles present in Fig. 6.19 are split to smaller bubbles and a new characteristic peak centered at about 700 μm is formed. At a depth of 0.65 m the size distribution starts changing in shape and a new peak, not observed in the case with no intergroup transfer, forms centered around 150 μm. This peak becomes more evident at greater depths than 0.7 m, what would suggest again that these bubbles are generated in the boundary layer and then transported downstream.

Figure 6.24 shows the void fraction size distribution along the streamlines in Fig. 6.20. Recall that in these figures, for Streamlines 1 and 2, the size distribution is extracted from $x = 0$ and thus these streamlines go from an entrainment location (or close to it) to the stern of the ship. Therefore, it is clear from Streamlines 1 and 2 (the first two rows in Fig. 6.24), that the peak covering the range of sizes between 100 μm and 200 μm is formed in the first quarter of the ship's length by the breakup of large entrained bubbles.

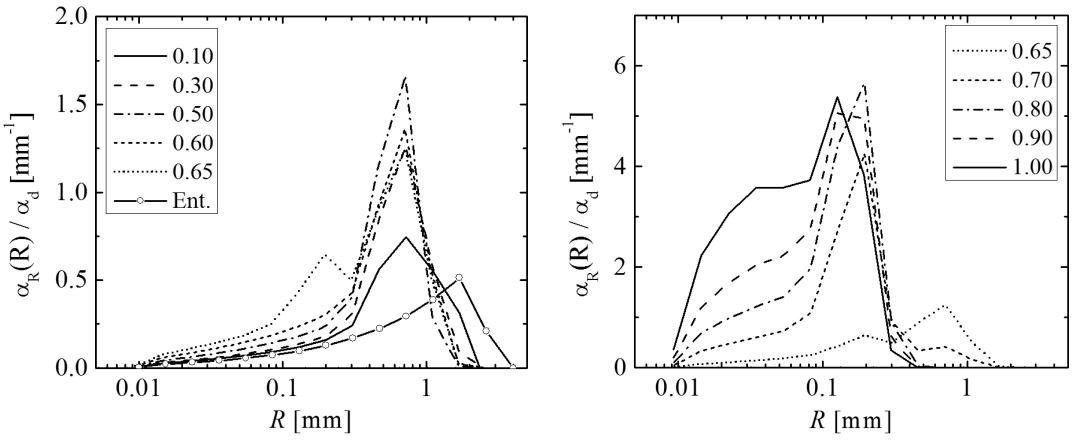

Figure 6.23: Size distribution at the stern. Breakup only (B).

6.5.1.5 Size Distribution. Coalescence Only

Computed void fraction distributions at the stern for the case considering coalescence only are shown in Fig. 6.25. The computed size distributions are similar to those shown in Fig. 6.19 not considering intergroup transfer but some differences are observed. As with the previous cases, the size distribution for depths below 0.65 m is strongly dominated by the entrainment of bubbles and mixing at the stern and therefore the size distribution is close to the entrainment size distribution. However, and comparing with the case with no intergroup transfer shown in Fig. 6.19, the size distribution tail for sizes smaller than ~100 μm decays faster.

The reader should recall that the coalescence model for coalescence in salt water presented in Section 3.2.1, strongly inhibits the coalescence between bubbles with an equivalent radius $R_{m,m'}$ (defined in Eq. (3.62)) smaller than a transitional radius R_t. Coalescence between bubbles with $R_{m,m'} < R_t$ is not inhibited at all but assumed to be as in fresh water. For the salt concentrations found in sea water the transitional radius is estimated at $R_t \sim 160$ μm. This explains the faster drop in the size distribution at smaller sizes than $R_t = 160$ μm. Moreover, a new peak,

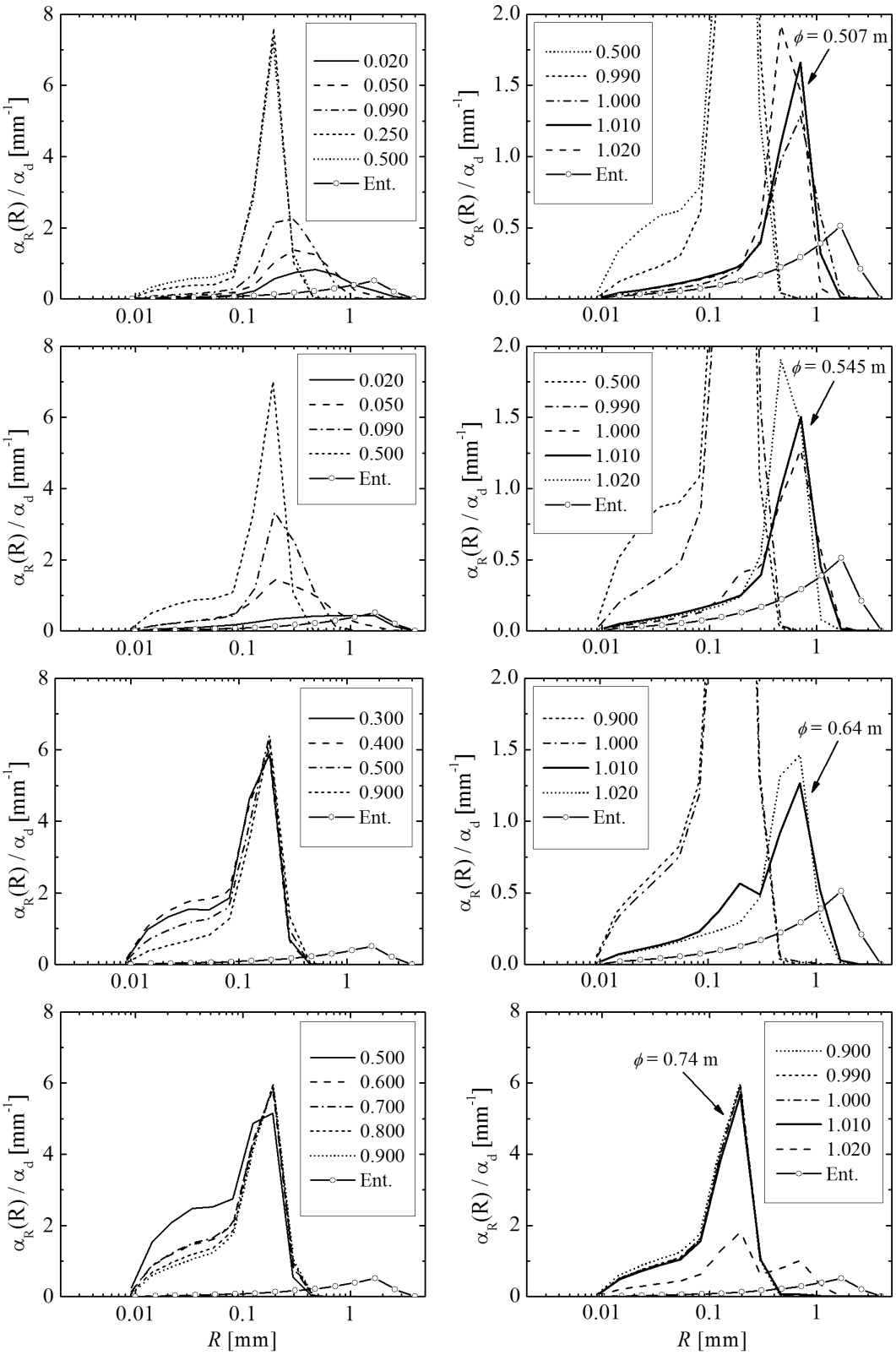

Figure 6.24: Size distribution along streamlines (B).

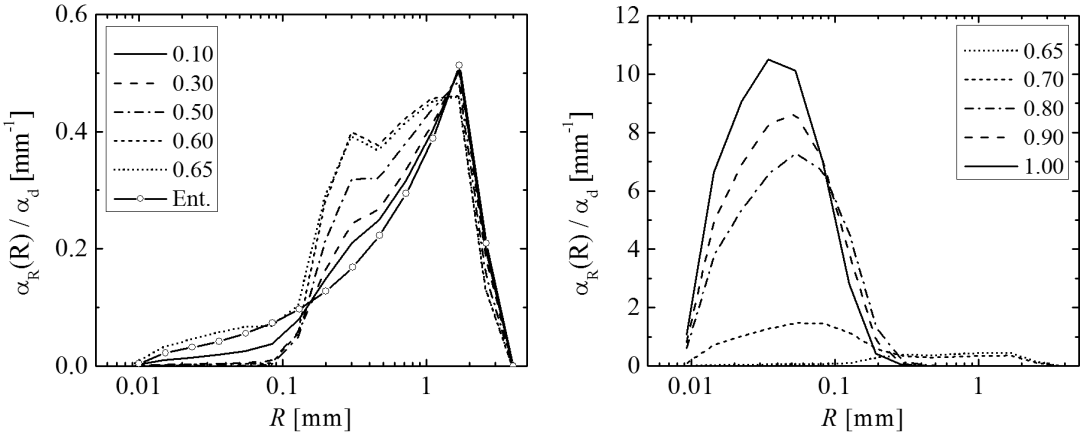

Figure 6.25: Size distribution at the stern. Coalescence only (C).

although not very marked, is formed at bubble sizes around 300 μm. This peak is the result of the coalescence of small bubbles into larger ones.

At depths deeper than 0.7 m the predicted size distributions shown in Figs. 6.19 (None) and 6.19 (C) are very similar, suggesting that the effect of coalescence at these depths is not very strong. This is consistent with the fact that, below the transom bottom, the void fraction suddenly drops to low levels and therefore the collision rate drops as well (recall that the collision rate is proportional to the product of two number densities and thus it drops with the void fraction squared).

The void fraction size distribution along streamlines are shown in Fig. 6.26. The results are similar to the ones obtained with no intergroup transfer, shown in Fig. 6.22: before reaching the stern flow, $x < 1.0$, the size distribution continuously shifts towards small sizes in the range $R \lesssim 200$ μm. For the case with coalescence, however, before reaching the flow at the stern, $x < 1.0$, streamlines 1, 2 and 3 exhibit a lower peak of bubbles with $R \lesssim 200$ μm, indicating the occurrence of coalescence. Nonetheless, at depths below 0.7 m, the size distribution a the stern does not show this peak of bubbles with $R \lesssim 200$ μm since the void fraction of

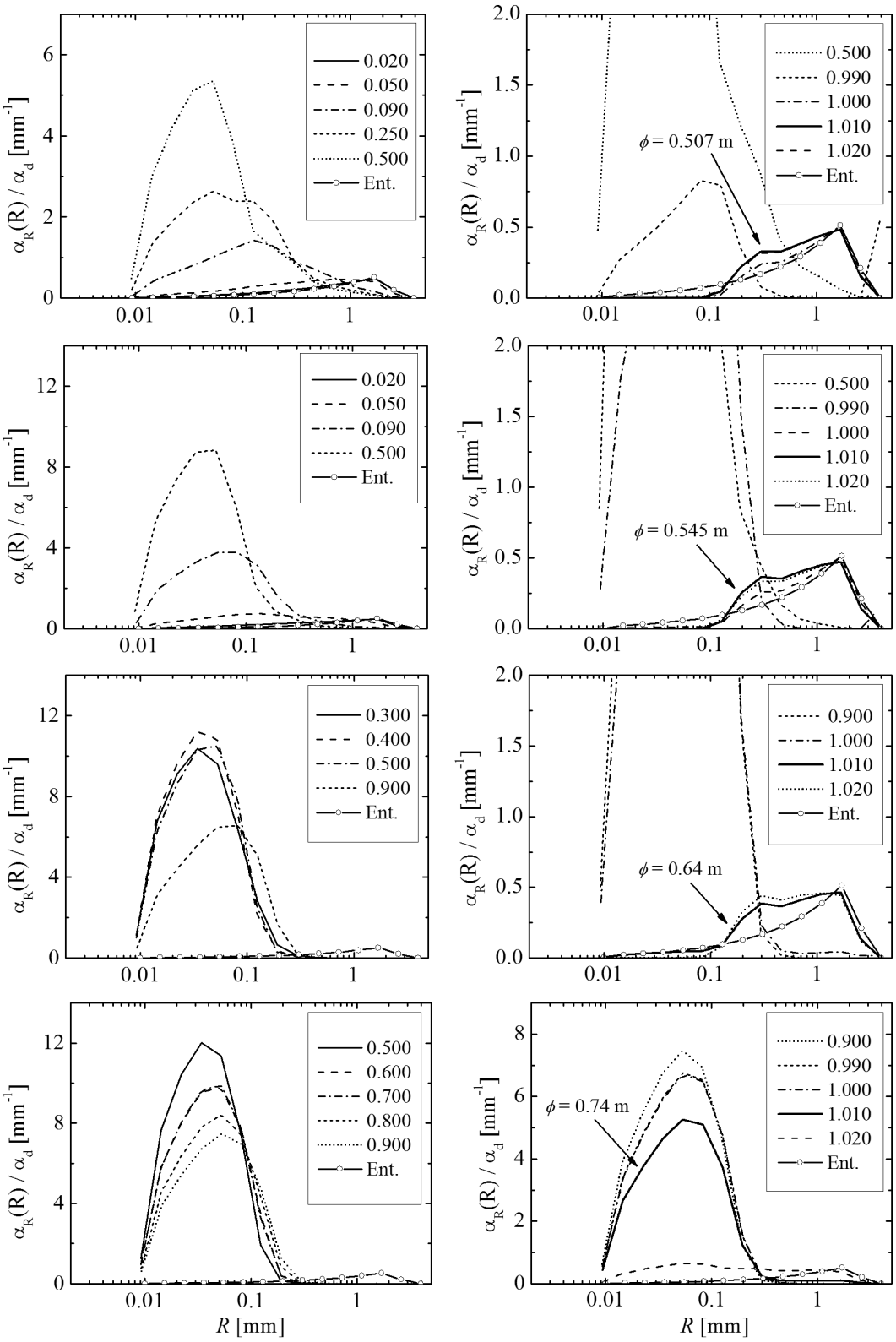

Figure 6.26: Size distribution along streamlines (C).

this contribution is negligible when compared to the entrained void fraction at the stern. Therefore, the fast decaying tail for small sizes and the peak at around ~300 μm observed at the stern does not come from below the hull but it is formed at the stern where coalescence is important due to the high void fraction. The results along Streamline 4 are very similar, if not indistinguishable, from the results computed with no intergroup transfer. This is expected given that at the low void fractions along Streamline 4 the coalescence is negligible.

6.5.1.6 Size Distribution. Breakup and Coalescence

So far, the individual effects of buoyancy, breakup and coalescence were analyzed independently. Figure 6.27 shows the void fraction distribution at the stern when both breakup and coalescence are active. These results are very similar to

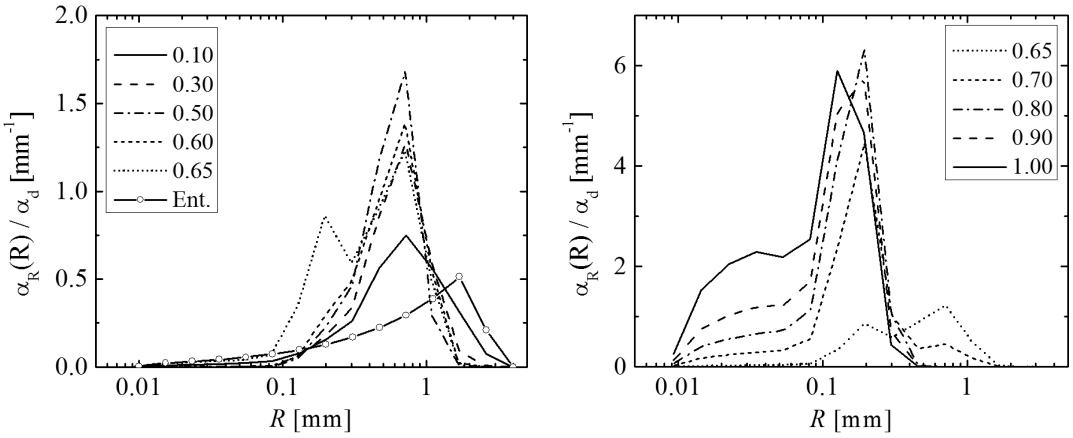

Figure 6.27: Size distribution at the stern. Breakup and coalescence (BC).

the ones computed with breakup only (shown in Fig. 6.23) indicating that the effect of breakup on the solution is more important. However, when comparing Figs. 6.27 and 6.23 the effect of coalescence on the solution can be observed. A

fast decaying tail for bubbles smaller than R_t, not observed when only breakup is active, is noticeably now at depths below 0.6 m. At depths deeper than 0.7 m the effect of coalescence is not as important as it is above the transom bottom. Still, the effect of coalescence becomes noticeable in a lower bubble population for bubbles of radii $R < R_t$ when comparing with the results for breakup only in Fig. 6.23. At $\phi = 0.65$ m the case with breakup only exhibits a peak at 200 μm and the case with coalescence only exhibits a peak at 300 μm, but the combined effect of breakup and coalescence seems to sharpen the peak at 200 μm since smaller bubbles coalesce to this size. However, since the contribution by breakup dominates at 300 μm, the coalescence peak in Fig. 6.25 at this radius is not longer observed.

Size distributions for this case along the streamlines are shown in Fig. 6.28. The same observations made for the size distribution at the stern apply for the size distribution along the streamlines: by comparing with the results using breakup only in Fig. 6.24, breakup is observed to be the dominant effect and the effect of coalescence is observed on the lower tail for bubbles with radius $R < R_t$. Once again the peak at around 200 μm is observed to be formed along the boundary layer while the peak observed at the stern for bubbles around 700 μm is formed at the stern, not in the boundary layer, by the breakup of entrained bubbles.

6.5.1.7 Size Distribution. Breakup, Coalescence and Dissolution

The effect of dissolution on the computed size distribution at the stern is examined by comparing the solutions with no dissolution shown in Fig. 6.27 and with dissolution shown in Fig. 6.29. The effect of dissolution is observed to decrease the amount of bubbles for radii lower than 100 μm. Its effect on larger bubbles is negligible since the surface area to volume ratio is small.

Streamlines in Fig. 6.30 show the same trend observed at the stern: dissolution lowers the population of bubbles smaller than 100 μm.

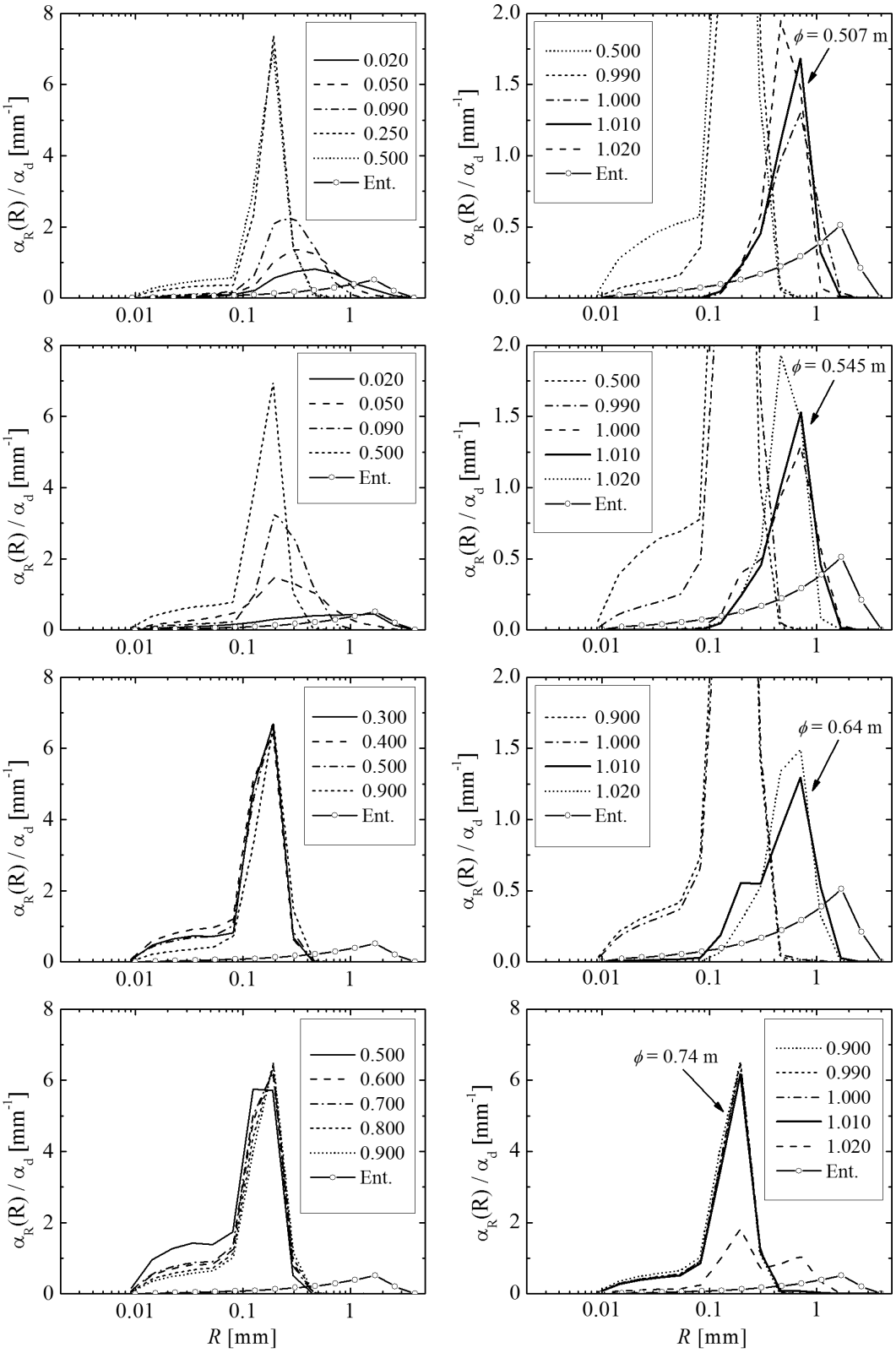

Figure 6.28: Size distribution along streamlines (BC).

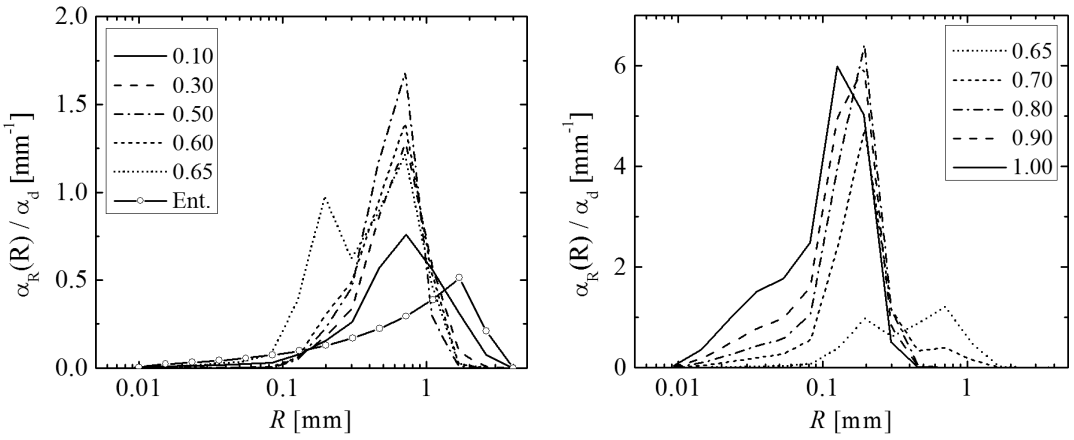

Figure 6.29: Size distribution at the stern. Breakup, coalescence and dissolution (BCD).

6.5.1.8 Size Distribution. Full case

For the Full case all intergroup transfer mechanisms are active and in addition it includes the oceanic background measured by Melville et al. (1995) and presented in Section 3.9, and the rectified diffusion model presented in Section 3.10 based on the work by Raju et al. (2009). The size distribution at the stern for the Full case is shown in Fig. 6.31. In this figure, in addition to the entrainment size distribution drawn in solid line with open circles, the oceanic background size distribution is drawn in solid line with solid circles. Given that the void fraction at greater depths in this case is higher due to the oceanic background and rectified diffusion models, two additional plots show size distribution for depths from 1.0 m to 3.0 m. The effect of the oceanic background on the solution is evident and it practically determines the size distribution in regions where previously, with no background, the void fraction is small (compared with the void fraction levels introduced by the background). These regions are from 0.7 m to 1.1 m, between the transom bottom and the propeller wake, and from 2.1 m and deeper for the flow below the propeller wake. At depths of less than 0.6 m the size distribution is similar

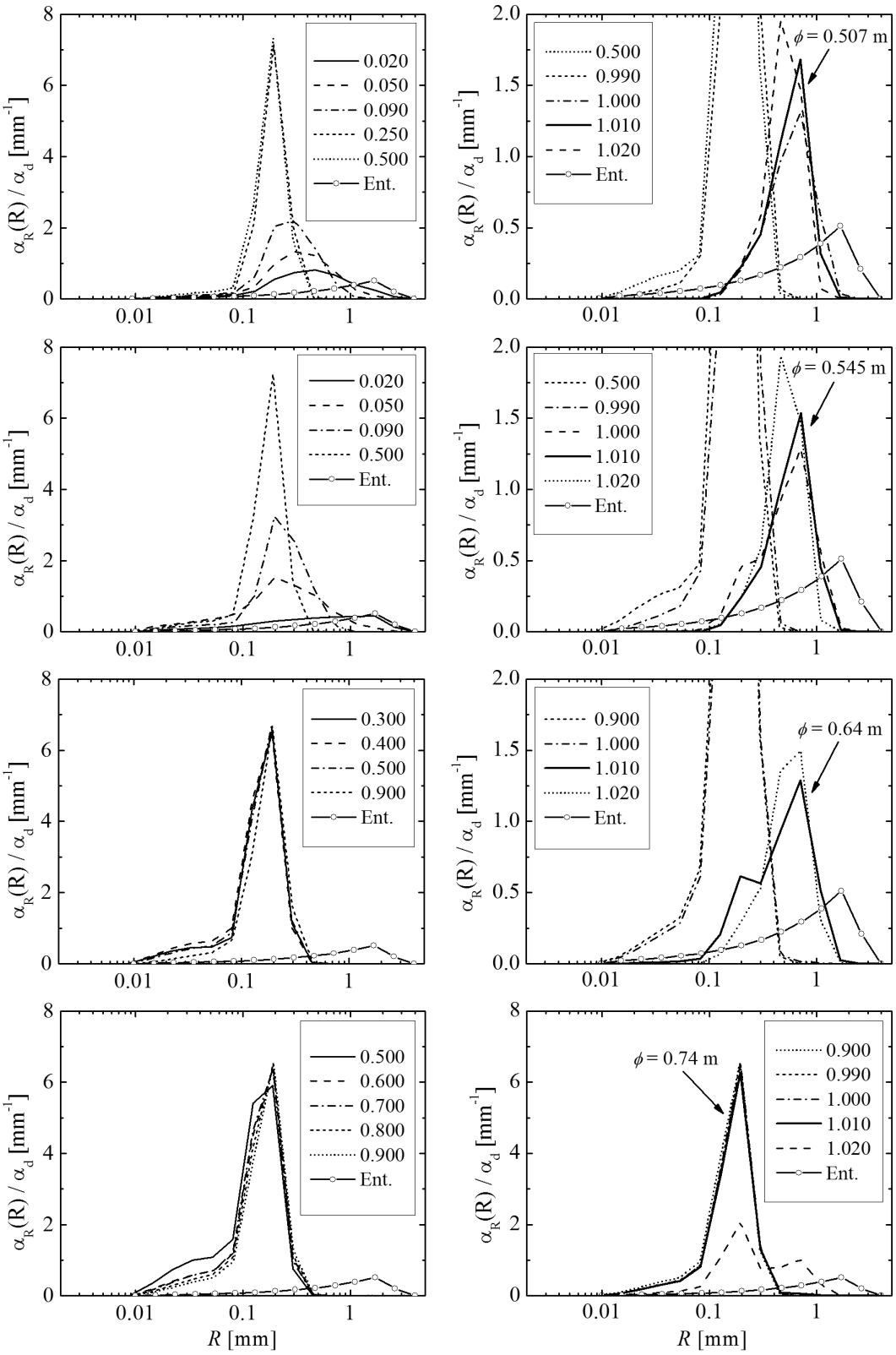

Figure 6.30: Size distribution along streamlines (BCD).

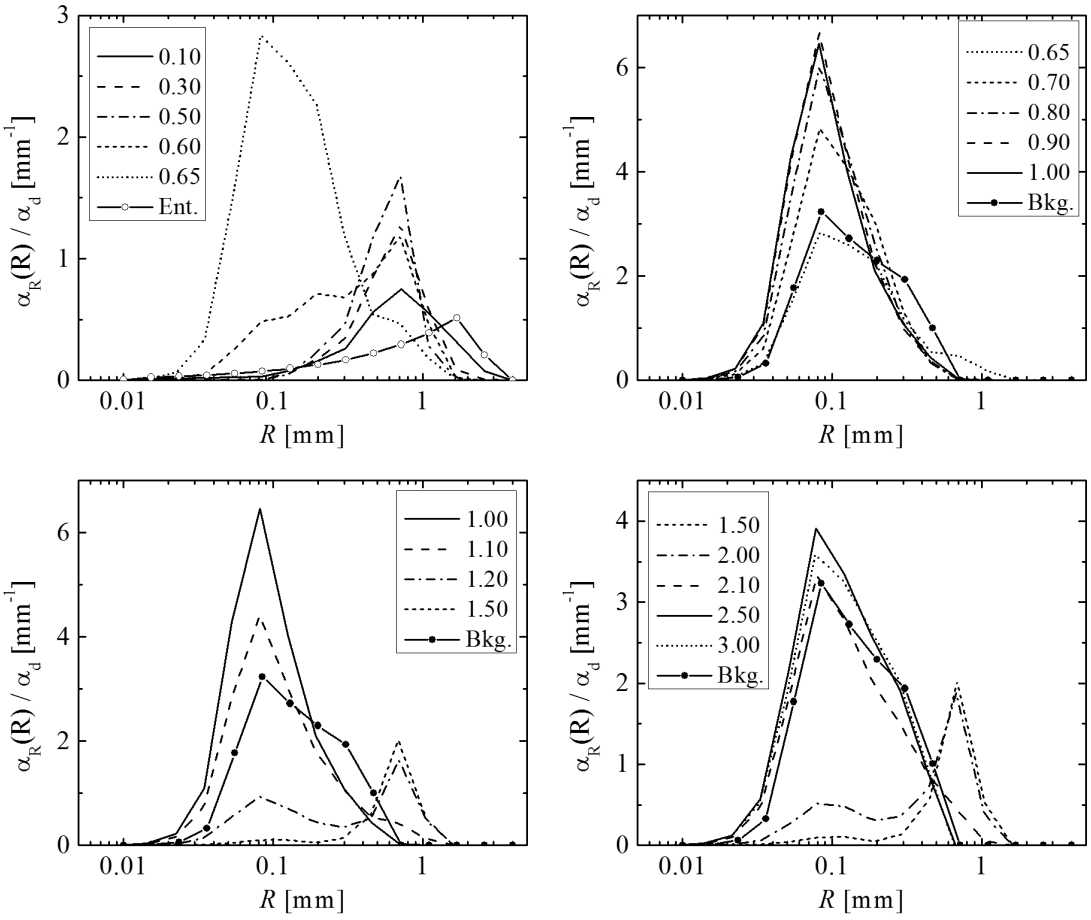

Figure 6.31: Size distribution at the stern. Full case (Full).

to the one computed with the BCD model: entrainment dominates this region, breakup splits very large entrained bubbles and coalescence is responsible for a fast decaying tail at small sizes. The propeller wake is observed at depths between 1.2 m and 2.0 m. This is characterized by bubbles around 700 μm in radius. As shown in Fig. 3.6, and as predicted by the model, bubbles with radius around 130 μm preferentially grow to bubbles with a radius around 700 μm. Bubbles around 130 μm are introduced by the oceanic background and therefore the peak at 700 μm.

Figure 6.32 shows size distribution along the streamlines for the Full case. For

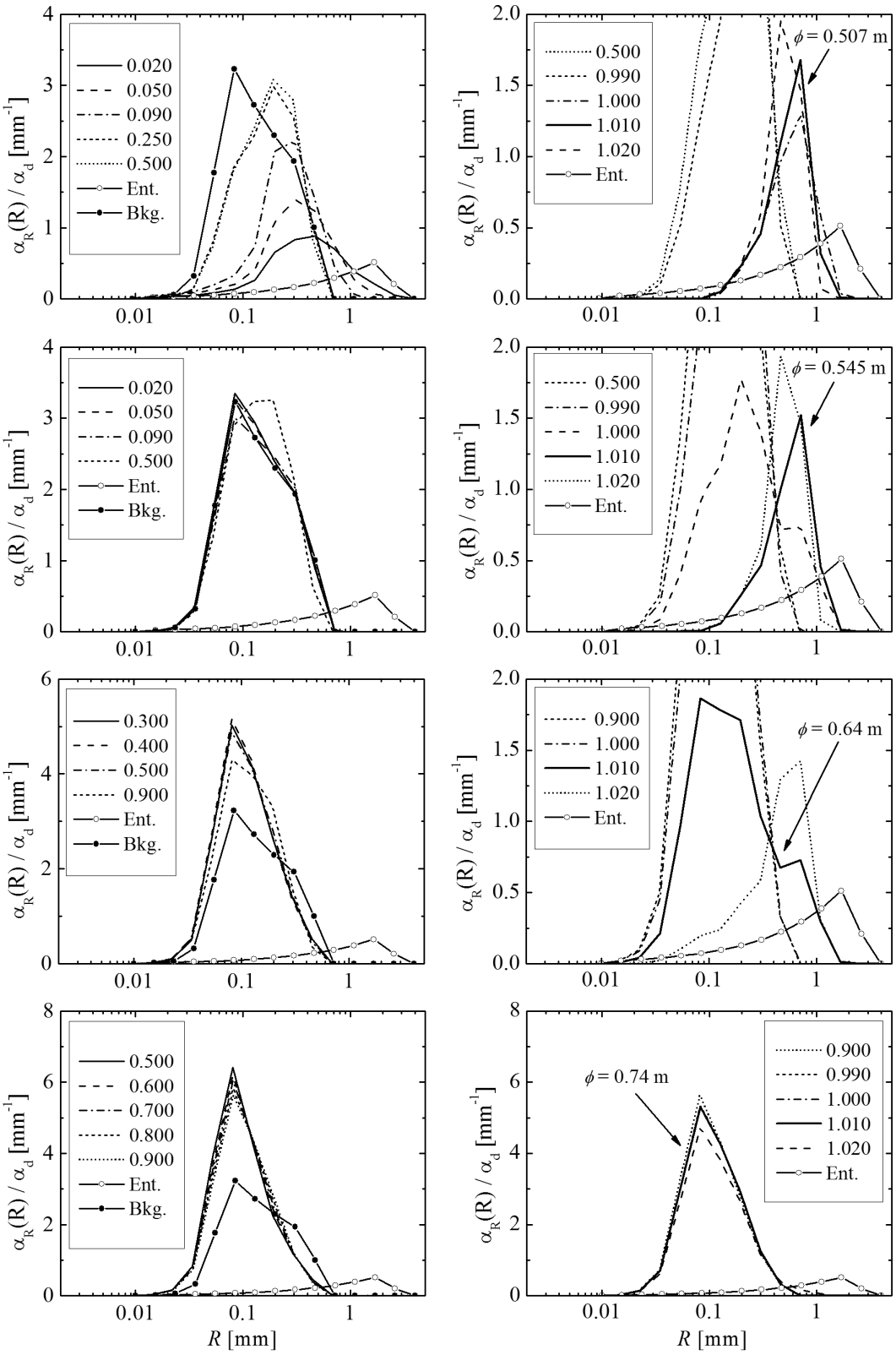

Figure 6.32: Size distribution along streamlines (Full).

Streamline 1 the size distribution starts close to the entrainment distribution at the bow and continuously shifts towards a size distribution similar to the background distribution which contains smaller bubbles. For the other three streamlines the void fraction distribution changes to a size distribution very similar to the background distribution in a shorter distance given that the contribution by entrained bubbles is smaller at those depths.

6.5.1.9 Comparison with Experimental Results

In the experimental results from Johansen et al. (2010), size distributions are reported in terms of ten group-g void fractions (as defined in Eq. (2.28)). The groups defined by Johansen et al. (2010) are summarized in Table 6.4.

Table 6.4: Groups defined by Johansen et al. (2010) used to report bubble size distribution at the stern.

Group	R_g [μm]
1	31.25
2	80.86
3	128.35
4	203.75
5	323.43
6	513.41
7	814.98
8	1293.70
9	2053.62
10	3009.92

In order to compare the predicted size distributions with the results from the experiments, the computed void fraction distribution $\alpha_R(R)$ is integrated on each group-g interval as defined in Table 6.4. Figure 6.33 compares the predicted size

distribution at the stern of Athena with the measurements by Johansen et al. (2010). Predicted results are shown in black lines while the experimental results from

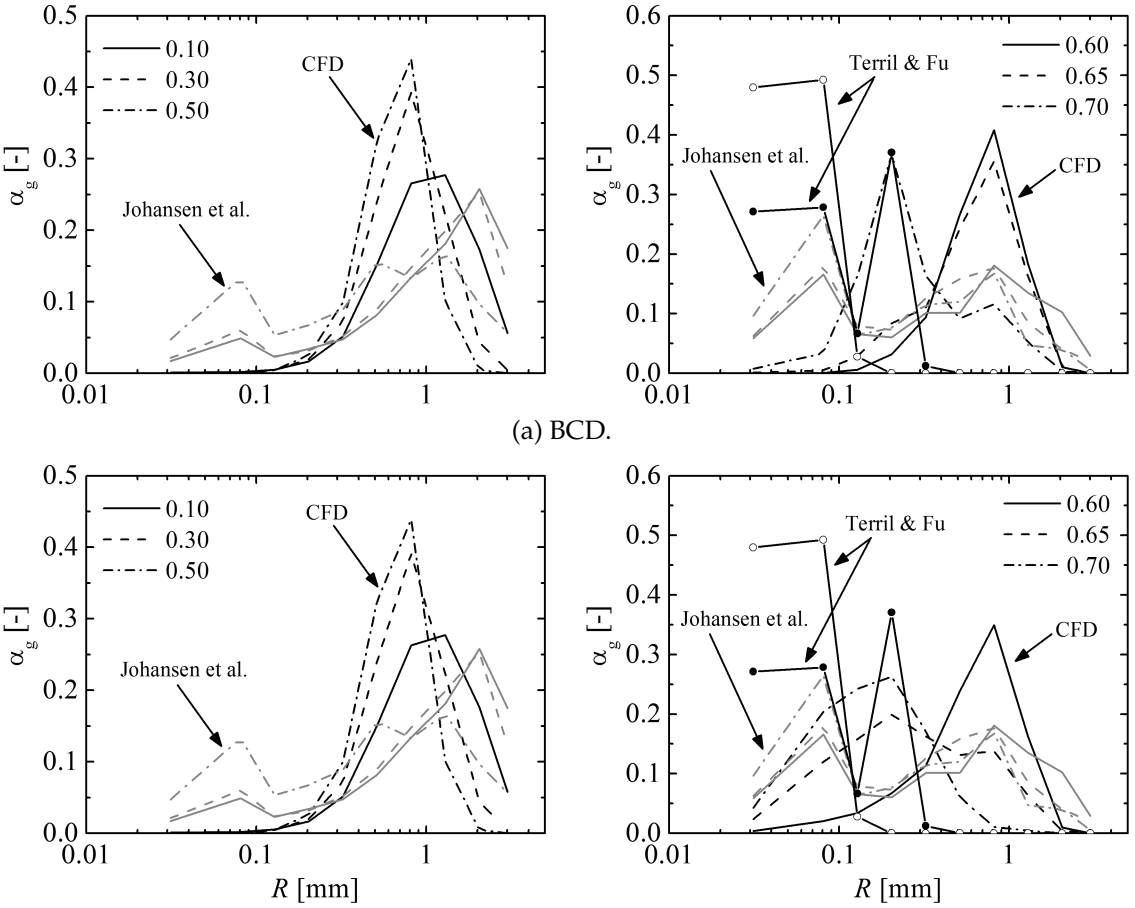

(a) BCD.

(b) Full.

Figure 6.33: Group-g void fraction (with groups as defined in Johansen et al. (2010)) predicted by BCD and Full models compared against measurements.

Johansen et al. (2010) are shown in gray lines. In addition, the size distribution reported by Terril and Fu (2008) is shown in solid lines with circles. To be consistent, the size distribution from Terril and Fu (2008) is integrated over each group-g interval defined in Table 6.4.

Two cases are shown: Fig. 6.33a shows the predicted results with the BCD

model while Fig. 6.33b shows the results obtained with the Full model including oceanic background and rectified diffusion. For the depths shown in these figures bubble growth by rectified diffusion does not play any role. The experimental results pf Johansen et al. (2010) exhibit two characteristic peaks. The first peak starts centered at about $R \sim 2000\mu$m and it moves down to about $R \sim 800\mu$m for depths deeper than 0.6 m. The second peak is for much smaller bubbles of about $R \sim 80\mu$m. Near the free surface, for depths lower than 0.6 m, the predicted results show a peak that starts centered at $R \sim 1000\ \mu$m at 0.1 m and it moves down to $R \sim 800\mu$m for depths deeper than 0.3 m. Even when the experimental and predicted peaks are not located at the same radii, they do correspond with each other. While the experimental size distribution of Johansen et al. (2010) exhibits a peak for bubbles with $R \sim 2000\ \mu$m and this peak persists up to depths of about 0.3 m, the simulation predicts instead a peak at $R \sim 1000\ \mu$m and it quickly shifts to 800 μm at 0.3 m. In other words: the simulation predicts a peak but its position in radius is underpredicted and, the shift to smaller sizes at deeper locations observed in the experiment is predicted as well but it occurs earlier. One reason for this difference could be the break model overestimating the breakup rate and therefore breaking bubbles earlier in depth. Another reason could be that the turbulence modeling at the free surface underestimates the turbulence intensity and mixing and therefore the entrained bubbles do not reach deeper locations. The modeling of turbulence near the free surface is of utmost importance not only to predict the proper mixing but also because breakup and coalescence rates are mostly determined by the turbulent field. Moreover, turbulent intensity at the free surface is one of the parameters determining the intensity of the entrainment source and therefore the amount of entrained air. Predictions using the BCD and Full models are practically indistinguishable from each other at depths lower than 0.5 m, closer to the surface. Below the transom bottom the BCD model predicts a new peak

located at 200 μm. This peak is produced by the breakup of bubbles as they are pulled down underneath the hull as revealed by the comparison between the BCD model and the model with no intergroup transfer. However, the correspondence between this peak and the the one at 80μm in the experimental results of Johansen et al. (2010) is more difficult to establish. When adding the oceanic background, the size distribution at depths deeper than 0.65 m is mostly determined by the oceanic background bubbles. Still, the peak at 80μm, or a closer one, is not predicted by the model. This mismatch could be caused by different reasons: turbulence prediction close to the free surface, entrainment modeling, breakup and coalescence modeling, especially inside the boundary layer, that could lead to the formation of small bubbles by breakup in the boundary layer, etc.

The results reported by Terril and Fu (2008) are for a different location and ship speed. These are at 58'' starboard of the centerline (*i.e.* $y = 0.0313$, dimensionless) for 6 knots and at 0.92 m from the calm water line (this corresponds to a depth of 0.645 m with the water elevation at the experimental location of Johansen et al. (2010)). The experimental size distribution reported by Terril and Fu (2008) exhibits a flat tail for bubbles larger than $R \approx 120$ μm suggesting that this tail could be background noise. It is for this reason, that in Fig. 6.33 the results by Terril and Fu (2008) are reported as they are, with solid circles, and by removing the constant tail for sizes larger than $R \approx 120$ μm, with open circles. The raw results, without removing the tail, surprisingly exhibit a peak for bubbles with radius at 200 μm, as predicted by the simulations. However, if the tail in the experimental results from Terril and Fu (2008) is removed, the 200 μm peak disappears. In any case, the experimental results from Terril and Fu (2008) show a population of very small bubbles, below 10 μm, not shown in the predicted results. This population at very small bubble sizes is also observed in the experimental results from Johansen et al. (2010).

6.5.1.10 Intergroup Transfer Budget and Time Scales

The polydispersed model for bubbly flows used in this work provides a wealth of information, well beyond the bubble size distribution and void fraction. For instance, the intergroup transfer budget (introduced in Section 2.4.3 and previously used in Chapter 5) can be analyzed to help understand the importance of each intergroup transfer mechanism in the solution. In what follows, the budget and time scales are analyzed for the BCD case.

Budget at the stern experimental location for different depths is shown in Fig. 6.34. The line style used for each term is defined in the legend in Fig. 6.34a. Recall that each of these terms represents the number of events per second per unit of volume for a given contribution. The reader should keep in mind that the absolute value of these contributions also depends on the number number density of bubbles at that location. For instance, the number of events per second for any contribution is zero if the number density is zero.

The contribution of coalescence is higher than the one by breakup in Fig. 6.34a. As the void fraction decreases with depth and so does the collision frequency, the contribution by coalescence becomes less important and the number of breakup events eventually exceeds those by coalescence in Fig. 6.34d. It should be pointed out that in Figs. 6.34a and 6.34c the line for breakup deaths breaks at a given size. The reason is that this size is the maximum stable diameter at this depth and breakup does not occur for smaller bubbles. On the other hand, bubble births are continuous for all sizes. At 0.7 m breakup is not shown since at this depth turbulence is not strong enough to induce breakup. The reader could be confused at first by the fact that coalescence events are much higher than breakup events at 0.1 m and 0.3 m when it was previously stated that the peak around 700 μm bubbles appearing in Fig. 6.29 is formed by the breakup of entrained bubbles. However, according to Fig. 6.34, coalescence deaths and births are practically equal at large

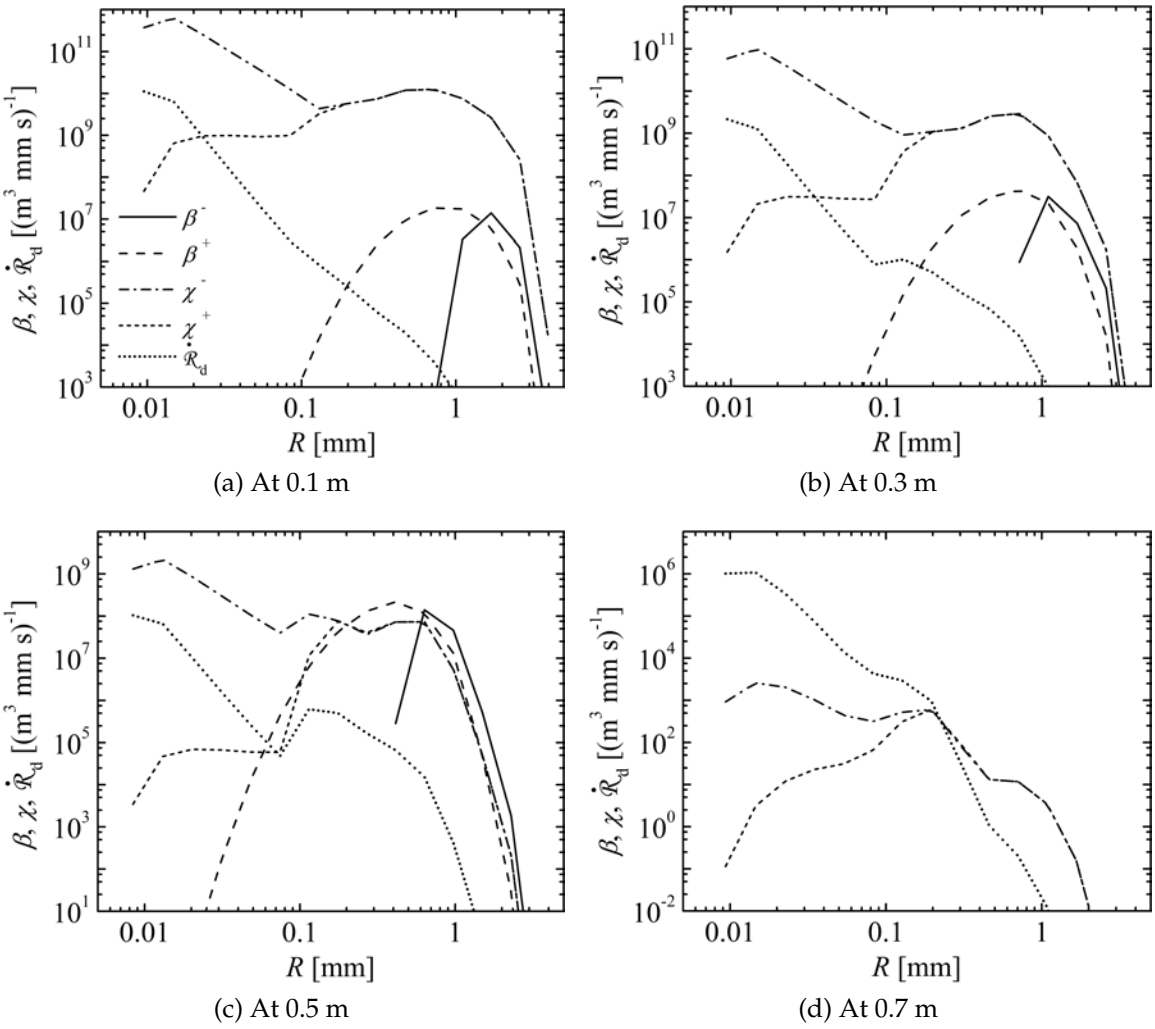

Figure 6.34: Ingergroup transfer budget at the stern experimental location for different depths.

sizes and thus they almost cancel out. On the other hand, for large sizes, breakup deaths are higher than births and therefore large bubbles mainly split into smaller ones explaining the peak observed in Fig. 6.29. Still, even when coalescence births and deaths events cancel out, the reader may still be confused by the large number of coalescence events per second (comparing with the number of breakup events). This is explained by the fact that the coalescence model for salt water (presented in Section 3.5) allows the coalescence between bubbles with an equivalent radius $R_{m,m'}$

(defined by Eq. (3.62)) smaller than a transitional radius R_t which for ocean water is estimated to be 160 μm. Consider the collision event between a bubble of radius R' and a much smaller bubble of radius R, *i.e.* $R \ll R'$. For this case $R_{m,m'} \approx R/2$ and therefore coalescence is not inhibited if $R < 2\,R_t$. Then, and according to this model, coalescence between large bubbles is strongly inhibited but it is still possible for a large bubble to coalesce with a small bubble. At the high void fraction at the stern, the coalescence rate for small bubbles is high and so is the coalescence rate between large and small bubbles. This is why, in Fig. 6.34, coalescence is high at large bubble sizes, because these bubbles are coalescing with small bubbles. Now, when a large bubble coalesces with a small bubble a slightly larger bubble is created and this bubble contributes to the coalescence births term. However, since the large bubble lost and the new generated bubble are almost equal size, the newly born bubble contributes to a size nearly identical to the original large bubble size. This explains why coalescence deaths and births practically balance each other for sizes greater than R_t. Also shown in Fig. 6.34 is the dissolution rate density $\dot{\mathcal{R}}_d$ defined in Eq. (2.96). As expected, dissolution is important at small sizes and becomes dominant at greater depths where coalescence and breakup are negligible.

Intergroup transfer frequencies as defined in Section 2.4.4 are shown in Fig. 6.35. The reader should recall that these frequencies provide the mean number of events per second per bubble. Then, according to Figs. 6.35a and 6.35a, coalescence is the dominant effect at 0.1 m and 0.3 m. However, as previously discussed with the budget analysis, the coalescence rate for large bubbles is high since they coalesce with small bubbles which are allowed to coalesce according to the model for sea water. Since this coalescence events practically do not change the size of large bubbles, the effect of these coalescence events on the size distribution for large bubbles is negligible. Since the void fraction decreases with depth, the breakup eventually becomes more important as shown in Fig. 6.35c. At greater depths, as

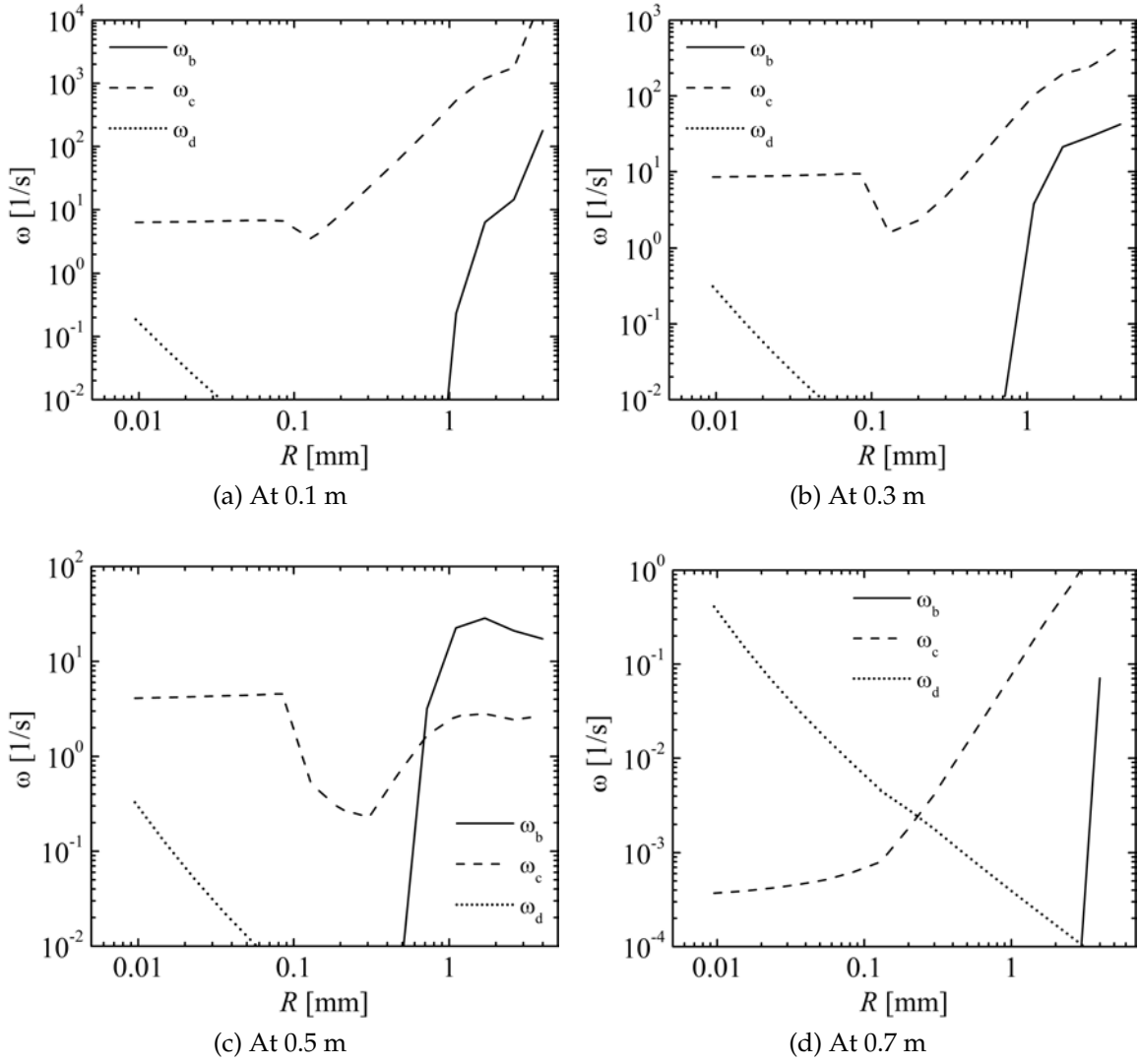

(a) At 0.1 m (b) At 0.3 m

(c) At 0.5 m (d) At 0.7 m

Figure 6.35: Ingergroup transfer frequencies at the stern experimental location for different depths.

in Fig. 6.35d, dissolution is the dominant effect.

It should be noticed from Fig. 6.35 the wide range of frequencies, time scales, introduced by the polydispersed model. Breakup introduces time scales in the order of 10 ms and coalescence can introduce time scales as short as 1 ms. On the other hand, the time scales introduced by dissolution are much larger, on the order of 2 min for 100 μm bubbles and on the order of 2.5 s for 10 μm bubbles.

These time scales should probably be compared against the time step used in the simulations. For Athena with body force propeller the time step is δt = 43.52 ms and for Athena with discretized propeller δt = 2.87 ms. Therefore, the time step used for Athena with body force propeller would not even be enough to capture the dynamics introduced by breakup. This is where the power of the time splitting strategy comes in, allowing to implicitly integrate intergroup transfer in time. For Athena with discretized propeller, the time step is smaller and closer to the time scales involved. Still, the integration of the intergroup transfer terms would be very difficult to perform accurately, *i.e.* implicitly, if the time splitting strategy was not used.

6.5.2 Self-propelled Athena with discretized propeller

This section presents a final computation of the bubbly flow around Athena where the rotating propellers are added to the previous static geometry. The objective of this computation is to test the new capability implemented in a scenario where, in addition to the already complex features of the fixed two-phase computation, includes the rotating surfaces of the propeller and meshes move to accordingly. The inclusion of the discretized propellers and incoming waves to the simulation adds realism and hence it simulates better the experimental conditions. Initially, a single phase run is carried out to find Athena's self propulsion point. Athena possesses controllable pitch propellers, *i.e.* the propeller pitch can be adjusted to make changes in the advance velocity. The specific pitch of the propellers set at the moment the measurements by Johansen et al. (2010) were taken is not know but only the ship's velocity U_0. In order to perform a self-propelled computation comparable to experiments, the pitch of the propellers is set to p/D = 1.11, matching the one used by Crook (1981) who reports propeller's RPM as a function of cruise speed. With the geometry of the propeller fixed, a self-propelled computation is

performed to attain the cruise speed reported in the experiment by Johansen et al. (2010), $U_0 = 5.4$ m/s (10.5 Knots). The procedure detailed in Carrica et al. (2010a) is used to find the self-propulsion point. This procedure uses a PI speed controller[3] to automatically adjust the propeller rotational speed and attain a predefined cruise speed. The single phase computation is performed using a DES model for turbulence where the k-ω blended turbulence model is active near the walls and it switches to an LES model away from the walls (Travin et al., 2004; Xing et al., 2007). The simulation time step is set to $\delta t = 3.3 \times 10^{-4}$ (2.87 ms) to resolve the propeller dynamics.

Figure 6.36 compares the computed self propulsion point with the experimental data from Crook (1981). The data by Crook (1981) is extrapolated to the ship speed used in the simulation to compare against the predicted RPM and a remarkably good agreement is found. The predicted rotational speed is 192.4 RPM and therefore 110.6 time steps are needed to complete one revolution of the propeller. This predicted propeller rotational speed is used to fix the propeller RPM's for the two-phase computation.

Iso-surfaces of the second invariant of the rate of strain tensor $Q = 10000$ are shown in Fig. 6.37. The iso-surfaces and ship hull are colored with piezometric pressure. The DES model of turbulence is able to resolve the very rich vortical structure at the stern and the tip vortices shed from the propeller's blades. The tip vortices travel downstream the propeller, interact with the rudder, and eventually disappear at the end of the propeller refinement where the mesh coarsens its spatial resolution.

It was found in previous runs that the DES model underpredicts the turbulence dissipation ε when comparing with results obtained with the k-ω model. This problem was investigated with simulations of homogeneous and isotropic turbulence

[3]PI stands for Proportional Integral.

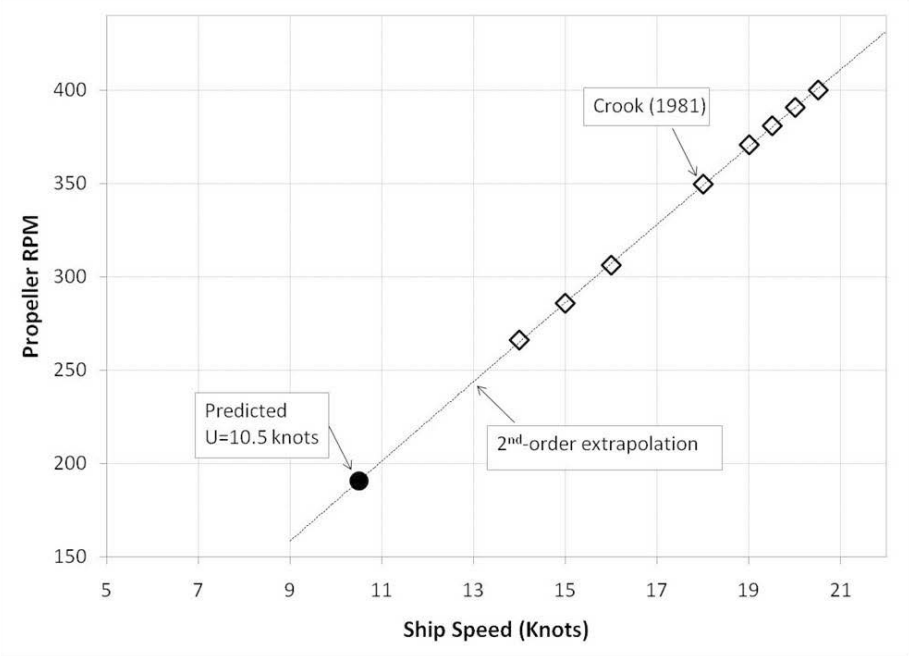

Figure 6.36: Comparison of the predicted self propulsion point with experimental data from Crook (1981).

performed in a box with periodic boundary conditions. The results revealed that a considerable portion of the mechanical energy contained in the large coherent structures resolved by the grid are numerically dissipated instead of being transfered to the modeled part of the turbulent kinetic energy. This excessive numerical dissipation of energy causes the modeled turbulence to be less intensive and the turbulence dissipation is underpredicted. This is topic of ongoing research.

To have a more accurate estimation of the dissipation rates so important for the prediction of breakup and coalescence rates, or at lest to avoid the extra numerical dissipation, the two-phase computation is performed using RANS with the k-ω blended model of turbulence instead of DES. The single phase computation is extended for two more ship lengths using the k-ω blended model to have a well developed single phase solution.

The two-phase computation is restarted from the last available single phase

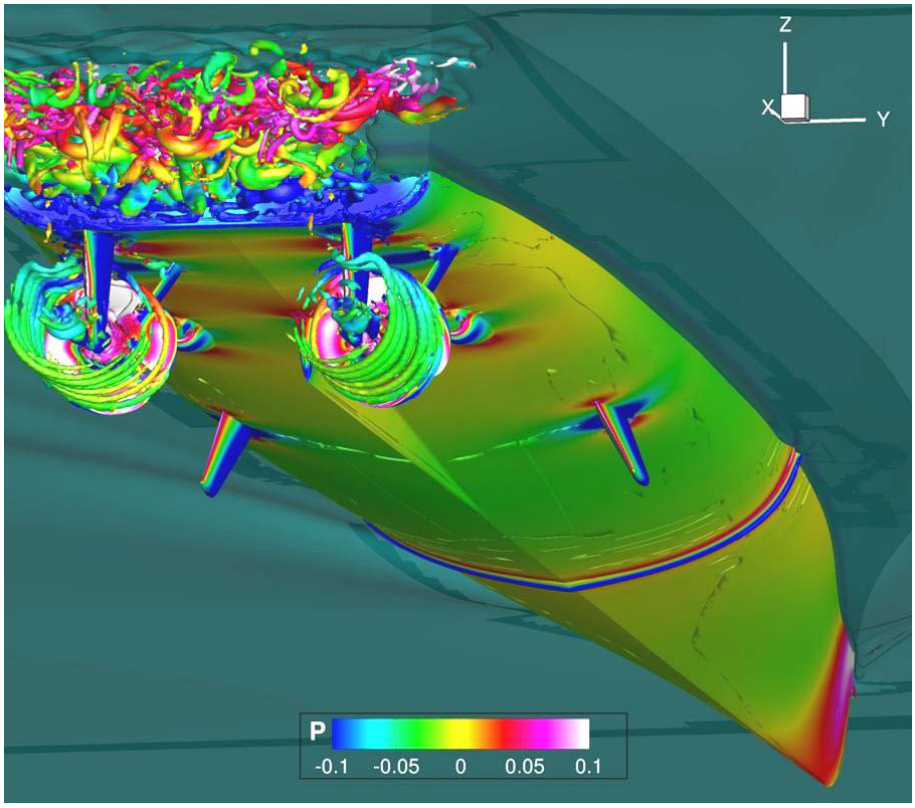

Figure 6.37: Isosurfaces of $Q = 10000$ colored with contours of piezometric pressure.

computation. This simulation attempts to replicate better the conditions of the experiments and its main features are:

- Fully appended geometry.
- Discretized rotating propeller. Self-propulsion point is predicted. Grids move along with the geometry of the propeller.
- Full scale computation for both continuous and dispersed phase. Wall functions used.
- Complete polydispersed model includes breakup, coalescence and dissolution models.

- Incoming waves with the wavelength observed in the experiments by Johansen et al. (2010).
- Oceanic background model (Section 3.9) based on measurements by Melville et al. (1995).
- Rectified diffusion model (Section 3.10) based on transfer tables provided by Raju et al. (2009).
- The grid system, including the propeller, contains 22.6 million grid points.
- The full model solves for 1.68 billion of unknowns per time step.
- 6060 time steps are needed to run two ship lengths and it takes 5 days on a Cray XE6 supercomputer using 448 processors.

The number of processors used in the two-phase computation is doubled (with respect to the number of processor used in the single phase run) to decrease the running time. The load is distributed among 416 processors and 4 processes are used for the overset solver though 32 processors are requested for the overset solver to allocate a full computational shared-memory node per overset solver instance since each of these requires a significant amount of memory. In total, the computation uses 448 processors and is run on a Cray XE6 supercomputer.

The computation takes a total of 72 seconds per time step. Of these, 29.5 seconds are spent by the multiphase solver (*i.e.* 41.0% of the total time). In the multiphase solver, 18.3% of this time is spent by the momentum solver, 48.5% by the number density transport solver, and 30.9% by the intergroup transfer solver.

Due to the fact that the propeller rotates during the computation, and then the geometry changes with time, instantaneous results are presented instead of mean quantities as done with the case with a body force model. An additional difference with the case using a body force model is that the rectified diffusion model is

activated only in regions with a second invariant of the rate of strain tensor greater than a certain threshold. Then, the rectified diffusion model is activated inside the propeller disk only if $Q > 4000$. This restriction is used to replicate the results from the simulations performed by Raju et al. (2009) that show that the bubbles grown by rectified diffusion at the propeller tips are trapped by the tip vortices. The threshold used is arbitrarily set for the purpose of demonstration.

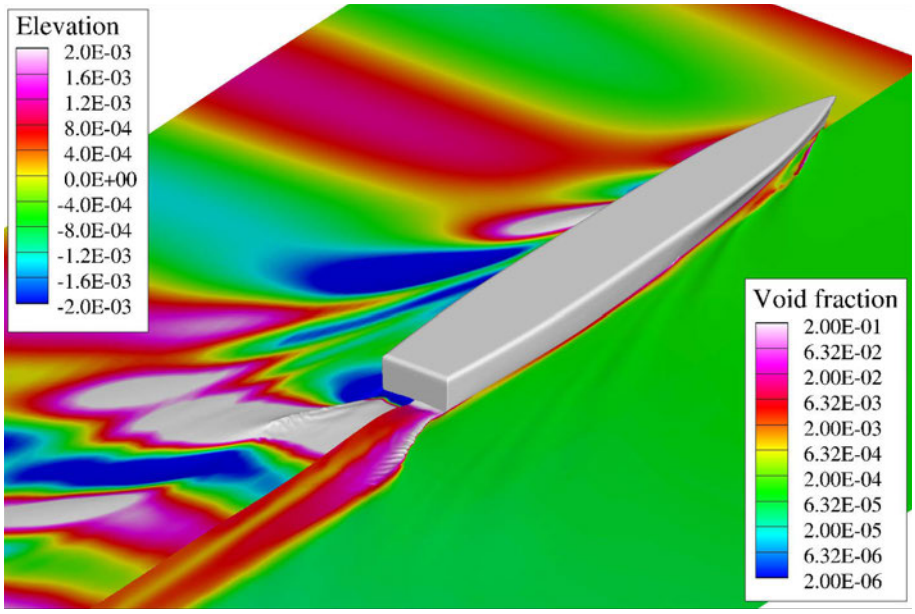

Figure 6.38: Free surface colored with instantaneous void fraction on starboard and with surface elevation on port.

Figure 6.38 shows the computed free surface colored with void fraction on the starboard side and with elevation on the port side. Contour levels for elevation are made to saturate to highlight the incoming waves. The void fraction levels shown in this figure are as high as 20% but, as with the case with the body force model, the void fraction can be as high as 30% or more in some regions of the domain during some transients. This illustrates once again the robustness of the code in this more

complex computation. The shoulder waves at the stern exhibit short scale ripples not observed in the case with the body force model. These short length ripples have a time scale that is not resolved in the computations of Athena with no discretized propeller due to the larger time step used.

Slices colored with void fraction are shown in Fig. 6.39 and show the evolution of the bubbly wake around and behind the ship. The predicted void fraction

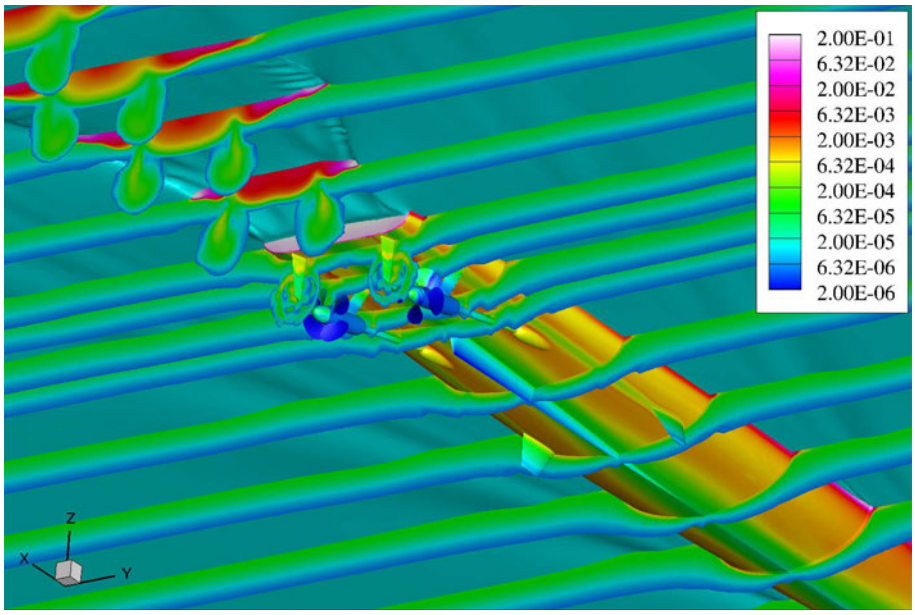

Figure 6.39: Slices and hull colored with instantaneous void fraction.

levels on the hull are very similar to the ones predicted for Athena with body force model. This is expected since the solution remains practically unchanged near the hull upstream the propellers. As before, the bubbly wake transported with the boundary layer flow underneath the ship is pulled down by vortices shed from the shaft and attracted by the propeller suction. As bubbles go through the propeller they grow in size by rectified diffusion, but in this model they are only allowed to grow in regions with $Q > 4000$. There are no corrections accounting for

the fact that, for this model with discretized propeller, the effective volume where rectified diffusion is active is smaller than in the case with the body force propeller model, where the rectified diffusion model is active all inside the propeller disk. Therefore, the void fraction downstream the propeller is not as high as it is for Athena with body force model. In other words, the volumetric source for rectified diffusion remains the same but it is active inside a smaller volume. This effect is not important for the demonstration purposes of this case, but it should be considered in the future.

The computations using a discretized propeller provide very detailed flow structures behind the propeller. These structures are very strong and mix the bubbly flow very efficiently. Comparing the slices in Fig. 6.15 for Athena with body force model and in Fig. 6.39 for Athena with discretized propeller, it can be observed that the wake far behind the ship stays deep at the propeller's depth longer in the case with discretized propeller, while in the case with the body force model the wake is observed to rise up towards the free surface.

In Fig. 6.40 the very strong vortices shed from the tip of the propeller blades are shown with an iso-surface of $Q = 4000$ colored with void fraction. The hull is colored with void fraction as well. The shape of the bubbly wake around the ship is visualized using a translucent iso-surface of $\alpha_d = 10^{-3}$. The same depleted wake behind the stabilizers observed for Athena with body force propellers is predicted for this case as well. The contours on the hull and the iso-surface of void fraction exhibit a wavy pattern along the hull which is induced by the periodic entrainment of bubbles driven by the incoming waves. Figure 6.40 shows vortices shed from the base of the struts which carry void fraction with them. In addition, the strong horse shoe vortices at the base of the rudders attract a large amount of bubbles as well and the iso-surface of void fraction wraps around them.

Figure 6.41 shows the void fraction and depth as a function of time at $(x;\ y;\ z) =$

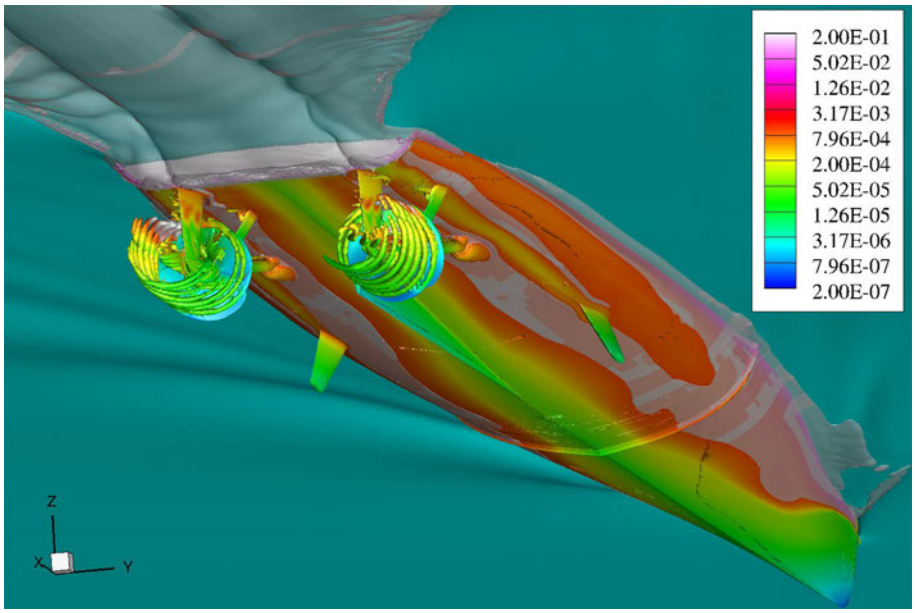

Figure 6.40: Iso-surface of $\alpha_d = 10^{-3}$ and iso-surface of $Q = 4000$ and hull both colored with void fraction.

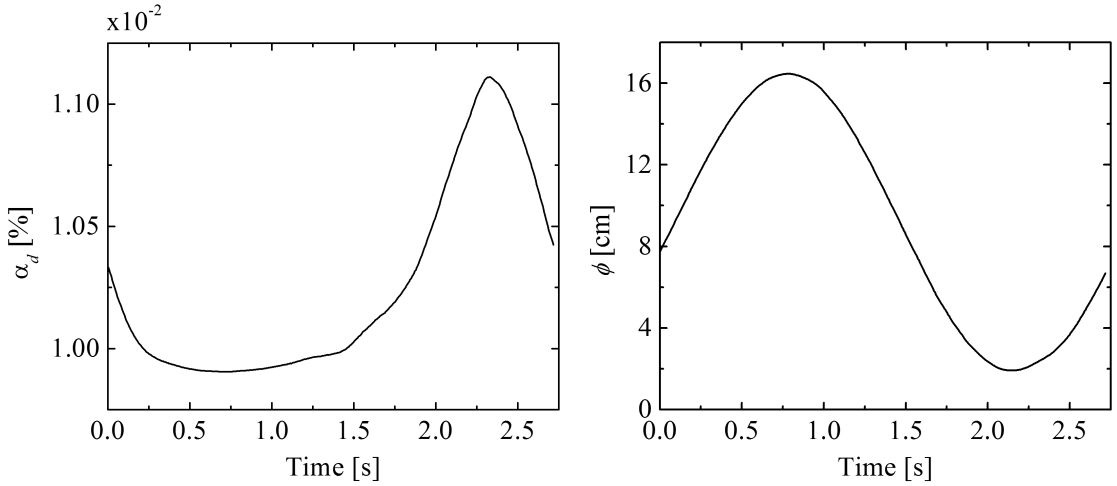

(a) Void fraction.

(b) Surface elevation

Figure 6.41: Void fraction and surface elevation at the bow monitor.

(0.284; 0.0779; −0.004), the bow experimental location shown in Fig. 6.13, for one wave encounter period. Due to the continuous arrival of waves, the wave breaking at the bow is unsteady with the period of arrival, or encounter period.

This unsteady breaking at the bow drives the periodic entrainment of bubbles which are transported downstream and cause the void fraction peak in Fig. 6.41. Depth at this location changes periodically as expected due to the incoming waves.

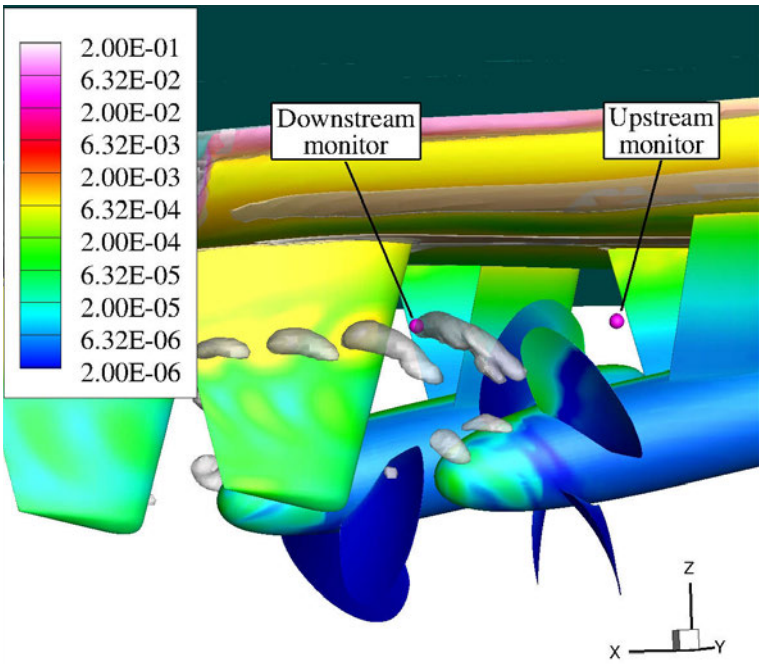

Figure 6.42: Monitors upstream and downstream the propeller used to analyze the solution. In addition, the iso-surface of $\alpha_d = 10^{-3}$ and hull colored with void fraction are shown.

To illustrate the effect of the rectified diffusion model on the results, the solution is analyzed on two monitor points located upstream and downstream the propeller. These locations are upstream at $(x;\ y;\ z) = (0.939;\ 0.0368;\ -0.0265)$ and downstream at $(x;\ y;\ z) = (0.965;\ 0.0368;\ -0.0265)$, both shown in Fig. 6.42.

The void fraction as a function of time for one encounter period is shown in Fig. 6.43 for the location upstream the propeller and in Fig. 6.44 for the downstream location. Upstream the propeller, the void fraction exhibits fluctuations which are mainly induced by the continuous vortex shedding coming from the shaft.

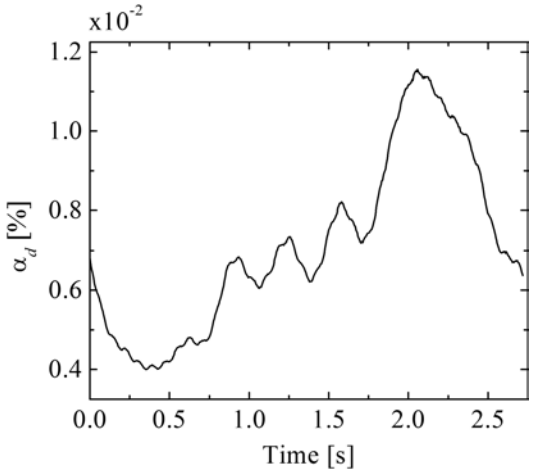

Figure 6.43: Void fraction at location upstream the propeller.

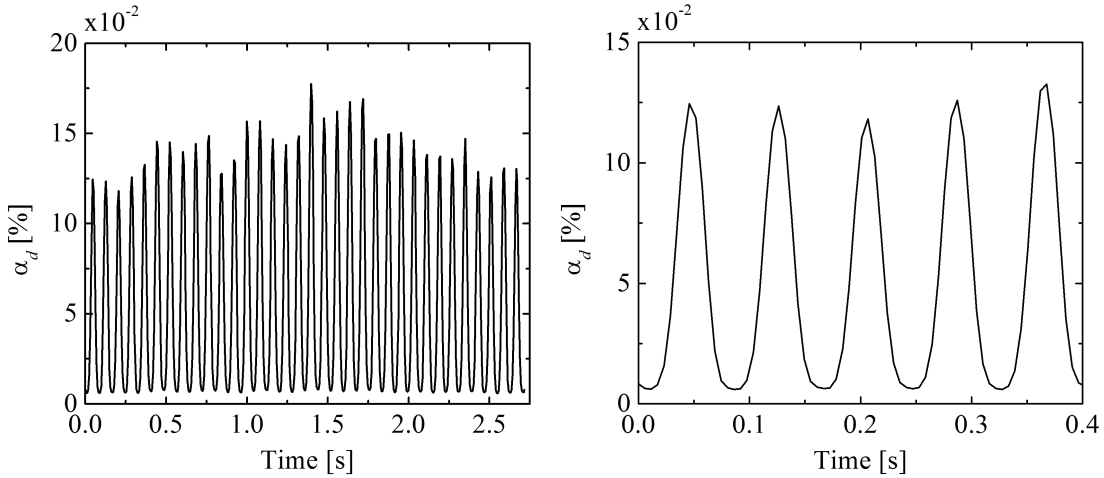

(a) Time evolution during one wave length period.

(b) Smaller time window where the period of one blade passage can be appreciated.

Figure 6.44: Void fraction at the location downstream the propeller.

Downstream the propeller, as shown in Fig. 6.44a, the void fraction shows high frequency fluctuations that if analyzed in the shorter time window in Fig. 6.44b are found to have the period of one blade passage. In addition, these figures show the significant increase in void fraction due to the growth of the bubbles at expense of the air dissolved in the water.

CHAPTER 7
SUMMARY, CONCLUSIONS AND FUTURE WORK

In this thesis a mathematical model for the modeling of polydisperse bubbly flows with a focus on ship hydrodynamics is implemented in CFDShip-Iowa V4.5. The model is based on a two-fluid formulation coupled with a Boltzmann transport equation describing the polydispersed bubbly phase. The numerical implementation of the model used in this work is two-way coupled, *i.e.* the bubbly phase solution depends on the surrounding continuous phase and, conversely, it modifies the continuous phase solution as well[1]. The mathematical model and numerical methods are reviewed and analyzed in depth. This Ph.D. thesis contributes with the development of novel numerical methods for the accurate, robust and efficient numerical solution of the governing equations. The implemented model is applied to the computation of the polydispersed bubbly flow around a real full scale ship using the latest available models and computational techniques. In addition, this thesis contributes with the identification of modeling and numerical implementation issues that can be improved and need further study.

7.1 Main Conclusions

The main conclusions of this research are:

Physical models:

- The model of Luo and Svendsen (1996a) underpredicts the breakup rate and some physical inconsistencies are observed in the modeled daughter bubble size distribution.

- The Lehr et al. (2002) model predicts a maximum stable bubble diameter which is in agreement with the well accepted Hinze's correlation. The Luo

[1]Many implementations found in the literature use a one-way coupling approximation, *i.e.* the dispersed bubbly phase does not have any affect on the surrounding fluid. Therefore, the continuous phase is decoupled from the dispersed phase and can be computed separately.

and Svendsen (1996a) model does not agree well with Hinze's correlation.

- A model to estimate shear induced by turbulence is proposed in Section 3.3.2. This is used in the estimation of breakup by shear.

- Breakup by shear in Athena's boundary layer is studied in Section 6.4. The model predicts almost no breakup by shear. However, this phenomenon is expected to be important in the generation of small bubbles observed at the wake of a ship and therefore further research on this topic is needed.

- Section 3.5 attempts to provide a model to correct for the presence of dissolved salt in ocean water. However, ocean water contains many other impurities and the proposed model may be an oversimplification. More experimental work on this topic is indispensable for the development of new models.

Numerical methods:

- The fixed pivot method of Kumar and Ramkrishna (1996) is analyzed in detail in Chapter 2 and appropriate boundary conditions are developed which ensure conservation of mass of the dispersed phase.

- The novel two-phase projection method developed for this thesis in Section 4.4 implicitly solves the coupling between pressure and void fraction that otherwise would lead to the divergence of the solution.

- The time splitting procedure presented in Section 4.2 allows to accurately and efficiently integrate the Boltzmann equations in both space and bubble sizes. The problems presented in this work would have been impossible to solve without this method.

- TVD convection schemes minimize wiggles in the solution of the number density transport that could lead to unphysical negative results.

- Disperesed phase velocity may decouple from number density when dispersive forces are included in the model. Section 4.8 presents a numerical method that successfully solves this problem.

Bubbly flow around Athena:

- Model implementation and performance is assessed with the simulation of a real full scale ship. The model includes fully appended geometry, rotating propellers (and therefore moving meshes are used), incoming waves, full polydispersed model, oceanic background and rectified diffusion. Many of these features are unique to this computation making it the first of its kind.

- Main entrainment locations are predicted at the bow and masker breaking waves, at the highly aerated stern flow and at the stern shoulder waves.

- When calibrating the entrainment model to match with experiments the void fraction profile with depth at the stern, the void fraction at the bow is underpredicted by at least two orders of magnitude. This problem illustrates the need for more accurate models of air entrainment.

- A finger of bubbles in the wake behind Athena is predicted. These bubbles are entrained upstream and pulled down the hull from the surface and further transported downstream. Vortex shedding from the propellers' shafts pulls them down even deeper where the suction flow of the propellers traps and accelerates them into the wake of the ship.

- The void fraction around the hull increases significantly when the breakup model is enabled. This is caused by the breakup of large entrained bubbles that otherwise would escape faster given their higher terminal velocity.

- Size distribution measured at the stern by Johansen et al. (2010) exhibits two main peaks for large bubbles at about 2000 μm and for small bubbles at 80 μm.

The model predicts a peak of large bubbles at 1000 μm and a peak of small bubbles at 200 μm.

- The 1000 μm peak from the model is caused by the breakup of large entrained bubbles.

- The larger bubbles observed in the experimental results from Johansen et al. (2010) are mixed deeper underneath the free surface indicating a possible underprediction of the modeled turbulent mixing near the free surface.

- The 80 μm bubbles observed in the experimental results from Johansen et al. (2010) appear at depths below the transom bottom suggesting that these bubbles are transported with flow coming from the boundary layer. Similarly for the 200 μm bubbles predicted by the model. No solid explanation for the mismatch of these peaks was found. However, possible causes are discussed.

- The size distribution reported by Terril and Fu (2008) exhibits a peak for bubble radii of 200 μm in agreement with the simulation results. However, this peak disappears if suspicious data is removed from their results.

- Analysis of the solution along fluid streamlines underneath the ship reveal that the predicted 200 μm bubbles by the model are generated by the breakup of bubbles as they are transported along the hull.

7.2 Limitations of the Model

One of the contributions of this thesis, and not of less importance, is the identification of issues that need further research. This section is a summary of these issues and, if possible, proposes possible solution strategies and guidelines that attempt to provide a path for future research tackling these problems.

Entrainment model. The simulations performed for Athena in Chapter 6 show that the calibration of the entrainment strength S_0 in Eq. (3.102) with the void fraction at one location, does not necessarily predict the right void fraction at another entrainment location. For Athena, the entrainment strength is calibrated with the experimental data available at the stern but the void fraction at the bow location is underpredicted by at least two orders of magnitude.

Another drawback of the entrainment model used in this work is that the entrainment size distribution must be provided by the user. A fully predictive model would not only predict the amount of air entrained but also the bubble size distribution.

Breakup in the boundary layer. The current models for breakup and coalescence assume that bubbles are immersed in an homogeneous turbulent field, or more precisely, that a nearly homogeneous turbulent field across the size of a bubbles is a reasonably valid assumption. However, as discussed in Section 6.4, the turbulent flow in the boundary layer is highly inhomogeneous and bubbles in it are exposed to large variations if velocity and turbulence across their diameter. The assumption of a nearly homogeneous turbulent field is not longer valid and the breakup models (as well as the coalescence models) need to be revised.

The study on Athena's boundary layer presented in Section 6.4 reveals that breakup by shear (either resolved or modeled shear as presented in Section 3.3.2) is not strong enough to induce the breakup of bubbles in the boundary layer. This result is surprising since breakup in the boundary layer is expected be one of the main contributors to the population of small bubbles observed at the wake of a ship. However, breakup by turbulence and by shear are considered separately while in a turbulent boundary layer these contributions act simultaneously. The non-linear interaction between these effects has not been studied in the literature

and further research on the topic is needed. Section 6.4.3 presents a more in-depth discussion about this problem.

Another issue found in the boundary layer is that, close to a wall, turbulence length scales can be smaller than the size of the bubbles themselves. It is typically assumed in the available breakup models that the breakup of bubbles immersed in a turbulent field is caused by the interaction with turbulent eddies with sizes ranging from the Kolmogorov length scale[2] to the size of the bubble. This assumption is not longer valid if the turbulent length scales are smaller than the bubble diameter and therefore it needs to be revised.

Near wall integration. This problem is intimately related with the problem of breakup and coalescence modeling in the boundary layer. As explained in Section 4.6.1, the dispersed phase equations are averaged out in the direction normal to the wall within the first cells discretizing the boundary layer. This integration near the wall is performed by merging cells in the direction normal to the wall such that the resulting cell size is in the order of the maximum bubble size in the model. Such merging prevents from an excessive and uncontrolled accumulation of void fraction in the first cells of the boundary layer. However, this integration averages out the rapidly changing velocity and turbulence profiles along the boundary layer. New models for breakup and coalescence in the boundary layer that account for this averaging are needed. These models most likely will resemble a wall function like model.

Coalescence in sea water. The coalescence of bubbles in sea water is a very important phenomena to be included in models for polydispersed bubbly flows but it is, however, an almost uninvestigated subject. The model proposed in Sec-

[2]Actually, the smallest eddy size containing enough energy to break a bubble of a given size is given by the so called capillary condition (Lehr et al., 2002)

tion 3.5 provides some fundamental ideas on the subject but clearly more work is needed, both theoretical and experimental. This model is based on observations made on coalescence in electrolytes. However, modeling sea water as a simple electrolyte solution may be a crude approximation due to the fact that sea water contains, in addition to dissolved salt, dirt, suspended particles and even living microorganisms.

Dissolution in sea water. Dissolved salt and impurities in the water may affect the rate at which the air inside a bubble dissolves in the surrounding water. These impurities may stick to the bubble's surface forming a hard shell that effectively blocks the passage of gas from inside the bubble into the water outside it. In addition, the model presented in this thesis assumes that the concentration of air dissolved in the water is that of equilibrium at the atmospheric pressure. A further improvement to this model would be to include a transport equation for the concentration of dissolved gas.

Bubble growth by rectified diffusion. Numerical simulations by Hsiao and Chahine (2005); Raju et al. (2009) show that the bubble size distribution can significantly change as bubbles go across a propeller. This change in the size distribution is attributed to the phenomenon of rectified diffusion. It is of interest then to include this effect in the Eulerian framework presented in this thesis. Section 3.10 proposes a model for rectified diffusion suitable for an Eulerian framework that uses transfer functions. These transfer functions, however, need to be provided for the particular geometry and conditions of the propeller. The simulations presented in this thesis use the data provided by Raju et al. (2009) for the DTMB propeller P5168 as a demonstration only but tables for Athena's propeller must be generated for different loading conditions to perform consistent computations.

Oceanic background. The oceanic background model introduced in Section 3.9 is based on the experimental data taken by Melville et al. (1995). However, void fraction and bubble size distribution profiles with depth depend on the sea state and the data provided by Melville et al. (1995) covers only one case. It would be desirable then to have, either a theoretical model that predicts void fraction and size distribution with depth or, a comprehensive data set for different sea state conditions, or a combination of both.

7.3 Future Work

Future work that would help to extend the two-phase capability implemented in CFDShip-Iowa V4.5 is directly related with the limitations summarized in the previous section. This work can be categorized according to the amount of work and development required.

7.3.1 Short-term improvements

These include the implementation of models already available in the literature and that can easily be added into the current structure of the code. Examples are:

- Implementation of the correlation by Tomiyama et al. (2002) for the lift coefficient.
- Newer correlations for virtual mass, drag and other coefficients that would include additional effects such as high void fraction.
- Disperse phase velocity gradients in the collision kernel for coalescence as in Carrica et al. (1999).

7.3.2 Medium-term improvements

These include the implementation of models already available in the literature but require a deeper understanding of the overall structure of the code and programming skills. These would include:

- Implementation of the two-phase turbulence model proposed by Kataoka et al. (1993), which claims to model both turbulence generation and suppression by the presence of the bubbly phase.

- Cavitation modeling. Simple models are available in the literature but their implementation is challenging since the code needs to handle very large void fraction levels.

- File handling and post-processing tools. The large amount of output data generated by a polydispersed bubbly flow simulation requires special tools for its efficient analysis. This work contributes with a new binary format (raw format in CFDShip-Iowa V4.5) and an Add-On for Tecplot, Inc. that allows to easily import the solution for visualization. Additional tools to directly extract already post-processed size distributions and intergroup budget on iso-surfaces and at selected monitor locations would greatly accelerate the post-processing step and enhance the user productivity.

- Algebraic solver for the dispersed phase momentum. The dispersed phase momentum could be solved algebraically if the virtual mass term is neglected. An algebraic system of equations does not couple different spatial locations and therefore converges faster to the solution. It is of interest, however, to consider the virtual mass term but still solve an easier algebraic equation for every point. This could be achieved, for instance, with an *quasi-algebraic* solver that could use a previous solution to compute the virtual mass term.

7.3.3 Long-term improvements

Improvements to the code in the long term would include the implementation of models that currently are in an early stage of development and therefore require an important amount of additional work before their implementation in the code. Additional work could, and should include, not only theoretical and computational developments but also full experimental campaigns as in both laboratory and full scale environments.

Enhancement and development of numerical algorithms would most likely fall in this category as well.

A list of long-term plans include:

- Development of new entrainment models. The modeling of air entrainment is a very challenging problem by itself and it deserves especial attention. The development of new entrainment models must combine theoretical and experimental studies. The ideal entrainment model would predict not only air entrainment rates but also size distribution of the entrained bubbles and penetration depth based on the local resolved velocities and turbulence levels. The model should be as much grid independent as possible.

- Modeling of turbulence near the free surface. Most CFD codes do not modify the turbulence models near the free surface. CFDShip-Iowa V4.5 uses a zero gradient boundary condition at the free surface but the equations of turbulence do not include any modification to account for the free surface. Turbulence modeling and air entrainment are two phenomena treated independently of each other in the past. New approaches should consider the study of these two phenomena simultaneously since turbulence fluctuations drive entrainment and the entrained two-phase mixture modifies the turbulent field.

- Rectified diffusion. Bubbles growing by rectified diffusion undergo high frequency oscillations impossible to resolve with the time steps used in CFD simulations and therefore the phenomena requires modeling. The model presented in Section 3.10 is one possible solution to the problem but it requires the preparation of transfer function specific for a given propeller and loading conditions. A more general approach could use the information from a simulation with discretized propeller to solve a mean Rayleigh-Plesset equation or similar to predict a mean rectified diffusion rate. The derivation of such an equation is non-trivial and would require the closing of some of the terms in the original Rayleigh-Plesset equation.

- Breakup (coalescence) in the boundary layer. The large gradients present in the boundary layer and the scales involved require the revision of the models used for breakup and coalescence (these problems are discussed in detail in Section 6.4.3). In addition, the wall integration introduced in Section 4.6.1 averages out these gradients in a thin layer close to a wall. Therefore, new breakup (and coalescence) models that provide a mean rate of breakup (coalescence) in this layer and that consider the large gradients involved need to be developed. In addition, these models must be able to include the combined effect of breakup induced by shear and turbulence. This coupling has not been studied in the past and it is of interest since it has the potential for the generation of the small bubbles observed in the wake of a ship.

- Coalescence in sea water. It is well known in the literature that coalescence in sea water is strongly inhibited by the dissolved salt contained in it. However, quantitative studies are scarce and no reliable models are available. This subject needs to be studied with experiments performed in real sea water since the impurities and microorganisms contained in it may also affect the

coalescence rates. Reliable metrics to characterize the chemistry of the water should be developed to propose models accounting for water with different chemical characteristics.

- Numerical dissipation in DES models. Simulations performed with CFDShip-Iowa V4.5 revealed a large underprediction of turbulence dissipation when using a DES model of turbulence. Additional work on homogeneous and isotropic turbulence in a box revealed a large numerical dissipation of mechanical energy as the cause of this problem. Further work is needed to arrive to a practical solution of the problem.

- Improvement of the transport solver efficiency. The transport solver for the group-g number densities is currently the most time consuming stage of the two-phase code. However, most of the bubbly flow around a ship is confined in the very near field and a numerical method that takes advantage of this to reduce computational work in zones with low void fraction levels could eventually be developed.

- Transport equation for the concentration of dissolved gas in water. The bubble dissolution model from Section 3.4 uses an homogeneous concentration of dissolved gas in water which is assumed to be that of equilibrium at the atmospheric pressure. This assumption is only valid at low void fraction levels and for low gas dissolution rates. Spatial and temporal variations on the concentration of dissolved gas can be considered by solving an additional transport equation for this quantity. This approach is used in Politano et al. (2009) for the modeling of TDG.

- Salt concentration, temperature and stratification. Water stratification consists in the formation of layers of water with different densities. These layers are normally arranged with the least dense layer sitting above the denser

ones. Density variations may be caused, for instance, by variations in salinity or in temperature. The effect of stratification is of interest in the prediction of the bubbly wake shape and size distribution behind a ship. Local salt concentration affects coalescence rates (assuming a reliable correction with salt concentration is available) and variations in both salinity and temperature change water density. Therefore, transport equations for both salinity and temperature would allow to account for these effects and stratification due to variations in water density.

In addition to code development and improvement, future work is also required in the following areas:

- Convergence study with grid resolution, especially to asses entrainment modeling dependence with grid resolution.
- Convergence study on the number of groups used to discretize the bubble size distribution.
- Assessment of two-phase turbulence models for bubbly flows. RANS and DES models, turbulence generation and suppression. Two-phase models should consider the relative magnitude of bubble sizes compared against eddy sizes as in the work by Kataoka et al. (1993).

APPENDIX A
MASS AND NUMBER CONSERVATION

A.1 Properties of the Breakup and Coalescence Kernels

Some of the properties that the intergroup transfer kernels must satisfy are physical requirements. For instance, the coalescence kernel must be symmetric *i.e.* $Q(m,m') = Q(m',m)$ since the probability of having coalescence between a bubble of size m with another of size m' is clearly the same as the probability of coalescence between a bubble of size m' with another of size m. Now, is this also a requirement of the evolution equations for $f(m)$? is this the only requirement? What about the breakup kernel?

In this section it will be shown that the following properties are required in order to satisfy mass conservation and bubble balance

$$\int_0^{m'} dm\, h(m,m') = n \tag{A.1}$$

$$\int_0^{m'} dm\, m\, h(m,m') = m' \tag{A.2}$$

$$Q(m,m') = Q(m',m) \tag{A.3}$$

where n is the number of daughter bubble generated in one breakup event. Note also that Eq. (A.1) allows more than two daughter bubble per breakup event as long as the resulting size distribution is always the same on every single breakup event. Note also that the daughter bubble size distribution does not need to be symmetric *i.e.* $h(m,m') = h(m'-m,m')$ is not a required property either for mass or number conservation. As an example of this the daughter size distribution describing the breakup of a bubble in n equalsized fragments is analyzed in what follows. However, the symmetry of the daughter size distribution is a physical requirement that binary breakups must satisfy since the mass of the original bubble

is the combined mass of the two daughter bubble.

A.2 Proof of Mass Conservation

If only intergroup transfer due to breakup and coalescence is considered in Eq. (2.8) the number density equation reduces to

$$\frac{\partial f(m)}{\partial t} = \beta^+(m) - \beta^-(m) + \chi^+(m) - \chi^-(m) \tag{A.4}$$

with breakup sources computed according to Eqs. (2.10)-(2.11) and coalescence sources computed as in Eqs. (2.14)-(2.15)

$$\beta^+(m) = \int_m^\infty dm'\, h(m,m')b(m')f(m') \tag{A.5}$$

$$\beta^-(m) = b(m)f(m) \tag{A.6}$$

$$\chi^+(m) = \frac{1}{2}\int_0^m dm'\, Q(m-m',m')f(m-m')f(m') \tag{A.7}$$

$$\chi^-(m) = f(m)\int_0^\infty dm'\, Q(m,m')f(m') \tag{A.8}$$

The mass of gas per unit volume, also called bubble mass density, is computed as

$$\varepsilon_m = \int_0^\infty dm\, m f(m) \tag{A.9}$$

Since no convection or external sources are present in Eq. (A.4) the bubble mass density should be conserved. This will be shown to be a property naturally derived from Eq. (A.4). When deriving the discrete version of this equation it will be desirable to retain this property and hence this derivation will provide to be an useful exercise.

The conservation of mass equation can be obtained by multiplying Eq. (A.4) by

m and then integrating over all sizes

$$\frac{\mathrm{d}\varepsilon_m}{\mathrm{d}t} = \frac{d}{dt}\int_0^\infty dm\, m f(m) = \int_0^\infty dm\, m \frac{\partial f(m)}{\partial t} = \int_0^\infty dm\, m\, \beta^+(m) - \int_0^\infty dm\, m\, \beta^-(m) + \int_0^\infty dm\, m\, \chi^+(m) - \int_0^\infty dm\, m\, \chi^-(m) \tag{A.10}$$

In what follows it will be shown that for both, breakup and coalescence, births and deaths cancel out exactly.

A.2.1 Breakup

The generation of bubbles by births in Eq. (A.10) can manipulated by changing the order of integration

$$\begin{aligned}\int_0^\infty dm\, m\, \beta^+(m) = \int_0^\infty dm\, m \int_m^\infty dm'\, h(m,m') b(m') f(m') = \\ \int_0^\infty dm' \int_0^{m'} dm\, m\, h(m,m') b(m') f(m') = \\ \int_0^\infty dm'\, b(m') f(m') \int_0^{m'} dm\, m\, h(m,m')\end{aligned} \tag{A.11}$$

The inner integral over the daughter size distribution can be computed by considering two general cases.

Binary breakup

For binary breakup the daughter size distribution satisfies

$$\int_0^{m'} dm\, h(m,m') = 2 \tag{A.12}$$

$$h(m,m') = h(m'-m,m') \tag{A.13}$$

and with these two properties it can easily be verified that

$$\int_0^{m'} dm\, m\, h(m, m') = m' \tag{A.14}$$

Breakup in n equal sized bubbles

In this case the daughter size distribution can be written as

$$h(m, m') = n\delta\left(m - \frac{m'}{n}\right) \tag{A.15}$$

Then it follows that

$$\int_0^{m'} dm\, h(m, m') = n \tag{A.16}$$

$$\int_0^{m'} dm\, m\, h(m, m') = m' \tag{A.17}$$

In either case the general properties to be satisfied by the daughter size distribution are that its zero-th order moment should equal the number of bubbles generated per breakup, as in Eqs. (A.12) and (A.16), and that its first order moment must equal the mass of the source bubble, as in Eqs. (A.13) and (A.17).

With this Eq. (A.11) is reduced to

$$\int_0^{\infty} dm\, m\, \beta^+(m) = \int_0^{\infty} dm'\, b(m') f(m') m' \tag{A.18}$$

which exactly cancels out the breakup deaths.

Remark Note that the daughter size distribution does not need to be symmetrical when more than one bubble are generated per breakup.

A.2.2 Coalescence

The coalescence births term in Eq. (A.10) can be manipulated by first changing the order of integration

$$\begin{aligned}\int_0^\infty dm\, m\, \chi^+(m) &= \frac{1}{2}\int_0^\infty dm\, m \int_0^m dm'\; Q(m-m',m')f(m-m')f(m') \\ &= \frac{1}{2}\int_0^\infty dm' \int_{m'}^\infty dm\, m\, Q(m-m',m')f(m-m')f(m') \end{aligned} \tag{A.19}$$

then the change of variables $m'' = m - m'$ is made for the inner integral

$$\begin{aligned}\int_0^\infty dm\, m\, \chi^+(m) &= \frac{1}{2}\int_0^\infty dm' \int_{m'}^\infty dm\, m\, Q(m-m',m')f(m-m')f(m') \\ &= \frac{1}{2}\int_0^\infty dm' \int_0^\infty dm''\, (m''+m')\, Q(m'',m')f(m'')f(m') \\ &= \int_0^\infty dm' \int_0^\infty dm''\, m'\, Q(m'',m')f(m'')f(m') \end{aligned} \tag{A.20}$$

the last identity is obtained by distributing the addition in parenthesis and by noticing that the integration over these two integrands is the same due to the symmetry of the kernel $Q(m,m')$.

This last term exactly cancels out the coalescence deaths.

A.3 Total Number of Bubbles Balance

The total number of bubbles per unit volume is computed as

$$N = \int_0^\infty dm\, f(m) \tag{A.21}$$

It is not possible to show that the total number of bubbles is conserved as it was done with the total mass. Consider coalescence, every time two bubbles coalesce, only one bubble is left. Hence, one bubble is lost per coalescence event. Similarly, if n bubbles are generated on a breakup event and considering that the original

bubble is lost, $n-1$ bubbles are generated per breakup event. This result can be derived from Eq. (A.4) in a similar way as mass conservation was derived.

The number of bubbles total balance is obtained by integrating Eq. (A.4) over all bubble sizes

$$\frac{dN}{dt} = \frac{d}{dt}\int_0^\infty dm\, f(m) = \int_0^\infty dm\, \frac{\partial f(m)}{\partial t} = \int_0^\infty dm\, \beta^+(m) - \int_0^\infty dm\, \beta^-(m) + \int_0^\infty dm\, \chi^+(m) - \int_0^\infty dm\, \chi^-(m) \tag{A.22}$$

as with mass conservation the birth terms will be manipulated in order to resemble the death terms.

A.3.1 Breakup

As with births in the mass balance equation births in the number of bubbles balance is manipulated by changing the order of integration

$$\begin{aligned}\int_0^\infty dm\, \beta^+(m) &= \int_0^\infty dm \int_m^\infty dm'\, h(m,m')b(m')f(m') \\ &= \int_0^\infty dm' \int_0^{m'} dm\, h(m,m')b(m')f(m') \\ &= \int_0^\infty dm'\, b(m')f(m') \underbrace{\int_0^{m'} dm\, h(m,m')}_{n} \\ &= n\int_0^\infty dm'\, b(m')f(m')\end{aligned} \tag{A.23}$$

the last integral in Eq. (A.23) exactly equals the total deaths rate. Hence

$$\int_0^\infty dm\, \beta^+(m) - \int_0^\infty dm\, \beta^-(m) = (n-1)\int_0^\infty dm'\, b(m')f(m') \tag{A.24}$$

and a total of $n-1$ bubbles are gained per breakup event.

A.3.2 Coalescence

As with the birth term in the mass equation the birth term in the number of bubbles balance is manipulated by first changing the order of integration

$$\begin{aligned}\int_0^\infty dm\,\chi^+(m) &= \frac{1}{2}\int_0^\infty dm \int_0^m dm'\; Q(m-m',m')f(m-m')f(m') \\ &= \frac{1}{2}\int_0^\infty dm' \int_{m'}^\infty dm\, Q(m-m',m')f(m-m')f(m')\end{aligned} \tag{A.25}$$

and then the change of variables $m'' = m - m'$ is performed

$$\int_0^\infty dm\,\chi^+(m) = \frac{1}{2}\int_0^\infty dm' \int_0^\infty dm''\, Q(m'',m')f(m'')f(m') \tag{A.26}$$

this is exactly half of the total deaths by coalescence. Then

$$\int_0^\infty dm\,\chi^+(m) - \int_0^\infty dm\,\chi^-(m) = -\frac{1}{2}\int_0^\infty dm \int_0^\infty dm'\, Q(m,m')f(m)f(m') \tag{A.27}$$

note that since the kernel $Q(m,m')$ is symmetric the above integral is counting the number of coalescence events twice and it can be written as

$$\int_0^\infty dm\,\chi^+(m) - \int_0^\infty dm\,\chi^-(m) = -\int_0^\infty dm \int_0^m dm'\, Q(m,m')f(m)f(m') \tag{A.28}$$

Hence, one bubble is lost per coalescence event, as expected.

APPENDIX B
TURBULENT DISPERSION

A popular approach used by the two-phase community to model the dispersion of the bubbly field by turbulent fluctuations is to use an extra interfacial momentum term $\boldsymbol{M}_g^{TD}$ in Eq. (3.20). The model proposed by Carrica et al. (1998) for the interfacial force $\boldsymbol{M}_g^{TD}$ is well accepted since in the limit for small bubble sizes it predicts that bubbles behave as fluid tracers, as physically expected (see the discussion in Section 3.1.4 on turbulent dispersion). In this model the interfacial force is modeled as

$$\boldsymbol{M}_g^{TD} = -\rho_c \alpha_g \frac{3}{8} \frac{C_D \|\boldsymbol{u}_{r,g}\|}{R_g} \frac{\nu_t}{Sc_b} \frac{\nabla N_g}{N_g} \tag{3.32}$$

As discussed in Section 4.8, this kind of force proportional to the gradient of the number density generates numerical instabilities that may lead to the divergence of the solution. A numerical algorithm that solves this problem is presented in Section 4.8. With this numerical problem solved, the model given by Eq. (3.32) is used and it is observed that, in regions with strong turbulence fluctuations like in a boundary layer or the wake behind a ship the solution is discontinuous. It is important to remark that this problem is not caused by the decoupling of the dispersed phase velocity and number density as discussed in Section 4.8, but it is a new problem caused by the physical model.

The problem is found to be the existence of multiple solutions for the gas momentum equations when the model in Eq. (3.32) is used. The rest of this appendix discusses the problem in detail.

B.1 Simple cases with analytical solution

Taking into account only the buoyancy, drag and turbulent dispersion forces, the gas momentum equation in Eq. (3.136) reduces to

$$\widehat{C}_D \, \|\boldsymbol{u}_r\| \, \boldsymbol{u}_r = -\frac{(1-\rho_d/\rho_c)}{Fr^2}\,\hat{k} - \widehat{C}_D \|\boldsymbol{u}_r\| \frac{\nu_t}{Sc_b}\frac{\nabla N}{N} \qquad \text{(B.1)}$$
$$\text{with, } \widehat{C}_D = \frac{3}{8}\frac{C_D(Re)}{R}$$

where the group-g subscripts are omitted since only one bubble size is considered.

This equation is non-dimensionalized using a characteristic velocity U_0 and a characteristic length L_0. For the problem of bubbles rising in a fluid, the characteristic velocity used is the terminal velocity of the bubbles v_t and the characteristic length the bubble diameter D. Then, the Reynolds number is $Re_t = v_t\, D/\nu$ and the Froude number is $Fr = v_t/\sqrt{g\,D} = Re_t\,\nu/\sqrt{g\,D^3}$. This selection of characteristic scales leads to

$$\begin{aligned} Re &= Re_t \|\boldsymbol{u}_r\| \\ \tilde{n} &= \frac{1}{v_t}\frac{\nu_t}{Sc_b}\frac{\nabla N}{N} \\ \widehat{C}_D &= \frac{3}{4} C_D \end{aligned}$$

where the dimensionless turbulence induced velocity $\tilde{n}$ is defined and the last relation comes from the fact that with this non-dimensionalization $R = 1/2$. Multiplying Eq. (B.1) by Re_t and considering the z direction only it simplifies to

$$\widehat{C}_D \, Re \, u = (1-\rho_d/\rho_c)\frac{Re_t}{Fr^2} - \widehat{C}_D \, Re \, \tilde{n} \qquad \text{(B.2)}$$

where the Reynolds number Re is defined with the actual bubble velocity u.

In Section 3.1.4 the drag coefficient is modeled as (ignoring the Eötvös number

dependence)

$$C_D(Re) = \frac{24}{Re}(1 + 0.168Re^{0.75}) \tag{B.3}$$

Unfortunately, with this model, the above equation can only be solved numerically. To help understand how this equation behaves, different simplifications for the drag coefficient are used. These are summarized below

- Constant $C_D(Re) = C_D$.
- Stokes' drag. $C_D(Re) = \frac{24}{Re}$.
- Oseen's drag. $C_D(Re) = \frac{24}{Re}(1 + \frac{3}{16}Re)$.

The solution to Eq. (B.2) using these models are

Constant C_D

$$u = \begin{cases} -\frac{\tilde{n}}{2} + \sqrt{\frac{\tilde{n}^2}{4} + 1} & \text{if } u > 0 \\ -\frac{\tilde{n}}{2} \pm \sqrt{\frac{\tilde{n}^2}{4} - 1} & \text{if } u < 0 \end{cases} \tag{B.4}$$

Stokes' C_D

$$u = 1 - \tilde{n} \tag{B.5}$$

Oseen's C_D

$$\begin{aligned} u &= \begin{cases} \frac{-(18 + B\tilde{n}) + \sqrt{(18 + B\tilde{n})^2 + 4B(A - 18\tilde{n})}}{2B} & \text{if } u > 0 \\ \frac{-(B\tilde{n} - 18) \pm \sqrt{(B\tilde{n} - 18)^2 - 4B(A - 18\tilde{n})}}{2B} & \text{if } u < 0 \end{cases} \\ A &= 18 + \frac{27}{8}Re_t \\ B &= \frac{27}{8}Re_t \end{aligned} \tag{B.6}$$

The solution obtained using Oseen's drag coefficient is the only one that exhibits a dependence with the Reynolds number. The Stokes and constant C_D solutions

are the limiting cases for $Re_t \to 0$ and $Re_t \to \infty$ respectively. These two are shown in Figure B.2 together with Oseen's case.

The most important and alarming feature of these solutions is that they show that, eventually, there could coexist more than one possible solution to the same problem. This is shown to happen for $Re_t \gtrsim 4.0$.

The solution obtained with the Stoke's drag coefficient can be recast to have units as

$$u_r = u_t - \widehat{C}_D \|u_t\| \frac{\nu_t}{Scb} \frac{\nabla N}{N} \tag{B.7}$$

showing that in the limiting case for which Re_t goes to zero, the terminal and *turbulence induced velocity* can in fact be linearly added.

These solutions also show that in the limiting case for which $\tilde{n} \to \pm\infty$ (zero gravity or large turbulent fluctuations for instance), the motion of the gas phase is fully diffusive, $u = -\tilde{n}$.

Figure B.1 shows the numerical solution obtained using the drag coefficient in Eq. (B.3). This is shown to be in good agreement the predicted behavior by the analytical solutions.

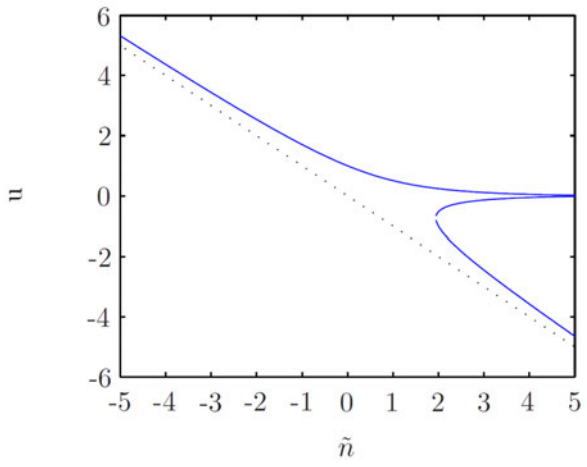

Figure B.1: Numerical solution using the drag coefficient in Eq. (B.3)

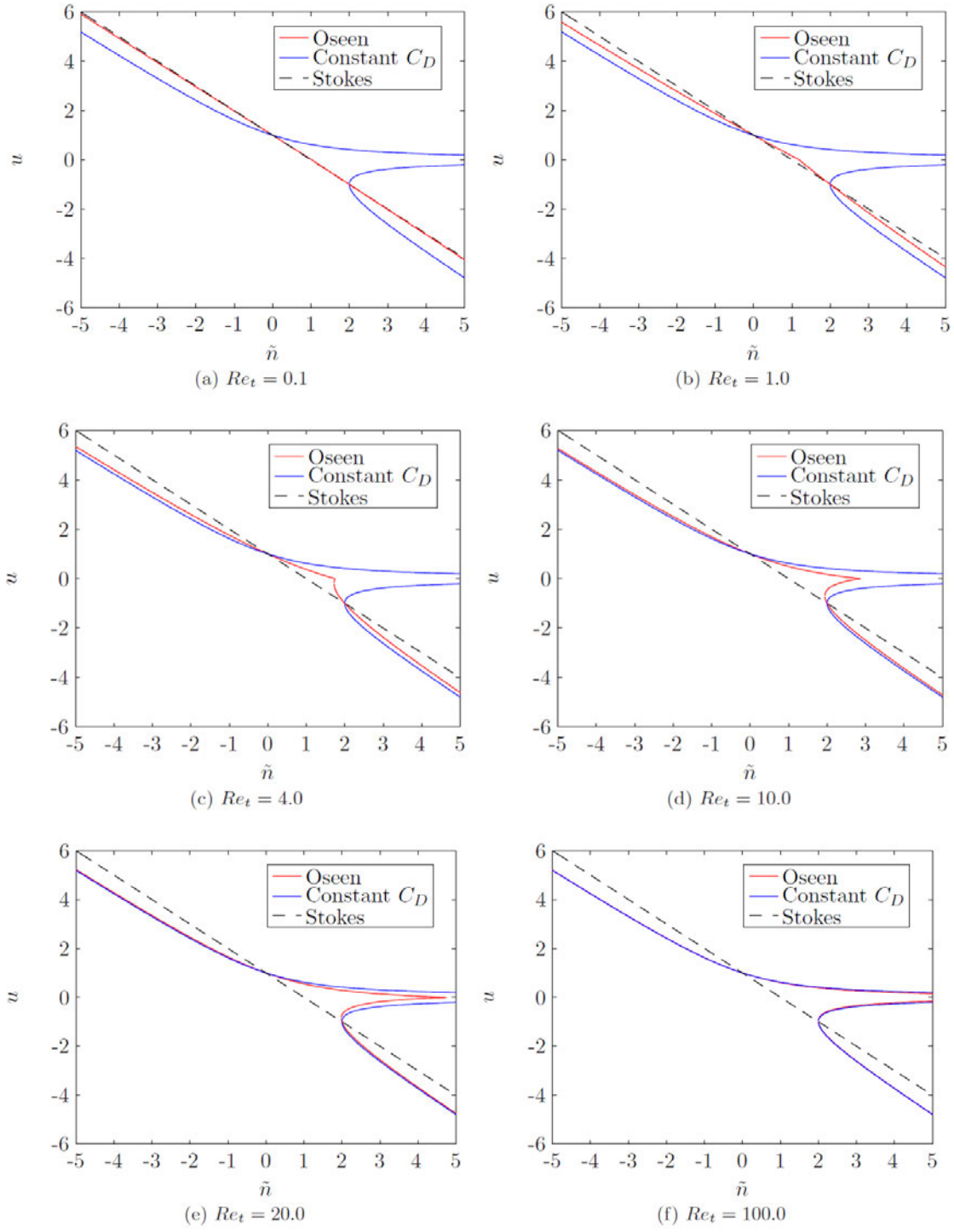

(a) $Re_t = 0.1$ (b) $Re_t = 1.0$

(c) $Re_t = 4.0$ (d) $Re_t = 10.0$

(e) $Re_t = 20.0$ (f) $Re_t = 100.0$

Figure B.2: Analytical cases. The solution obtained with Oseen's model is the only one dependent on the Reynolds number. The Stokes and Constant C_D solutions are limiting cases to Oseen's solution.

REFERENCES

J.-L. Achard. *Contribution l'tude thorique des coulements diphasiques en rgime transitoire*. PhD thesis, University Scientifique et Medicale et Institut National Polytechnique de Grenoble, Grenoble, 1978.

S. S. Alves, C. I. Maia, J. M. T. Vasconcelos, and A. J. Serralheiro. Bubble size in aerated stirred tanks. *Chem. Eng. J.*, 89(1-3):109 – 117, 2002.

S. P. Antal, R. T. Lahey Jr., and J. E. Flaherty. Analysis of phase distribution in fully developed laminar bubbly two-phase flow. *Int. J. Multiphase Flow*, 17(5):635 – 652, 1991.

S. V. Apte, M. Gorokhovski, and P. Moin. LES of atomizing spray with stochastic modeling of secondary breakup. *Int. J. Multiphase Flow*, 29(9):1503 – 1522, 2003a.

S. V. Apte, K. Mahesh, and T. Lundgren. A eulerian-lagrangian model to simulate two-phase/particulate flows. Center for Turbulent Research. Annual Research Briefs, 2003b.

S. Balay, W. D. Gropp, L. C. McInnes, and B. F. Smith. Efficient management of parallelism in object oriented numerical software libraries. In E. Arge, A. M. Bruaset, and H. P. Langtangen, editors, *Modern Software Tools in Scientific Computing*, pages 163–202. Birkhäuser Press, 1997.

S. Balay, J. Brown, K. Buschelman, V. Eijkhout, W. D. Gropp, D. Kaushik, M. G. Knepley, L. C. McInnes, B. F. Smith, and H. Zhang. PETSc users manual. Technical Report ANL-95/11 - Revision 3.0.0, Argonne National Laboratory, 2008.

S. Balay, J. Brown, K. Buschelman, W. D. Gropp, D. Kaushik, M. G. Knepley, L. C. McInnes, B. F. Smith, and H. Zhang. PETSc Web page, 2009. http://www.mcs.anl.gov/petsc.

A. Basset. *A treatise on hydrodynamics: with numerous examples*. Number v. 2 in A Treatise on Hydrodynamics: With Numerous Examples. Deighton, Bell and Co., 1888.

E. Bayraktar, O. Mierka, F. Platte, D. Kuzmin, and S. Turek. Numerical aspects and implementation of population balance equations coupled with turbulent fluid dynamics. *Comput. Chem. Eng.*, In Press, Corrected Proof, 2011.

K. Beckurts and K. Wirtz. *Neutron physics*. Springer, 1964.

J. B. Bell, L. H. Howell, and P. Colella. An efficient second-order projection method for viscous incompressible flow. In 10^{th} *AIAA Computational Fluid Dynamics Conference*, pages 360–367, Honolulu, HI, 1991.

S. Bhushan, T. Xing, P. M. Carrica, and F. Stern. Model- and full-scale URANS simulations of Athena resistance, powering, seakeeping, and 5415 maneuvering. *J. Ship. Res.*, 53:179–198(20), 2009.

B. Borowski, A. Sutin, H. Roh, and B. Bunin. Passive acoustic threat detection in estuarine environments. In *Society of Photo-Optical Instrumentation Engineers (SPIE) Conference Series*, volume 6945, 2008. doi: 10.1117/12.779177.

C. Brennen. *Fundamentals of multiphase flow*. Cambridge University Press, 2005.

A. Buffo, D. L. Marchisio, M. Petitti, M. Vanni, N. Mancini, and F. Podenzani. Investigation of mass transfer in poly-disperse gas-liquid systems by using a multivariate population balance computational techniques for multiphase flows. In *7th International Conference on Multiphase Flow - ICMF 2010 Proceedings*, Tampa, Florida, 2010.

C. O. E. Burg, K. Sreenivas, and D. G. Hyams. Unstructured nonlinear free surface simulations for the fully-appended DTMB model 5415 series hull including rotating propulsors. In 24^{th} *ONR Symposium on Naval Hydrodynamics*, Fukuoka, Japan, 2002.

P. Carrica, K.-J. Paik, H. Hosseini, and F. Stern. URANS analysis of a broaching event in irregular quartering seas. *J. Mar. Sci. Technol.*, 13:395–407, 2008.

P. M. Carrica and F. Stern. DES simulations of KVLCC1 in turn and zigzag maneuvers with moving propeller and rudder. In *SIMMAN 2008*, Copenhagen, Denmark, 2008.

P. M. Carrica, F. J. Bonetto, D. A. Drew, and R. T. Lahey Jr. The interaction of background ocean air bubbles with a surface ship. *Int. J. Numer. Methods Fluids*, 28:571 – 600, 1998.

P. M. Carrica, D. A. Drew, F. J. Bonetto, and R. T. Lahey Jr. A polydisperse model for bubbly two-phase flow around a surface ship. *Int. J. Multiphase Flow*, 25(2): 257 – 305, 1999.

P. M. Carrica, R. V. Wilson, R. W. Noack, and F. Stern. Ship motions using single-phase level set with dynamic overset grids. *Comput. Fluids*, 36(9):1415 – 1433, 2007a.

P. M. Carrica, R. V. Wilson, and F. Stern. An unsteady single-phase level set method for viscous free surface flows. *Int. J. Numer. Methods Fluids*, 53:229–256, 2007b.

P. M. Carrica, A. M. Castro, and F. Stern. Self-propulsion computations using a speed controller and a discretized propeller with dynamic overset grids. *J. Mar. Sci. Technol.*, 15:316–330, 2010a.

P. M. Carrica, J. Huang, R. Noack, D. Kaushik, B. Smith, and F. Stern. Large-scale DES computations of the forward speed diffraction and pitch and heave problems for a surface combatant. *Comput. Fluids*, 39(7):1095 – 1111, 2010b.

A. M. Castro, P. M. Carrica, and F. Stern. Full scale self-propulsion computations using discretized propeller for the KRISO container ship KCS. *Comput. Fluids*, 51 (1):35–47, 2011.

B. S. Chan and Y. H. Tsang. A theory on bubble-size dependence of the critical electrolyte concentration for inhibition of coalescence. *J. Colloid. Interf. Sci.*, 286 (1):410 – 413, 2005.

W. Chao-Yang and C. Beckermann. A two-phase mixture model of liquid-gas flow and heat transfer in capillary porous media–I. Formulation. *Int. J. Heat Mass Transfer*, 36(11):2747 – 2758, 1993.

P. Chen, J. Sanyal, and M. Duduković. CFD modeling of bubble columns flows: implementation of population balance. *Chem. Eng. Sci.*, 59(22-23):5201–5207, 2004. ISCRE18.

P. Chen, M. P. Duduković, and J. Sanyal. Three-dimensional simulation of bubble column flows with bubble coalescence and breakup. *AlChE J.*, 51(3):696–712, 2005a.

P. Chen, J. Sanyal, and M. Duduković. Numerical simulation of bubble columns flows: effect of different breakup and coalescence closures. *Chem. Eng. Sci.*, 60(4): 1085–1101, 2005b.

A. K. Chesters and G. Hofman. Bubble coalescence in pure liquids. *Appl. Sci. Res.*, 38:353–361, 1982.

H. K. Christenson, R. E. Bowen, J. A. Carlton, J. R. M. Denne, and Y. Lu. Electrolytes that show a transition to bubble coalescence inhibition at high concentrations. *J. Phys. Chem. C*, 112(3):794–796, 2008.

D. Colella, D. Vinci, R. Bagatin, M. Masi, and E. A. Bakr. A study on coalescence and breakage mechanisms in three different bubble columns. *Chem. Eng. Sci.*, 54 (21):4767 – 4777, 1999.

G. W. Collins II. *The Fundamentals of Stellar Astrophysics*. 2003. Web edition. Available online at: http://bifrost.cwru.edu/personal/collins/astrobook/.

V. S. J. Craig, B. W. Ninham, and R. M. Pashley. Effect of electrolytes on bubble coalescence. *Nature*, 364:317 – 319, 1993.

L. B. Crook. Powering predictions for the R/V Athena (PG 94) represented by model 4950-1 with design propellers 4710 and 4711. David W. Taylor Naval Ship Research and Development Center, DTNSRDC/SPD-0833-05, 1981.

R. L. Culver and M. F. Trujillo. Measuring and modeling bubbles in ship wakes, and their effect on acoustic propagation. In *Proceedings of the 2nd International Conference on Underwater Acoustic Measurements: Technologies and results*, FORTH, Crete, 2007.

D. Darmana, N. Deen, and J. Kuipers. Detailed modeling of hydrodynamics, mass transfer and chemical reactions in a bubble column using a discrete bubble model. *Chem. Eng. Sci.*, 60(12):3383 – 3404, 2005.

R. A. De Bruijn. *Deformation and breakup of drops in simple shear flows*. PhD thesis, Technische Universiteit, Eindhoven, Netherlands, 1991.

R. A. De Bruijn. Tipstreaming of drops in simple shear flows. *Chem. Eng. Sci.*, 48 (2):277–284, 1993.

A. G. Dickson and C. Goyet. *Handbook of methods for the analysis of the various parameters of the carbon dioxide system in sea water*. University of California Press, 1992.

D. Drew. Averaged field equations for two-phase media. *Studies Appl. Math.*, 50: 133–166, 1971.

D. A. Drew. Mathematical modeling of two-phase flow. *Annu. Rev. Fluid Mech.*, 15 (1):261–291, 1983.

D. A. Drew. A turbulent dispersion model for particles or bubbles. *J. Eng. Math.*, 41:259–274(16), 2001.

D. A. Drew and R. T. Lahey Jr. Application of general constitutive principles to the derivation of multidimensional two-phase flow equations. *Int. J. Multiphase Flow*, 5(4):243–264, 1979.

D. A. Drew and R. T. Lahey Jr. The virtual mass and lift force on a sphere in rotating and straining inviscid flow. *Int. J. Multiphase Flow*, 13(1):113–121, 1987.

D. A. Drew and R. T. Lahey Jr. Some supplemental analysis concerning the virtual mass and lift force on a sphere in a rotating and straining flow. *Int. J. Multiphase Flow*, 16(6):1127–1130, 1990.

D. A. Drew and S. L. Passman. *Theory of multicomponent fluids*. Applied mathematical sciences. Springer, 1999.

H. A. Dumbrell. Comparison of excess attenuation and backscatter measurements of ship wakes. In T. G. Leighton, editor, *Natural Physical Processes Associated with Sea Surface Sound*, pages 171–178, University of Southampton, UK, 1997.

B. R. Elbing, E. S. Winkel, K. A. Lay, S. L. Ceccio, D. R. Dowling, and M. Perlin. Bubble-induced skin-friction drag reduction and the abrupt transition to air-layer drag reduction. *J. Fluid Mech.*, 612:201–236, 2008.

P. H. M. Elemans, H. L. Bos, J. M. H. Janssen, and H. E. H. Meijer. Transient phenomena in dispersive mixing. *Chem. Eng. Sci.*, 48(2):267 – 276, 1993.

S. E. Elghobashi and T. W. Abou-Arab. A two-equation turbulence model for two-phase flows. *Phys. Fluids*, 26(4):931–938, 1983.

J. H. Ferziger and H. G. Kaper. *Mathematical theory of transport processes in gases*. North-Holland Pub. Co., 1972.

T. Frank, P. J. Zwart, J.-M. Shi, E. Krepper, and U. Rohde. Inhomogeneous MUSIG model–A population balance approach for polydispersed bubbly flows. In *Proceedings of the International Conference "Nuclear Energy for New Europe 2005"*, Bled, Slovenia, 2005.

T. Frank, P. J. Zwart, E. Krepper, H.-M. Prasser, and D. Lucas. Validation of CFD models for mono- and polydisperse air-water two-phase flows in pipes. *Nucl. Eng. Des.*, 238(3):647–659, 2008.

S. K. Friedlander. *Smoke, dust, and haze: fundamentals of aerosol behavior*. Topicals in chemical engineering. Wiley, 1977.

X. Y. Fu and M. Ishii. Two-group interfacial area transport in vertical air-water flow: I. Mechanistic model. *Nucl. Eng. Des.*, 219(2):143–168, 2003.

D. Gidaspow. *Multiphase flow and fluidization: continuum and kinetic theory descriptions*. Academic Press, 1994.

H. P. Grace. Dispersion phenomena in high viscosity immiscible fluid systems and application of static mixers as dispersion devices in such systems. *Chem. Eng. Commun.*, 14(3):225–277, 1982.

J. Grienberger. *Untersuchung und Modellierung von Blasensäulen*. PhD thesis, University Erlangen-Nürnberg, 1992.

G. Guido-Lavalle, P. M. Carrica, A. Clausse, and M. K. Qazi. A bubble number density constitutive equation. *Nucl. Eng. Des.*, 152(1-3):213 – 224, 1994.

J. O. Hinze. Fundamentals of the hydrodynamic mechanism of splitting in dispersion processes. *AlChE J.*, 1(3):289–295, 1955.

C. W. Hirt and B. D. Nichols. Volume of fluid (VOF) method for the dynamics of free boundaries. *J. Comput. Phys.*, 39(1):201 – 225, 1981.

G. R. Hough and D. E. Ordway. The generalized actuator disk. Technical Report TAR-TR 6401, Therm Advanced Research, Inc., 1964.

C.-T. Hsiao and G. L. Chahine. Scaling of tip vortex cavitation inception noise with a bubble dynamics model accounting for nuclei size distribution. *J. Fluids Eng.*, 127(1):55–65, 2005.

B. Hu, A. Pacek, E. Stitt, and A. Nienow. Bubble sizes in agitated air-alcohol systems with and without particles: Turbulent and transitional flow. *Chem. Eng. Sci.*, 60 (22):6371 – 6377, 2005.

J. Huang, P. M. Carrica, and F. Stern. Coupled ghost fluid/two-phase level set method for curvilinear body-fitted grids. *Int. J. Numer. Methods Fluids*, 55:867–897, 2007.

J. Huang, P. M. Carrica, and F. Stern. Semi-coupled air/water immersed boundary approach for curvilinear dynamic overset grids with application to ship hydrodynamics. *Int. J. Numer. Methods Fluids*, 58:591–624, 2008.

J. Huang, P. M. Carrica, and F. Stern. A method to compute ship exhaust plumes with waves and wind. *Int. J. Numer. Methods Fluids*, 2010. In press. DOI: 10.1002/fld.2499.

L. Huilin, H. Yurong, and D. Gidaspow. Hydrodynamic modelling of binary mixture in a gas bubbling fluidized bed using the kinetic theory of granular flow. *Chem. Eng. Sci.*, 58(7):1197 – 1205, 2003.

H. Hulburt and S. Katz. Some problems in particle technology. a statistical mechanical formulation. *Chem. Eng. Sci.*, 19(8):555–574, 1964.

M. Ishii. *Thermo-fluid dynamic theory of two-phase flow*. Collection de la Direction des études et recherches d'Électricité de France. Eyrolles, 1975.

M. Ishii and N. Zuber. Drag coefficient and relative velocity in bubbly, droplet or particulate flows. *AlChE J.*, 25(5):843–855, 1979.

F. Ismail, P. M. Carrica, and T. Xing. Evaluation of linear and nonlinear convection schemes on multidimensional non-orthogonal grids with applications to KVLCC2 tanker. *Int. J. Numer. Methods Fluids*, 2010.

R. I. Issa. Solution of the implicitly discretised fluid flow equations by operator-splitting. *J. Comput. Phys.*, 62(1):40–65, 1986.

H. A. Jakobsen, B. H. Sannæs, S. Grevskott, and H. F. Svendsen. Modeling of vertical bubble-driven flows. *Ind. Eng. Chem. Res.*, 36(10):4052–4074, 1997.

H. A. Jakobsen, H. Lindborg, and C. A. Dorao. Modeling of bubble column reactors: Progress and limitations. *Ind. Eng. Chem. Res.*, 44(14):5107–5151, 2005.

J. J. M. Janssen, A. Boon, and W. G. M. Agterof. Influence of dynamic interfacial properties on droplet breakup in simple shear flow. *AlChE J.*, 40(12):1929–1939, 1994.

D. Jeon, E. Graff, and M. Gharib. Measurement of large scale bubbly flows. In 27^{th} *Symposium on Naval Hydrodynamics*, Seoul, Korea, 2008.

J. P. Johansen, A. M. Castro, and P. M. Carrica. Full-scale two-phase flow measurements on Athena research vessel. *Int. J. Multiphase Flow*, 36(9):720 – 737, 2010.

A. Kamp, A. Chesters, C. Colin, and J. Fabre. Bubble coalescence in turbulent flows: A mechanistic model for turbulence-induced coalescence applied to microgravity bubbly pipe flow. *Int. J. Multiphase Flow*, 27(8):1363–1396, 2001.

I. Kataoka, A. Serizawa, and D. C. Besnard. Prediction of turbulence suppression and turbulence modeling in bubbly two-phase flow. *Nucl. Eng. Des.*, 141(1-2): 145–158, 1993.

R. D. Kirkpatrick and M. J. Lockett. The influence of approach velocity on bubble coalescence. *Chem. Eng. Sci.*, 29(12):2363 – 2373, 1974.

E. Krepper, D. Lucas, and H.-M. Prasser. On the modelling of bubbly flow in vertical pipes. *Nucl. Eng. Des.*, 235(5):597 – 611, 2005.

S. Kumar and D. Ramkrishna. On the solution of population balance equations by discretization–I. a fixed pivot technique. *Chem. Eng. Sci.*, 51(8):1311 – 1332, 1996.

R. F. Kunz, W. S. Yu, S. P. Antal, and S. M. Ettorre. An unstructured two fluid method based on the coupled phasic exchange algorithm. In 15^{th} *AIAA Computational Fluid Dynamics Conference*, Anaheim, California, 2001. AIAA-2001-2672.

R. F. Kunz, H. J. Gibeling, M. R. Maxey, G. Tryggvason, A. A. Fontaine, H. L. Petrie, and S. L. Ceccio. Validation of two-fluid eulerian CFD modeling for microbubble drag reduction across a wide range of reynolds numbers. *J. Fluids Eng.*, 129(1): 66–79, 2007.

M. Laakkonen, P. Moilanen, T. Miettinen, K. Saari, M. Honkanen, P. Saarenrinne, and J. Aittamaa. Local bubble size distributions in agitated vessel: Comparison of three experimental techniques. *Chem. Eng. Res. Des.*, 83(1):50 – 58, 2005.

R. T. Lahey Jr. The simulation of multidimensional multiphase flows. *Nucl. Eng. Des.*, 235(10-12):1043–1060, 2005.

R. T. Lahey Jr. and D. A. Drew. The analysis of two-phase flow and heat transfer using a multidimensional, four field, two-fluid model. *Nucl. Eng. Des.*, 204(1-3): 29–44, 2001.

R. T. Lahey Jr., D. A. Drew, S. Kalkach-Navarro, and J. W. Park. The relationship between void waves and flow regime transition. In *Int. Conf. on Multiphase Flow Instabilities*, INSA de Rouen, 1992.

R. T. Lahey Jr., M. Lopez de Bertodano, and O. C. Jones Jr. Phase distribution in complex geometry conduits. *Nucl. Eng. Des.*, 141(1-2):177–201, 1993.

R. Latorre, A. Miller, and R. Philips. Micro-bubble resistance reduction on a model SES catamaran. *Ocean Eng.*, 30(17):2297–2309, 2003.

F. Laurent, M. Massot, and P. Villedieu. Eulerian multi-fluid modeling for the numerical simulation of coalescence in polydisperse dense liquid sprays. *J. Comput. Phys.*, 194(2):505–543, 2004.

D. Legendre and J. Magnaudet. The lift force on a spherical bubble in a viscous linear shear flow. *J. Fluid Mech.*, 368:81–126, 1998.

F. Lehr, M. Millies, and D. Mewes. Bubble-size distributions and flow fields in bubble columns. *AlChE J.*, 48(11):2426–2443, 2002.

G. J. Lengyel. Department of Defense Energy Strategy. Teaching an Old Dog New Tricks, 2007. The Brookings Institution, Washington, D.C.

V. G. Levich. *Physicochemical Hydrodynamics*. Prentice Hall, New York, 1962.

Y. Liao and D. Lucas. A literature review of theoretical models for drop and bubble breakup in turbulent dispersions. *Chem. Eng. Sci.*, 64(15):3389 – 3406, 2009.

S. Lo and D. Zhang. Modelling of break-up and coalescence in bubbly two-phase flows. *J. Comput. Multiph. Flows*, 1(1):23–38, 2009.

M. Lopez de Bertodano, R. T. Lahey Jr., and O. C. Jones. Development of a k-ε model for bubbly two-phase flow. *J. Fluids Eng.*, 116, 1994.

M. Lopez de Bertodano, F. J. Moraga, D. A. Drew, and R. T. Lahey Jr. The modeling of lift and dispersion forces in two-fluid model simulations of a bubbly jet. *J. Fluids Eng.*, 126(4):573–577, 2004.

L. O. Lübke. Numerical simulation of the flow around the propelled KCS. In *CFDWS05*, Tokyo, Japan, 2005.

D. Lucas, E. Krepper, and H.-M. Prasser. Use of models for lift, wall and turbulent dispersion forces acting on bubbles for poly-disperse flows. *Chem. Eng. Sci.*, 62 (15):4146 – 4157, 2007.

H. Luo and H. F. Svendsen. Theoretical model for drop and bubble breakup in turbulent dispersions. *AlChE J.*, 42(5):1225–1233, 1996a.

H. Luo and H. F. Svendsen. Modeling and simulation of binary approach by energy conservation analysis. *Chem. Eng. Commun.*, 145(1):145–153, 1996b.

J. Ma, A. A. Oberai, D. A. Drew, R. T. Lahey Jr., and F. J. Moraga. A quantitative sub-grid air entrainment model for bubbly flows – plunging jets. *Comput. Fluids*, 39(1):77–86, 2010a.

J. Ma, A. A. Oberai, M. C. Hyman, R. T. Lahey Jr., and D. A. Drew. A generalized subgrid air entrainment model for RaNS modeling of bubbly flows around ship hulls. In *7th International Conference on Multiphase Flow - ICMF 2010 Proceedings*, Tampa, Florida, 2010b.

J. Ma, A. A. Oberai, R. T. Lahey Jr., and D. A. Drew. Modeling air entrainment and transport in a hydraulic jump using two-fluid RANS and DES turbulence models. *Heat Mass Transfer*, 2011. DOI: 10.1007/s00231-011-0867-8.

M. Manninen and V. Taivassalo. On the mixture model for multiphase flow. VTT Publications 288, Technical Research Centre of Finland, 1996.

C. Marchioli, M. Fantoni, and A. Soldati. Orientation, distribution, and deposition of elongated, inertial fibers in turbulent channel flow. In *7th International Conference on Multiphase Flow - ICMF 2010 Proceedings*, Tampa, Florida, 2010.

D. Marchisio and R. Fox. Solution of population balance equations using the direct quadrature method of moments. *J. Aerosol Sci.*, 36(1):43–73, 2005.

G. Marrucci. A theory of coalescence. *Chem. Eng. Sci.*, 24(6):975 – 985, 1969.

C. Martínez-Bazán, J. L. Montañés, and J. C. Lasheras. On the breakup of an air bubble injected into a fully developed turbulent flow. Part 1. Breakup frequency. *J. Fluid Mech.*, 401:157–182, 1999a.

C. Martínez-Bazán, J. L. Montañés, and J. C. Lasheras. On the breakup of an air bubble injected into a fully developed turbulent flow. Part 2. Size PDF of the resulting daughter bubbles. *J. Fluid Mech.*, 401:183–207, 1999b.

R. McGraw. Description of aerosol dynamics by the quadrature method of moments. *Aerosol Science and Technology*, 27(2):255–265, 1997.

W. K. Melville, E. J. Terrill, and L. Ding. Field measurements of air entrainment by breaking waves. In *Third International Symposium on AirWater Gas Transfer*, pages 285–295, 1995.

F. R. Menter. Two-equation eddy-viscosity turbulence models for engineering applications. *AIAA J.*, 32:1598 – 1605, 1994.

F. Moraga, A. Larreteguy, D. Drew, and R. T. Lahey Jr. A center-averaged two-fluid model for wall-bounded bubbly flows. *Comput. Fluids*, 35(4):429 – 461, 2006.

F. J. Moraga, A. E. Larreteguy, D. A. Drew, and R. T. Lahey Jr. Assessment of turbulent dispersion models for bubbly flows in the low stokes number limit. *Int. J. Multiphase Flow*, 29(4):655 – 673, 2003.

F. J. Moraga, P. M. Carrica, D. A. Drew, and R. T. Lahey Jr. A sub-grid air entrainment model for breaking bow waves and naval surface ships. *Comput. Fluids*, 37(3): 281 – 298, 2008.

C. Morel, P. Ruyer, N. Seiler, and J. M. Laviville. Comparison of several models for multi-size bubbly flows on an adiabatic experiment. *Int. J. Multiphase Flow*, 36 (1):25–39, 2010.

N. Müller-Fischer, P. Tobler, M. Dressler, P. Fischer, and E. J. Windhab. Single bubble deformation and breakup in simple shear flow. *Exp. Fluids*, 45:917–926, 2008.

Y. Murai, H. Fukuda, Y. Oishi, Y. Kodama, and F. Yamamoto. Skin friction reduction by large air bubbles in a horizontal channel flow. *Int. J. Multiphase Flow*, 33(2): 147 – 163, 2007.

S. Navarro-Valenti, A. Clausse, D. Drew, and R. T. Lahey Jr. A contribution to the mathematical modeling of bubbly/slug flow regime transition. *Chem. Eng. Commun.*, 102(1):69–85, 1991.

R. Noack. SUGGAR: a general capability for moving body overset grid assembly. In 17^{th} *AIAA Computational Fluid Dynamics Conference*, Toronto, Ontario, Canada, 2005.

T. O. Oolman and H. W. Blanch. Bubble coalescence in stagnant liquids. *Chem. Eng. Commun.*, 43:237 – 261, 1986.

S. Osher and J. A. Sethian. Fronts propagating with curvature-dependent speed: algorithms based on hamilton-jacobi formulations. *J. Comput. Phys.*, 79(1):12 – 49, 1988.

K.-J. Paik, P. M. Carrica, D. Lee, and K. Maki. Strongly coupled fluid-structure interaction method for structural loads on surface ships. *Ocean Eng.*, 36(17-18): 1346 – 1357, 2009.

R. Pankajakshan, M. G. Remotigue, L. K. Taylor, M. Jiang, W. R. Briley, and D. L. Whitfield. Validation of control-surface induced submarine maneuvering simulations using UNCLE. In 24^{th} *Symposium on Naval Hydrodynamics*, Fukuoka, Japan, 2002.

N. A. Patankar and D. D. Joseph. Lagrangian numerical simulation of particulate flows. *Int. J. Multiphase Flow*, 27(10):1685–1706, 2001.

E. G. Paterson, M. Hyman, F. Stern, P. M. Carrica, F. Bonetto, D. A. Drew, and R. T. Lahey Jr. Near- and far-field CFD for a naval combatant including thermal-stratification and two-fluid modeling. In *Proceedings of the* 21^{st} *Symposium on Naval Hydrodynamics*, Trondheim, Norway. National Academy Press, Washington, DC., 1996.

M. Petitti, A. Nasuti, D. L. Marchisio, M. Vanni, G. Baldi, N. Mancini, and F. Podenzani. Bubble size distribution modeling in stirred gas-liquid reactors with QMOM augmented by a new correction algorithm. *AlChE J.*, 56(1):36–53, 2010.

M. S. Politano, P. M. Carrica, and J. Converti. A model for turbulent polydisperse two-phase flow in vertical channels. *Int. J. Multiphase Flow*, 29(7):1153 – 1182, 2003.

M. S. Politano, P. M. Carrica, and L. J. Weber. A multiphase model for the hydrodynamics and total dissolved gas in tailraces. *Int. J. Multiphase Flow*, 35(11):1036 – 1050, 2009.

S. B. Pope. *Turbulent flows*. Cambridge University Press, 2000.

M. J. Prince and H. W. Blanch. Bubble coalescence and break-up in air-sparged bubble columns. *AlChE J.*, 36(10):1485 – 1499, 1990a.

M. J. Prince and H. W. Blanch. Transition electrolyte concentrations for bubble coalescence. *AlChE J.*, 36(9):1425 – 1429, 1990b.

R. Raju, C.-T. Hsiao, and G. L. Chahine. Influence of propeller presence and cavitation on liquid nuclei population. In *CAV2009 - 7th International Symposium on Cavitation*, Ann Arbor, MI, 2009.

S. H. Rhee and F. Stern. Unsteady RANS method for surface ship boundary layer and wake and wave field. *Int. J. Numer. Methods Fluids*, 37(4):445–478, 2001.

W. C. Sanders, E. S. Winkel, D. R. Dowling, M. Perlin, and S. L. Ceccio. Bubble friction drag reduction in a high-reynolds-number flat-plate turbulent boundary layer. *J. Fluid Mech.*, 552:353–380, 2006.

J. Sanyal, S. Vásquez, S. Roy, and M. P. Dudukovic. Numerical simulation of gas-liquid dynamics in cylindrical bubble column reactors. *Chem. Eng. Sci.*, 54(21): 5071–5083, 1999.

Y. Sato, M. Sadatomi, and K. Sekoguchi. Momentum and heat transfer in two-phase bubble flow–I. theory. *Int. J. Multiphase Flow*, 7(2):167–177, 1981a.

Y. Sato, M. Sadatomi, and K. Sekoguchi. Momentum and heat transfer in two-phase bubble flow–II. a comparison between experimental data and theoretical calculations. *Int. J. Multiphase Flow*, 7(2):179–190, 1981b.

D. P. Schmidt and C. Rutland. A new droplet collision algorithm. *J. Comput. Phys.*, 164(1):62–80, 2000.

M. H. Sharqawy, J. H. Lienhard V, and S. M. Zubair. Thermophysical properties of seawater: A review of existing correlations and data. *Desalin. Water Treat.*, 16:354 – 380, 2010.

P. N. Singh and D. Ramkrishna. Solution of population balance equations by MWR. *Comput. Chem. Eng.*, 1(1):23–31, 1977.

M. Sommerfeld. Modelling particle collisions and agglomeration in gas-particle flows. In *7th International Conference on Multiphase Flow - ICMF 2010 Proceedings*, Tampa, Florida, 2010.

Tecplot, Inc. http://www.tecplot.com.

E. J. Terril and T. Fu. At-sea measurements for ship hydromechanics. In 27^{th} *Symposium on Naval Hydrodynamics*, Seoul, Korea, 2008.

E. J. Terril, K. Melville, G. Lada, M. Otero, J. Hazard, T. Harris, A. Pierson, B. Middleton, and T. Jenkins. 2004 field measurements. 2005 ONR Bubbly Flows Program Review. Pasadena, CA., 2005.

E. J. Terrill, W. K. Melville, and D. Stramski. Bubble entrainment by breaking waves and their influence on optical scattering in the upper ocean. *J. Geophys. Res.*, 106 (C8):16815–16823, 2001.

R. M. Thomas. Bubble coalescence in turbulent flows. *Int. J. Multiphase Flow*, 7(6): 709 – 717, 1981.

J. F. Thompson, Z. U. A. Warsi, and C. W. Mastin. *Numerical grid generation: foundations and applications*. North-Holland, 1985.

A. Tomiyama. Struggles with computational bubble dynamics. In *Proceedings of the third international conference on multiphase flows, ICMF98*, Lyon, France, 1998.

A. Tomiyama, H. Tamai, I. Zun, and S. Hosokawa. Transverse migration of single bubbles in simple shear flows. *Chem. Eng. Sci.*, 57(11):1849 – 1858, 2002.

A. Travin, M. Shur, M. Strelets, and P. R. Spalart. Physical and numerical upgrades in the detached-eddy simulation of complex turbulent flows. In R. Friedrich and W. Rodi, editors, *Advances in LES of Complex Flows*, volume 65 of *Fluid Mechanics and Its Applications*, pages 239–254. Springer Netherlands, 2004. ISBN 978-0-306-48383-7.

M. V. Trevorrow, S. Vagle, and D. M. Farmer. Acoustical measurements of microbubbles within ship wakes. *J. Acoust. Soc. Am.*, 95:1922–1930, 1994.

A. A. Troshko and Y. A. Hassan. A two-equation turbulence model of turbulent bubbly flows. *Int. J. Multiphase Flow*, 27(11):1965 – 2000, 2001a.

A. A. Troshko and Y. A. Hassan. Law of the wall for two-phase turbulent boundary layers. *Int. J. Heat Mass Transfer*, 44(4):871 – 875, 2001b.

Y. H. Tsang, Y.-H. Koh, and D. L. Koch. Bubble-size dependence of the critical electrolyte concentration for inhibition of coalescence. *J. Colloid. Interf. Sci.*, 275 (1):290 – 297, 2004.

UNCTAD. Maritime transport and the climate change challenge. In *United Nations Conference on Trade and Development. Summary of Proceedings*, Geneva, 2009.

S. O. Unverdi and G. Tryggvason. A front-tracking method for viscous, incompressible, multi-fluid flows. *J. Comput. Phys.*, 100:25–37, 1992.

J. F. Walter and H. W. Blanch. Bubble break-up in gas–liquid bioreactors: Break-up in turbulent flows. *Chem. Eng. J. Bioch. Eng.*, 32(1):B7 – B17, 1986.

T. Wang, J. Wang, W. Yang, and Y. Jin. Bubble behavior in gas-liquid-solid three-phase circulating fluidized beds. *Chem. Eng. J.*, 84(3):397 – 404, 2001.

T. Wang, J. Wang, and Y. Jin. A novel theoretical breakup kernel function for bubbles/droplets in a turbulent flow. *Chem. Eng. Sci.*, 58(20):4629 – 4637, 2003.

T. Wang, J. Wang, and Y. Jin. Population balance model for gas-liquid flows: Influence of bubble coalescence and breakup models. *Ind. Eng. Chem. Res.*, 44 (19):7540–7549, 2005a.

T. Wang, J. Wang, and Y. Jin. Theoretical prediction of flow regime transition in bubble columns by the population balance model. *Chem. Eng. Sci.*, 60(22):6199 – 6209, 2005b. 7th International Conference on Gas-Liquid and Gas-Liquid-Solid Reactor Engineering.

T. Wang, J. Wang, and Y. Jin. A CFD-PBM coupled model for gas-liquid flows. *AIChE Journal*, 52(1):125–140, 2006.

R. M. Wellek, A. K. Agrawal, and A. H. P. Skelland. Shape of liquid drops moving in liquid media. *AlChE J.*, 12(5):854–862, 1966.

G. Weymouth, R. V. Wilson, and F. Stern. RANS CFD predictions of pitch and heave ship motions in head seas. *J. Ship. Res.*, 49:80–97, 2005.

S. Whitaker. Forced convection heat transfer correlations for flow in pipes, past flat plates, single cylinders, single spheres, and for flow in packed beds and tube bundles. *AlChE J.*, 18(2):361 – 371, 1972.

D. C. Wilcox. Reassessment of the scale-determining equation for advanced turbulence models. *AIAA J.*, 26:1299–1310, 1988.

D. C. Wilcox. *Turbulence modeling for CFD*. DCW Industries, 2006.

M. M. R. Williams and S. K. Loyalka. *Aerosol science: theory and practice : with special applications to the nuclear industry*. Pergamon Press, 1991.

R. V. Wilson and F. Stern. Unsteady CFD method for naval combatants in waves. In 22nd *ONR Symposium on Naval Hydrodynamics*, Washington, DC, U.S.A., 1998.

R. V. Wilson, F. Stern, H. W. Coleman, and E. G. Paterson. Comprehensive approach to verification and validation of CFD simulations—part 2: application for RANS simulation of a cargo/container ship. *J. Fluids Eng.*, 123(4):803–810, 2001.

Q. Wu, S. Kim, M. Ishii, and S. G. Beus. One-group interfacial area transport in vertical bubbly flow. *Int. J. Heat Mass Transfer*, 41(8-9):1103–1112, 1998.

T. Xing, J. Shao, and F. Stern. BKW- RS-DES of unsteady vortical flow for KVLCC2 at large drift angles. In 9^{th} *International Conference on Numerical Ship Hydrodynamics*, Ann Arbor, Michigan, 2007.

J. Xu, M. R. Maxey, and G. E. Karniadakis. Numerical simulation of turbulent drag reduction using micro-bubbles. *J. Fluid Mech.*, 468:271–281, 2002.

J. Yang, S. Bhushan, J. S. Suh, Z. Wang, B. Koo, N. Sakamoto, T. Xing, and F. Stern. Large-eddy simulation of ship flows with wall-layer models on cartesian grids. In 27^{th} *Symposium on Naval Hydrodynamics*, Seoul, Korea, 2008.

D. Zhang, N. Deen, and J. A. Kuipers. Numerical simulation of the dynamic flow behavior in a bubble column: A study of closures for turbulence and interface forces. *Chem. Eng. Sci.*, 61(23):7593 – 7608, 2006.

X. Zhang and G. Ahmadi. Eulerian-Lagrangian simulations of liquid-gas-solid flows in three-phase slurry reactors. *Chemical Engineering Science*, 60(18):5089–5104, 2005.